Understanding surface and sub-surface phenomena in nickel-based superalloy castings

Matthew Colin Appleton

Darwin College

University of Cambridge

United Kingdom

A dissertation submitted for the degree of Doctor of Engineering

February 2017

Understanding surface and sub-surface phenomena in nickel-based superalloy castings – Matthew Colin Appleton

Nickel-based superalloys are high-temperature materials, created to operate in the aggressive conditions found within gas turbine engines. Single crystal turbine blades are investment cast, followed by a complex series of operations including heat treatment, machining, blasting, etching and polishing to produce a product ready for coating. Coating systems provide environmental protection, tribological resistance and enable efficient gas-path sealing. This thesis seeks to examine the root causes of various defects and features that render components unsuitable for service. The impact of increasing our understanding of these expensive materials is to increase process yield, and thus lower unit costs

Investment casting of turbine blades is highly challenging; despite tight process control some variability in manufacturing operations results in scrapped components. Internal surface melting was found on intermediate pressure turbine blades following high-temperature heat-treatment; it consists of a layer enriched in aluminium and tantalum on the surface of the internal cooling passage. The discovery led to a systematic investigation of the silica-based ceramic cores used to form the cooling passage to better understand core / casting interactions. The silica-based core displayed a degree of pressure assisted liquid phase sintering at those locations where the nickel-based superalloy exerted a crushing force on the surface due to differential contraction after solidification. The areas affected matched that which later displayed surface melting. This was clearly related to casting height since the severity of pressure assisted liquid phase sintering could be mapped and decreased with the height of the casting. Further findings include the formation of a thin alumina layer at the interface between the superalloy and the silica-based core, this layer prevents volatilisation or sublimation from the surface of the component during the heat treatment. In the bespoke castings undertaken to further explore this phenomena clear evidence emerged of zircon particles, an integral constituent of the core, pinning the superalloy during the casting process. The result was a rough undulating surface with depressions formed by the hard, immovable zircon particles and peaks where the small silica grains where able to sinter and retreat against the pressure of the superalloy. A theory has been proposed that these zircon particles effectively indent the casting in specific locations at high temperatures. At the top of the casting where more effective stress and strain are experienced, this can translate into local stresses reaching the threshold for inducing recrystallisation during subsequent heat treatment.

High pressure turbine blades are coated using the aluminising process to provide oxidation resistance at high operating temperatures. Masking is applied to those areas that need to be left bare. Unfortunately these masking materials are not inert at the deposition temperatures, leading to the inadvertent carburisation of a sub-surface layer of the blade

alloy. Elemental carbon forms as the polymer-based binder thermally degrades during the ramp to aluminising deposition temperatures of ca 1030°C. This highly mobile elemental carbon moves interstitially through the superalloy where its concentration is at its maximum just beneath the surface. If the temperature is high enough to enable the precipitation of carbides before the carbon source is depleted, then very small carbides form in the γ channels. These carbides are detrimental in that they tie up the elements molybdenum, tantalum and tungsten. Very numerous small 'proto-carbides' form immediately beneath the surface and inhibit further growth of the larger carbides by depleting the finite carbon source. 'River-lines' of earlier elemental segregation can lead to the preferential formation of carbides in strings that wind through the material and alternative morphologies include carbide platelets that sit upon the (111) planes. The final carbide morphology seen was larger and consisted of a two-layer structure, the inner core most likely comprises a titanium-based carbo-nitride whilst the outer layer forms later upon the surface of the core and is composed of molybdenum, tantalum and tungsten. As the carbide forms it denudes the surrounding γ/γ' of important strengthening elements. Work has been undertaken to better understand the processing parameters which generate these undesired precipitates in an attempt to mitigate their effects.

Slurry aluminide coatings are a cost-effective protective coating widely used in gas turbine engines, but new restrictions on additives, especially hexavalent chromates, challenge the established coating systems. Before progress can be made on developing more environmentally-friendly alternatives the current state-of-the-art process needs to be investigated and understood. In this work, a water-based industry-standard slurry, has been air sprayed on three nickel-based superalloys designed for blade applications. The alloys were in an as-cast or solution heat-treated condition, before a diffusion heat treatment was used to form the coating microstructure ready for service operation. Altering the underlying substrate resulted in the formation of markedly different microstructures within the final coating and has implications for in-service corrosion resistance. It was found that the concentration of key elements, such as chromium, tungsten and cobalt are evenly distributed throughout the newly-formed coating, this is a departure from the more traditional inward or outward growing aluminides formed by pack or vapour methods. The formation of the slurry aluminide is accompanied by a volume expansion as the nickel used to form the NiAl intermetallic is extracted from the FCC nickel-based superalloy. The slurry deposited consists predominantly of aluminium and silicon. A clear gradient in grain size for the dispersed silicide phase strongly supports a cascading reaction mechanism that slowly consumes the substrate through the wetting of the surface by liquid aluminium before a rapid surge of exothermic energy causes the newly formed coating to break away from the surface and move up in to the mushy coating above.

Preface

This dissertation is submitted to the University of Cambridge in fulfilment of the requirements of the degree of Doctor of Engineering. The work described herein was conducted at the University of Cambridge in the Department of Materials Science and Metallurgy and within Rolls-Royce Plc (Derby) between October 2012 and November 2016, under the academic supervision of Professor C.M.F. Rae and the industrial supervision of Dr. G.J.J. Brewster. The content of this dissertation is entirely original and is the result of my own work which, unless where stated, includes nothing that is the outcome of collaborative work. This dissertation is less than 60,000 words in length.

Matthew C Appleton

February, 2017

Acknowledgements

I would like to sincerely thank my academic supervisor, Professor Cathie Rae, for all of the time and effort spent supporting me throughout the course of my EngD. The enthusiasm and patience with which Professor Rae has approached my research has been genuinely appreciated.

I would also like to thank my industrial supervisor Dr. Gyn Brewster for being optimistic and helping to drive my work forwards, always with humour and positivity.

I owe a great debt of gratitude to the Rolls-Royce Corporate Surface Engineering Group for helping me, teaching me and giving me plenty of laughs along the way. I especially want to thank: Glen Pattinson, Lloyd Pallett, Alan Johnstone, Jonathan Leggett and Andrew Hewitt.

I want to thank the Rolls-Royce UTC group at the University of Cambridge for making me feel welcome every single time I was there. I'm grateful to all who assisted, worked with me or simply asked how I was getting on.

Thanks goes to the research and development technicians at Turbines Surface Technology Ltd: Manny Mudhar, Mick Taylor and Andrew Laidlaw. They have always been willing and able to help me when I needed it.

Carburisation project

Thanks goes to James Carroll of Turbines Surface Technology Ltd for always being helpful, kind and courteous.

Melting project

For this project I enlisted help from the following Rolls-Royce Plc employees: Dr. Paul Withey, Dean Welton, Dr. Duncan Putman, Zoe Forsyth and Dr. Neil D'Souza. Each has been exemplary, professional and capable.

I was ably assisted by two technicians from the University of Birmingham: Grant Holt and Peter Cranmer. The EPMA work at the University of Edinburgh would not have been possible without the assistance of Dr Chris Hayward.

Slurry diffusion project

From the University of Cambridge I wish to thank Dr. Olivier Messé and Alison Wilson for helping to run analysis on my behalf. Equally I wish to acknowledge the assistance from researchers at Loughborough University: Dr. Zhaoxia Zhou and Dr. Geoff West who were both instrumental in performing TEM work which was invaluable in this project.

Thanks goes to Richard Banks of Indestructible Paint Ltd. for coating test specimens without which this project would not have proceeded.

I would also like to thank my brother, Christopher Appleton for his contribution to the some of the diagrams in this work which he created for me.

I would like to especially mention some individuals who have enabled me to complete this work.

Firstly I want to sincerely thank Steve and Lucy Lainé for providing me somewhere to stay during my visits to Cambridge, I was always made to feel welcome in their home and I will miss seeing them as frequently as I once did. I wish them both, and newly arrived baby Mori, all the best for their future.

I wish to thank my parents, Peter and Julie, for all they have done to get me here. They have always been supportive and positive, I wish them many happy years in their new home by the sea.

Finally I wish to thank my fiancée Laura, for being there, for listening to me and for saying yes.

Abstract

Nickel-based superalloys are high-temperature materials, created to operate in the aggressive conditions found within gas turbine engines. Single crystal turbine blades are investment cast, followed by a complex series of operations including heat treatment, machining, blasting, etching and polishing to produce a product ready for coating. Coating systems provide environmental protection, tribological resistance and enable efficient gas-path sealing. This thesis seeks to examine the root causes of various defects and features that render components unsuitable for service. The impact of increasing our understanding of these expensive materials is to increase process yield, and thus lower unit costs

Investment casting of turbine blades is highly challenging; despite tight process control some variability in manufacturing operations results in scrapped components. Internal surface melting was found on intermediate pressure turbine blades following high-temperature heat-treatment; it consists of a layer enriched in aluminium and tantalum on the surface of the internal cooling passage. The discovery led to a systematic investigation of the silica-based ceramic cores used to form the cooling passage to better understand core / casting interactions. The silica-based core displayed a degree of pressure assisted liquid phase sintering at those locations where the nickel-based superalloy exerted a crushing force on the surface due to differential contraction after solidification. The areas affected matched that which later displayed surface melting. This was clearly related to casting height since the severity of pressure assisted liquid phase sintering could be mapped and decreased with the height of the casting. Further findings include the formation of a thin alumina layer at the interface between the superalloy and the silica-based core, this layer prevents volatilisation or sublimation from the surface of the component during the heat treatment. In the bespoke castings undertaken to further explore this phenomena clear evidence emerged of zircon particles, an integral constituent of the core, pinning the superalloy during the casting process. The result was a rough undulating surface with depressions formed by the hard, immovable zircon particles and peaks where the small silica grains where able to sinter and retreat against the pressure of the superalloy. A theory has been proposed that these zircon particles effectively indent the casting in specific locations at high temperatures. At the top of the casting where more effective stress and strain are experienced, this can translate into local stresses reaching the threshold for inducing recrystallisation during subsequent heat treatment.

High pressure turbine blades are coated using the aluminising process to provide oxidation resistance at high operating temperatures. Masking is applied to those areas that need to be left bare. Unfortunately these masking materials are not inert at the deposition temperatures, leading to the inadvertent carburisation of a sub-surface layer of the blade

alloy. Elemental carbon forms as the polymer-based binder thermally degrades during the ramp to aluminising deposition temperatures of ca 1030°C. This highly mobile elemental carbon moves interstitially through the superalloy where its concentration is at its maximum just beneath the surface. If the temperature is high enough to enable the precipitation of carbides before the carbon source is depleted, then very small carbides form in the γ channels. These carbides are detrimental in that they tie up the elements molybdenum, tantalum and tungsten. Very numerous small 'proto-carbides' form immediately beneath the surface and inhibit further growth of the larger carbides by depleting the finite carbon source. 'River-lines' of earlier elemental segregation can lead to the preferential formation of carbides in strings that wind through the material and alternative morphologies include carbide platelets that sit upon the (111) planes. The final carbide morphology seen was larger and consisted of a two-layer structure, the inner core most likely comprises a titanium-based carbo-nitride whilst the outer layer forms later upon the surface of the core and is composed of molybdenum, tantalum and tungsten. As the carbide forms it denudes the surrounding γ/γ' of important strengthening elements. Work has been undertaken to better understand the processing parameters which generate these undesired precipitates in an attempt to mitigate their effects.

Slurry aluminide coatings are a cost-effective protective coating widely used in gas turbine engines, but new restrictions on additives, especially hexavalent chromates, challenge the established coating systems. Before progress can be made on developing more environmentally-friendly alternatives the current state-of-the-art process needs to be investigated and understood. In this work, a water-based industry-standard slurry, has been air sprayed on three nickel-based superalloys designed for blade applications. The alloys were in an as-cast or solution heat-treated condition, before a diffusion heat treatment was used to form the coating microstructure ready for service operation. Altering the underlying substrate resulted in the formation of markedly different microstructures within the final coating and has implications for in-service corrosion resistance. It was found that the concentration of key elements, such as chromium, tungsten and cobalt are evenly distributed throughout the newly-formed coating, this is a departure from the more traditional inward or outward growing aluminides formed by pack or vapour methods. The formation of the slurry aluminide is accompanied by a volume expansion as the nickel used to form the NiAl intermetallic is extracted from the FCC nickel-based superalloy. The slurry deposited consists predominantly of aluminium and silicon. A clear gradient in grain size for the dispersed silicide phase strongly supports a cascading reaction mechanism that slowly consumes the substrate through the wetting of the surface by liquid aluminium before a rapid surge of exothermic energy causes the newly formed coating to break away from the surface and move up in to the mushy coating above.

Contents

1. General introduction

1.1. Gas turbine engines

Gas turbine engines convert chemical potential energy into aircraft propulsion, electrical generation or facilitate gas extraction upon oil rigs. The gas passing through the core of the engine goes through four stages; compression, combustion, expansion and exhaust. Simple turbojets ingest air to be compressed and mixed with fuel before ignition within the combustor. Expanding combustion gases flow through the turbine and are exhausted through the rear nozzle providing propulsive thrust. The Carnot and Brayton cycles provide useful insight into thermodynamic changes occurring within a gas turbine engine. [1,2]

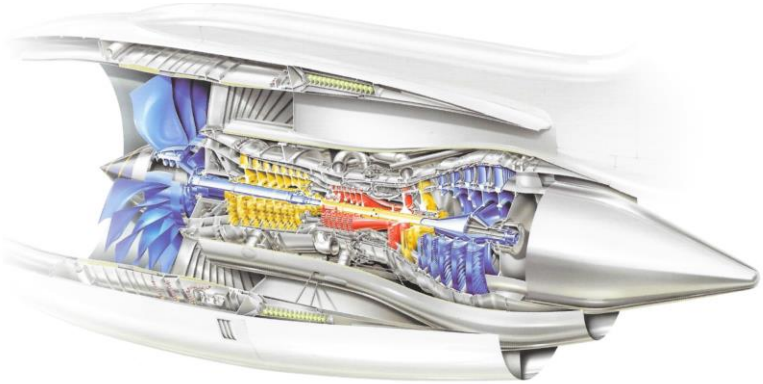

Fig. 1.1 – civil aviation gas turbine engine; blue denotes the low pressure system, yellow is the intermediate pressure system and red is the high pressure system [1]

Modern axial compressors, linked by shafts, rotate with energy extracted from the hot gas stream by rotor blades attached at the turbine discs' outer circumference. These turbine blades alternate with stationary aerofoils which modify airflow speed and direction to direct the expanding combustion gases.[1] Civil turbofan engines today regularly feature high-bypass ratios, of ca 10:1, to gain economic advantage through higher propulsive efficiency. The bypass ratio is the ratio between the total mass of air that enters through the fan that bypasses the engine core (un-combusted) to the mass of air flowing through the engine core. Only Rolls-Royce plc utilise the more complex three shaft architecture, over two shafts, this choice results in separation of the fan and the high-pressure compressor allowing different shaft speeds, enabling optimal stage velocity and aerodynamic advantages. An example of one of these engines comprises:

- A low-pressure system including a single fan being powered by five turbine stages
- An intermediate-pressure system made up of eight compressor stages driven by a single turbine stage
- A high-pressure system including six compressor stages driven by a single turbine stage [3]

Materials for application in gas turbines are optimised by balancing and maximising the following criteria:

Customer requirements	Design requirements
Safety ↑	Strength ↑
Performance ↑	Temperature capability ↑
Environmental impact ↓	Density ↓
Cost ↓	Cost ↓

Table. 1.1 – engine materials improvement criteria [4]

High-pressure turbine blades are the key power harnessing component of the gas turbine engine; simultaneously withstanding high centrifugal loading, cyclic loading, vibration and significant temperatures whilst resisting rapid oxidation and corrosion due to the complex environment. [4]

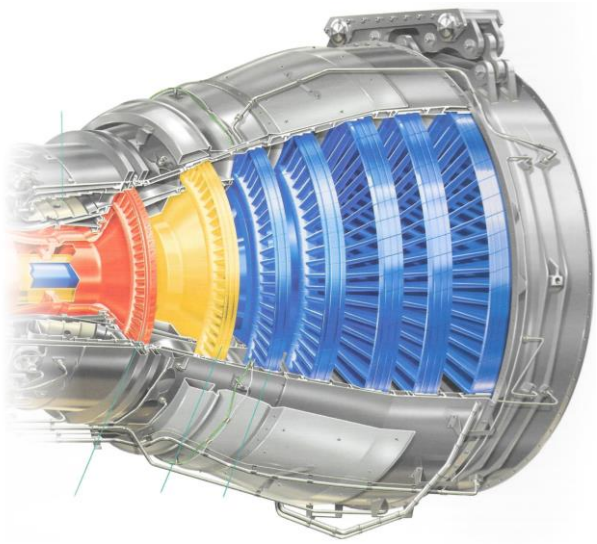

Fig. 1.2 – engine turbine stages [1]

1.2. Turbine blades

Turbine blades extract power from rapidly moving, expanding gases upon the blade aerofoil and transfer it to rotating turbine discs via a 'fir-tree' root configuration. Higher turbine entry temperatures increase the power available from the turbine as well as increasing overall engine thermal efficiency, which is highly desirable. Turbine entry temperatures for a large civil engine today regularly exceed 1600°C, posing a significant materials challenge which is overcome through innovative design and modern materials technology. [1]

These high turbine entry temperatures mean blades today incorporate cooling air driven through internal passages before exiting through rows of holes to provide both internal convection and a protective external film of cooler gas. The drive to incorporate such internal cooling was a result of available materials reaching both thermal and mechanical limits. Cooling gas is bled from the high-pressure compressor and feed into each turbine blade though the drawback of internal cooling is that siphoned gas from the compressor is no longer available for combustion within the engine core despite having already being compressed. [5]

The blades' internal passage incorporates high surface area features to better facilitate heat transfer to the passing gas; which in effect lowers the component temperature during operation. [2] Direct axial stresses on turbine blades are as a result of high centrifugal loading during engine operation. Additional stresses are induced by bending moments incurred from turning high-pressure gas across the blades' aerodynamic surface but are small relative to the axial load. The life of high-pressure blades can be limited by creep, oxidation and thermal fatigue mechanisms. Creep is the gradual extension of a material under stress at high temperature and is a function of the time held under load. [6] Low cycle fatigue is a function of the number of operating cycles the blade endures, this is how many times the engine is started, accelerated and stopped with the expected raising and lowering of the turbine temperature.

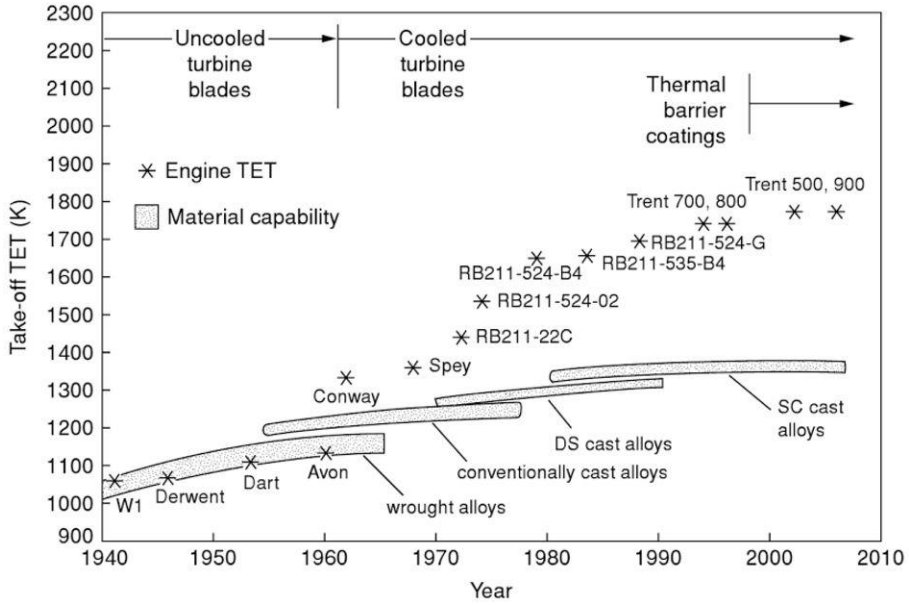

Fig. 1.3 – progress of turbine entry temperature capability, Rolls-Royce Plc civil aero engines [2,7]

Turbine blade materials are high-temperature materials and as such they require:

1. *“An ability to withstand mechanical loading at operating temperatures close to its melting point”.* [8]
2. *“A substantial resistance to mechanical degradation over extended periods of time”*. [9]
3. Materials must possess a *“tolerance of severe operating environments”*. Blades must be able to withstand high-temperatures, the presence of fuel impurities and corrosive species within the engine ingested air. [7]

Historically turbine blade manufacture has transitioned from forging to conventional equiaxed castings before progressing into directionally solidified and eventually single-crystal technology. Wrought components made from early nickel alloys were found to have severe creep strength limitations prompting the search for alternative technologies and alloys. Early conventional casting provided limited improvement in creep and fatigue properties over wrought components, though its polycrystalline nature meant that grain-boundaries required stabilisation using elements such as carbon and boron. Rapid progress was made developing a directional solidification methodology that reduced the number of axial grain boundaries and aligned the orientation of those that remained along the length of the blade. Today single-crystal turbine blades are free of detrimental high-angle grain-boundaries. [6]

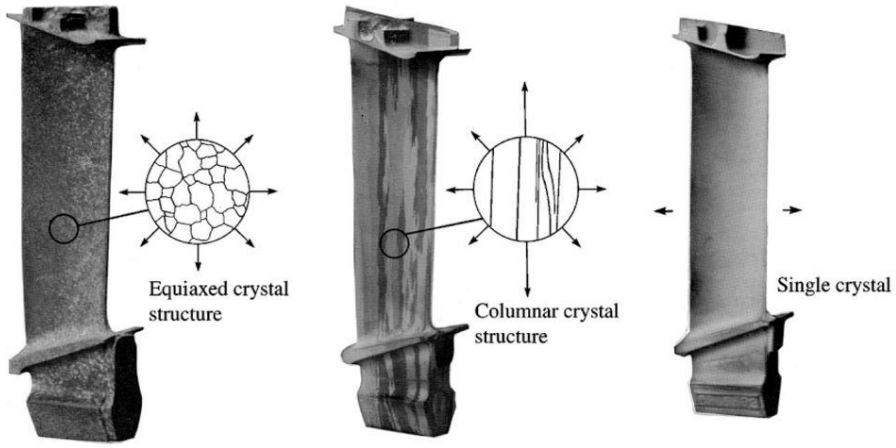

Fig. 1.4 – turbine blades, equiaxed (a), columnar (b) and single-crystal (c) [7]

Modern high-pressure turbine blades use spiral grain-selectors, or alternatively seeding technology, at the casting base within the mould design. When combined with directional solidification these selectors enable the choice of a single grain orientation for the entire as-cast component. The material family developed to fit harsh turbine stage criteria are termed the nickel-based superalloys.

Fig. 1.5 – high-pressure turbine blade for a civil aviation engine, fully processed

1.3. Nickel-based superalloys for turbine blades

A combination of unique chemical composition, phase constitution and microstructure define the potency of the nickel-based superalloys. Nickel became the base element of choice due to its relatively high melting point (1455°C) as well as its characteristic toughness and ductility.[7] Nickel, once alloyed, forms two separate phases, the γ matrix and the γ' precipitate phase, it is this γ' phase which imparts essential high temperature strength. Nickel has a high solubility for alloying elements that increase both oxidation and creep resistance. Since it has no phase transition it shows great thermal stability and a reduced potential for expansion or contraction; dimensional stability is an essential quality in engineering materials.[7] Engine parts must maintain their fit to ensure safe and successful operation, turbine blades within the gas flow path must limit gas flow over the top of the component. Blades that increase in length over time, through thermally activated creep, are unable to maintain engine efficiency and it is for this reason that early in gas turbine development the favoured material changed from steel to nickel. A reduced creep capacity can be attributed to nickels FCC slow diffusion rate helping microstructural stability.[7]

Superalloy additional elements aluminium and titanium are γ' formers, but used in excess they form deleterious brittle phases. Aluminium's role is the primary γ'-former but it is also the most important element imparting oxidation resistance. Refractory metal additions, such as rhenium, tungsten, molybdenum and tantalum provide solid solution strengthening. First-generation single-crystal alloys contain no rhenium, second-generation and third-generation alloys contain 3 and 6% respectively. Fourth generation nickel-based superalloys utilise ruthenium additions but for various economic and manufacturing factors have yet to find main stream use in aero engines.[10]

Carbon was deliberately present in early alloys as metal carbides act as grain boundary strengtheners. Carbon was quickly eliminated as an alloy addition upon development of single-crystal compositions, these elements were no longer needed because there are no grain boundaries to strengthen and crucially enabled superior solutioning heat treatment profiles to eradicate microsegregation and high eutectic levels.[7,9,11] The elements nickel, cobalt, chromium, molybdenum, rhenium and tungsten partition most strongly to the γ matrix phase. The γ phase is continuous and displays the FCC crystal structure.

The second group of elements aluminium, titanium and tantalum together with nickel form the ordered γ' phase which imparts crucial mechanical properties to the alloy. The γ' phase is an ordered precipitate phase forming on cooling and developed during the post-casting heat treatment. It is coherent within the γ matrix and provides a superalloy with its high temperature strength.[12,13]

The γ' phase has a high degree of chemical order within the Ni - Al binary system. This system displays a series of intermetallic compounds including Ni_3Al, NiAl, Ni_2Al_3 etc. Each of these compounds has a unique enthalpy of ordering with the most stable being NiAl. The γ' phase in superalloys is dependent entirely upon the Ni_3Al stoichiometry which possesses the primitive cubic, $L1_2$, crystal structure. This phase features significant directional covalent bonding, hence the precise stoichiometric ratios as well as a preference for Ni-Al bonds over Ni-Ni and Al-Al bonding. This ordered phase confers high temperature strength to the nickel superalloys by forcing dislocations to move though the γ matrix else they need to expend further energy to enter and pass though the γ' phase.

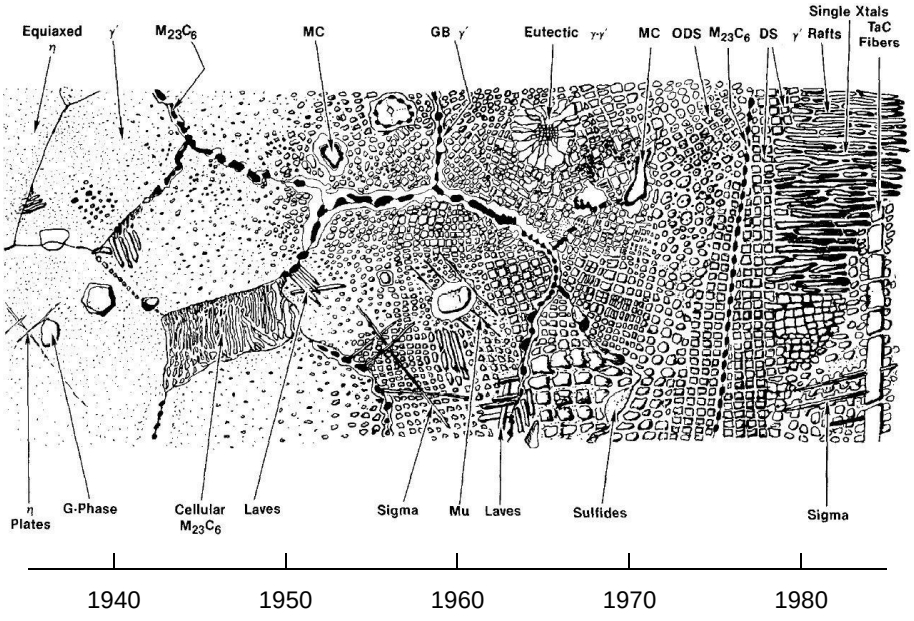

Fig. 1.6 – nickel-based superalloy microstructure during development, useful and deleterious phases [9]

Modern gas turbine engines use single-crystal casting for blades in the high pressure turbine stage.

1.3.1. Guidelines for single-crystal compositions

Nickel-based superalloys developed for single-crystal use have been widely studied and researched which has helped us understand how composition affects performance.

1. *"Proportions of γ'-forming elements, including aluminium, titanium and tantalum should be high, such that the γ' fraction is ca 60 – 70 %"* [14]

   These elements impact alloy strength and ductility and, for mechanical property control of cast alloys, a difference of between 30 and 110°C between the hardening precipitate phase solvus temperature and the alloy melting point permits re-solutioning and re-precipitation of the strengthening γ' phase. [5]

2. *"The composition of the alloy must be chosen such that the γ/γ' lattice misfit is small; this minimises the γ/γ' interfacial energy restricting further γ' coarsening*" [15]

3. *"Concentrations of creep-strengthening elements; rhenium, tungsten, tantalum, molybdenum and ruthenium, must be significant but not so great that precipitation of topologically close-packed phases are encouraged"* [7]

   Additional elements within the alloy, disregarding nickel and aluminium, can be ordered in terms of their creep-strengthening potency.[7]

   Least Co → Cr → Ta → W → Re *Most*

   Rhenium, most capable at slowing creep, segregates heavily to the γ phase helping to block dislocation movement. Unbalanced alloying additions results in persistent formation of topologically close-packed phases after prolonged periods of service. Alloys become weakened by exhaustion of key matrix elements and embrittled by the acicular shape of TCP phases.[5]

4. *"Alloy composition must be chosen such that surface degradation through exposure to the hot, working gases is to be avoided"* [16]

   Turbine environmental conditions make it vital that alloys resist extensive oxidation. Nickel, chromium and aluminium form oxides of varying stability and between them can aid resistance. It is alumina (Al_2O_3) that forms the most stable, slow growing, adherent oxide reducing the rate of material loss. A good example of an alloy with the kind of quantity of chromium and aluminium required for resistance to degradation is that of CMSX-4. It features 5.6 Wt % aluminium and 6.5 Wt % chromium and is considered an alloy which is good at resisting moderate corrosion and oxidation mechanisms. The chromium aims to temporarily fill the gap left by the slower growing alumina, which once formed is a potent protective layer.

1.4. Research outline

This Engineering Doctorate has focussed around understanding the root cause of surface phenomena affecting nickel-based superalloy components during the fabrication sequence. Process control of complex manufacturing methods is required to ensure the highest standards when creating priority components, strict quality control filters out parts afflicted with even minor defects.

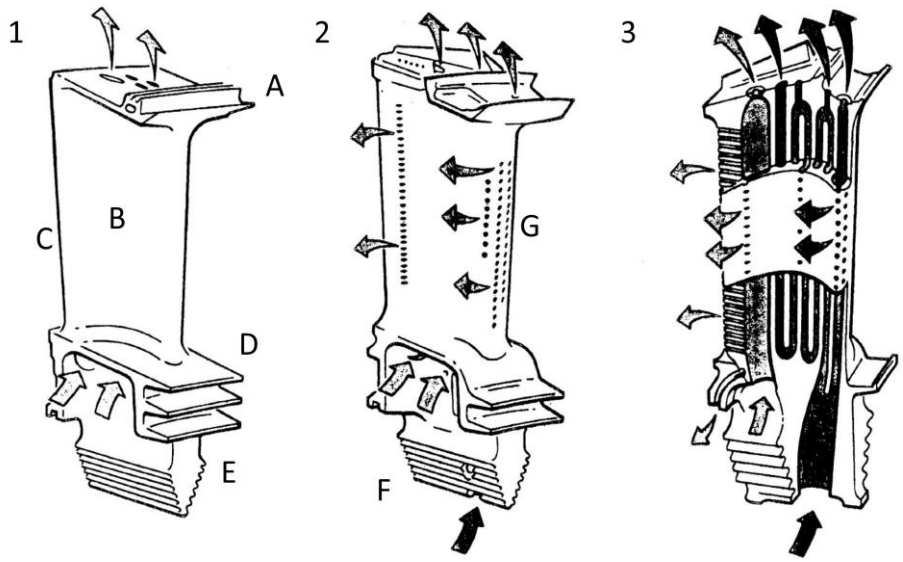

Fig. 1.7 – turbine blade cooling schemes; single pass internal (1), single pass, multi-feed, internal and film cooling (2) and multiple pass, multi-feed, internal cooling and additional film cooling (3) [1,17]*, blade anatomy descriptors; shroud (A), concave aerofoil pressure surface (B), aerofoil trailing edge (C), root leading edge seal (D), root shank (E), root firtree (F) and aerofoil leading edge (G)*

Single-crystal turbine blades, manufactured using investment casting, feature internal cooling passages, see *Fig. 1.7*, formed using sacrificial silica-based ceramic cores. After casting and the "knock off" of external shell the superalloy and internal core are subject to leaching, a chemical removal process using highly alkaline solutions. The intent is to dissolve the remaining ceramic and leave behind the cast superalloy component. After core removal the blade is vacuum heat treated to reduce inherent elemental segregation formed as a result of directional solidification, displayed as a dendritic microstructure. The heat treatment for CMSX-10N takes place at 1365°C, 20°C beneath the incipient melting point where small eutectic pools melt before homogenisation.

This work looks at a defect that sporadically affects blades during solution heat treatment causing a "melting phenomena" to be present upon the internal surface of the component in geometry and processing specific locations. This defect causes parts to be discarded since etching cannot reveal potential secondary grains or recrystallisation that could be present. The work regarding this topic is presented in chapters 3 and 4.

Modern blade alloys are designed for optimal mechanical properties and to be resistant to creep, meaning that turbine blades must utilise protective coatings to enhance oxidation, corrosion and thermal resistance as well as provide a tip seal to maintain gas path pressure. Coatings can be applied using methods including electroplating, chemical vapour deposition, thermal spraying and electron-beam physical vapour deposition. During aerofoil aluminising certain regions upon a turbine blade require masking to block aluminium deposition, this includes the root firtree at the blade base. The maskant used during this coating process consists of carbon polymer-based binders, ceramic fillers and a powdered nickel – chromium – aluminium alloy that provides a gas tight seal. During high-temperature processing the maskant can interact detrimentally with the superalloy to yield sub-surface precipitates. Evidence suggests that this phenomena has detrimental effects upon material mechanical properties by initiating crack growth. This work is presented in chapters 5 and 6.

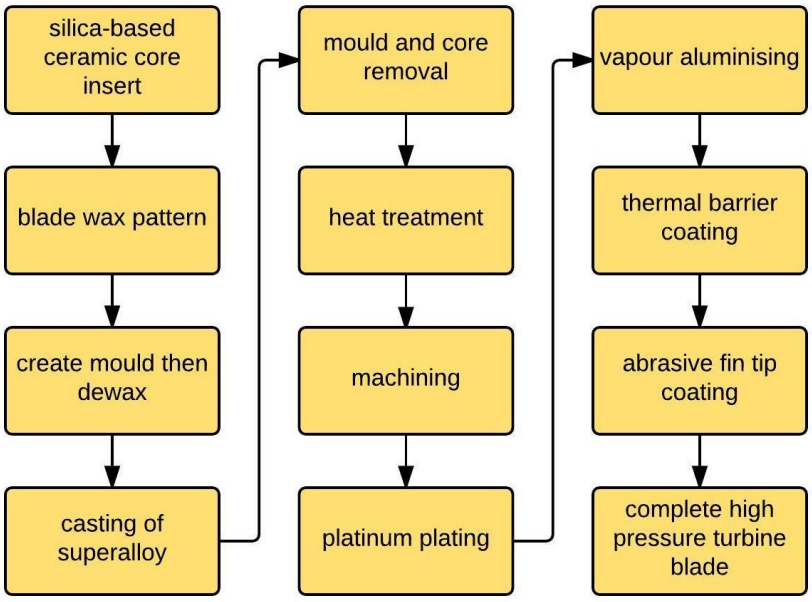

Fig. 1.8 – high-pressure turbine blade fabrication sequence

Turbine blades used in marine derivative engines face more intense environmental degradation mechanisms than aerospace derivatives. Different operating regimes means marine engines experience less cycles but may remain at high operating temperatures for longer time periods. Engines operating at sea level ingest a greater concentration of sea-borne chemical species compared to high-flying aero engines. In addition they burn comparatively impure fuels often with a higher sulphur concentration. Different coating systems tailored to the component, include the use of slurry diffusion aluminide coatings, these are generally applied to low-pressure turbine blades. Slurry aluminides make use of a mixture of water, powdered aluminium and silicon, along with various binders and additives.

This mixture is air sprayed upon the nickel-based superalloy blade before a low temperature thermal treatment is used to drive off solvents and dry the mixture onto the surface. Following this bake the component is heat treated instigating a self-propagating exothermic formation of the nickel aluminide intermetallic coating in-situ. This coating and similar has been in use for over 30 years but has always contained hexavalent chromate additives, which will soon be limited by legislation against hazardous chemicals in manufacturing. Better understanding of the current state of the art is essential for progress. This work will be presented in chapters 7 and 8.

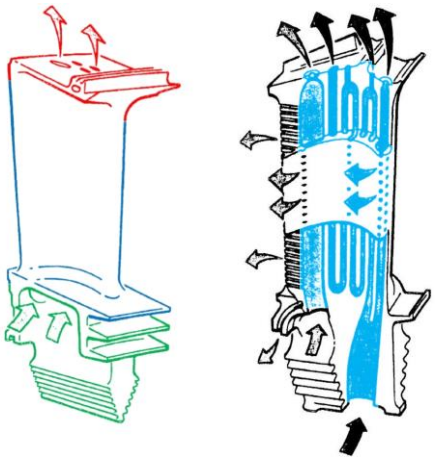

Fig. 1.9 – coating locations high-pressure turbine blade; abrasive fin tip (red), aerofoil platinum plated and thermal barrier coating (blue), platinum plated (green) and internal cooling passages aluminised (cyan)

This thesis is split into eight chapters, the first and second highlights and provides relevant background literature. The third and fourth chapters discuss the investigation into the source of internal surface melting of blades manufactured using investment casting and the trials run to replicate the effect. The fifth and sixth chapters regard the formation of sub-surface carbides following maskant interaction during aluminising, as well as the means to mitigate the phenomena. Chapters seven and eight outline research undertaken to better understand current slurry aluminide systems and look at variables that affect coating microstructure and therefore performance in corrosion resistance.

2. Investment casting and turbine blade manufacture

Engine manufacturers, like Rolls-Royce Plc, use a highly refined and improved version of the tried and tested ancient technology, investment casting. This process has numerous stages which are bulleted below and also represented in *Fig. 2.1*.

1. A wax replica of the component to be cast is made using a die. To create internal cooling passages requires a ceramic core which sits within the die as wax is inserted
2. Several wax replicas are connected together with downpipes and feeder tubes to form the complete assembly. This undergoes a series of dips in slurry, to build-up the investment mould. The slurry consists of a mixture of alumina (Al_2O_3), zircon ($ZrSiO_4$) and silica (SiO_2) along with binding agents
3. Once the shelling is complete and a layer of sufficient thickness is generated the wax inside is melted and removed using a steam autoclave
4. The mould is strengthened by firing in a furnace to sinter the ceramic
5. The shell is placed in the furnace ready to receive the superalloy charge at ca 1550°C
6. Following the casting procedure there are a series of finishing steps including knocking off the used ceramic shell and cutting and grinding the part

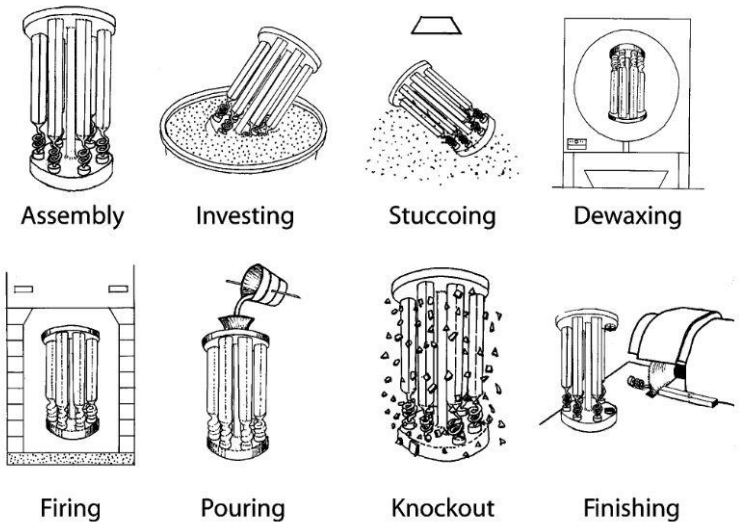

Fig. 2.1 – investment casting [7]

Conventional investment casting involves shutting the furnace down and allowing the mould to cool, resulting in many simultaneous nucleation events and the growth of a polycrystalline structure. Slow withdrawal of the mould from the furnace leads to a directionally solidified grain structure, which was an essential step towards single-crystal casting technology.[7]

2.1. Single-crystal casting

Directionally solidified components display superior creep properties by producing columnar grains throughout the part, with the preferred <001> crystallographic orientation parallel to the primary stress axis. This methodology eliminates grain boundaries normal to the stress axis by unidirectional heat flow through the casting, this causes the solidus at the solidification front to move slowly in a single direction. In addition ahead of the solidus there can be no nucleation events within the melt. A retractable water-cooled copper chill plate functions as the thermal sink and is used to impose a steep temperature gradient that promotes the growth of grains with a <001> orientation.[18]

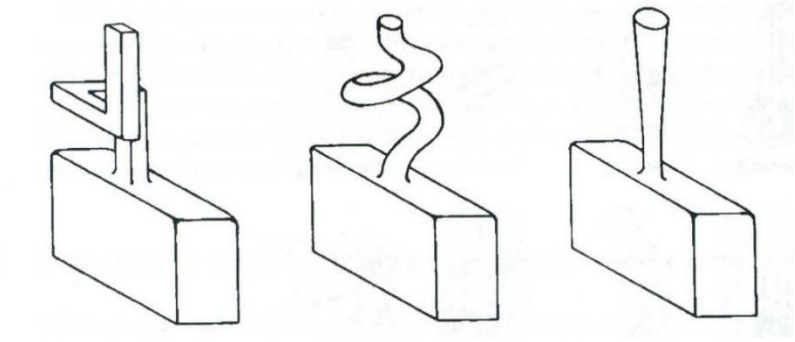

Fig. 2.2 – grain selectors [7]

Directional solidification furnaces are based upon the withdrawal of an investment shell mould, across a heat baffle, through a steep thermal gradient. Crucial criteria for alloy castability include freedom from stray grain and sliver formation, chemical segregation and porosity. It is imperative that alloys be able to develop their single-crystal microstructure at an economical mould withdrawal rate.[19] Directional solidification moulds enable rapid, uninterrupted pouring and to promote fast, uniform columnar grains, the most successful feature constant or decreasing cross sections vertically. Industrial foundries commonly use bottom fed mould systems to give controlled, predictable filling of the blade cavities and enable the use of a ceramic filter ensuring clean castings free of dust and debris.[20] Temperature control is sustained until the top of the casting has passed through the baffle and below the solidus temperature ensuring interdendritic feeding, and preventing vertical grain-boundary hot tears. The casting is subsequently cooled under vacuum to below 540°C.[21]

Casting blades in the single-crystal format uses either a seed crystal or a grain selector. A seed crystal is a small single-crystal with known orientation that is installed at the bottom of the mould. The molten superalloy then melts back some of the seed crystal before withdrawal begins, its presence enables the entire component to have its crystal orientation controlled.

The grain selector is a mould incorporated device, utilising in the shape of a small spiral, which only permits the passage of a single grain orientation. As the solvus front moves upwards the most favourably oriented of these grains gradually crowds out the other less favourably oriented grains. These poorly aligned grains become trapped within the spiral and are outgrown by the preferred orientation <001>, which features the lowest Young's, modulus helping to minimise the effects of thermo-mechanical fatigue. As the solvus continues to climb upwards, through the spiral, fewer grains remain and eventually one remains, hence single-crystal formation. The crystallographic orientation of the final casting should ensure that there is not more than a ca 10° offset between the primary axis of the component and the <001> as measured on the standard stereographic projection. This confirms the orientation sensitivity of a blade under loading and the appropriate tolerances.

Directional solidification casting accumulate defects due to two primary causes. Either from a deviation from the time-temperature relationship essential for the control of directional growth or else from unsuitable materials or equipment. Withdrawal rate defects can lead to loss of the desired orientation as well as the formation of equiaxed grains, freckle segregation or shrinkage porosity. Unsuitable materials or equipment may result in metal-mould interaction [22], material inclusions [23], loss in dimensional accuracy [24], or grain divergence in the case of columnar grains [24]. [12,25]

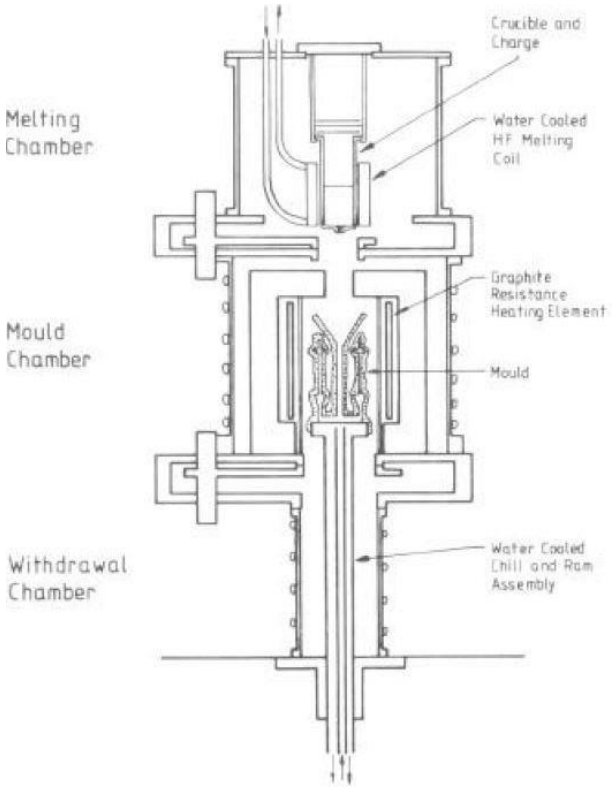

Fig. 2.3 – directional solidification furnace [19]

2.2. Oxide formation

Oxidation is a chemical reaction between a metal and oxygen which obeys the laws of thermodynamics, to determine whether a reaction will proceed we use the second law:

$$\Delta G = \Delta H - T\Delta S$$

If the change in Gibbs free energy is less than 0 then the reaction is termed spontaneous and will proceed, however, if the value is greater than 0 the reaction is improbable. The term ΔG° is the free energy change assuming all species begin in their standard state. By plotting the term ΔG° against temperature it is possible to compare the relative stability of compounds of a similar type, i.e. oxides, sulphides, etc., these are Ellingham diagrams, see *fig. 2.4*.

Wagner's theory [26] seeks to explain oxide formation kinetics making a number of assumptions:

1. Oxide is a compact, adherent scale,
2. Migration of ions or electrons across the scale is the rate controlling process,
3. Thermodynamic equilibrium is established at both the metal - scale and scale - gas interface,
4. Oxide scale shows small deviations from stoichiometry and, hence, ionic fluxes are independent of position within the scale,
5. Thermodynamic equilibrium is established locally throughout the scale,
6. The scale is thick compared with the distances over which space charge effects (electrical double layer) occur,
7. Oxygen solubility in the metal may be neglected.

It is through the work of Wagner that simple oxide growth can be shown to grow according to the parabolic rate law:

$$k_p = \xi^2/t$$

In reality oxidation is a competitive and dynamic process. When oxides become thicker the rate determining step is the diffusion of ions and electrons through the layer, giving rise to the parabolic rate law. For alloys there are more than one type of oxide that can form, selection is dependent upon the activity of the metallic elements, the oxygen partial pressure as well as the exposure temperature.

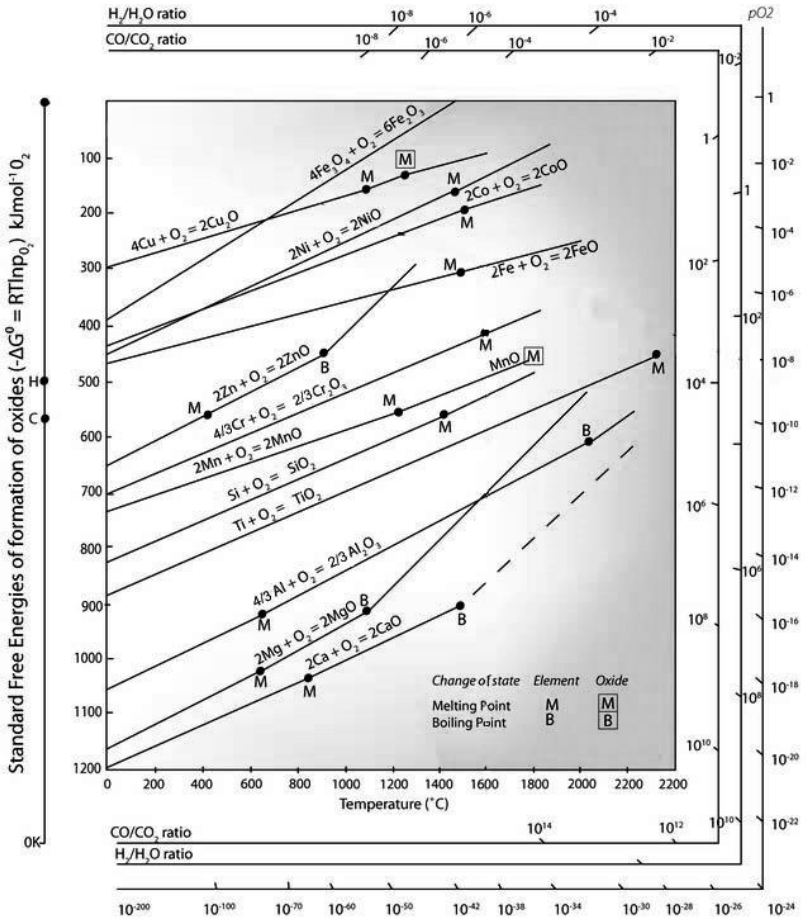

Fig. 2.4 – ellingham diagram [27]

The following factors contribute to oxide formation on alloys:

1. Metals in an alloy have different oxygen affinities, reflected by different free energies of oxide formation,
2. Solid solubility may exist between the oxides; resulting in the formation of mixed oxides,
3. Metal ions have different mobilities in the oxide,
4. Metals will have different diffusivities within the alloy,
5. Dissolution of oxygen into the alloy may result in sub-surface precipitation of oxides of one or more alloying elements known as internal oxidation.

The most important factor in alloy design against excessive oxidation is a balance of fast and slow growing oxide species as well as ensuring that more adherent, potent oxides are able to form at service temperatures to provide long term protection. This oxide should ideally be slow growing, adherent to the surface and cohesive to avoid spallation events and material loss.

The nickel – chromium – aluminium alloys, simple analogues for superalloys, display competition during oxidation causing the formation of multiple oxide phases [27–29]:

- **NiO**
- **Cr_2O_3** – important below temperatures of 1000°C and acts to assist alumina formation
- **$Ni(Cr,Al)_2O_4$** – Spinels often form at higher temperatures
- **α – Al_2O_3** – crucial to the success of the oxidative stability of superalloys, forms a coherent, continuous layer

Alumina grown on superalloy components is ideally α (corundum) structure, though this is temperature dependent, α is adherent and slow growing in nature.[30–33] At lower temperatures the θ and γ phase are more likely. During single-crystal alloy development there has always been aluminium for oxidative resistance. The amount of aluminium available sub-surface will determine the formation of oxide upon the surface, see *Table. 2.1*.[34,35]

Regime	Wt (%)	At (%)	Oxide species
1	0 – 6	0 – 13	Internal Al_2O_3 (+ $NiAl_2O_4$) + NiO external scale
2	6 – 17	13 – 31	Initially external Al_2O_3, supply dwindles and is overtaken by an NiO + $NiAl_2O_4$ + Al_2O_3 mixture
3	≥ 17	≥ 31	External Al_2O_3 is maintained by Al supply

Table. 2.1 – binary Ni-Al isothermal oxide species, superalloy analogue – real superalloy have complex oxides [27]

Chromium has a synergistic effect upon the formation of alumina layers. A sub-scale layer forms beneath the mixed oxide surface altering the oxygen activity and blocking both internal Al_2O_3 and NiO / spinel growth. Thus allowing Al_2O_3 to become the most stable continuous oxide layer. Evidence of superalloys during oxidation testing showed that the Al_2O_3 morphology varied depending on whether it formed on the surface of a dendrite or an interdendritic phase region. This elemental segregation determines the local composition and therefore results in different levels of elements, like aluminium, being available.[36,37]

2.3. Turbine blade coating systems

Economics drives continuous improvement in engine efficiency, consequently operating temperatures within the turbine stage have steadily increased over the last 30 years. Mean temperatures of high-pressure blades are around 1050°C, with peaks in excess of 1150°C. Internal air cooling reduces the blade metal temperature to between 850 and 900°C. [38,39]

Improving engine efficiency inevitably increases the demand on materials due to the greater thermal energy and exposure to more aggressive environments, including the presence of engine ingested sulphates, chloride salts and fuel contaminants such as sulphur. Oxidation and hot corrosion processes can become the life-limiting factors to a materials degradation in the combustor and turbine stages and development of superalloy technology has progressed in tandem with coating protection systems. The general trend has been to focus on tailoring substrate composition regarding mechanical strength and creep capability and to mitigate the resulting alloy environmental resistance penalties with coatings. Materials exposed to aggressive environments depend on the formed corrosion or oxide product which must act as a diffusion barrier to prevent further attack progress. The oxide layer must be chemically stable and retard diffusion of both reacting gases and the metal species as well as be mechanically stable. [38,40]

The atmosphere in which turbine blades operate is highly oxidising with oxygen, nitrogen, carbon dioxide and water vapour being experienced during operation. The primary role of a coating system is to protect the alloy against environmental attack, but it must also provide erosion resistance and be able to tolerate minor impact damage. Coatings must also withstand blade stresses due to centrifugal force and resist those stresses caused by both thermal and mechanical fluctuations.[41]

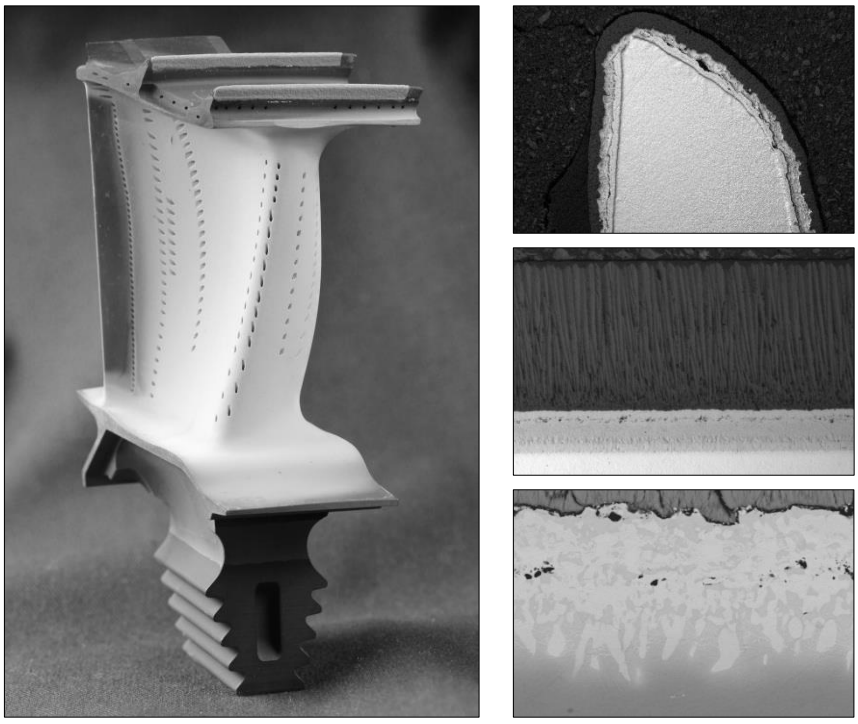

Fig. 2.5 – high-pressure turbine blade; abrasive fin tip coating (a), ceramic thermal barrier coating (b) and diffused platinum layer (c)

Gas turbine engines and their arduous conditions have given rise to a number of coating systems aimed at:

- Maintaining dimensional integrity of the blade aerofoil, compromising between making efficient use of cooling air and prolonging component lives
- Maintaining mechanical integrity of turbine components [42]

The in-service performance of a coating is dependent upon factors including; temperature, the operating environment, component geometry, alloy composition and the thermo-mechanical stresses imposed on a material.

High-pressure turbine blades for large civil engines are complex, they consist primarily of a thin shell with an internal array of filigree-like cooling passages and drilled film cooling holes. Commercial economics demands blades last in service between 10,000 and 15,000 hours making coating integrity essential. [42]

2.3.1. Aluminising

Aluminising supplies aluminium to the superalloy surface before high temperatures are used to diffuse the two together. Variants include; pack, above-the-pack and externally generated chemical vapour deposition. In above-the-pack and externally generated the component is placed inside a reaction vessel within a sealed outer vessel. In the above-the-pack process the aluminium halide source, the chemical transport medium for aluminium, is placed beneath the components. Alternatively the aluminium halides are generated externally from the reaction vessel and transferred once at deposition temperature. In all variants when the vessel has reached temperature the atmosphere within the apparatus begins to deposit aluminium via one of two processes that is dependent upon overall temperature. The method used in this work is the above-the-pack variant ensuring a cleaner coating without particle entrapment associated with pack. The key factors defining this method are the nature and concentration of activators, the composition of the pack used as well as the temperature used. *Fig. 2.6* displays the aluminising process chemistry.[43]

In the low activity or outward growing process growth is dictated by outward diffusion of nickel and the result is the formation of β-NiAl. This process occurs at high temperature so interdiffusion occurs during the aluminising cycle. After deposition heat treatment enables the interdiffusion of these two layers. The high activity or inward growing process relies upon the inward growing aluminium to form δ-Ni_2Al_3 and occasionally β-NiAl. Heat treatment is needed to transform the δ-Ni_2Al_3 into the required β-NiAl by extracting nickel from the substrate. Aluminising lifespan is dictated by the time it takes for this layer to lose aluminium via oxide formation and internal diffusion and subsequently transform into γ'-Ni_3Al. [44]

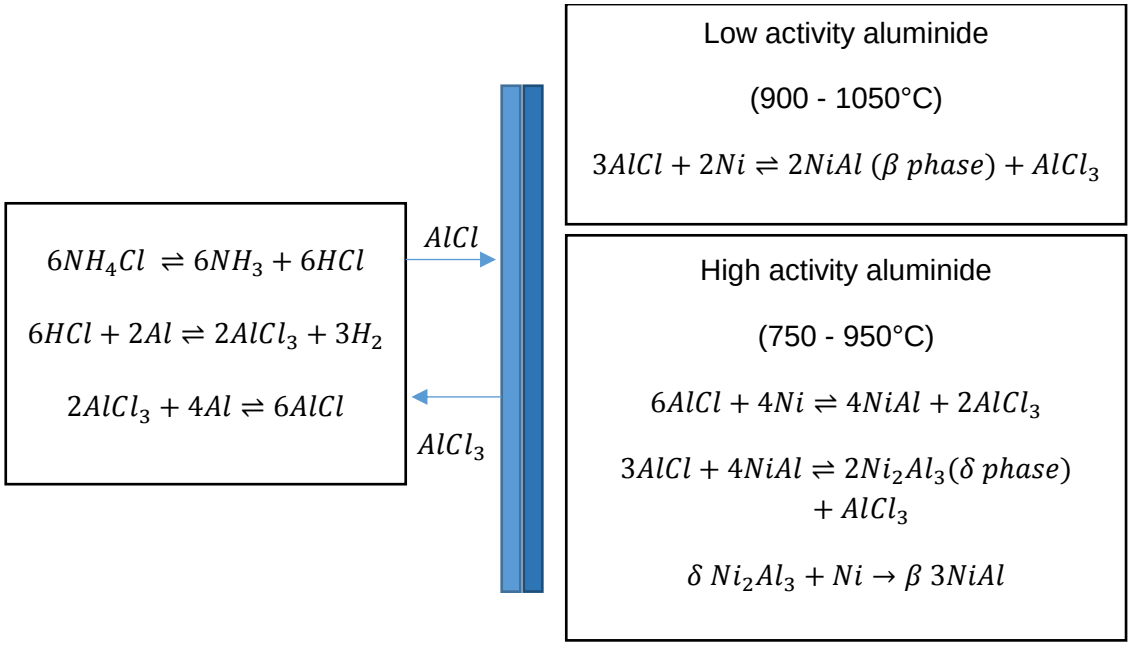

Fig. 2.6 – chemical vapour deposition aluminising [43]

Aluminising using pack cementation utilises solid state diffusion, when the aluminium source reacts with the substrate, as well as gas phase diffusion of aluminium halides. Aluminising of nickel-based superalloys yields δ-Ni_2Al_3 and hyperstoichiometric β-NiAl, the latter if the aluminium content is higher than 51% atomic.[45] In work by Wöllmer et al. [46] diffraction patterns taken from within the nickel-based substrate showed the expected face centred cubic structure with $L1_2$ superlattice reflections. Approaching the interdiffusion zone from the substrate, the common γ/γ' microstructure undergoes rafting with the elongation parallel to the surface with this being an indication for local internal stresses. Two additional topologically closed-packed phases are observed at the interdiffusion zone, containing a mixture of the elements chromium, cobalt, molybdenum, tungsten and rhenium, with both needle-shaped and compact precipitates being found. The coating matrix comprising β-NiAl made up mainly of the elements nickel and aluminium was confirmed by the diffraction pattern of a single grain which revealed the CsCl (B2) ordered body centred cubic crystal structure. Wöllmer believed the β-NiAl coating to grow in a columnar manner with randomly distributed orientations into the coating.[46] Shen et al. added to this by claiming the presence of significant amounts of MC, $M_{23}C_6$ and M_6C precipitates together with Σ lamellae which are formed at the interdiffusion zone.[47]

Gale et al. [48] examined aluminide coated single crystal nickel base superalloys and the following structure was observed moving from surface to substrate; oxide layer, coating surface layer, main coating layer, coating interdiffusion zone, substrate interdiffusion zone and finally substrate. Gale observed the coating matrix of β-NiAl, retained some evidence of $L1_2$ type precipitates of the γ' phase, nominally $Ni_3(Al,Ti)$, and confirmed the presence of an $M_{23}X_6$ type phase (in which M is chromium and X is most likely carbon).[48,49]

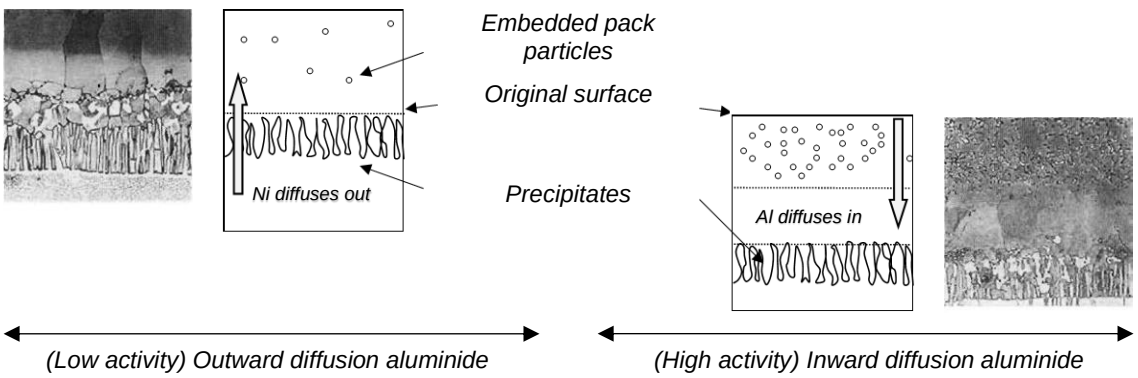

Fig. 2.7 – high activity versus low activity aluminising [43]

Two temperature dependent aluminium activities, low and high, can be achieved for deposition with low aluminium activity yielding an external β-NiAl layer forming by the greater outward diffusion of nickel. To an extent additional alloying elements are carried outwards, to meet the aluminium. High aluminium activity means the formation of δ-Ni_2Al_3 and the coating grows inwards from the original surface. Since these coatings are thermally activated they require high temperatures to be economically viable often resulting in adverse effects upon the substrate microstructure. Additionally masking of regions not to be coated can be problematic at such temperatures. The thickness of these coatings increases approximately as the square root of the process duration, typical ranges of 50 - 100 μm are seen for durations of ca 20 hours.[45]

Coating performance can be affected by substrate chemistry with coatings on several superalloys proven to have different lifetimes in hot corrosion testing. Difference is thought to be related to chromium contents of the parent substrates. Chromium has been found to permit selective oxidation of aluminium in chromium-aluminium containing alloys, where contents of ca 15 % Wt are required for satisfactory hot corrosion resistance. One way in which these alloys achieve this is by forming a continuous chromia scale which inhibits the basic fluxing of the alumina.[50] Chromium advantages also operate in the β-NiAl phase and ca 10 % Wt chromium is necessary to yield improvement. Aluminide coatings formed on high chromium containing nickel-base superalloy substrates are more resistant under hot corrosion conditions. This observation implies that part of the chromium in the alloy is incorporated into the final coating microstructure, and the amount of chromium required depends on the transport mechanisms involved in the coating growth.[50]

2.3.2. Platinum aluminides

Platinum aluminide coating systems involve the use of a platinum electroplating technique prior to a high-temperature pack aluminising process.[42] The deposition of platinum by electroplating is well established however, deposits are usually highly stressed and prone to porosity. In addition, poor cleaning before electroplating can cause entrapment of non-metallic deposits between the substrate and the deposited platinum, leading to poor adhesion and incomplete diffusion of aluminium and platinum.[51]

Degradation of conventional nickel-aluminide coatings involves the degeneration of NiAl to lower aluminides by the inward diffusion of aluminium to the substrate and the diffusion of aluminium to the external coating surface to form and maintain the protective Al_2O_3. The added presence of platinum acts as a diffusion medium which, during processing, allows aluminium to establish a nickel-aluminide sub-surface structure (still containing platinum) and simultaneously generate a platinum-aluminium intermetallic skin. Platinum has great affinity for aluminium and increases the activity of aluminium within the alloy resulting in surface enrichment therefore maintaining the surface aluminium concentration delaying the transformation of β-NiAl into γ'-Ni_3Al. By slowing the transformation it lengthens the time period before oxidation compromises the substrate. The platinum promotes selective oxidation and catalyses the interaction between aluminium and oxygen to Al_2O_3.[51,52]

Within the total coating the surface structure normally consists of a continuous layer of Pt_2Al_3 which is gradually replaced by a duplex $[Pt(Ni)]_2Al_3$ + PtAl structured zone. The composition of the layer would indicate a duplex PtAl + [Ni(Pt)]Al zone. The central portion of the coating structure consists of the β-NiAl intermetallic. The portion of this layer incorporates platinum as a solid-solution component substituting for nickel in both the Al-rich hyperstoichiometric β-NiAl and the Ni-rich hypostoichiometric β-NiAl. The remaining part of this central layer is virtually free of platinum and consists of Ni-rich β-NiAl.[51] The diffusion zone below β-NiAl is sequentially composed of β-NiAl + α-Cr and γ'(Ni,Al) + α-Cr, with intermetallics and carbides rich in refractory elements. The coating terminates with the alloy microstructure of γ (solid solution matrix) + γ'.[41] Owing to the higher binding energy of $PtAl_2$ and β-(Ni,Pt)Al in comparison with β-NiAl thermal diffusivity in the outer coating layers of platinum aluminide coatings can be expected to be considerably slower, increasing coating stability against diffusion at elevated temperatures.

Platinum in aluminide coatings on superalloys has been found to:

(1) increase coating stability towards aluminium or nickel diffusion
(2) eliminate chromium-rich precipitates from the outer coating layers
(3) prevent refractory elements like tungsten from diffusing into the outer coating, the presence of which degrades the coatings oxidation resistance.[51]

2.3.3. Slurry aluminising

In a typical slurry process, a suspension of aluminium and silicon, or an aluminium-silicon alloy, in an organic binder is sprayed onto the component surface. The deposit, which also contains small amounts of phosphate and chromate binder, is cured at 350°C and then given a high-temperature heat treatment to produce the diffusion reaction with the substrate. They are used for patch-repair of damaged aluminide coatings deposited by pack cementation, although they have been used as a blade coating in their own right. Further background and discussion of slurry coatings can be found in the introduction to chapters seven and eight which is the primary research topic of that part of the thesis.[42]

2.3.4. Thermal barrier coatings

Thermal barrier coatings (TBCs) provide thermal insulation to metallic components in the hot gas stream in gas turbine engines. A TBC, combined with integral internal cooling passages, considerably reduces the surface temperature of the alloy. Engines can therefore operate at gas temperatures well above the superalloy melting temperature, improving engine efficiency and performance. TBCs also act to extend the life of components by retarding the rate of heat flux through the material.[53] The physical vapour deposition process uses evaporation to deposit many types of inorganic material - metal, alloy, compound, or a mixture.[54] A TBC system typically comprises four layers;

(i) the substrate;
(ii) the bond-coat;
(iii) the thermally grown oxide (TGO);
(iv) the ceramic top-coat

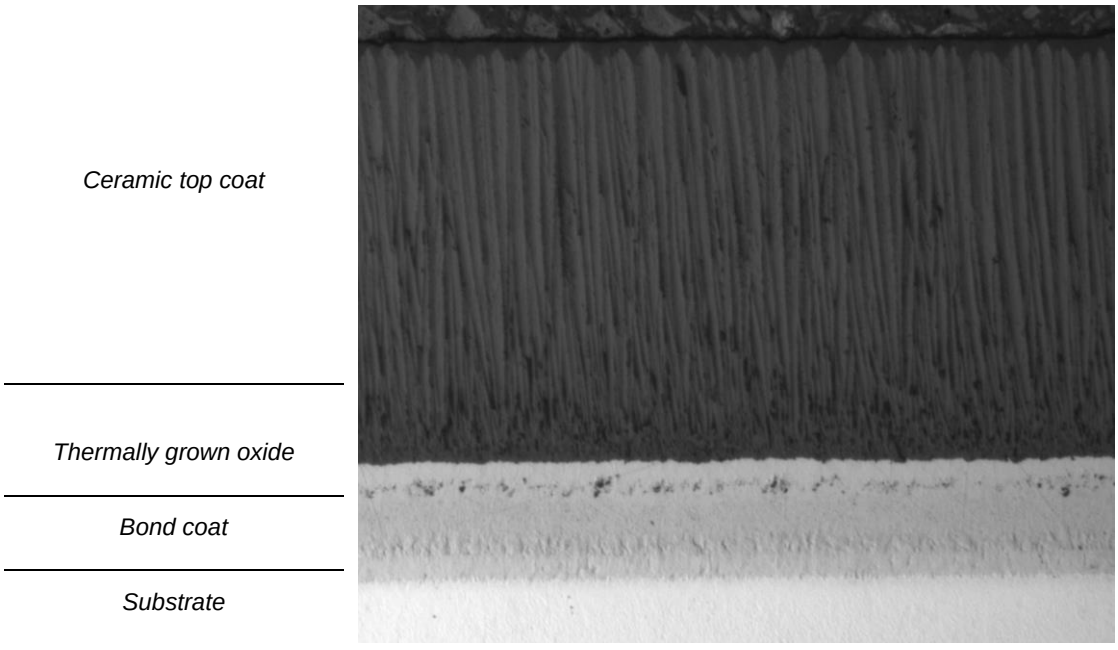

Fig. 2.8 Thermal barrier coatings consist of bond coat on the substrate and ceramic top coating on top [43]

The nickel-based superalloy is the substrate, it is air cooled from the inside through internal cooling passages, and establishes a temperature gradient across the component wall. The bond-coat is an oxidation-resistant metallic layer normally formed of aluminides of nickel and platinum. At service temperatures exceeding 700°C, the bond-coat undergoes oxidation forming the third layer - the thermally grown oxide, (TGO). The TGO sits between the bond-coat and the ceramic top-coat. Ideally the bond-coat should form α-Al_2O_3, its growth being slow, uniform, and defect free. In addition Al_2O_3 has a low oxygen ionic diffusivity, providing a diffusion barrier, reducing bond-coat oxidation.

The ceramic top-coat provides the thermal insulation and is typically made of Y_2O_3-stabilized ZrO_2 (YSZ). YSZ has low thermal conductivity at elevated temperature because of its high concentration of point defects such as oxygen vacancies and substitutional solute atoms, which help scatter heat-conducting phonons. YSZ also has a high thermal expansion coefficient (11×10^{-6} °C^{-1}), this helps minimise stress arising from the thermal expansion mismatch between the ceramic top-coat and the substrate. YSZ has a hardness of 14 GPa, making it erosion resistant and tolerant of foreign body impact. YSZ is high temperature capable due to a melting point of 2700°C and exists as three different polymorphs - monoclinic, tetragonal, and cubic - depending on the composition and temperature. The addition of 7 to 8 weight % Y_2O_3 stabilizes the t' phase, the most desirable phase for TBC application. This tetragonal phase variant does not undergo the martensitic transformation and is as a result more stable in service.[55]

3. Internal surface melting

3.1. Introduction

Successive generations of nickel-based superalloys are defined by increasing rhenium levels and by additional refractory additions; molybdenum, tantalum and tungsten and then eventually ruthenium to aid phase formation control. These elements improve high-temperature strength through solid-solutioning but display significant partitioning between the solid and liquid phases. This, combined with their slow solid-state diffusivity imparts substantial segregation and a highly cored non-equilibrium eutectic microstructure following directional solidification. The as-cast microstructure features dendrite cores enriched in tungsten and rhenium in contrast to the interdendritic regions rich in aluminium, titanium and tantalum. Subsequent solution heat treatment facilitates the dissolution of the interdendritic regions and promotes chemical homogeneity across the cast component. Nickel-based superalloys are heated above the γ' solvus temperature, but below the solidus, before being quenched and age heat treated to form an even distribution of the essential cubic γ' precipitates.

During directional solidification the primary solidification begins with freezing of the γ dendrites. The alloy CMSX-10N, used extensively in this work, features a liquidus of 1424°C, solidification commences at 1419°C and terminates at 1357°C.[56,57] Following primary solidification interdendritic pools freeze comprising fine γ/γ' phases and is proposed, by some authors, to be the product of a eutectic reaction.[58] Pang et al. however, concluded that differing distinct morphologies within the interdendritic region are the product of a peritectic reaction. Even within the nickel-aluminium binary system, a simple analogue of the nickel-based superalloys, there is contention regarding the presence of either a eutectic or peritectic reaction during solidification, the temperature interval separating these reactions was found to be ca 2°C meaning that slight differences in composition or solidification conditions may favour one reaction over the other.[59] Detailed work, on superalloys, indicated that following the solidification of the dendrite the interdendritic region began solidification starting with finely spaced γ/γ' before progressing to a coarse cellular structure.[58] The presence of porosity within the interdendritic phase pinpoints the location of the last liquid to solidify. Superalloys with high rhenium concentrations increase the tendency for segregation of that rhenium to the dendrite core and to a lesser extent also increase segregation of tungsten and chromium too.[57,58,60,61] The elements chromium, tungsten and rhenium all display limited solubility within the γ' phase, in some instances this shared tendency for rejection results in them combining to form stable intermetallic topologically close packed phases.[62,63]

For turbine blades cast using a single-crystal grain selector the properties along the <001> preferred growth direction, are fortuitously superior to those along <110> or <111>. Nickel displays an elastically anisotropic tendency which means that the stiffness is dependent upon the crystallographic orientation of loading.[7] Therefore turbine blades created from nickel-based superalloys are used in single crystal form, though in reality cast blades can deviate from the precise <001> orientation by up to 10–15°, where the deviation in properties can be tolerated. This allowance is due to manufacturing process yield considerations, and casting limitations. The directional solidification process means that the rate of dendrite growth is controlled by the rate of solute diffusion with the growth velocity increasing monotonically with the square of the undercooling. Dendrites misaligned compared to the maximum temperature gradient must grow faster than those which are well-aligned, and through using spiral mould designs it is possible to preferentially select an orientation.[64]

On the external surface of certain blade geometries, a continuous layer of eutectic phase ca 20 μm thick can be observed. This segregated interdendritic material prevents examination of the grain structure and must be removed from the external surfaces using abrasive blasting or grinding, but not before high-temperature solution heat treatment due to the risk of inducing recrystallisation. Material solidification results in shape contraction, the cause proposed for the continuous eutectic layer is shrinkage-driven interdendritic liquid flow. Lateral contraction at the external mould wall results in the secondary dendritic arms, still wetted by the liquid, being displaced inward. Moving the solid dendrite inward will unavoidably induce flow of interdendritic liquid outwards. This circulation of interdendritic liquid leads to an amplified segregation ahead of the arms leading to the formation of a eutectic layer at the mould surface.[65,66]

An as-cast superalloy's highly segregated microstructure must be eliminated prior to high-temperature service. Solution heat treatment of single-crystal alloys is challenging; the coarse eutectic γ' dissolves slowly and the segregated microstructure has local interdendritic solidus temperatures lower than the solvus temperature of the dendrites. The result is that the super-solvus homogenisation solution heat treatment can lead to localised incipient melting of eutectic pools.[67] To counteract this, superalloys are heated step-wise to the γ' solvus, gradually homogenising while keeping the temperature just below the melting point of the eutectic. The treatment of CMSX-10N involves multiple intermediate steps and takes 40+ hours at temperatures greater than 1300°C.[68,69] One of two features explored in this chapter is akin to the incipient melting of eutectic pools, it is the formation of an enriched melt zone (EMZ) upon the external surface of heat treated blade components where eutectic is extruded to the surface.

The CMSX-10N heat treatment at 1340°C results in full solutioning of the γ' and the eutectic γ/γ', however chemical segregation persists even after treatments at 1360°C with dendrite cores still clearly visible. For those 3rd generation superalloys with a large eutectic percentage the priority in solution heat treatment is the requirement to reduce chemical segregation and not the dissolution of γ', as it was in earlier superalloys. The refractory metal elements present within the alloy, especially rhenium, require temperatures exceeding 1360°C or more before adequate homogenisation is observed.[70,71]

Superalloys can incur serious microstructural instabilities both during manufacture and service, these include but are not limited to; recrystallisation, discontinuous precipitation and discontinuous coarsening. Though high-temperature exposure is essential to these instabilities being present, there must always be other contributing factors. Nucleation of these microstructural events is usually affected by the following factors and conditions:

1. Chemical supersaturation (residual segregation, coatings e.g. aluminising),
2. Residual strain energy imparted during surface preparation (grit blasting and machining),
3. Quantity of heterogeneous sites,
4. Amount of rhenium present (2nd generation, 3rd generation superalloys, etc.).

In this work the focus is discontinuous precipitation which, driven by the factors listed above, occurs during the subsequent high temperature exposure of heat treatment. Work on cellular discontinuous precipitation found that, at grain boundaries newly formed phases were growing into adjacent grains, initiating at regions of irregular intercellular boundaries. The major driving force is the reduction in high chemical potential that results from elemental supersaturation, the end result being that cellular growth is rapid at high temperatures as the material moves from a metastable state to re-establish stability.[72]

Cellular colonies of discontinuous precipitation can be found; beneath the diffusion zone of aluminide coatings, now called the secondary reaction zone (SRZ), and are also seen along grain boundaries and occasionally within dendrite cores. Relatively balanced alloys like CMSX-4® are usually capable of tolerating an aluminide coating by forming an interdiffusion zone at the interface which does not feature TCP phases and microstructural instability and is therefore not classed as an SRZ. Under certain conditions, alloys like CMSX-10N®, possessing a supersaturation of rhenium, chromium, tungsten and molybdenum, permit the SRZ structure to form beneath the interdiffusion zone which consists of a γ' matrix containing γ and *P*-phase TCP needles. There is limited solubility for these high levels of refractory elements within the γ' phase. The γ and *P*-phase grow with the plates coherent to the <111> matrix plane but aligned as close as possible to the moving interface orientation.[73]

The original γ/γ’ matrix transforms from γ to γ’ after the incoherent boundary passes. *P*-phase, composed primarily of rhenium, with high levels of tungsten and chromium in the SRZ is continuous with the γ phase at the interface.[74]

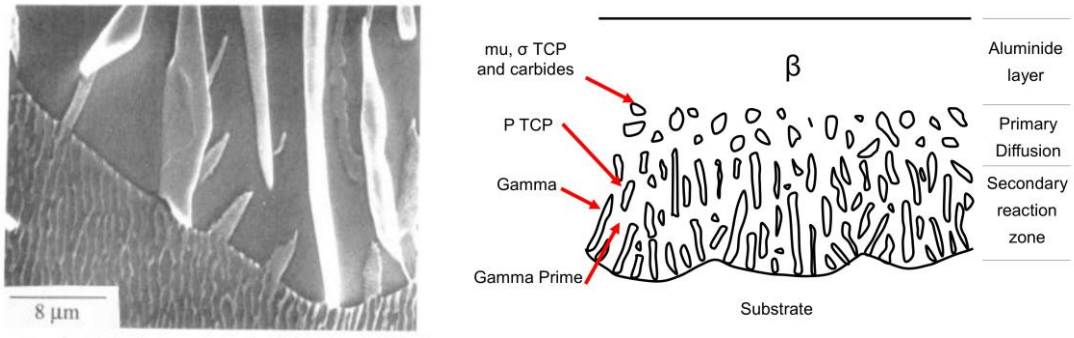

Fig. 3.1 – BSE SEM image SRZ and alloy interface (a), schematic of SRZ under aluminide (b) [72]

Interdiffusion between the aluminide coating and the substrate creates a situation in which γ and γ’ are no longer thermodynamically stable. The high aluminium activity of the coating and the residual stress state of the surface initiate phase precipitation. The stress state is a function of surface preparation techniques including grit blasting or machining.

Grain boundary discontinuous precipitation only forms on one side of a high angle grain boundary (>10°) forming the cell morphology with lamellar precipitates. The reaction transforms the two-phase γ/γ' microstructure into a three-phase cellular structure;

$$(\gamma + \gamma')_{parent} \rightarrow \gamma'_{cell} + \gamma_{cell} + P$$

Three different rhenium-enriched TCP phases are observed: δ phase, μ phase, and *P*-phase. The common connection between accumulated surface strain and discontinuous precipitation is the occurrence of recrystallisation during thermal exposure. Recrystallisation sees the formation of grains with a high-angle grain boundary that can favour the initiation of discontinuous precipitation.[75] The growth of the cell boundary is driven by local reductions in chemical free energy between the supersaturated matrix ahead of the cell boundary and the matrix within the cell which contains the equilibrium structure. The lead interface serves as a high diffusivity mobile reaction front. Under severe plastic deformation with precipitate shearing and a high dislocation density reductions in strain energy may influence the development of the transformation to a greater extent.[74,76–80]

3.2. Experimental

3.2.1. Methodology

This investigation examined one design of intermediate pressure turbine blade, referred to as blade X, at various stages during manufacturing, as detailed in *Fig. 3.4*. Blade X, cast from CMSX-10N, displayed an enriched melt zone feature, as well as discontinuous precipitation, upon the internal surface of the cooling passage post heat-treatment, detrimentally affecting production yield. This defect prevented direct observation of the internal surface of a type X blade which would ensure conformance to single-crystal specifications: specifically the absence of potentially detrimental secondary grain growth.

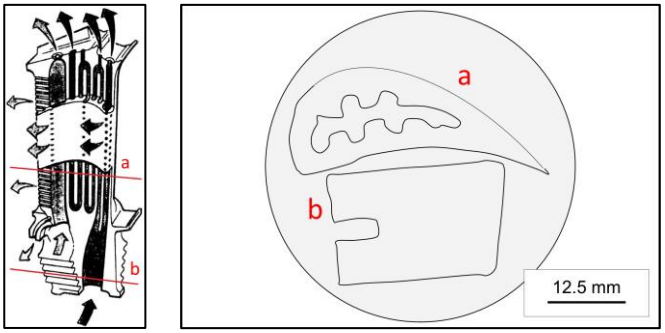

Fig. 3.2 – sections a and b from turbine blade X (a), impression of 50 mm micro with section a and b (b)

3.2.1.1. Core

Two core types are used as part of this work, the first is designated MD™, made by Ross Ceramics and has a primary chemistry of ca 84 wt. % silica (SiO_2), ca 14 wt. % zircon ($ZiSiO_4$) and ca 1 wt. % alumina (Al_2O_3). The second is P-35™, made by Morgan Advanced Materials and it has a primary chemistry of ca 93 wt. % silica, ca 3 wt. % zircon and ca 4 wt. % alumina. The microstructure is in *Fig. 3.7* and the manufacturer's data is in *Table. 3.1*.

Material	Major Chemistry	Content (wt. %)	Porosity (%)	Bulk density (g/cc)
MD	SiO_2 (fused)	84	37.3	1.59
	$ZrSiO_4$ (fine-grained)	14		
	Al_2O_3 (agglomerated)	1		
P-35	SiO_2 (fused)	93	31.1	1.58
	$ZrSiO_4$ (fine-grained)	3		
	Al_2O_3 (agglomerated)	4		

Table. 3.1 – manufacturer material property data

3.2.1.2. Wax and shell

The ceramic core is placed in the centre of a steel die that is used to form the blade wax pattern. Once closed the steel die has hot wax injected into the mould filling the cavity and covering the ceramic core. Once cool the steel die is opened to reveal the wax pattern of the blade with the core in-situ, this wax blade then has hot platinum pins inserted to assist in keeping the ceramic core correctly positioned during the later stage of manufacture. The hot pattern wax used in this instance is Blaysons A7 FR/60 virgin. Following platinum pinning several of the wax blades are assembled into a complete array using feeder tubes and a central pour cup to enable filling of the final mould. The entire array undergoes a wash in combined wax pattern cleaner and etchant, in this case, Blaysons Trisol 60 Plus to remove silicones and surface debris. Once dry the assembly was subject to a dip in the first sol gel parting layer and application of stucco to accelerate drying times and aid stress relief.

All shelling materials used in the PCF at Rolls-Royce plc in Derby are defined as the Standard Rolls-Royce Single Crystal Shelling System. Once dry a series of additional secondary layers were added to provide strength. All slurries are silica-based sol binders with a zircon filler as well as wetting agents and anti-foaming agents.

3.2.1.3. Casting

All blades of type X were cast as single-crystals using directional solidification within a Bridgeman furnace. This casting was carried out at the Precision Casting facility (PCF), Rolls-Royce plc, Derby, UK. Casting parameters were as follows; furnace heater temperature of ca 1550°C and a vacuum level of 0.1 Pa (10^{-6} atm). The mould withdrawal from the furnace hot zone was ca 5.0×10^{-5} m s^{-1}. These blades are cast in numbers depending on the bore size of the furnace.

3.2.1.4. Leaching

Removal of the sacrificial ceramic cores was carried out using either sodium hydroxide or potassium hydroxide. Components are loaded into a basket which is placed within an autoclave. Once closed the autoclave vessel is filled with a solution of either sodium hydroxide (ca 20% w/v) or potassium hydroxide (ca 40% w/v). The solution within the vessel is heated to ca 150°C and pressurised to ca 6 – 7 bar, which suppresses boiling. The process uses cyclical venting and re-pressurising to bring about physical agitation of the now loose core material. This process is monitored, those blades which still contain core material even after a single cycle may be subject to further cycles to ensure adequate removal of internal material. This results in variable time exposures but a typical cycle lasts several hours.

3.2.1.5. Heat treatment

Heat treatment was carried out in a Schmetz furnace located at Bodycote, Derby, UK. Heat treatment typically consists of a high temperature solutioning, *Fig. 3.3*, to reduce the elemental segregation within an as-cast component and a subsequent aging heat treatment in order to grow the γ/γ' microstructure (*thermal trace for aging not shown*). The heat treatment profile for aging is proprietary information but the hold temperature is ca 1150 °C for 5 hours.

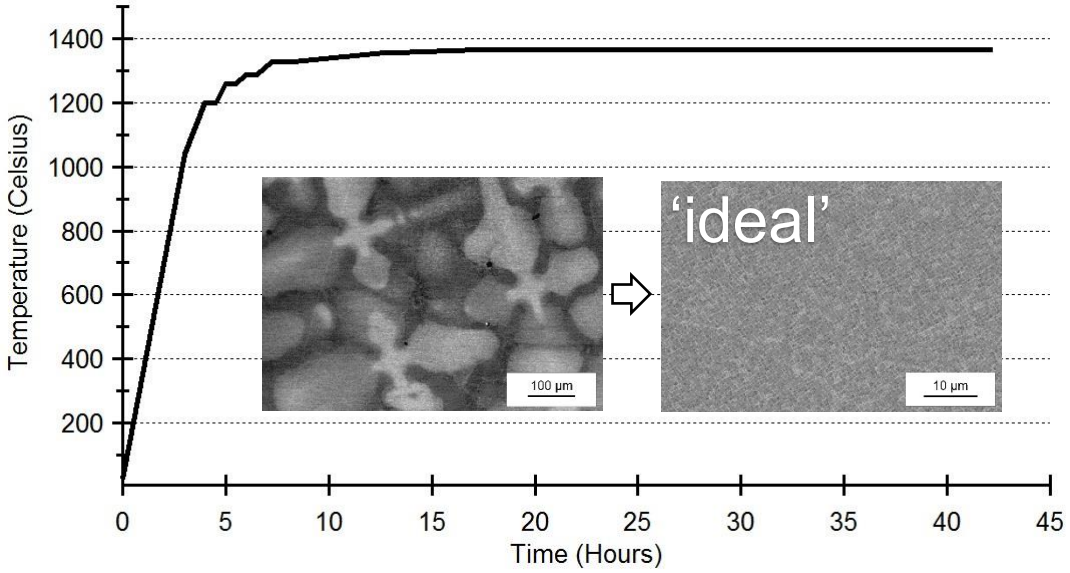

Fig. 3.3 – solution heat treatment cycle used for CMSX-10N cast components

In solutioning there are a series of ramps and holds used to allow partial solutioning to occur gradually, the objective is to reduce the likelihood of incipient melting during the climb to the ultimate hold temperature, which for this alloy is 1364 °C. During solutioning, the vacuum level was 10^{-3} mBar. After solutioning the components received a rapid gas fan quench using argon gas.

3.2.2. Samples

The following exemplify the point in the manufacturing route (*Fig. 3.4*) from which a blade X specimen was taken, all data taken from each specimen is from transverse section through the blade base from half-way up what is termed the root block. (*Fig. 3.2 – section B*)

Sample	Cast	Core leached	Heat-treatment (Sol^{n} and Age)	Figure and Section	Notes
As manufactured core – green state – pre heat treated casting	✗	✗	✗	*Fig. 3.4 (1*)* *See results 3.3.1*	examples of the ceramic core used to form the cooling passage of a blade X
Root block section – as cast turbine blade – core in-situ	✓	✗	✗	*Fig. 3.4 (2*)* *See results 3.3.2*	type X blade has been cast and has had the root block sectioned **prior** to the core leach process
Root block section – as cast turbine blade – core leached away	✓	✓	✗	*Fig. 3.4 (3*)* *See results 3.3.3*	type X blade was cast, was core leached and was **subsequently** sectioned
Root block section – heat treated turbine blade – internal surface melting	✓	✓	✓	*Fig. 3.4 (4*)* *See results 3.3.4*	type X blade was obtained **post** solution and age heat treatment and displayed the enriched melt zone (EMZ) feature and DP
Root block section – heat treated turbine blade – heavy surface melting	✓	✓	✓	*Fig. 3.4 (5*)* *See results 3.3.5*	type X blade was obtained **post** solution and age heat treatment and displayed an **extreme** example of the enriched melt zone feature

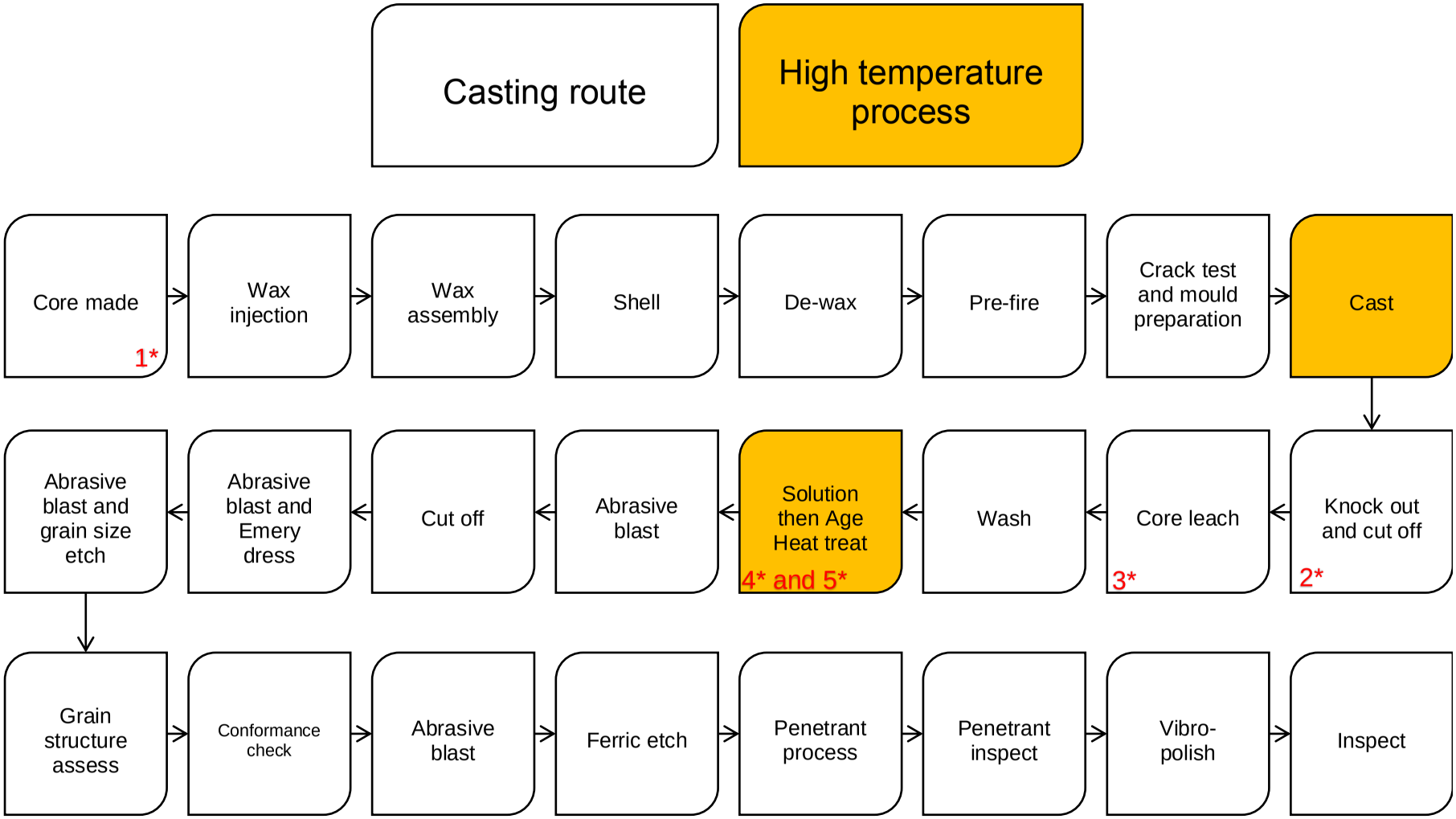

Fig. 3.4 –casting processing for a single-crystal turbine blade, high-temperature processing is >200°C

3.2.3. Microstructural characterisation

3.2.3.1. Metallographic preparation

All specimens are from the root block and were sectioned transverse to the blade long axis in order to provide an ‘in-plane’ view of the enriched melt zone (EMZ) and discontinuous precipitation within the microstructure. Unless otherwise stated in the results specimens were examined in the polished state and received no further etching or electropolishing treatments.

Cutting

Cut-off machine	Met – prep Cut-off wheels
Discotom – 5	Type FES or 2HA

Mounting – Met-prep conducto-mount

Grinding – (Direction of grinding is same-direction rotation)

Step	SiC grit paper + quantity	Lubricant	Force (N) – single 50mm samples	Time (s)	RPM
1	120 (2)	Water	35	120	150
2	180 (2)	Water	35	120	150
3	220 (2)	Water	35	120	150
4	320 (2)	Water	35	120	150
5	1000 (2)	Water	35	120	150
6	2400 (2)	Water	35	120	150
7	4000 (2)	Water	35	120	150

Polishing – (Direction of polishing is same-direction rotation)

Step	Abrasive	Cloth	Lubricant	Force (N) – single 50mm samples	Time (s)	RPM
1	1µm diamond	MD Nap	‘Green’	35	360	150
2	0.04 µm OPS	MD Chem	Water	35	60	150

Etching – (*where applicable*) – Electrolytic 10% phosphoric acid using a voltage of between 3 and 4 volts.

3.2.3.2. Optical microscopy

Olympus AX70 Provis optical microscope. Image capture system was Imagic. Magnifications used include, 5x, 10x, 20x, 50x and 100x. (*Not all displayed*)

3.2.3.3. Scanning electron microscopy

SEM images were taken at 15 or 20 kV using either a field emission gun (FEG), a FEI Nova NanoSEM FEG, a tungsten filament, Jeol XL30 or a thermionic (CeB_6) source, a Phenom ProX.

3.2.3.4. Energy dispersive spectroscopy

Jeol XL30 fitted with EDS detector, running Aztec software from Oxford instruments

3.2.3.5. Electron probe micro analysis

EMPA was carried out using a Cameca SX100 electron probe micro-analyser. All analyses were made using WDS. The instrument was operated at 20 kV. Processing of raw x-ray data applied the PAP corrections using Cameca's PeakSight software. X-ray lines were chosen, as is standard practice in EPMA, to maximise count rates while eliminating overlaps with other X-ray lines.

3.2.3.6. Electron back scattered diffraction

EBSD scans were conducted at 30 kV using a FEG source, a FEI Nova NanoSEM FEG running the Bruker EBSD acquisition system. The EBSD data was analysed using the HKL Channel 5 software package distributed by Oxford Instruments.

3.3. Results

This investigation looked at the interaction of CMSX-10N cast against a silica-based core (MD™) used to form the turbine blade internal cooling passage. Data was collected from the root block of type X turbine blades from various points during the manufacturing process.

3.3.1. As manufactured core – green state – pre heat treated casting

Silica-based ceramic cores are injection moulded then receive a pre-fire at the supplier before they become incorporated within the wax pattern replica of the turbine blade.

3.3.1.1. Optical microscopy

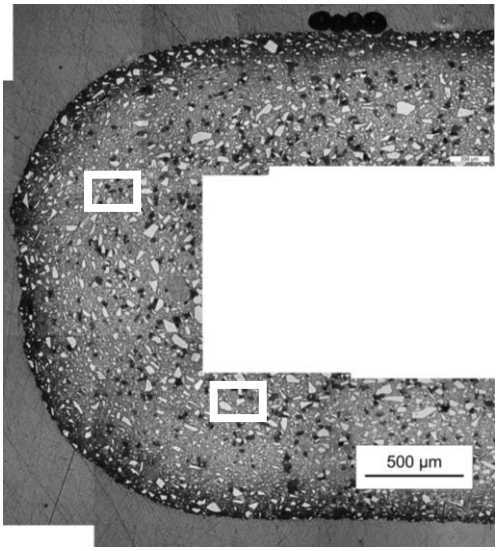

Fig. 3.5 – montage ceramic core pre casting

The montage in *Fig. 3.5* shows a transverse section through the silica-based ceramic core, its microstructure is in the green state; prior to casting. The structure is composed of a grey matrix, some larger brighter grains distributed throughout and pores that appear as dark regions. The level of sintering between individual silica grains is low throughout the material.

3.3.1.2. Energy dispersive x ray - Mapping

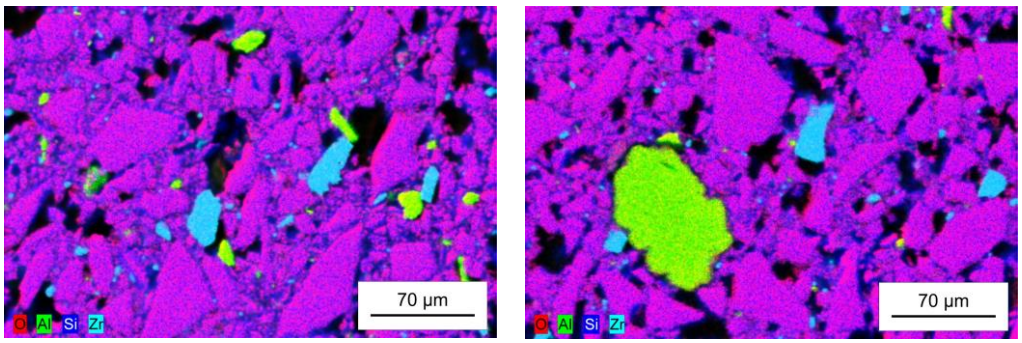

Fig. 3.6 – elemental mapping of ceramic core; O is red, Si is blue, Al is green and Zr is cyan

Elemental mapping (*Fig. 3.6*) confirms the ceramic matrix as silica (SiO_2) and the presence of small grains (ca 30 µm across) of both zircon ($ZiSiO_4$) and alumina (Al_2O_3). The

dark regions are induced porosity within the structure to provide crushability during casting. The microstructure was consistent from bulk to outer surface. The magnification offered by SEM proves the lack of sintering between separate silica grains in the pre-casting condition.

3.3.2. Root block section – as cast turbine blade – core in-situ

3.3.2.1. Optical microscopy

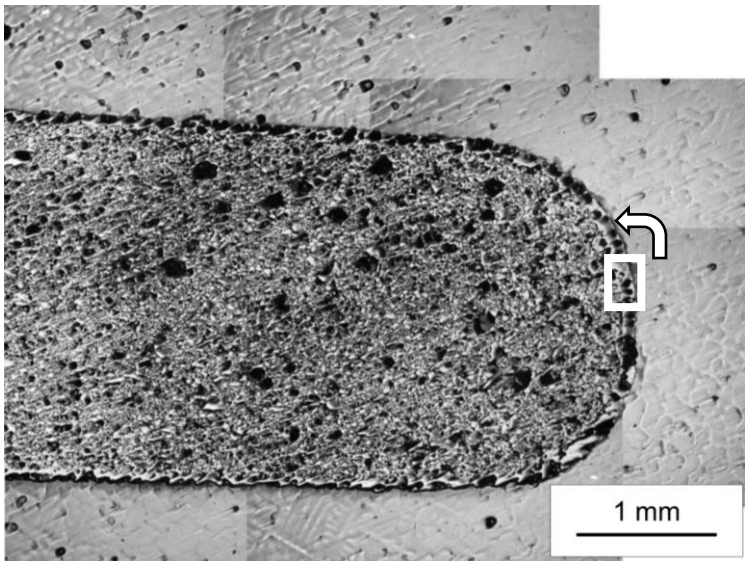

Fig. 3.7 – montage ceramic core retained within turbine blade sectioned root block

The montage in *Fig. 3.7* shows how the microstructure of the ceramic core has changed as a result of the casting process. There is strong evidence for pressure-assisted (or assisted) liquid phase sintering observed at the outer surface, the thickness of the layer increases as the peak of the apex is reached and this diminishes to a background level upon the long straight edges. Applied pressure provides a potent driving force for increased densification of sintering ceramics.[81]

3.3.2.2. Scanning electron microscopy

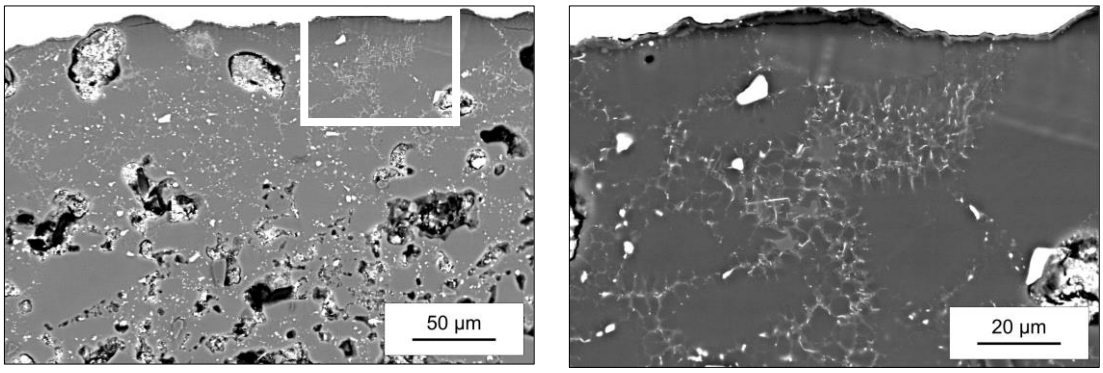

Fig. 3.8 – assisted sintering layer adjacent to as-cast superalloy

SEM image *Fig. 3.8* shows the silica-based ceramic core featuring the band of assisted sintering adjacent to the cast superalloy. Within the ca 100 µm thick band of sintering tendrils brighter needles appear. These are not present within the bulk of the as-cast core.

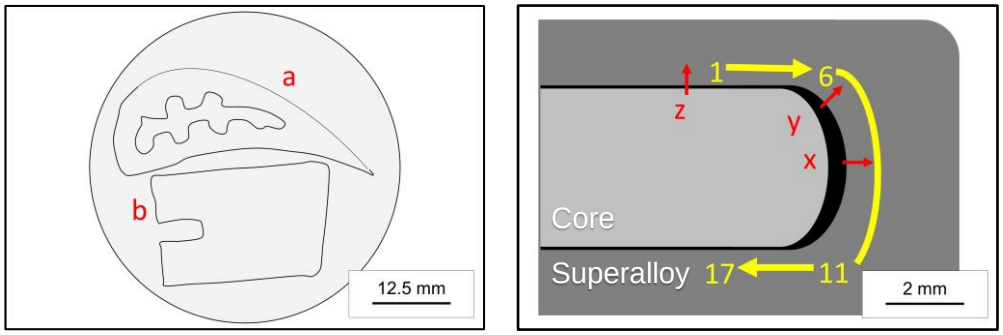

Fig. 3.9 – depiction of 50mm micro with section a and b prepared (a) and diagram detailing location around the apex of sintered layer thickness data (b)

The blade X with core retained was sectioned, (a) in *Fig. 3.2* shows the cut across the root block. Using optical microscopy in *Fig. 3.7* the thickness of the assisted sintering was measured 5 times and averaged in each of 17 high magnification images yielding a sintered ceramic value at points around the apex of the curved region, see *Fig. 3.9* (b). Multiple measurements reduced noise and artefacts enabling trends in the data to be better resolved.

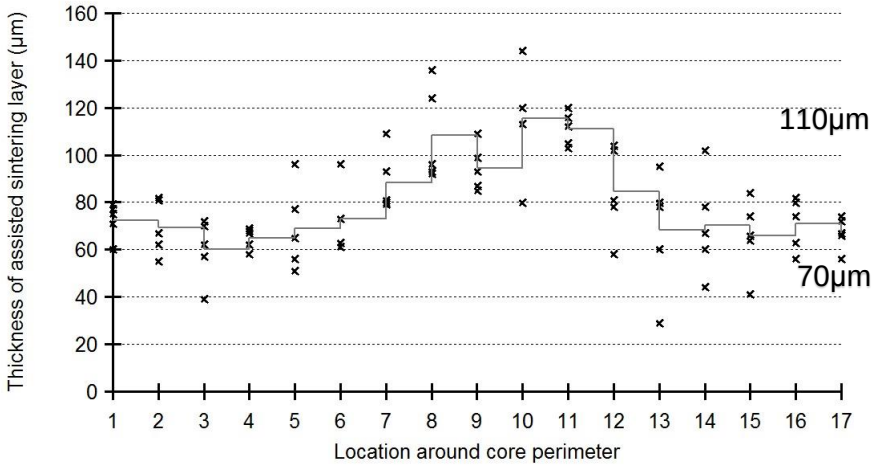

Fig. 3.10 – assisted sintering layer thickness versus arbitrary numbering (see Fig. 3.9 (b) *)*

Intentional pressure-assisted liquid phase sintering is used frequently in laboratories through the hot pressing technique. Both heat and pressure are applied to the ceramic using a die in order to obtain suitably dense samples.[82] The pressure at the curved apex, shown in *Fig. 3.7, 3.8 and 3.10*, is greater than along the straight edges due to the effect of the differential CTE and the aspect ratio of the ceramic core. As a result, at its maximum the thickness of the assisted liquid phase sintered region is ca 110 µm whilst the residual level of liquid phase sintering is ca 70 µm as displayed in the straight edges. The measurements support the initial optical examination.

3.3.2.3. Energy dispersive x ray – mapping

Using EDS mapping *Fig. 3.11* displays evidence of a chemical reaction between the ceramic core and the cast superalloy. The green aluminium map shows a continuous band of aluminium enrichment at the interface signifying where a new oxide phase has formed between the two materials over the duration of the casting process.

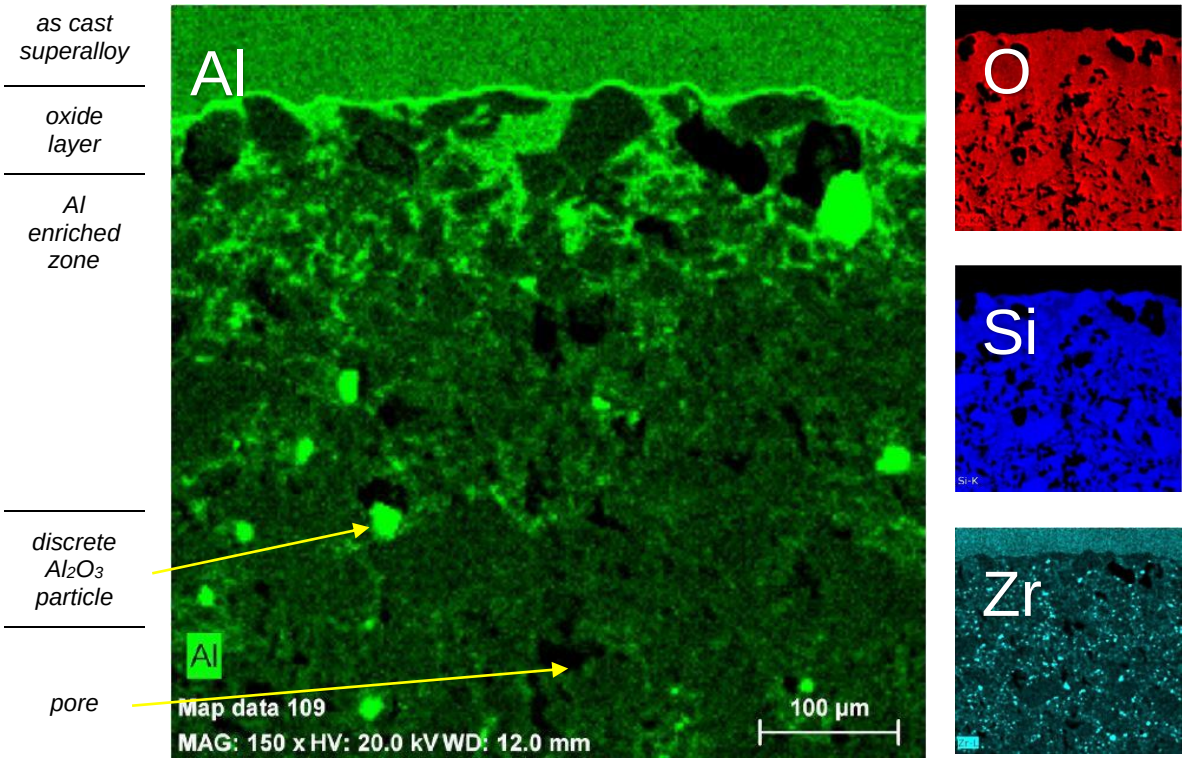

Fig. 3.11 – elemental mapping across interface between as-cast metal and silica-based ceramic core

Additional maps in *Fig. 3.11* show the main constituent of the core, silica, displayed in both the oxygen and silicon maps as well as by the presence of small zircon particles. Beneath the continuous aluminium interface can be seen a region of aluminium enrichment that coincides with the assisted sintering layer seen in the optical micrographs of *Fig. 3.7*. Further to the aluminium enrichment are regions of aluminium concentration, these discrete particles are the added alumina used to modify the physical properties of the ceramic core. The aluminium enrichment differs from the already present discrete alumina particles through the diffuse nature of the enriched tendrils, as mentioned in *Fig. 3.8.* These tendrils are present only in the ceramic core immediately adjacent to the as-cast superalloy and not deeper down within the bulk of the silica-based ceramic.

Fig 3.12 features elemental line traces confirming the aluminium oxide layer at the interface between ceramic core and cast superalloy. Thickness of the layer is between ca 2 and 5 µm with a thicker layer found at the curve apex where the trace was taken across an interdendritic region that was immediately sub-surface. The red x, y and z refer to *Fig. 3.9*.

3.3.2.4. Electron probe micro analysis – trace

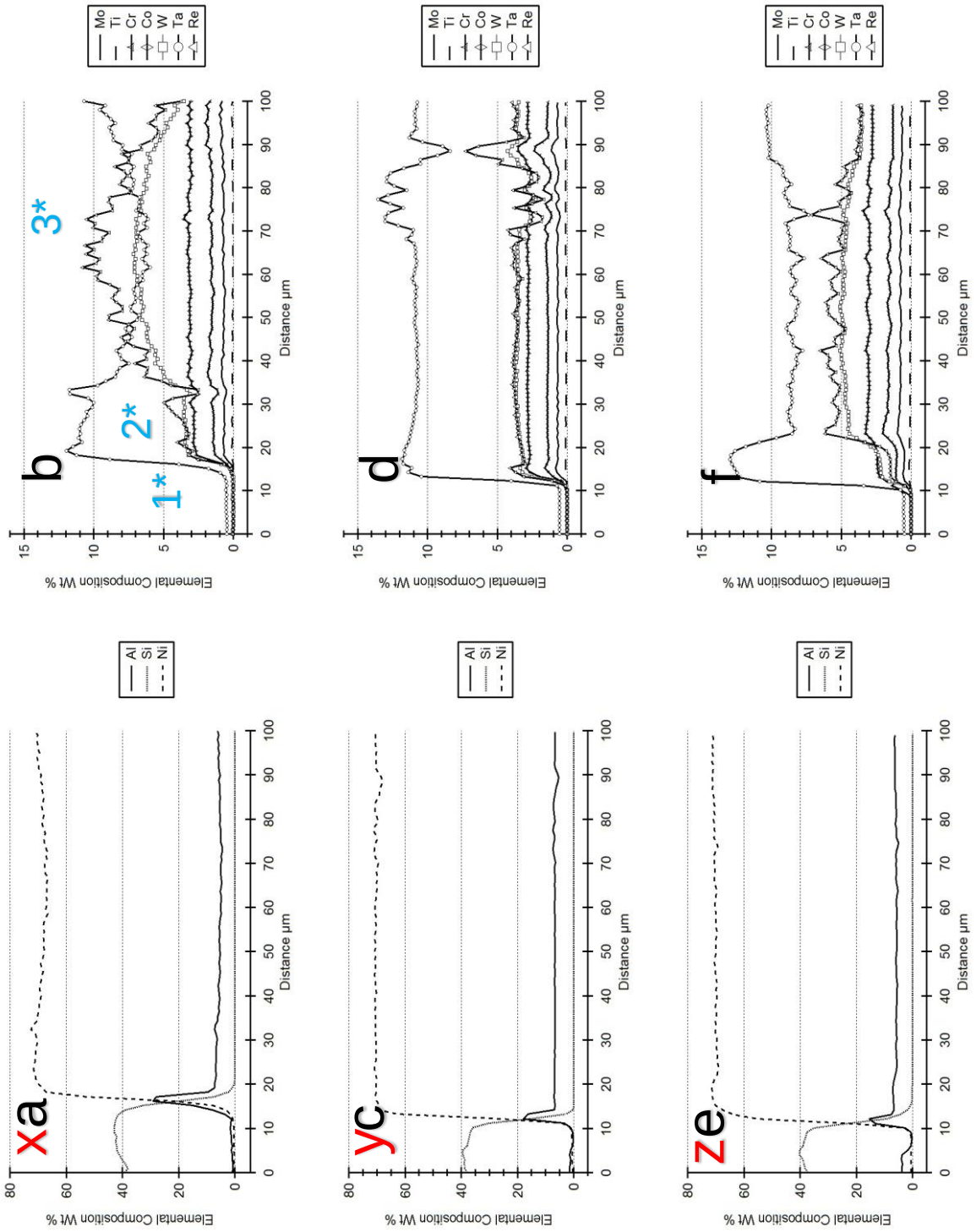

Fig. 3.12 – elemental traces across the interface at three locations; apex (a) and (b), ½ way around the curved region (c) and (d), upon the straight edge (e) and (f), within (b) are three highlighted features 1 is the core, 2* is an interdendritic region and 3* shows the line scan crossing a dendrite arm*

Data courtesy of C. Hayward

EPMA provides accurate elemental compositional data, features like dendrites and interdendritic regions within the material, to the RHS of *Fig. 3.12 (b), (d) and (f)* are observed.

3.3.2.5. Electron probe micro analysis – mapping

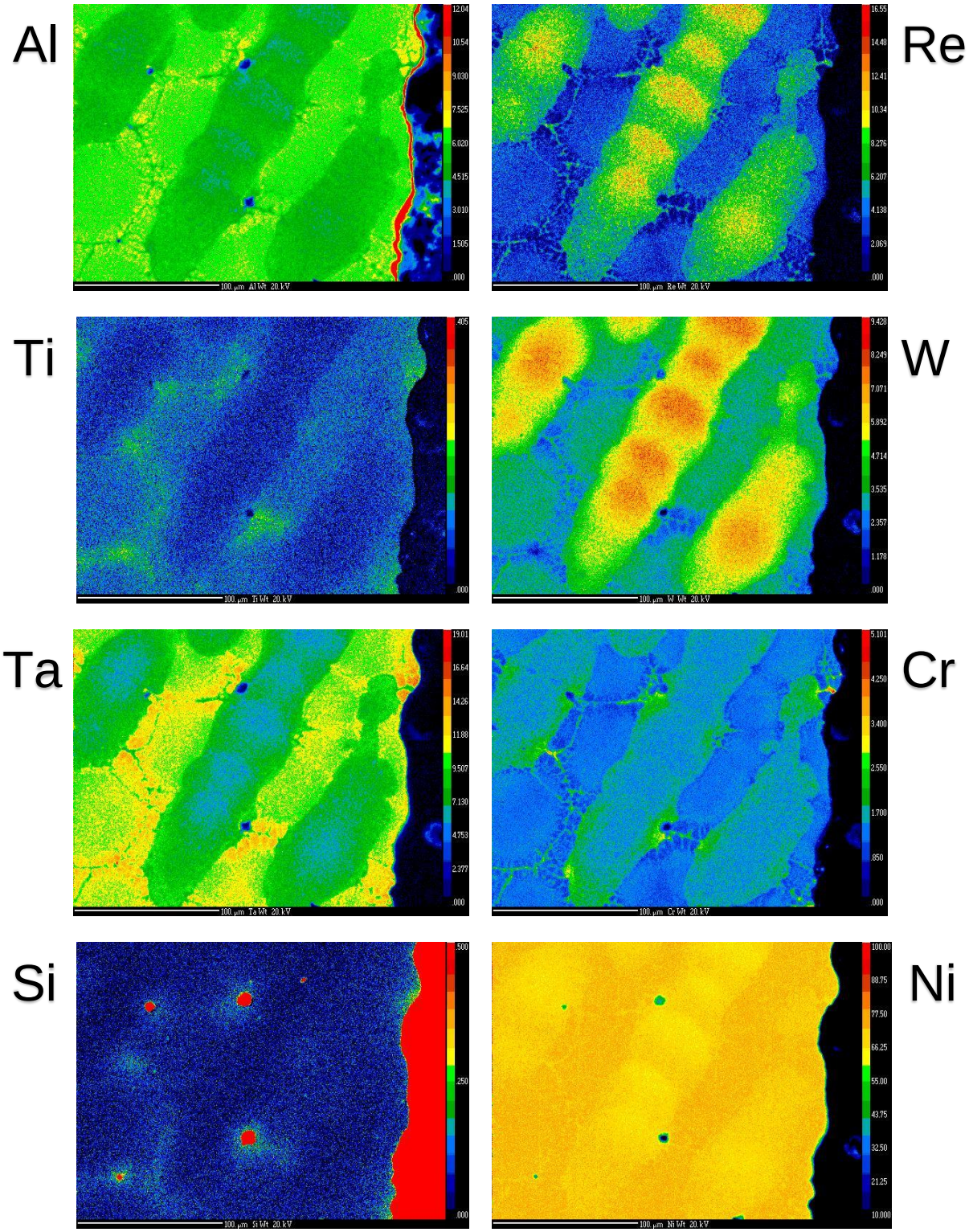

Fig. 3.13 – elemental mapping of the cast alloy CMSX-10N with core retained (Wt. %)

Data courtesy of C. Hayward

EPMA mapping, *Fig 3.13*, reveals the dendritic microstructure of the as-cast CMSX-10N and the presence of the alumina at the interface between core and the alloy. Aluminium enrichment within the silica-based core can be seen on the right side of the aluminium map.

3.3.3. Root block section – as cast turbine blade – core leached away

3.3.3.1. Optical microscopy

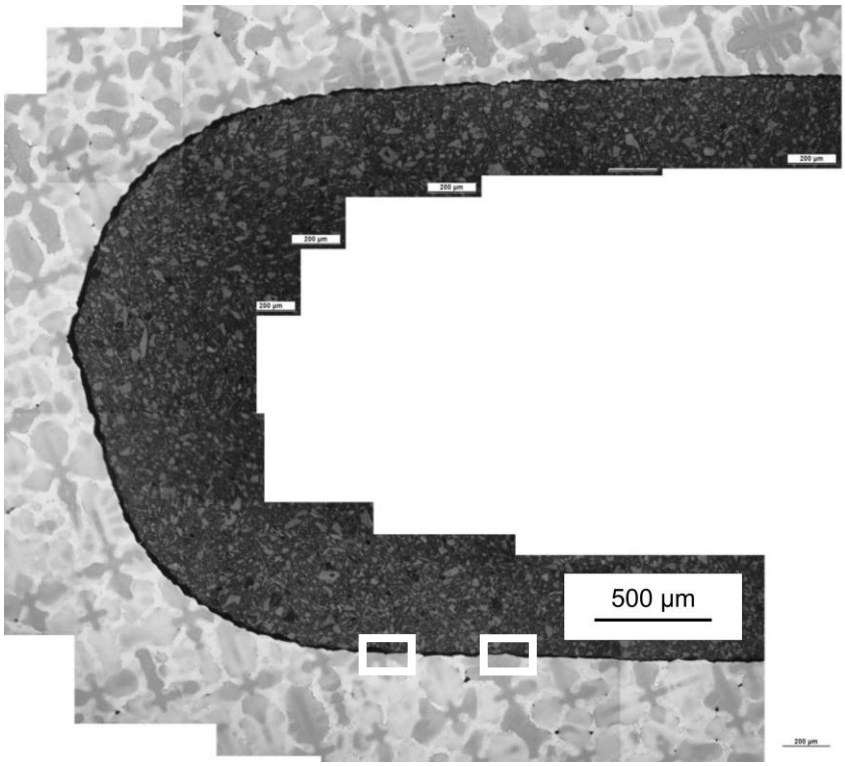

Fig. 3.14 – montage electrolytically etched sectioned root block in as cast condition

The optical microscopy montage (*Fig. 3.14*) shows the layout of cruciform dendrites and interdendritic spaces in the turbine blade root block. At this magnification it can be seen that there is no separate layer of eutectic around the internal surface of the geometry.

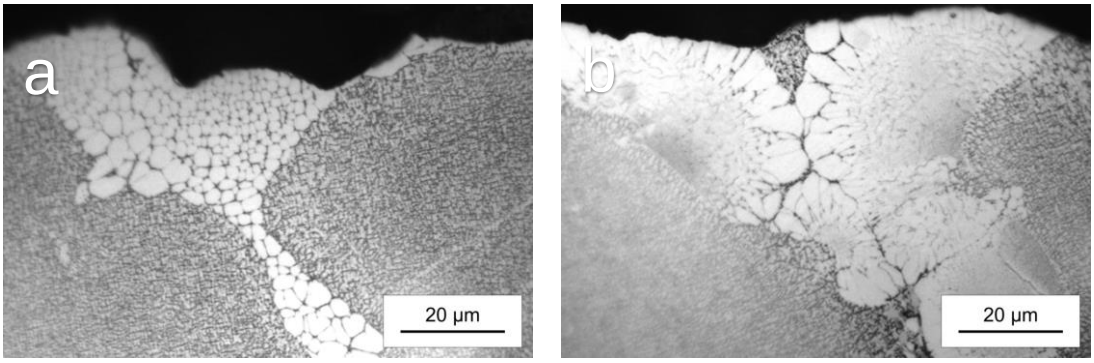

Fig. 3.15 – interdendritic phase impinging upon inner blade surface, coarse (a) mixture of coarse and fine (b)

Higher magnification images show various forms of interdendritic phase within the as cast microstructure. *Fig. 3.15* shows a collection of coarse cellular γ' sandwiched between lobes of γ dendrite. A variety of both coarse and fine cellular γ' is seen. In both instances the γ' is pressing upon the internal surface of the component but by no means continuously, there is no constant band of eutectic that runs parallel with the surface.

3.3.3.2. Scanning electron microscopy

Using SEM-BSE it is was possible to look down onto the blades internal surface of an as-cast region which had received the leaching process for core removal. *Fig. 3.16 (a)* shows the low magnification image, clearly visible is the trench formed as a result of cutting the root block from the blade X type and then sectioning again in order to look down upon the curved apex of the cooling passage though the root block. Box (b) in *Fig. 3.16 (a)* is at the very apex of the curved region and is shown at higher magnification in *Fig. 3.16 (b*) where the apparent coarseness of the as-cast and as-leached surface is revealed.

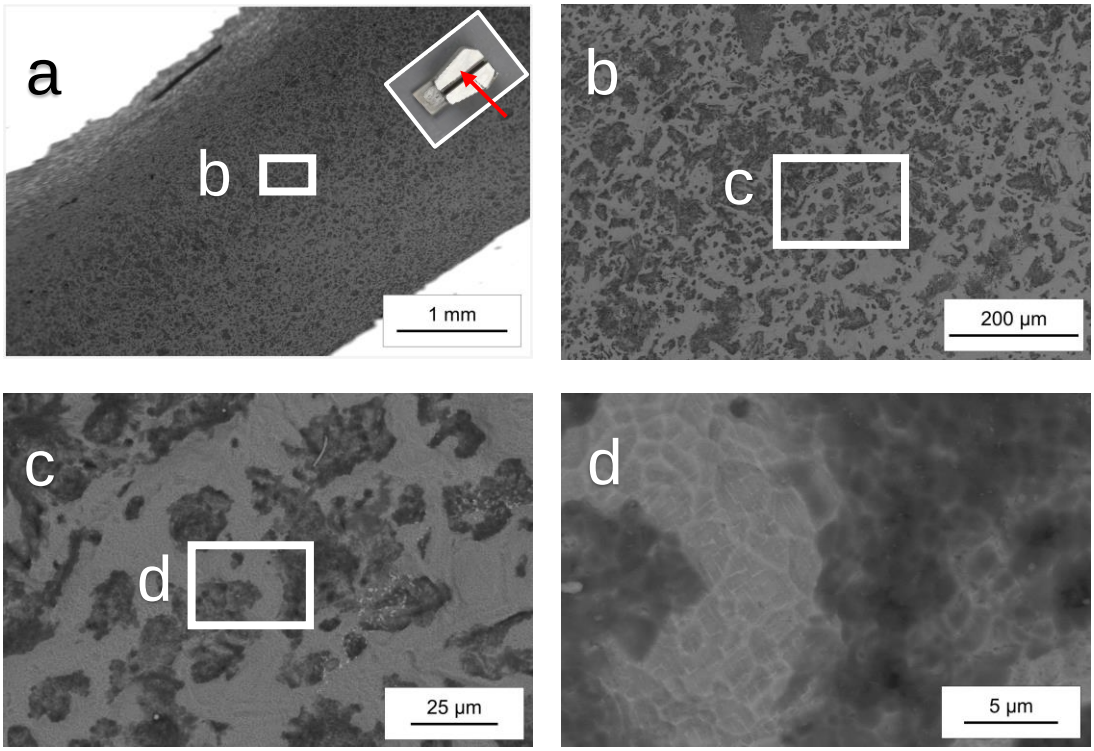

Fig. 3.16 – internal surface of turbine blade root block, post core leach, low magnification showing channel looking directly upon the apex of the cooling passage (a), rough surface of superalloy (b), (c) and (d)

Further magnification increases occur in *Fig. 3.16 (c*) and *(d*) where in (c) the cratered surface of the superalloy can be seen with ca 10 – 35 µm impressions penetrating into the surface. In *Fig. 3.16 (d*) the γ/γ' microstructure is faintly visible upon the surface. The use of backscatter electrons enables the γ/γ' to be distinguished but since this specimen was not metallographically prepared and was placed in the SEM in the rough, as-cast state, the dark regions actually correspond to depressions within the undulating superalloy surface. There is likely some difference between the craters and the protruding areas in terms of oxide thickness but the contrast is mainly due to the very coarse surface left as a result of casting against the silica-based ceramic core and the subsequent leach process. It is important to note that the external surfaces of a turbine blade undergo machining operations to clean the surface but internal surfaces are inaccessible and do not get mechanically dressed.

3.3.4. Root block section – heat treated turbine blade – internal surface melting

3.3.4.1. Optical microscopy

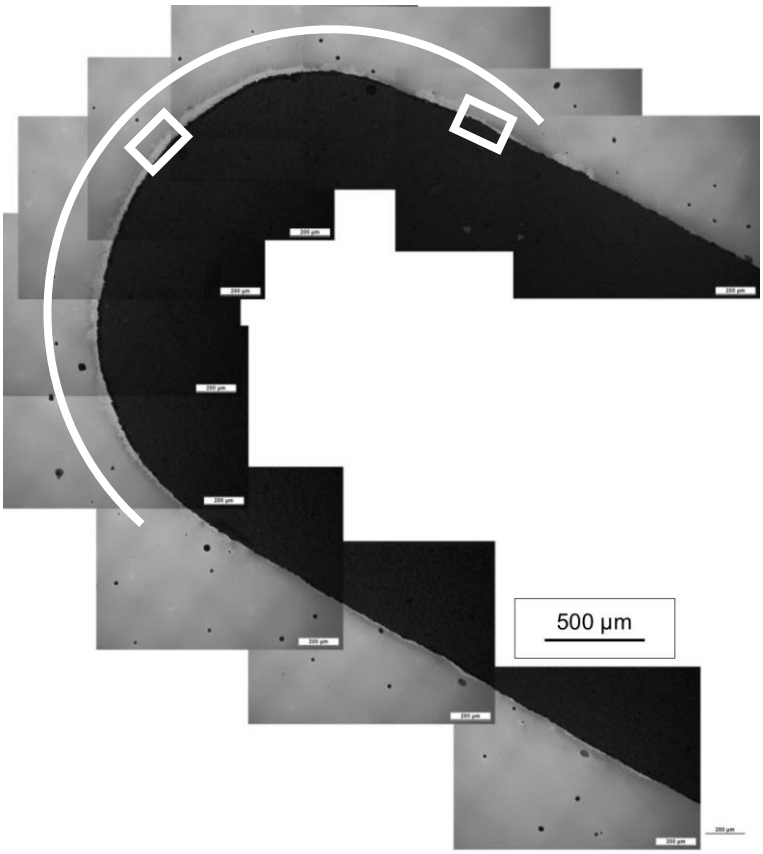

Fig. 3.17 – internal surface melting within cooling passage of a turbine blade root block

An optical microscopy montage (*Fig. 3.17*) shows the spatial distribution of the internal surface melting phenomena, its association with geometry is apparent. The defect is defined as two separate structures, first is the enriched melt zone that is present at the apex of the cooling passage but diminishes at the top and bottom corner and is almost non-existent upon the straight portions of the cooling passage. Second is the discrete discontinuous precipitation that inversely is to be found at the top and bottom corner and sporadically along the straight edges. Also visible within the alloy bulk is a level of porosity, a by-product of the directional solidification process, and a faint residual cross-hatch pattern showing that, in spite of long high temperature solution heat treatment, the high rhenium levels resist total homogenisation on economical timescales.

Using electrolytic etching and optical microscopy the microstructure of both the enriched melt zone and the discontinuous precipitation are determined. (*Fig. 3.18*) The enriched melt zone, total thickness ca 40 µm, appears bright and lighter than the substrate γ/γ’ but is similar in hue to the residual eutectic pools present in the bulk when similarly etched. There are three regions moving from outermost in; first is a band, 5 µm thick, which is comparatively featureless (*1**). Second is the central 25 µm and displays small precipitates

throughout, some are aligned into strands (*2**). Finally the innermost 10 µm is a blurred interface (*3**) between the enriched melt zone and the underlying bulk of the component (*4**). The discontinuous precipitation feature (*Fig. 3.18*) is fan-shaped, 30 µm thick at its deepest, and comprises three key structures: the main γ' phase interspersed with γ strands and what is likely to be lamella TCP *P*-phase precipitates. These microstructures and *P*-phase precipitates are similar to those discussed by both Walston and Scarlin.[72,74]

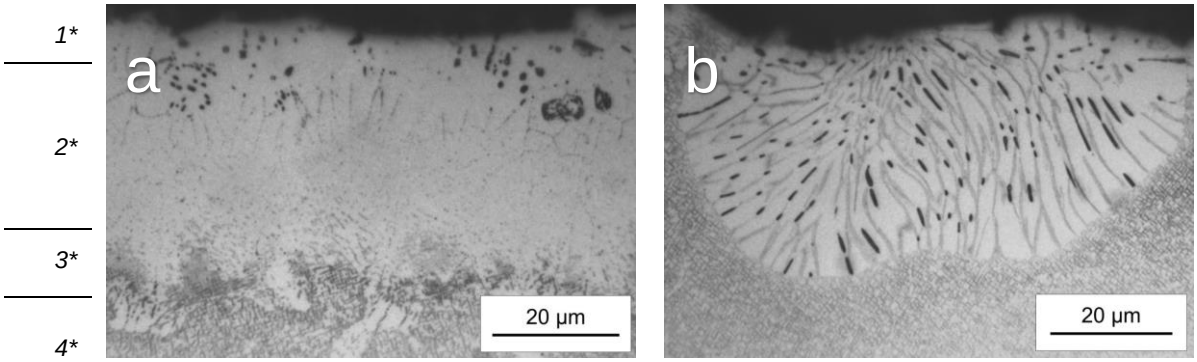

Fig. 3.18 – enriched melt zone (a) and discrete discontinuous precipitation feature (b)

In regions highly populated with discontinuous precipitation features (*Fig. 3.19*) the opportunity for contact and parallel growth is greater. Where two features coexist it is clear discrete colonies of precipitate *P*-phase aligned each with the direction of cellular boundary growth. (*Fig. 3.19*) shows two adjacent cells each with its own clearly defined direction of TCP growth insinuating at least two close but separate nucleation events.

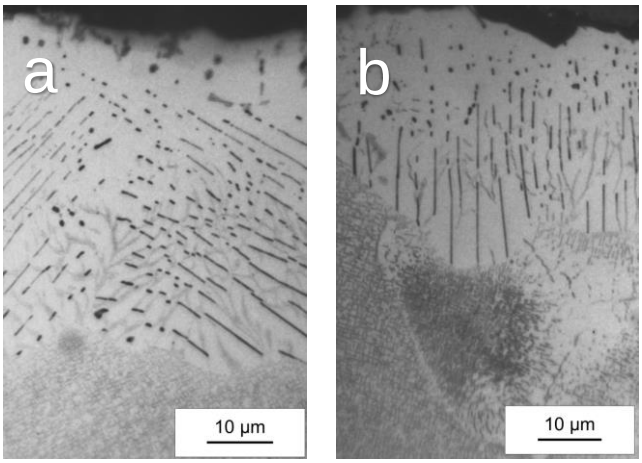

Fig. 3.19 – duo – discrete discontinuous precipitation feature (a) and single precipitation feature colliding with interdendritic eutectic pool (b)

Growth of discontinuous precipitation features is likely to occur during the later age heat treatment following the higher temperature solutioning period. This is corroborated by (*Fig. 3.19*) which shows the ingress of a precipitate feature into the pre-existing eutectic melt pool.

3.3.4.2. Scanning electron microscopy

Backscatter electron microscope images show additional features within the enriched melt zone. Examination of the entire enriched melt zone (*Fig. 3.20*) shows that there are a plethora of very small, < 1 μm, bright white precipitates clearly enriched in refractory elements including rhenium and tungsten, as evidenced by the contrast. These precipitates are likely to reside within thin γ channels lying within the predominantly γ' melt zone. The blurred interface between the enriched melt zone and the superalloy bulk shows a very fine cross-hatching within the microstructure as a result of the melting phenomena, this is likely γ precipitating from γ'. The bright precipitates are heavily concentrated towards the external region of the melt zone suggesting that upon quenching from high temperature, the heavy elements rhenium and tungsten, being of low solubility in the aluminium-rich γ' phase are swept forwards whilst in the liquid state and concentrated in the still liquid state as the melt zone solidifies from outwards. As the enriched melt zone solidifies and the heavy elements are concentrated towards the outside they eventually precipitate as small pinpoint precipitates. (*Fig. 3.20 (c)*)

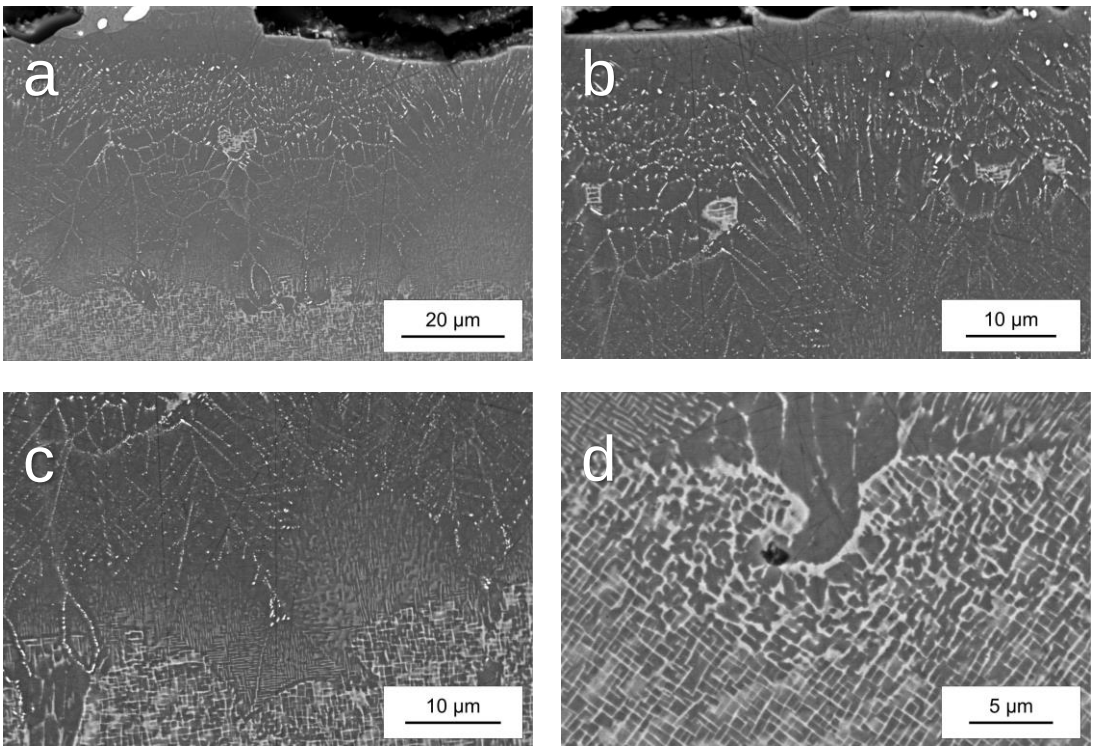

Fig. 3.20 – entire enriched melt zone (a), close up outer region (b), close up inner region and zone / bulk interface (c) and high magnification of zone / bulk interface with γ/γ' disruption and porosity (d)

At the blurred interface between the enriched melt zone and the bulk, clear evidence exists of severe disruption to the γ/γ', both coarse and fine residual eutectic cellular morphology that did not homogenise and a small pore at the tip of the residual interdendritic phase. (*Fig. 3.20 (d)*)

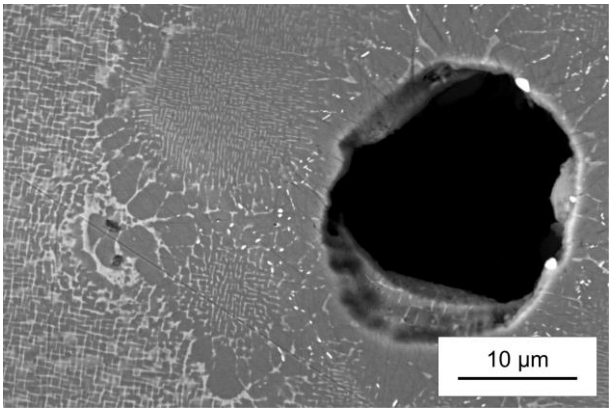

Fig. 3.21 – residual eutectic pool post heat treatment surrounding pore

Due to severe segregation and coring during the casting process, residual eutectic pools are commonly seen, even post solution heat treatment, fully 100% solutioned components would not be economically viable, particularly in this alloy which has a large γ' volume fraction. *Fig. 3.21* shows a large 20 µm diameter pore within the superalloy microstructure surrounded by a eutectic pool that has endured the solutioning process. *Fig. 3.21* is a close up of the surrounding eutectic microstructure and it shares some striking similarities to the aforementioned enriched melt zone. Moving from left to right in *Fig. 3.21* we see standard γ/γ' microstructure give way to an unstable disrupted form before crossing the threshold to the eutectic pool itself. Within this pool we see both coarse and fine interdendritic phase and finally the pore itself, an indicator of the last area to solidify.

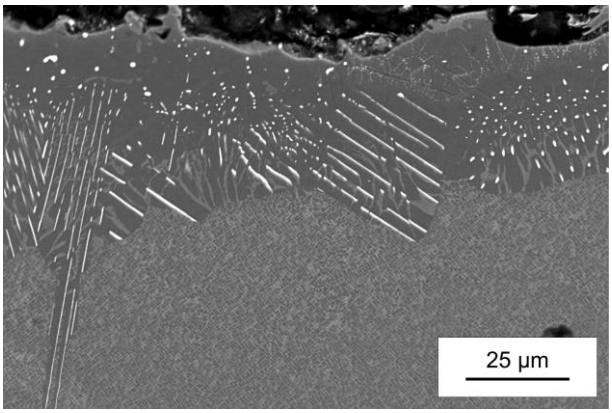

Fig. 3.22 – discontinuous precipitation, TCP phases and coarsened γ/γ' (a)

Discrete discontinuous precipitation has a different microstructure to the enriched melt zone. The precipitates are the result of moving boundary reaction that grows into the supersaturated substrate converting the tight knit γ/γ' into cellular colonies including a series of bright white parallel lamella, most likely *P*-phase TCP and elongated γ channels within a matrix of γ'. *Fig. 3.22* shows TCP growth occurs upon the closest <111> plane in relation to the direction of boundary movement. *Fig. 3.22* is an SEM-BSE micrograph taken of a similar colony to that seen in *Fig. 3.18 (b)* and is located in the RHS box in *Fig. 3.17*.

3.3.4.3. Energy dispersive x ray – Elemental composition

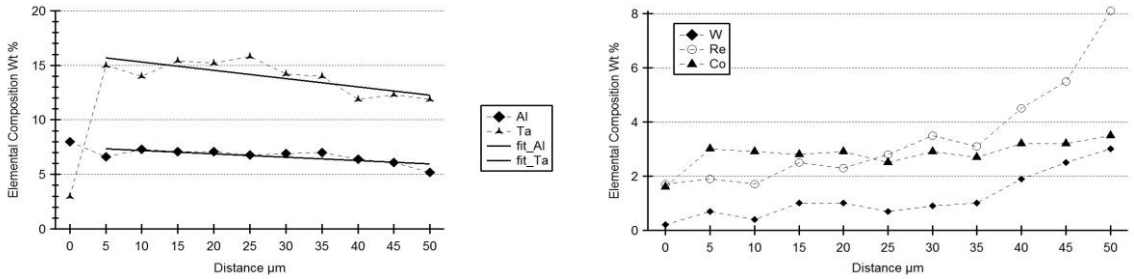

Fig. 3.23 – elemental composition across enriched melt zone, primary elements in Wt % (a), secondary elements in Wt % (b)

Fig. 3.23 details elemental variation across the enriched melt zone showing trends in distribution. Of the elements enriched in the melt zone aluminium and tantalum are the most pronounced, with nickel registering a slight increase (*not shown in Fig. 3.23*). Elements which suffer depletion within the melt zone include cobalt, tungsten and rhenium with levels returning to the alloy normal once we cross the interface back into the underlying substrate.

3.3.4.4. Energy dispersive x ray – Mapping

Fig. 3.24 shows elemental mapping support the conclusions above regarding which elements are enriched and which are depleted because of the internal melting phenomena.

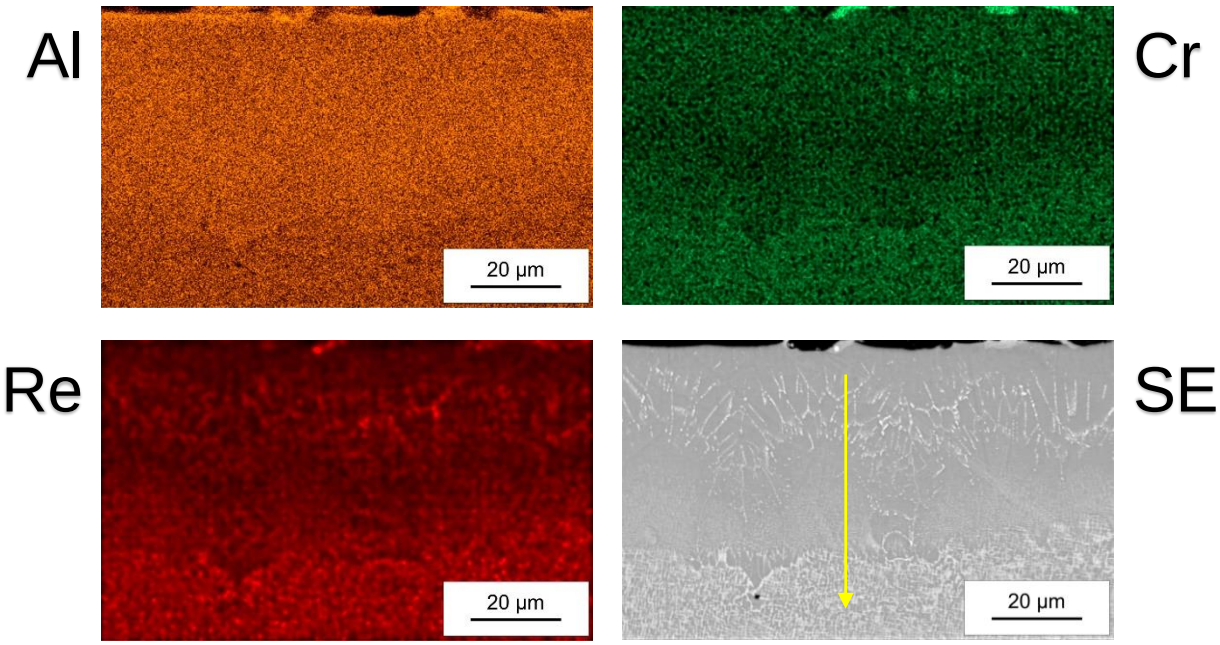

Fig. 3.24 – elemental mapping across the enriched melt zone, the yellow line shows from where the elemental concentration trace was obtained displayed in Fig. 3.23

3.3.4.5. Electron back scattered diffraction

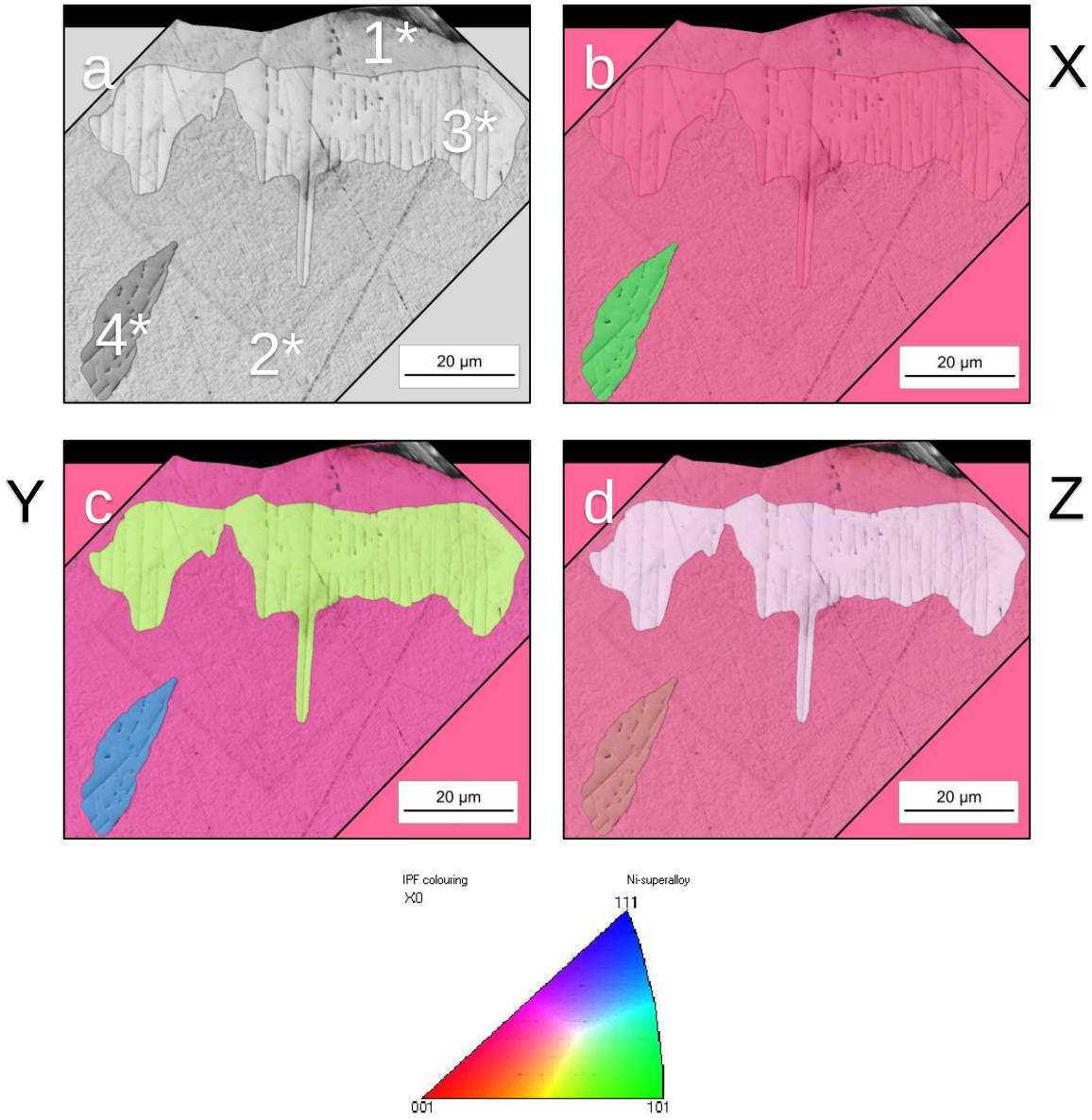

Fig. 3.25 – EBSD map; band contrast (a), inverse pole figure X (b), Y (c) and Z (d)

Electron back scatter diffraction has been used to determine the relative orientation of both the enriched melt zone (1*) and two regions of discontinuous precipitation (3* and 4*) with regards to the bulk superalloy component (2*) with its orientation fixed during directional solidification. The phase identification map (not shown) confirms that almost all indexed points were attributed to the FCC nickel superalloy pattern. Very low recordings of TCP phases were picked up upon the needles seen in (*Fig. 3.25 (a)*) but this was negligible.

DP region 3* can be seen to have the same orientation as the bulk superalloy in the X inverse pole figure (*Fig. 3.25 (b)*). However inverse pole figures Y and Z (*Fig. 3.25 (c) and (d)*) show a discrepancy between the orientation of the blade (2*) and the relative Y and Z orientations of the discontinuously precipitated cells (TCPs 3* and 4*).

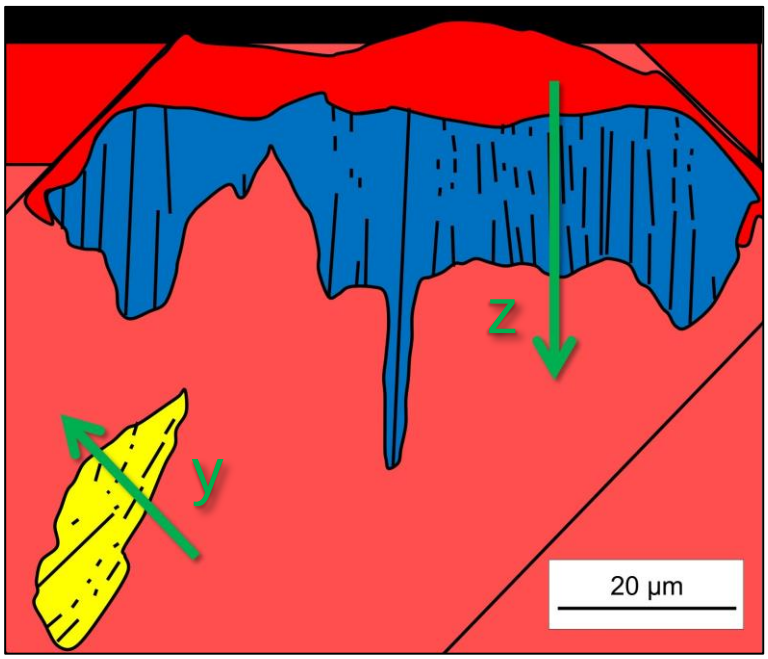

Fig. 3.26 – EBSD map diagram, RED is the enriched melt zone, BLUE is DP 3, YELLOW is DP 2* and PINK is the bulk underlying superalloy. GREEN arrows indicate the two lines of misorientation data displayed in Fig 3.27*

Fig. 3.26 is a false-colour diagram of the EBSD data shown in *Fig. 3.25* and displays two TCP filled DP cells as well as the enriched melt zone at the top and the standard single-crystal component at the bottom of the diagram. Of note are the two green lines displaying where a misorientation data trace was collected from to be displayed in *Fig. 3.27*. The misorientation degree as a function of relative distance along the trace clearly shows that there is a high-angle grain boundary that exists between the superalloy and the DP cells.

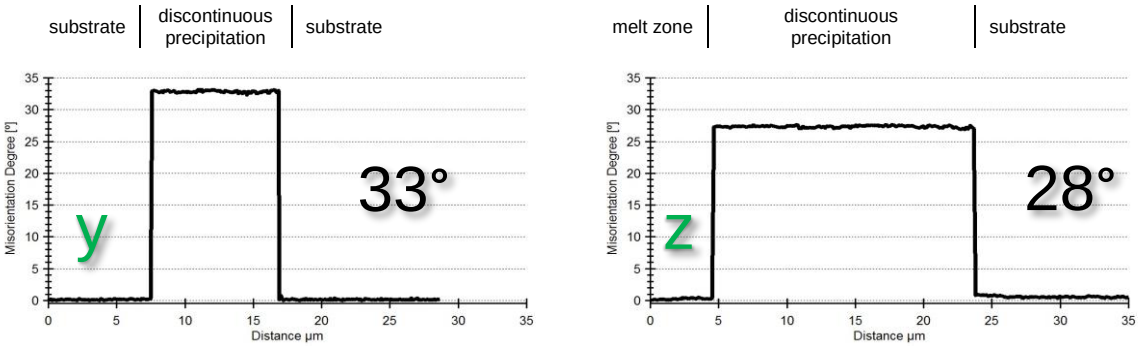

Fig. 3.27 – misorientation data collected from Fig. 3.26

3.3.5. Root block section – heat treated turbine blade – heavy surface melting

3.3.5.1. Optical microscopy

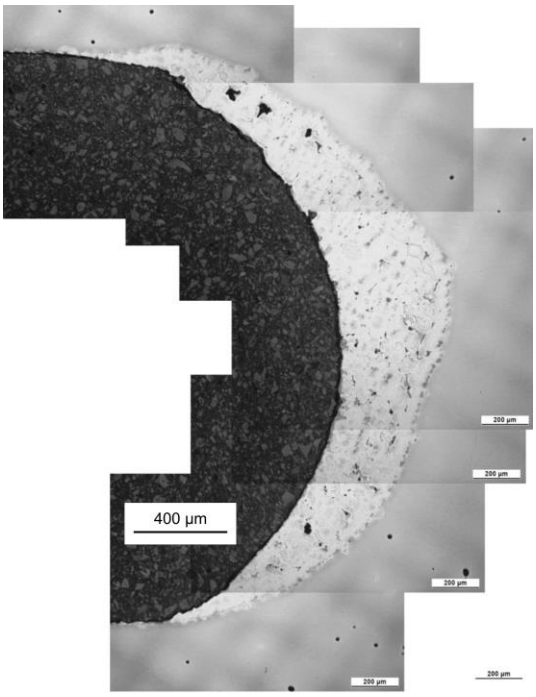

Fig. 3.28 – heavy internal surface melting within cooling passage of a turbine blade root block

An optical microscopy montage (*Fig. 3.28*) shows the spatial distribution of the heavy internal surface melting phenomena, its dependence on geometry is apparent and is very similar to *Fig. 3.17*. The defect primarily affects the enriched melt zone that is present at the apex of the cooling passage but again diminishes at the top and bottom corner and is non-existent upon the straight portions of the cooling passage. The thickness of the enriched melt zone in both the internal surface melting example (*section 3.3.4*) and this heavy surface melting example (*section 3.3.5*) were measured and is shown in *Fig. 3.29*.

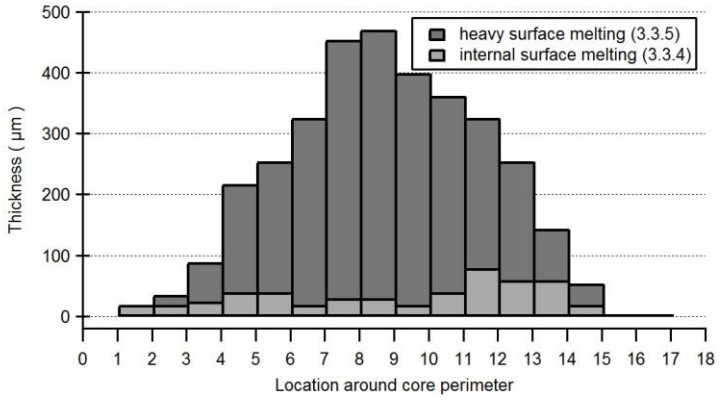

Fig. 3.29 – heavy internal surface melting versus internal surface melting (Fig. 3.17) within cooling passage of a turbine blade root block

3.4. Discussion

3.4.1. Core before and after – pressure-assisted sintering

Silica-based ceramic cores are a combination of amorphous silica, zircon and minor amounts of cristobalite and alumina. (*Fig. 3.6*) The β-cristobalite, is a high temperature polymorph of silica, and it undergoes a β → α phase transformation with a volume contraction of ca 5 vol % when it is cooled down to 200 – 270°C.[83,84] Once formulated the ceramic slurry is injected into dies to create the shape of the ceramic core. This mixture of oxide grains (*Fig. 3.6*) and induced porosity is the core microstructure throughout. During the casting process the ceramic core is in immediate contact with the liquid superalloy, at ca 1550 °C, whilst in the furnace hot zone. The temperature decreases as the mould is withdrawn from the furnace during the directional solidification process. The entire core that experiences this high temperature process undergoes a level of liquid phase sintering that results in the coalescence of individual silica grains into an interconnected matrix of silica. This occurs because fused silica crystallises at the superalloy casting temperature, and because of the aforementioned density difference between the amorphous and crystalline phases.[85]

Within the outer surface of the ceramic core, the region contacting the superalloy during casting, there is a band of continuously and densely sintered silica. External pressure has accelerated the liquid phase sintering process at high temperature (*Fig. 3.7 and 3.8*), the result is pressure-assisted liquid phase sintering. This force comes from the constricting effect generated by cooling contracting metal and likely causes the local ceramic to melt before later re-solidifying. According to Frye et al.[86], ceramic shell materials are multi-component systems and the opportunity for liquid phase formation is greater since the ceramic mixture melting temperatures are lower than the individual pure oxides melting temperatures. Additionally the effect of fluxing agents needs to be considered, conventional colloidal silica contains more than 0.6 Wt. % of Na_2O. Additional added Na_2O can reduce the melting temperature of SiO_2 from a maximum of 1720°C to as low as 837°C in extreme instances.[86]

This effect is exacerbated by two additional factors, the different coefficients of expansion between the ceramic core and the nickel-based superalloy as well as geometry effects of a rounded rectangular cross section within the root block geometry. A background level of pressure-assisted liquid phase sintering is visible along the straight edges, where there is minimal geometry effect. The degree of pressure-assisted liquid phase sintering is at its maximum upon the apex of the curved portion of the cooling passage. (*Fig. 3.9, 3.10 and Fig. 3.29*)

3.4.2. Oxide formation – thin Al_2O_3 layer

During the slow withdrawal of the mould from the furnace hot zone a thin oxide begins to form between the solidifying superalloy and the silica-based core due to high-temperature chemical interaction. Frye et al. discuss this reaction as "*the reduction of the…core…by the metal to form…metal oxide*".[86] Titanium and aluminium in nickel-based superalloys are known to react with mould oxides to produce thin layers of molten metal oxide at the metal-mould interface. These reactions are generally considered to be "*beneficial for the cast component by retarding further reaction between mould and the molten metal*."[86]

The thickness of this oxide layer is judged to be ca 3 μm in thickness (*Fig. 3.11* and *3.12*) and remains in place once formed at the interface. In the case of nickel-based superalloys it is aluminium from the substrate that reacts to form the stable alumina (Al_2O_3 – morphology unknown) oxide using oxygen removed from the silica present within the ceramic core surface. This oxide formation is a positive factor since its growth impedes further chemical ingress into the ceramic core. EMPA and EDS mapping and quantitative analysis (*Fig. 3.11, 3.12* and *3.13*) show no clear aluminium depletion layer within the superalloy immediately beneath the oxide layer. It must therefore be concluded that the oxide forms during casting at sufficiently high temperatures to enable rapid bulk diffusion of aluminium from within the component interior to the sub-surface to replenish the aluminium lost. Since this new oxide phase forms during casting it is prudent to determine what volume this new growth occupies, be it displacing the hot superalloy or chemically converting the core and mould material. This premise will be further explored in chapter 4, for now it will suffice to say it seems likely that oxide growth occurs within the surface of the ceramic core. This material permits the ingress of aluminium which reduces oxygen from the SiO_2 present. This conversion eventually blocks further ingress thereby stabilising the surface and what little silicon was freed is lost into the interior of the nickel-based superalloy. This scenario is more likely than the alternative which would see oxygen moving from the silica core into the superalloy before immediately reacting to form an oxide at the interface. This seems unlikely as small additions of oxygen to the hot alloy surface are likely to be readily absorbed and rapidly transported though into the component bulk.

This oxide is thin and likely to be easily removed post casting, this is supported by common practice within the casting foundry which involves insertion of a thin electrode within the narrow cooling passage cavity and the immersion of the component within an electrolytic etch designed to selectively etch the γ' within the microstructure. The purpose of this etchant is to enable trained borescope operators to inspect the internal surface of the component for potential recrystallisation. If this internally formed oxide were potent, strong and adherent then this etch would be rendered ineffective due to the resistant and insulating effect of the

oxide. The etchant is only capable of working if it is in contact with the superalloy metal directly or through a thin permeable oxide layer. This fact means that not only is the oxide layer thin once formed, but in addition it is likely susceptible to partial removal during the alkali leaching process designed to remove the silica-based core. This leach is likely to severely damage and puncture the thin alumina layer present internally. Further work carried out and discussed in chapter 4 reveals the nature of a thin alumina layer formed by chemical reaction during casting between the superalloy and the sacrificial core.

3.4.3. Chemical reactivity – sub-surface needles and aluminium enrichment

Upon examination of the pressure-assisted sintering layer of silica-based ceramic, there are additional aluminium containing phases observed. Besides the thin band of alumina discussed in section 3.4.2 (*Fig. 3.11* and *3.13*) there are also visible two additional aluminium rich features: The first is the discrete points of aluminium enrichment which have been identified as Al_2O_3 particles added to the silica-based ceramic to provide optimal mechanical properties of the ceramic core. The second feature is the small tendrils of aluminium enrichment that appear to originate from the superalloy and penetrate through the pressure-assisted sintering layer before ending before the bulk is reached. It is understood that the presence of the discrete alumina particles originated as part of the ceramic's manufacture but the tendrils of aluminium enriched needles (seen in *Fig. 3.8*) occur only within the pressure-assisted sintered region and only as a direct result of the high-temperature casting operation, these phases are not to be found within the core sectioned and microstructurally examined prior to casting. These aluminium tendrils appear to outline larger silica grains and exist at the point where two or more silica grains have become fused together as a result of the high temperatures and the addition of stress resulting from a contracting nickel superalloy.

At this time it has not been determined whether the aluminium that exists within these tendrils (having now formed alumina) has originated from within the nickel superalloy, absorbed by the surface of the core prior to the formation of the less permeable aluminium oxide barrier as discussed in section 3.4.2 or whether the aluminium has originated as impurities within the ceramic core that have been concentrated and precipitated as new phases at the boundaries between individual silica grains as a result of the pressure and assisted sintering mechanism. If additional aluminium had permeated the surface of the ceramic core prior to the oxide layer formation this will have happened at high temperatures since there is still no apparent depletion in the aluminium content of the superalloy beneath the oxide layer. This phenomena will be further examined in chapter 4.

3.4.4. Discontinuous precipitation

The internal surface defect explored during this investigation was composed of two microstructural phenomena, firstly is the enriched melt zone (EMZ) and secondly is the discontinuous precipitation (DP) (*Fig. 3.17 and 3.18*). The work of D'Souza et al. referenced within the introduction of Chapter 3 and 4 regarding volatilisation and the formation of an enriched melt zone is considered as being representative of the current understanding regarding this aspect of the defect. This discussion and subsequent chapter will discuss the hypothesised mechanism for the presence of discontinuous precipitation in this component.

Discontinuous precipitation is described by Nystrom et al. as the "*transformation of the metastable parent microstructure through a combined mechanism of boundary precipitation and interfacial migration, which accelerates the kinetics of the stabilisation reaction*".[78] The phenomena presents as "*the formation of a…colony containing a continuous gamma prime matrix and two sets of lamellae: disordered gamma and lamellae of a rhenium-rich TCP phase*" [78] and has been observed within several different nickel-based superalloys and can be triggered by a variety of events (*Fig. 3.19*). The increasing levels of refractory element addition in the 2nd and 3rd generation superalloys means that microstructural stability in these single-crystal alloys can become problematic, this is due to solubility limits and precipitation kinetics.[72] Precipitation of refractory-rich TCP phases occurs after periods of high temperature exposure.[78] Typically, *P*-phase TCPs are composed of ca 50% rhenium along with high levels of tungsten, chromium and cobalt with the formation leading to the remaining γ phase within the colony being depleted of those crucial elements compared to bulk alloy γ phase.[74]

DP has, in some instances, been observed beneath an aluminide coating upon the outer surface of an aluminised part as the alloy is destabilised by a large ingress of aluminium, this chemical instability leads to the formation of *P*-phase TCPs and the formation of coarse lamella γ and γ'. This DP feature is often generated during the post-aluminising heat treatment but can also occur during the aluminising process.[74] Other authors have successfully triggered DP events in superalloys by casting a test piece with two offset single-crystals, linked by a grain boundary, this high-angle grain boundary is sufficient to cause the growth of DP which proceeds to transform the γ/γ' prime lattice. Nucleation is controlled by; chemical supersaturation, surface energy, strain energy, and the availability of heterogeneous sites.[74] Initiation of *P*-phase TCP precipitates were seen to occur along high- and low-angle boundaries usually with misorientations greater than 10° linking to the necessity for boundaries to have high mobility and diffusivity.[78] Orthorhombic *P*-phase had been seen to precipitate in a cellular manner at heterogeneous nucleation points that exist as imperfections in superalloy single-crystals, including but not limited to low-angle

boundaries and small equiaxed grains, known as ‘freckles’ in alloys with a high degree of rhenium and tungsten supersaturation.[78] Various mechanisms have been proposed for columnar to equiaxed transition during casting (CET) and ‘freckling’. The two most pertinent to this work start with the detachment of dendrite arms and the following transfer of this material to a more central region of the casting, before subsequent growth. Secondly, during solidification of single crystals, one sees the development of chains of small equiaxed grains upon the casting surface, these channel-like defects occur when segregating elements adversely affect the liquid density leading to convective instability and the interdendritic fluid is depleted prior to freezing.[87]

The presence of a sufficiently high level of stress within the surface of a nickel superalloy can trigger recrystallisation which can lead to the discontinuous precipitation reaction. Under conditions of severe plastic deformation, precipitate shearing and high dislocation density, the resulting reduction in strain energy could enhance and accelerate the growth of the discontinuous transformation reaction.[77,78] Strain energy can be introduced by surface preparation techniques prior to a coating process or pre-existing misfit strains between γ and γ’.[74]

The DP features seen (*Fig. 3.19* and *3.22*) appear as fan structures originating from a single point of initiation upon the inner surface of the component. These DP fans are not found within the bulk of the material and their presence at the surface could indicate an event resulting in sufficient strain being induced at the inner surface in a localised region. This stress, during the subsequent solution heat treatment, enabled the formation of small high-angle recrystallised grains.

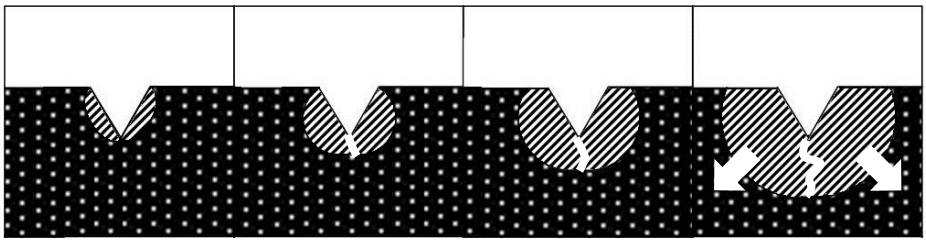

Fig. 3.30 – schematic of progressive growth of duo – discrete DP feature of Fig. 3.19

Following the solution heat treatment, the quench and then an aging heat treatment at a lower temperature, the small recrystallised grain provides the perfect high-angle grain boundary from which to start a DP reaction that grows as function of time and temperature during the aging heat treatment. The order in which DP occurs has been confirmed by microstructural examination (*Fig. 3.19*). During the high-temperature solution heat treatment the heavily segregated dendritic microstructure is slowly homogenised leading eventually to many interdendritic pools enriched in aluminium and tantalum that gradually shrink as they are absorbed into the increasingly homogenised microstructure. Eventually, following the

long high temperature heat treatment, quench occurs, though due to economic constraints the material is not entirely homogenised, thus there exists a background level of eutectic, present as small pools, dotted throughout the microstructure. These pools do not have substantial effect upon the physical properties of the material assuming the percentage volume is low enough. An example of one of these pools can be seen in *Fig. 3.19 and 3.21*.

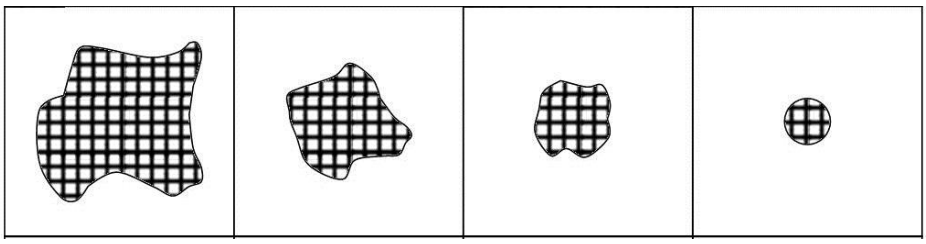

Fig. 3.31 – eutectic pool shrinking during the solutioning heat treatment, final cell depicts the kind of residual eutectic present going into the age heat treatment

Clearly seen in *Fig. 3.19* is a surface instigated DP event which is frozen in the act of transforming the γ/γ', as well as the eutectic pool, which is the path of the moving boundary reaction front. Once the previous solutioning heat treatment has finished, any eutectic pools that remain within the microstructure are frozen and will no longer reduce in size. The fact that in *Fig. 3.19* the DP event is clearly occurring and encroaching upon the eutectic pool means that the growth of the DP occurs during the aging heat treatment stage. Furthermore the DP must occur at a temperature below the γ' solvus or the γ would not be in lamellae, this microstructural phenomena will occur as a result of local differences in composition.

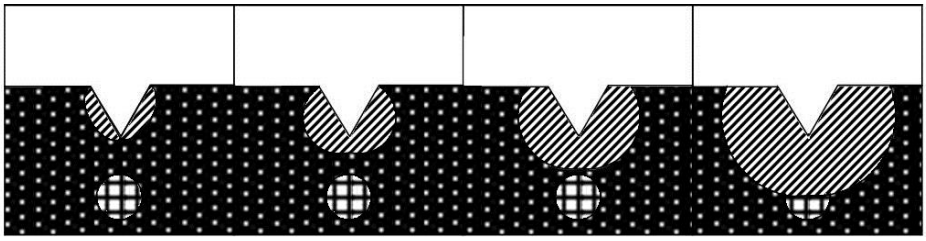

Fig. 3.32 – growth of DP from surface event encroaching upon residual eutectic pool sub-surface, see Fig. 3.19

The DP seen as part of this work is similar to structures previously noted in work by Nystrom et al. and consists of *P*-phase TCPs that grow as needles from the point of initiation and penetrate in the bulk γ/γ' microstructure of the nickel based superalloy gathering the rhenium and tungsten and depleting these elements from the surrounding phases. In response to the depletion, the γ/γ' structure becomes coarsened.[78]

3.4.5. Normal melting and heavy melting – macro landscape

When examining the enriched melt zone in the internally melted example and then the heavy melting example (*Fig. 3.17* and *3.28 respectively*) a geometry relationship becomes clear. In the case of the internally melted example, the enriched melt zone defect only exists

at the apex of the root block and upon traversing the sectioned sample toward the straight edges (*Fig. 3.17* and *3.18*) there appears several examples of the DP phenomena before returning to unaffected internal surface once upon the straight edged region. This suggests that both phenomena are linked to the tightly curved apex region of the as-cast component and that the straighter edges are not afflicted in the same way. This hypothesis is strongly supported by the presence of heavy melting upon an additional sample that shows a correlation between the point of the apex and the thickness and severity of the enriched melt zone defect, see *Fig. 3.29*. At the apex of the curved region the heavily melted enriched melt zone is over 450 μm thick which suggests a link to stress as a potential contributing factor.

3.5. Conclusion

This chapter has sought to explore the presence of a defect upon the internal surface of an intermediate pressure turbine blade which is discovered post-heat treatment. The various procedures and processes that a blade must undergo have been thoroughly examined and some important conclusions can be drawn now which have influenced the systematic study seen in the next chapter, chapter 4, Core / casting interactions.

1. Ceramic core microstructure prior to casting has been examined and the presence of many different oxide phases was discovered; alumina, silica and zircon as well as cristobalite and induced porosity.
2. During casting there are three key interface reactions between the silica-based core, the nickel-based superalloy and the alumina layer formed on the alloy.
3. The core, being a mixture of different oxides is capable of melting at lower temperatures than the melting points of the oxides and seems likely to melt at the casting temperatures of nickel-based superalloys, ca 1550 °C, at the pressure-assisted surface.
4. The nickel superalloy, immediately after passing the baffle of the furnace and exiting the hot zone, will solidify upon the ceramic core. The superalloy at high temperatures, ca 1300 °C, is not yet strong and is vulnerable at this stage of the casting process. This will be covered further in chapter 4.
5. The ceramic core and the solidifying nickel superalloy have very different thermal expansion coefficients which results in the metal contracting upon the ceramic and this exerts the force responsible for the pressure-assisted liquid phase sintering that occurs within the surface of the silica-based ceramic core. In addition geometry effects can be instrumental in acting as stress-raising features which focusses the crushing forces of the contacting nickel upon key regions of the ceramic core. This results in the observations that at the apex of curved regions the degree and

thickness of the pressure-assisted region is greater than on less geometry sensitive areas such as the long straight edges.

6. The oxide layer that forms at the interface of the ceramic core and the superalloy occurs due to a chemical interaction between the two. This aluminium driven reaction likely liberates oxygen from the silica and forms alumina within the surface of the ceramic hindering further ingress of aluminium in the core. This thin alumina layer is observed using several techniques and is likely partially removed during normal blade manufacture processing which involves alkali solutions of sodium hydroxide to dissolve the core away to leave the cooling passage. The oxide formed at the interface is integral to the silica-based ceramic core and since post leaching and post heat treatment electrolytic etching is used to selectively etch the internal surface for inspection it is very likely that that oxide is thin and permeable.
7. This thin oxide layer fits well with the current understanding of the process that leads to the formation of the enriched melt zone (EMZ) upon the internal surface. This process was proposed by D'Souza et al. and involves volatilisation of aluminium and nickel from the surface of the nickel superalloy resulting in the stabilisation of the γ' phase.[88]
8. Further to this hypothesis is that the internal surface of a turbine blade is rough and coarsely undulating which provides a larger surface area from which to lose material via sublimation than perhaps expected. This could accelerate the kinetics of aluminium and nickel sublimation resulting in the enriched melt zone forming during the solution heat treatment.
9. The presence of the second defect feature, the regions of discontinuous precipitation are likely instigated by plastic deformation accumulating within the nickel superalloy at specific sites which during the solution heat treatment instigate small grains of recrystallisation. Once the small grains have formed and the second stage of the heat treatment, the aging, begins the high-angle grain boundaries enable the formation of DP cellular colonies that grow into the bulk of the component eradicating the grains that first started them forming. EBSD confirms that the DP colonies exist with high-angle boundaries between the enriched melt zone and the underlying substrate.

4. Core / casting interactions

4.1. Introduction

4.1.1. Superalloy sublimation, volatilisation and oxide formation

Formation of an external superalloy surface scale during directional solidification is attributed to a mould-metal interaction where these reactions are only prevalent if the resultant oxides are characterised with large negative free energies of formation. Evidence suggests that aluminium and titanium from the liquid superalloy reacts with the silica (SiO_2) to form alumina (Al_2O_3) and rutile (TiO_2), which can, in some instances, account for an aluminium denuded zone beneath the casting surface. By way of example the following points describe how different regions are covered in oxides following casting upon CMSX-10N.[89]

- **Scaled Region**: elemental composition line scans proceeding inwards from the surface showed nickel, cobalt and aluminium in that order. Oxygen detected indicates that the scale was oxide and the thickness to be ca 800 nm
- **Un-Scaled Region**: the most prominent peaks were aluminium and oxygen, indicating the presence of Al_2O_3

Upon cooling below the solidus temperature, separation of the solidified metal from the mould wall occurs in certain regions. Here the Al_2O_3 layer is stripped from the metal surface and remains adhered to the mould. As the component cools further, there is oxidation of the bare casting surface to form an oxide scale. When the mould is separated from the casting, small patches of remnant mould prime coat as well as the Al_2O_3 layer are seen on the un-scaled region.[89–91]

During solutioning heat treatment volatilisation of nickel and chromium has been observed from the surface of the material, the extent is believed to be dictated by the nature of the oxide on the surface. Volatilisation depends on the nature of the vacuum under which heat treatment is carried out as well as the extent of elemental segregation following casting. Subsequent destabilisation of γ phase occurred resulting in a distinct surface layer showing a mixture of γ’ and refractory-rich precipitates. The stabilization of γ’ arises from enrichment in aluminium, while the formation of refractory rich TCP phases incorporates excess tungsten and rhenium. Destabilisation of γ phase requires significant depletion of nickel, this loss occurring by vaporisation during solutioning under argon. Subsequent solute redistribution leads to destabilization of γ phase and the presence of surface Al_2O_3 significantly suppresses elemental vaporisation from the sample.[88]

At the boundary of the γ’ surface layer with the substrate, there are some instance of discontinuous precipitation with the nucleation and growth of refractory-rich precipitates and γ-lamellae. The affected surface layer progresses incrementally into the substrate during

heat treatment. The nucleation of the TCP phases within grains is impeded by a high nucleation barrier and is associated with significant annealing times like those seen in the solutioning of CMSX-10N. Abrasive grit blasting induces damage along the surface of the material in the form of localized strain, and can result in recrystallisation. The nucleation of the γ recrystallized grain occurs at the interface of the molten surface layer and the unmolten substrate. Growth of this grain occurs through the matrix and is dependent on accumulated plastic strain. Subsequent freezing of the liquid at the surface via a 'chilling' effect during quenching after solutioning results in the nucleation of grains with random orientation resulting in predominantly γ' morphology.[88,92] It is the authors opinion that the enriched melt zone (EMZ) defect is explained by the current theory proposed by Dr. Neil D'Souza of Rolls-Royce Plc regarding the role of volatilisation, this particular chapter will focus on a the origin of the discontinuous precipitation in this work.

4.1.2. Residual casting stresses in superalloys – deformation and recrystallisation

Panwisawas et al. built an elasto-visco-plastic model of the superalloy investment casting process which accounts for thermal, elastic, plastic and creep strains. These strains generated within the superalloy occur over four key temperature zones in which differing behaviour was anticipated.[93]

A. The superalloy begins to yield during the early stages of cooling, between 1300 and 1200°C. At this temperature the alloy proof strength is low and potent thermal contraction stresses exceed it.
B. The alloy proof stress increases rapidly to exceed the thermal stress; causing the accumulation of plastic strain to cease. Temperatures of between 1200 to 1000°C is still sufficiently high for creep strain to be accumulated thus leading to creep and elastic deformation.
C. From 1000 to 600°C, the proof strength is greater than the thermal stress; there is only elastic deformation.
D. Below 600°C the proof strength is much lower than the thermal stress; as a result, plastic straining is predicted to occur up to ca 0.6%.

It was found that no plastic strain accumulated during solidification if laterally the superalloy was larger than a core; on the contrary, if the core cross section is larger than the superalloy cross section, then the plastic strain becomes more substantial. The larger the ceramic core, the higher the strain within the superalloy with the predicted plastic strains being relatively small, of the order 10^5 or 0.001%. With increasing external shell thickness, the stresses experienced within the superalloy were increased. Therefore stiffer shells lead to greater residual strains within the final casting.[94–96]

The deformation induced in directionally solidified superalloys during cooling and freezing are due to differential thermal contraction of the ceramic shell, core insert and the metal, arising primarily from their differing thermal expansion coefficients. This deformation is heavily influenced by the effects of geometry, stress concentration features, shell thickness, shell type, core diameter and core type. Shrinkages which occur mean the final casting will not exhibit the same dimensions as the wax pattern and plastic strains are produced which can be large enough to induce recrystallisation during subsequent solutioning heat treatment. Interdendritic regions showed an appreciable dislocation density, whereas the dendritic regions appeared relatively dislocation free. These differences in dislocation density suggest plasticity accumulating close to the γ' solvus temperature. This observation is consistent with the predictions that most of the deformation occurs between 1200°C and 1300°C. The plastic strains predicted by modelling were found to be consistently higher for the top of the casting than the bottom, and in general in the order top > middle > bottom. The intensity and distribution of normal stresses increases with solidification height, the cooling of the lower regions imparts contraction stresses on the regions above which remain at higher temperatures. The bottom part of the casting solidifies first and thereafter is always at a lower temperature than positions lying above it. The cooling of the lower regions would impart contraction stresses on the regions above which would be at higher temperatures. Plastic strains in the cored casting was higher on the inner surface than the outer surface.[94]

Plastic deformation of a superalloy is a necessary condition of the recrystallisation phenomenon. During deformation, internal strain energy is induced and stored in the alloy in the form of crystal defects, mainly dislocations. Annealing in the deformed alloy can lead to stress relaxation, in which stored internal strain energy is relieved by thermally activated dislocation motion. When the deformation intensity and annealing temperature is sufficiently high, a new set of strain-free grains are formed; recrystallisation.[97]

The extent of recrystallisation around high temperature indentation in CMSX-4 reveals that at 1300°C material plastically strained to just below 1% recrystallises showing that the concept of a critical strain value is highly dependent on annealing temperature. Annealing either above or below the γ’ solvus and the pinning effect that the γ’ precipitates has means that a reduction in annealing temperature to 1275°C produced no recrystallisation at all in specimens strained up to 4%.[98]

4.1.3. Silicon-based ceramics for investment casting

Investment casting uses liquid ceramic slurry to form moulds or ‘investments’ with an extremely smooth surface. These moulds are replicated from precise patterns and transmitted in turn to the casting creating dimensionally accurate components. Multi-component slurries are composed of a fine mesh refractory filler system and a colloidal binder system. Oxides including zircon, alumina, aluminosilicate, mullite and fused silica are common place, though materials including yttria and zirconia are used for reactive alloy castings like the superalloys. A wax pattern is dipped into the slurry, sprinkled with coarse refractory stucco and dried. The primary purpose of the stucco is to minimise drying stresses by presenting a number of stress concentration centres which distribute and reduce the magnitude of the local drying stress. The stucco’s secondary purpose is to form a rough surface, enhancing the mechanical bond between the primary coating and the secondary layers as the shell is built up. Shells are fired and filled with molten metal that solidifies. After casting, the ceramic shell is removed using mechanical and chemical means.

Key mould requirements are:

1. unfired strength enough to withstand wax removal without failure;
2. fired strength enough to withstand the weight of cast metal;
3. sufficiently weak to prevent hot tearing;
4. high thermal shock resistance to prevent cracking during pouring;
5. high chemical stability;
6. low reactivity to improve surface finish;
7. mould permeability and thermal conductivity to maintain adequate thermal transfer through the mould wall;
8. low thermal expansion to limit dimensional changes. [99]

The chemical reactions leading to metal mould reaction can be classified as being of the following types:

1. $MxOy = xM + yO$
2. $MxOy + zMA = MAz\ Oy_{(g)} + xM$
3. $MxOy + zMA = MAz\ Oy + xM$
4. $MxOy + zMA = MAzMx\text{-}w\ Oy + wM$
5. $MxOy = xM(g) + yO$
6. $MxOy = MxOy_{(l)}$

MxOy denotes an oxide, M and O dissolved metal and oxygen in the alloy respectively, MA an element in the alloy, and (*g*) a gaseous species.

Reaction 1 relates to dissolution of shell material into the liquid metal

Reaction 3 relates to reduction of the mould by the cast metal to form an alternative metal oxide, this route is hindered by using mould materials deliberately having an energy of formation substantially more negative than the oxide of the molten metal. One such example involves aluminium in superalloys chemically reacting with mould oxides producing thin layers of aluminium oxide at the interface forming reasonably stable, beneficial structures.

Reaction 6 represents solid to liquid transformation of ceramic in the shell mould. This formation is detrimental to a cast part through part deformation or metal penetration into the mould. However, formation of liquid phase increases the oxide mobility and lowers the mechanical stability of the shell mould. Ceramic shell moulds and cores, being multi-component systems generally display lower temperature liquid phase formation than the melting temperature of individual pure oxides would suggest. In this example from Frye [86] addition of Y_2O_3 to SiO_2 reduces the formation of liquid phase down from 1720°C to 1660°C. Furthermore addition of Al_2O_3 to this mixture will further reduce the liquidus to 1370°C.[86] *Fig. 4.0* displays the Na_2O-SiO_2 and SiO_2-Al_2O_3 phase diagrams to exemplify how when mixtures of oxides are used the realistic melting point of the mixture can be far beneath that which would otherwise be expected, hence the possibility of liquid phase sintering.[100,101]

Metal	Melting Temperature, °C	Ceramic	Melting Temperature, °C
Platinum	1772	Zirconia	2700
Titanium	1660	Zircon	2550
Cobalt	1495	Lanthana	2307
Nickel	1455	Alumina	2072
Gold	1064	Silica	1720

Table. 4.1 – melting temperature of selected metals and refractory oxides [86]

Fused silica-based ceramics are used as sacrificial cores in investment metal castings to produce hollow, precise, and complex-shaped structures within them. Silica-based ceramic cores are used for casting nickel-based superalloys due to high dimensional stability, thermal shock resistance and leachability. These cores comprise silica, with particle sizes of ca 50 – 100 μm, smaller zircon particles, and low levels of cristobalite and alumina. The β-cristobalite is a high temperature polymorph of silica and undergoes its β → α phase transformation with a volume contraction of about 5 vol % when it is cooled down to 200 – 270°C. Cristobalite has higher chemical resistance to leaching solution than fused silica, the formation of in-situ cristobalite layer on the surface of fused silica grains, especially after simulated casting heat treatment, protects them from corrosion, consequently decreasing the leachability of ceramic core intensively.

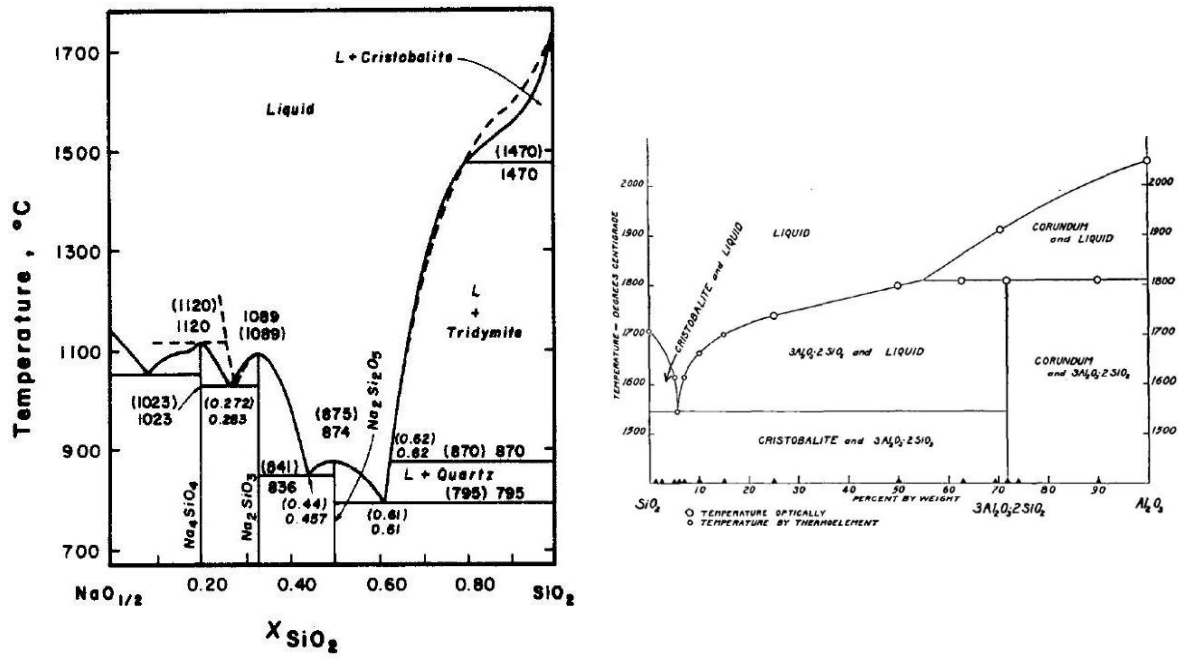

Fig. 4.0 – phase diagrams of the Na_2O-SiO_2 and SiO_2-Al_2O_3 binary systems for reference [100,101]

At the same time, the primary cristobalite particles can increase the leachability by introducing several micro cracks, opening leaching solution diffusion path into the ceramic core body, and increasing the chemical interaction between them.[83,102,103]

Zircon, $ZrSiO_4$, in silica-based ceramic cores, can improve high temperature properties due to its low thermal expansion coefficient, low coefficient of heat conductivity and high thermal and chemical stability. Zircon has a very high melting point which increases the mixtures sintering temperature and consequently the residual porosity of the silica-based ceramic core. Zircon also helps prevent consolidation by introducing a pinning force at the grain boundaries through its use as a Zener pinning agent. A nucleation and growth model for fused silica crystallisation showed that cristobalite seed can induce compressive stresses that result from volume expansion of the α-β cristobalite transformation at high temperatures. Porosity within these materials also affects the strength of ceramic core, with open porosity of the core body increasing with increasing zircon content both before and after heat treatment.[84,104]

Fused-silica crystallises near 1300 °C in the temperature regime that the metals are typically cast, this temperature is additionally affected by types of impurity, impurity content, and cristobalite seed content. Its temperature of activation can be altered somewhat, zircon enhances the crystallization of fused silica cristobalite which heterogeneously nucleates at the surfaces of individual fused silica particles and a crystalline front advances inward at the expense of the amorphous interior. Observed dimensional changes are therefore a result of a time and temperature dependent competition between two thermally activated processes

of viscous flow of the fused-silica and nucleation and growth of the cristobalite. Greater zircon concentrations accelerate cristobalite formation therefore less shrinkage would be expected than if lesser concentrations were present.[85]

The presence of silicon within superalloys are usually in levels of ppm and can inhibit the ability to cast and processes components. Zhu et al. looked at the effect of some minor elements, such as silicon, on the solidification segregation, microstructure and mechanical properties of bespoke superalloys.[105] Alloys, using IN738 as a template, were created adding small quantities of silicon. During alloy freezing this silicon was rejected from the solidifying material and partitioned forwards within the still liquid alloy. These minor elements lowered the solidification temperature of the alloy and caused the formation of interdendritic regions with a depressed melting point. It was found that the interval between solidus and liquidus increased by increasing the silicon content and the minor elements segregate to the interdendritic regions and promoted the segregation of other non-minor elements.[84,85]

4.2. Experimental

A casting trial was designed to recreate conditions found within the root block of an intermediate pressure turbine blade using the 3rd-generation alloy CMSX-10N. To this end a plastic 3D printed die was commissioned to exaggerate the dimensions of a blade root block (cuboid) that extended for the entire height of the die, width 41 mm, depth 23 mm, height 120 mm. In this manner the environment associated with the specific geometry of the root block was isolated and examined. The impact of casting height upon alloy-core interactions could be studied without the complication of the ever changing cross section seen in real blade components. The die featured a holder capable of supporting a smaller cuboidal ceramic core, width 12 mm, depth 4 mm, height 120 mm, fashioned from the same material used to create sacrificial ceramic cores used to form cooling passages within turbine blades.

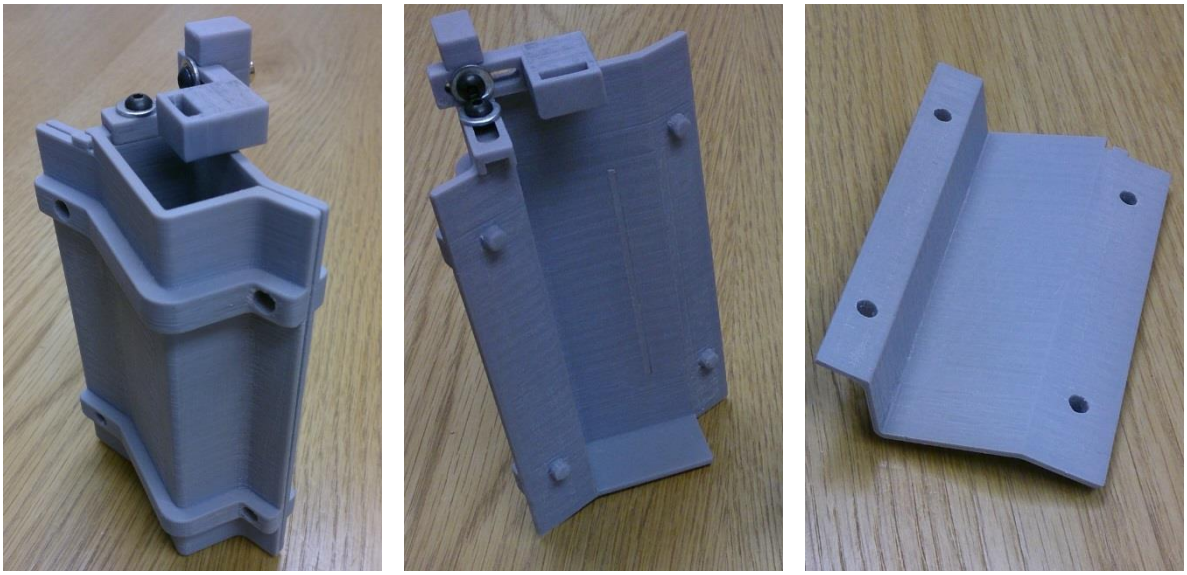

Fig. 4.1 – 3D printed die root block mimic cuboid

Two different manufacturers of ceramic core supplied test pieces for these experiments, Morgan Advanced Materials (P-35™) and Ross Ceramics (MD™). As seen in *table. 4.2* competitors have different chemical compositions but both are routinely used by Rolls-Royce plc for the formation of cooling passages in directionally solidified and single crystal castings.

	Silica (SiO_2) (amorphous fused)	Zircon ($ZrSiO_4$) (fine-grained)	Alumina (Al_2O_3) (agglomerated)
P-35™	93.0 %	3.0 %	4.0 %
MD™	83.5 %	14.2 %	1.3%

Table.4.2 – composition of ceramic core inserts

All work regarding wax pattern construction, shelling and directional solidification casting took place at the University of Birmingham, School of Metallurgy and Materials, Edgbaston. Following assembly of the die complete with ceramic core insert hot pattern wax (Blaysons A7 FR/60™ virgin) was poured in through the upper opening filling the cavity to create the wax pattern with core in situ. After topping up the die to ensure a complete pattern was made the cuboid was allowed to cool and harden for 24 hours. Once cooled the wax pattern was carefully removed from the die, smoothed and assembled as follows. The base is a wax plate featuring a bayonet fitting for affixing to the water cooled cooper chill plate during casting. Between the base and the cuboid a grain selector in form of a small spiral was fitted to enable single grain selection during directional solidification. Finally a pour cup and stem were attached to the top of the cuboid to enable transit of the molten superalloy charge down into the mould. Mullite cylinders were added as auxiliary struts to provide strength and support to the assembly both during the shelling and casting stages. (*Fig. 4.2 (b)*)

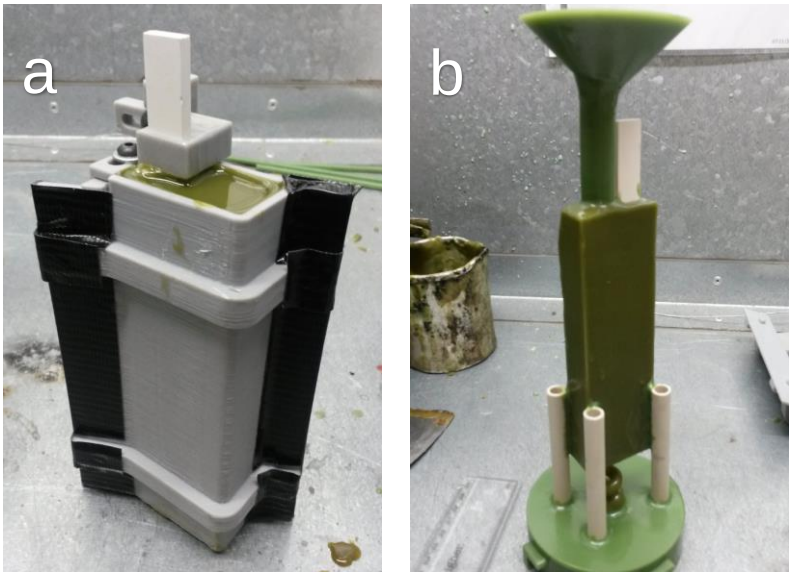

Fig. 4.2 – root block mimic die filled with wax (a), completed assembly with pour cup and grain selector (b)

Following construction the entire assembly underwent a wash in combined wax pattern cleaner and etchant (Blaysons Trisol 60 Plus™) to remove silicones and surface debris. Once dry the assembly was subject to a dip in the first sol gel parting layer and application of stucco to aid drying times and aid stress relief. All shelling materials are exact copies of those used in the Precision Casting Facility (PCF) Rolls-Royce plc in Derby to ensure correlation between commercial parts and my test castings and defined as the Standard Rolls-Royce Single Crystal Shelling System. Once each layer dried then a series of additional layers were added to provide strength as per *table. 4.3*. All slurries are silica-based sol binders with a zircon filler as well as wetting agents and anti-foaming agents.

Stage	Nomenclature	Quantity
1	complete wax assembly	-
2	rinse with pattern cleaner	undiluted cleaner then water rinse
3	primary slurry	1
4	primary “+1” slurry	1
5	secondary slurry	5
6	seal coat secondary slurry	1

Table.4.3 – ceramic shell mould building sequence

Once the ceramic shell application was complete then wax removal took place using a steam autoclave to quickly purge the wax from the ceramic mould whilst minimising the opportunity for mould damage. The empty mould was then fired at 800 °C for 1 hour to pre-sinter the material and make it capable of withstanding the casting process.

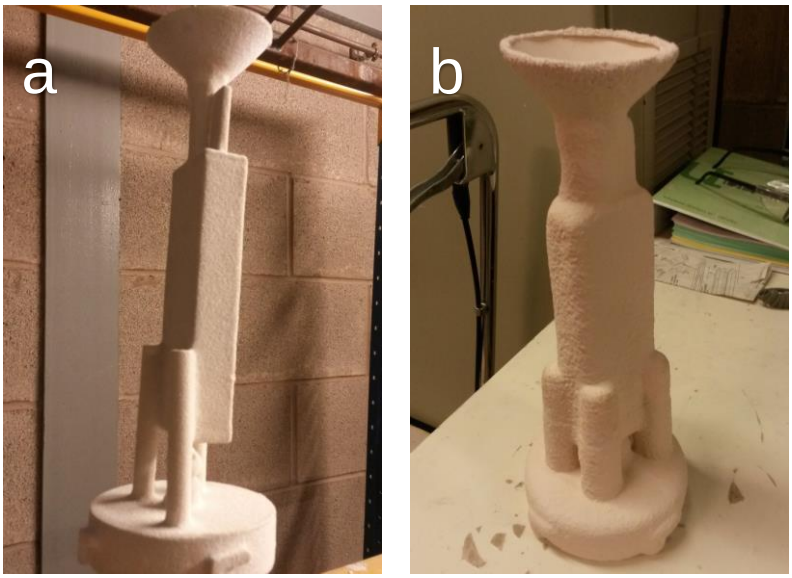

Fig. 4.3 – completed assembly with first coat parting layer applied (a), final mould de-waxed and fired (b)

Fig. 4.4 shows the as-cast cuboid immediately following shell removal. Clearly visible are the spiral grain selector at the base of the cuboid and some thin flash around the bottom where the auxiliary support struts were placed. There is also some visible roughness and scale upon the surface of the as-cast shape as a result of the external parting layer of ceramic interacting with the superalloy but this is not a topic of investigation in this work.

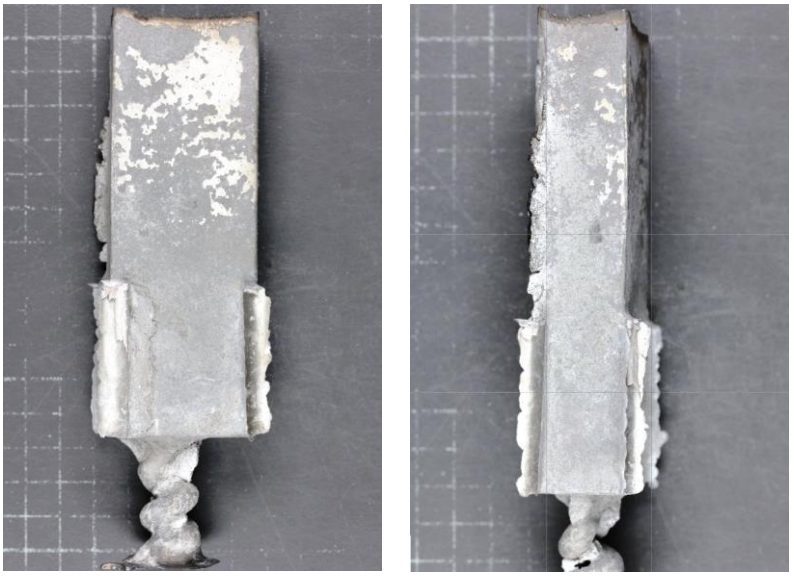

Fig. 4.4 – Casting 1 post shell removal

Fig. 4.5 displays a top down and bottom up view of the cuboid of casting 1. The bottom shows the base of the spiral grain selector, this was in contact with the copper chill plate at the top of the ram which withdrew the mould from the furnace hot zone. Visible in the top down view is the ceramic core cast within the cuboid to the LHS.

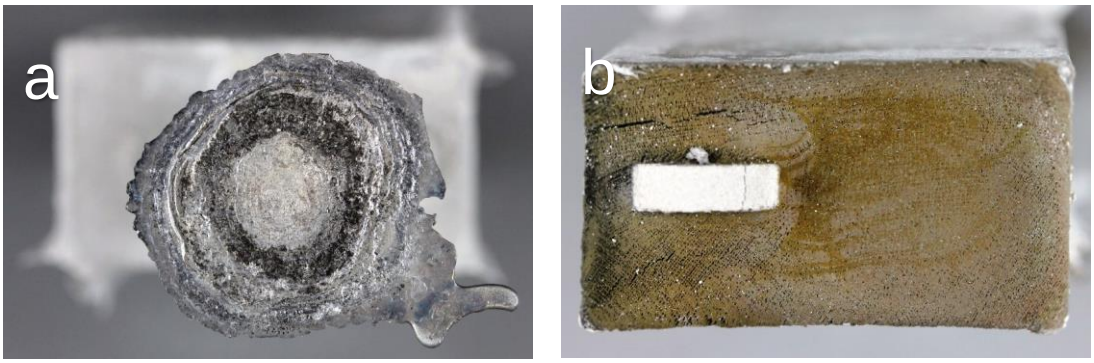

Fig. 4.5 – Casting 1 post shell removal, bottom of selector (a), top of casting, core insert visible (b)

Fig. 4.6 shows side views of the Casting 1 cuboid, marked in *(a)* is the twelve separate sections 1A (top) through to 1L (bottom) into which this casting was split for further analysis.

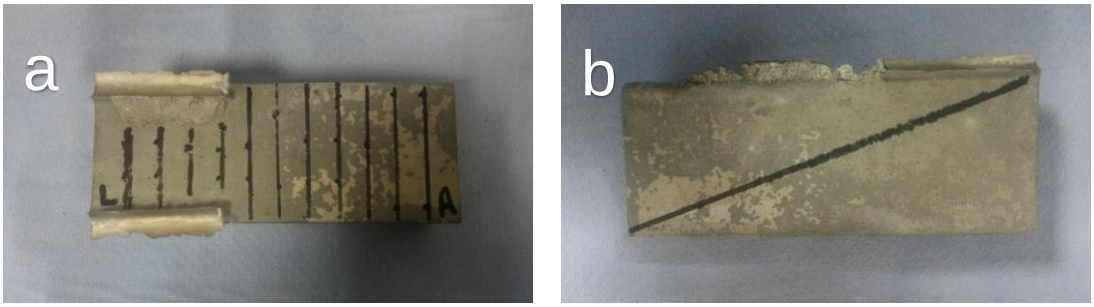

Fig.4.6 – Casting 1 post shell removal, side view marked for sectioning (a), reverse side view (b)

To understand the impact of casting height on core / casting interactions the castings were sectioned and the relative height was recorded. *Fig. 4.7* (a) shows a schematic of Casting 1 and six example sections. *Fig. 4.7 (b)* shows visually the information contained in *Table. 4.4*.

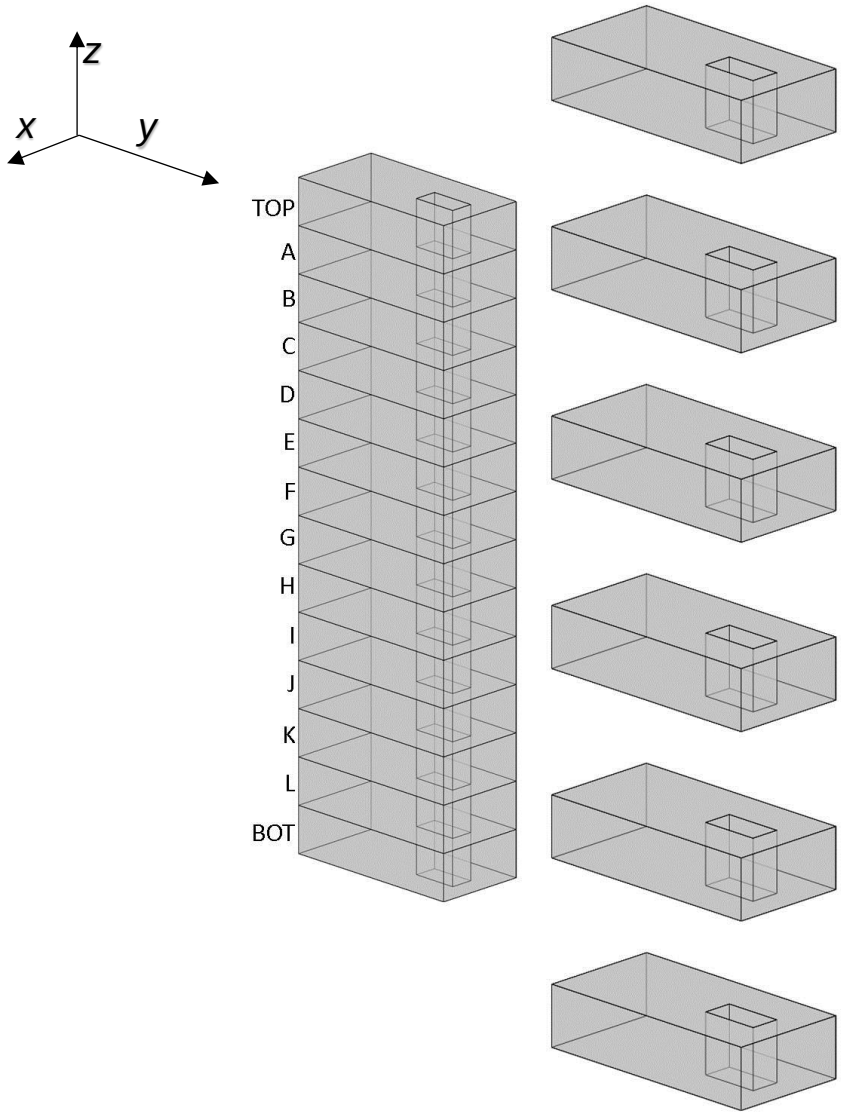

Fig.4.7 (a) – Casting 1 breakdown schematic

In total there are three casting trials; 1, 2 and 3. The difference between them is in *table. 4.4*.

Casting	Mould shape	Core material and dimensions	Position	Sections available
1	Cuboid	MD™ (12 x 4 x 120 mm)	central in *x* **offset** in *y*	top, A, B, C, D, E, F, G, H, I, J, K, L, bottom
2	Cuboid	P-35™ (12 x 4 x 80 mm)	central in *x* **offset** in *y*	A, B, C, D, E, F, G
3	Cuboid	MD™ (12 x 4 x 120 mm)	**offset** in *x* **offset** in *y*	A, B, C, D, E, F, G, H, I, J, K, L

Table.4.4 –cuboid castings 1, 2 and 3 different trials

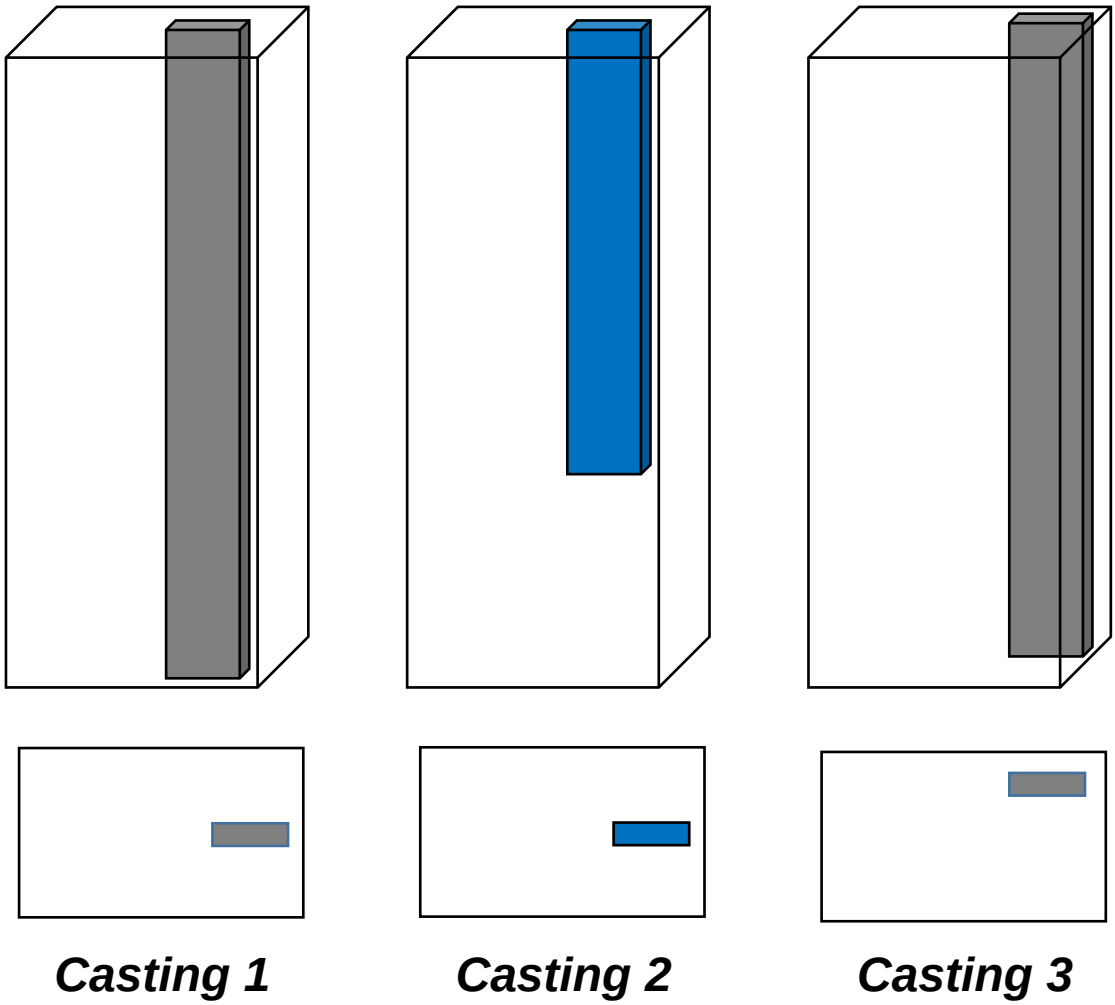

Fig.4.7 (b) – Casting 1, 2 and 3 breakdown schematics, see details in Table. 4.4, grey is core material MD and blue is core material P-35, top three images are isometric view, bottom three are top down view showing relative core placement within the cuboidal mould

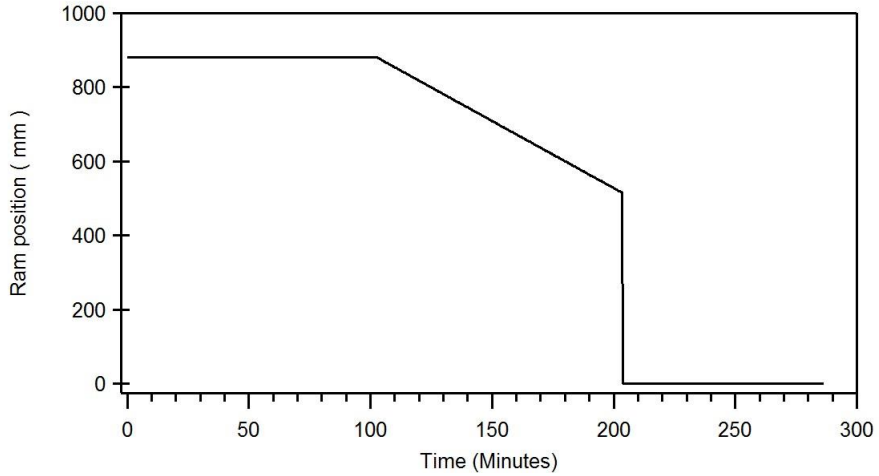

Fig.4.8 – ram position during casting 1

Fig. 4.8 shows the relative position of the withdrawing ram of the Bridgeman furnace used in this work.

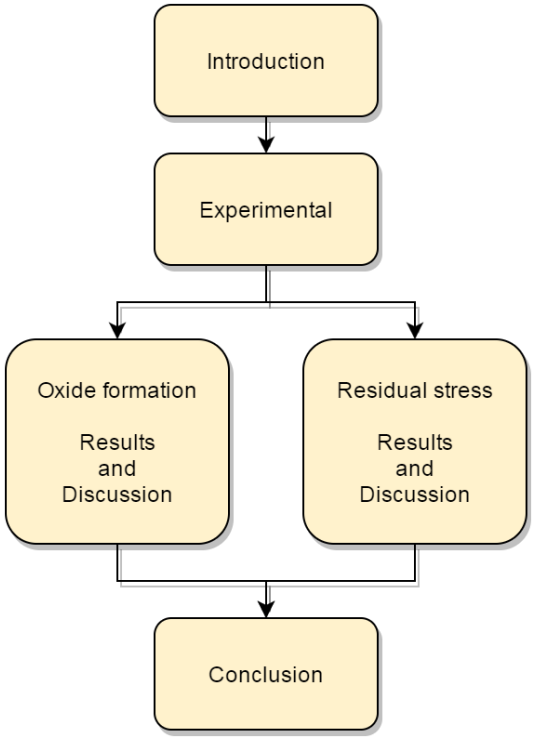

Fig.4.9 – chapter 4 layout

Fig. 4.9 displays a schematic layout of chapter 4 detailing how the relevant results and discussion sections are adjacent before a main discussion and conclusion.

4.3. Oxide formation

4.3.1. Results

4.3.1.1. Scanning electron microscopy

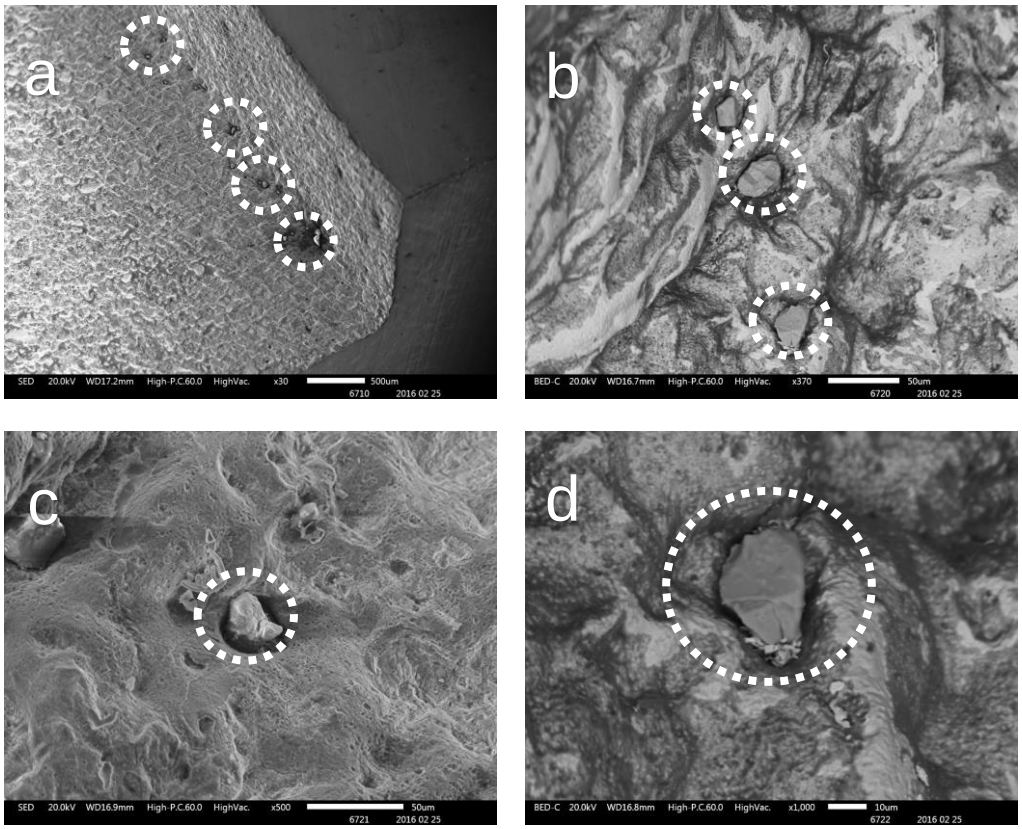

Fig. 4.10 – casting 1D – looking down upon as-cast and then as-leached surface (a), higher magnifications focussing on the presence of particles trapped within undulations of the superalloy surface (b), (c) and (d)

Following casting 1 the cuboid was sliced into twelve separate sections, labelled 1A through 1L. Section 1D, shown in *Fig. 4.10* was left in the as-leached state and cut open allowing inspection looking down upon the as-cast surface. *Fig. 4.10 (a)* shows 100x magnification under the scanning electron microscope. The image shows the corner region and small particles can be seen trapped along the corner region. *Fig. 4.10 (b), (c)* and *(d)* gradually increase the magnification of these entrapped particles and it becomes clear that in all three instances the topography of the underlying superalloy is moulded around the particle. Also apparent in *Fig. 4.10 (b)* and *(d)*, captured using backscatter electrons, is the apparent absence of a thin oxide layer upon part of the surface of the superalloy, this appearing as a brighter, white colour absent on these exposed regions. The presence of these particles is almost entirely confined to the corner region in this specimen, this strongly suggests that it is only in this geometry specific region that the particles have been able to remain during the leach cycle and that this moulded superalloy feature which enables the particle to cling on is not found on the flatter, straight portions of the inner surface.

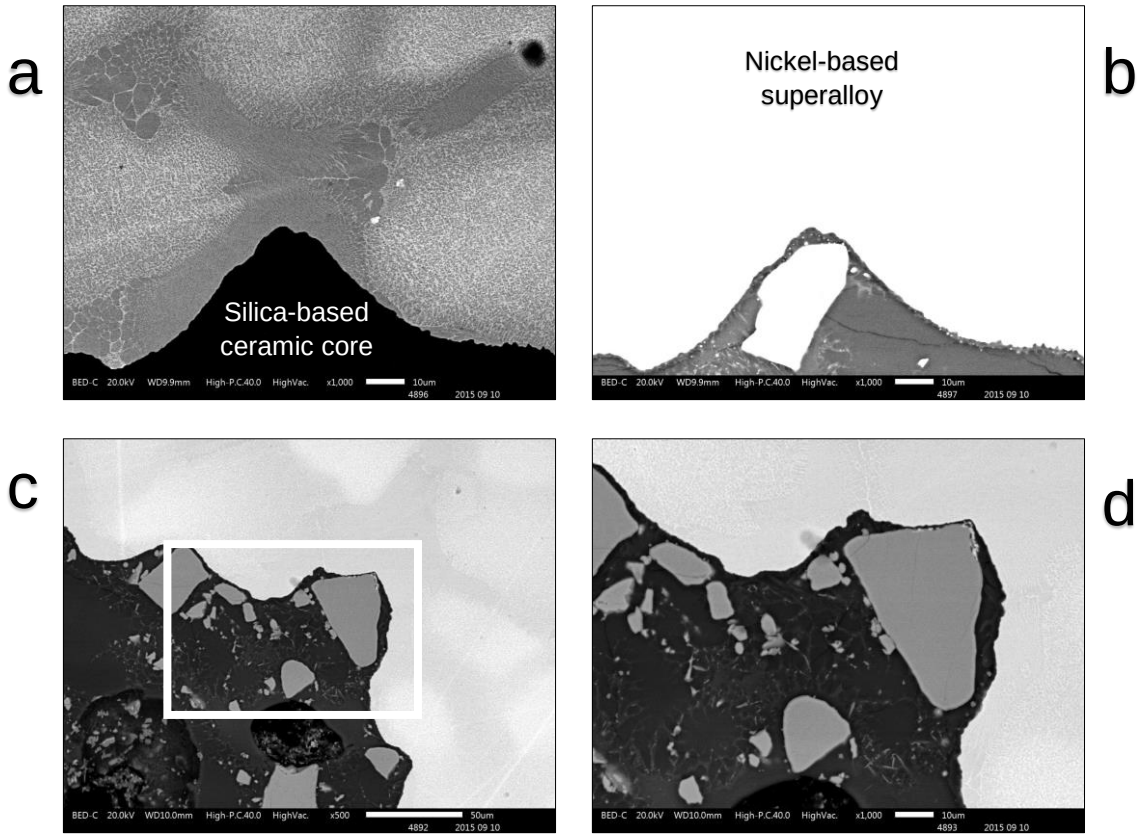

Fig. 4.11 – casting 1A – transverse sections through as-cast surface with core in-situ (a - d), same magnification focussing on presence of particles trapped within undulation of the superalloy with contrast for metal (a), ceramic (b) and an additional example in (c and d) with higher magnification in (d)

Fig. 4.11 displays SEM micrographs taken from casting 1 section A, the uppermost portion of the cuboid and the last to solidify. Visible in *Fig. 4.11 (a)* and *(b)* is the appearance of an apparently hard particle situated within the silica-based ceramic which has caused a scalloping effect to occur in the nickel superalloy cast against it (top of *(a)* and *(b)*). *Fig. 4.11 (a)* and *(b)* are both back scatter electron images though in *(a)* the contrast and brightness has been selected to actively observe the microstructure of the as-cast superalloy, whilst in *(b)*, which is of the exact same location, the brightness and contrast has enabled examination of the ceramic bound particle in more detail. Further images in *Fig. 4.11* include *(c)* and *(d)* which also feature examples of where, during the casting process, the contracting metal front has exerted force upon the silica-based ceramic until contacting the brighter large particle where the superalloy has been forced to halt its compressive movement. Also visible in *Fig. 4.11 (d)* are needle-like phases within the silica-based ceramic which were noted in chapter 3.

4.3.1.2. Energy dispersive x ray

Additional analysis of the particles trapped upon the as-cast and as-leached surface was conducted using EDS within the SEM. The maps, looking down upon the surface, are displayed in *Fig. 4.12* and show that the aluminium and oxygen results correlate well together indicating the possible presence of an aluminium oxide particle upon the surface of the superalloy in this condition. This oxide was formed during the casting process as a result of chemical interaction between the superalloy and the silica-based ceramic core. Further to this observation is that the silicon and zirconium maps identify the discrete central particle as zircon, an additive used to modify the mechanical properties of the core used to form the internal cooling passage. The presence of these elements confirms that the brighter particles seen in *Fig. 4.11* are likely large zircon particles resisting the force exerted by the nickel superalloy during casting.

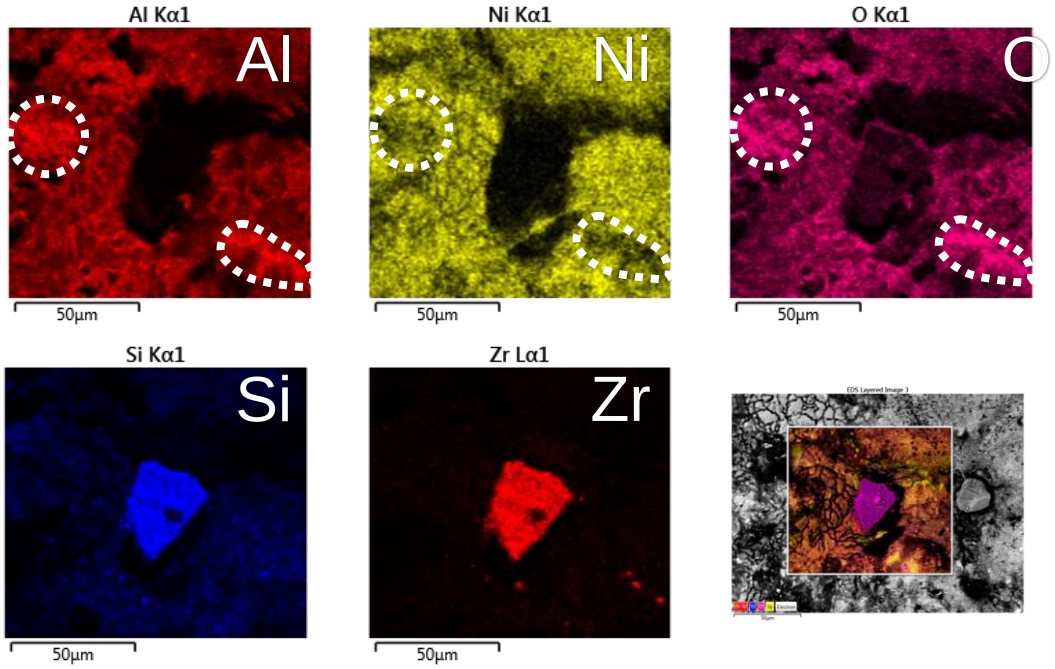

Fig. 4.12 – casting 1D – open face – looking down upon as-cast and as-leached surface

Transverse maps featured in *Fig. 4.13* confirm the presence of silicon within the amorphous silica of the core as well as part of the zircon particle, supported by the zirconium map. *Fig. 4.13* shows the aluminium map which displays an intense band of aluminium enrichment at the interface between the core and the as-cast superalloy. This band is likely the alumina layer that has formed as a result of chemical interaction between the superalloy and the core. Additional aluminium can be seen within the map inside the ceramic core, though crucially, it appears diffuse and not concentrated within the discrete alumina particles that are incorporated into the original silica-based ceramic of the core. This could be aluminium that has originated from within the core but equally the aluminium could have originated from within the superalloy.

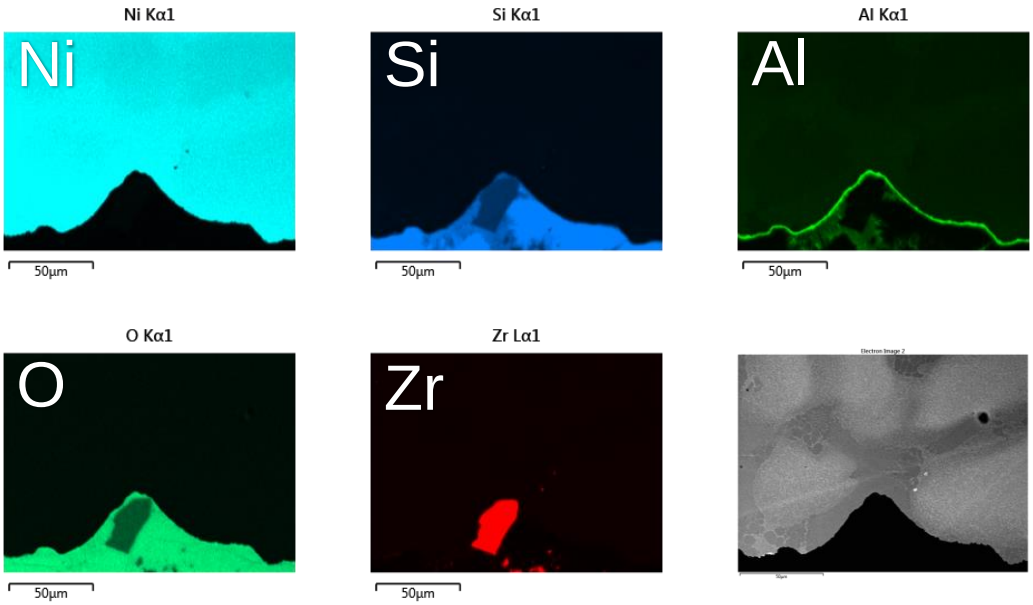

Fig. 4.13 – casting 1A – transverse sections through as-cast surface with core in-situ EDS elemental mapping,

4.3.1.3. Transmission electron microscopy – images

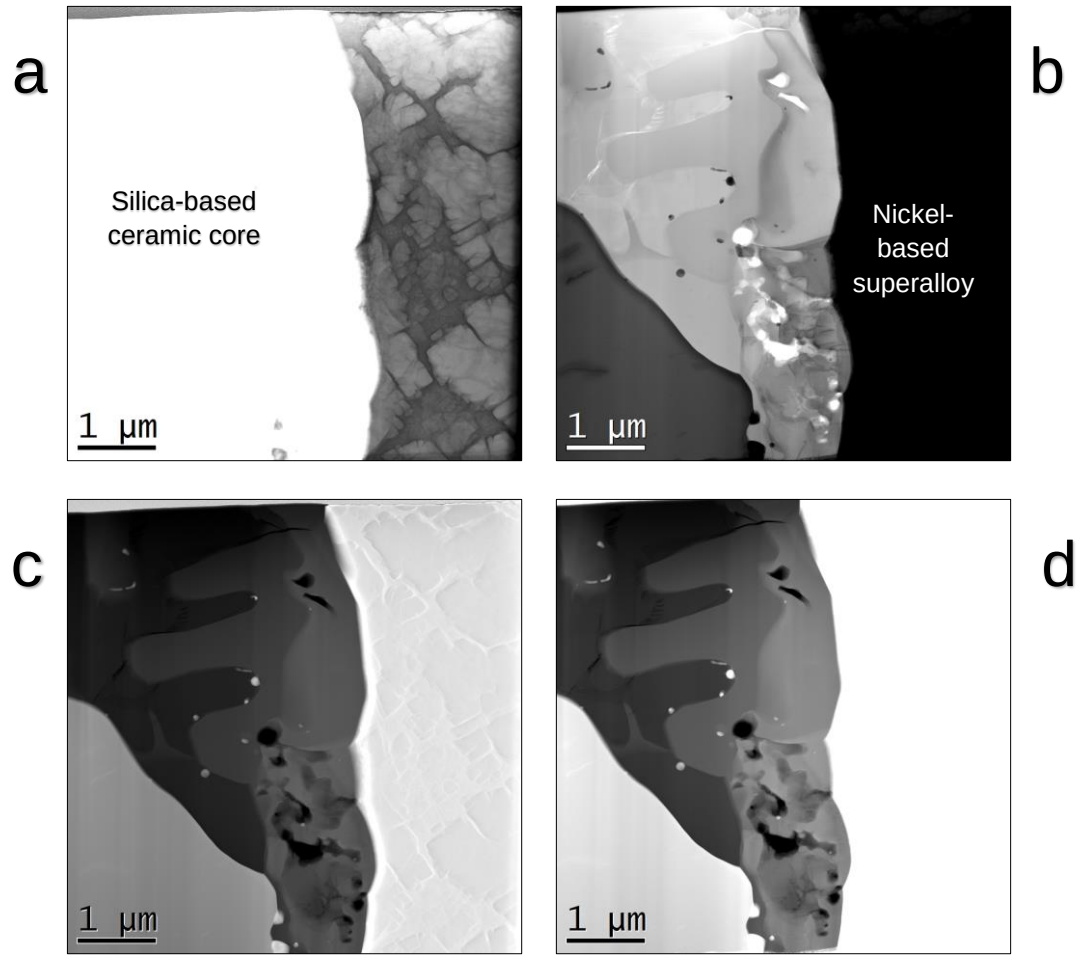

Fig. 4.14 – casting 1bottom – FIB section through as-cast surface with core in-situ, 20,000 time magnification bright field (a and b), HAADF (c and d). contrast and brightness are used to highlight the ceramic and metal

The FIB lift-out technique was employed to better understand the interface between the as-cast nickel superalloy and the silica-based ceramic at a magnification of 20,000 times. *Fig. 4.14* shows the TEM micrographs, *(a)* is a bright field (BF) image which focusses on highlighting the γ/γ' of the as-cast structure and it can be observed that in 1bottom the γ/γ' is present up to the extreme outer surface of the nickel superalloy and that there is no distinct band of eutectic or preferential phase formation. *Fig. 4.14 (b*) is another BF image of the same location with contrast and brightness adjusted for the ceramic and a large particle can be observed in the bottom LHS and a mixture of grey coloured phases that make up various parts of the silica-based ceramic. *Fig. 4.14 (c)* and *(d)* show the HAADF images of the same location, clear details emerge of 'fingers' protruding into the silica-based ceramic core originating from the superalloy. There is a three tone greyscale region which appears to be darkest for the original ceramic core and two different phases for the chemically formed oxide at the interface. Bright regions in *Fig. 4.14* are likely concentrated impurities present within the silica-based core, one example is calcium as observed in *Fig. 4.15*.

4.3.1.4. Transmission electron microscopy – elemental mapping

Following TEM imagery a series of TEM-based EDS maps were collected to understand the relative distribution of elements within the location. The silicon map clearly shows that the LHS is the ceramic core and that there is silicon present within the amorphous silica and to a lesser extent within the large particle on the lower LHS. The oxygen map displays a large presence both within the ceramic core but also heavily enriched at the interface between the ceramic core and the nickel superalloy. Next the aluminium map shows strongest presence within the oxide interface layer and a strong correlation with the oxygen map at this point.

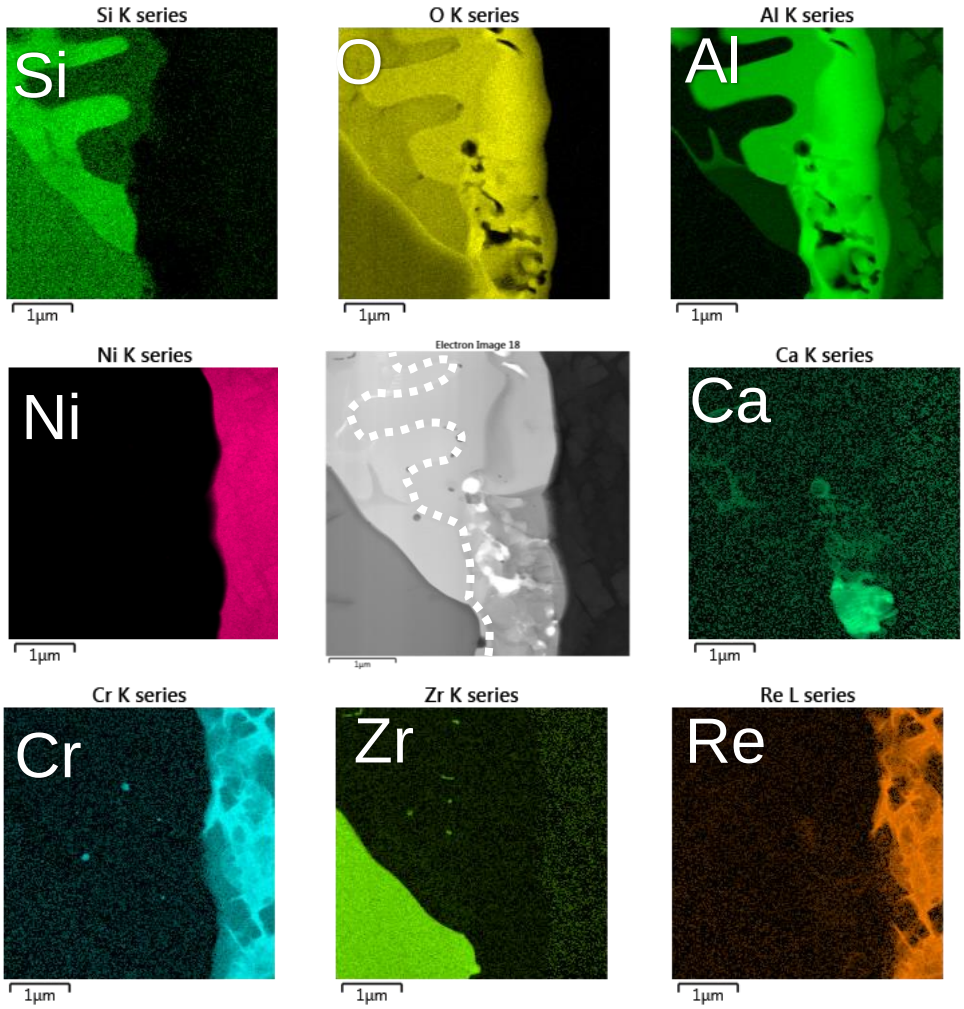

Fig. 4.15 – casting 1bottom – FIB section through as-cast surface with core in-situ close to large particle and scalloped effect on the superalloy, 20,000 times magnification TEM based elemental compositional maps

There is a residual level of aluminium within the nickel superalloy on the RHS and it has clearly partitioned to the γ' phase since the roughly cuboidal structure can be observed. There are a few interesting features within the aluminium trace, especially at what appears to be a degree of disruption in the otherwise continuous alumina layer which has formed

along the interface, this disruption is focussed around the tip of the zircon particle. Moving on to the maps for nickel, chromium and rhenium it can be seen that all of these elements sit within the nickel superalloy on the RHS and that there is very little interaction with the ceramic core. There appears to be very little ingress of these elements into the core which describes a distinct lack of chemical reactivity with the silica-based core. The map for zirconium displays a clear correlation with the large particle in the lower LHS of the mapping and previous images. This particle is clearly a zircon particle used to modify the mechanical properties of the silica-based ceramic core which exists at the extreme outer surface of the core. Finally the calcium map shows an interesting feature at the tip between the zircon particle and the alloy, this could be suggestive of impurities within the silica-based core which have become concentrated in this region.

4.3.2. Discussion

During the casting of the nickel superalloy CMSX-10N the material comes into contact with various media at temperatures starting at ca 1550 °C. The materials of interest in this work is that of the silica-based ceramic core used to form the cooling passage within an intermediate pressure turbine blade. This topic is primarily of interest due to the kind of defects explored as part of chapter 3 that often affect the internal surface of turbine blades and are usually expressed post heat treatment and crucially the internal surfaces are not currently machined to remove surface material like the external surfaces because of constricted passageways. Therefore this sub-chapter and chapter 4 overall has attempted to better understand the kind of events that occur at the internal surface of a cast component since this could enable better processes and techniques that avoid the formation of deleterious phases at a later stage in the manufacturing process. Since the kind of defects seen, explored in chapter 3, are sporadic and randomly affect some blades in each batch creating the conditions to pinpoint the exact chain of events can be challenging.

The SEM images of *Fig. 4.10* clearly show that the as-cast surface formed by the nickel superalloy as it presses against the silica-based ceramic core is very rough and features large undulations. Of particular interest is the corner region, a stress raising sharp 90° external corner upon the ceramic core is translated into a tight 90° internal corner and there are several small particles visible at the apex. *Fig. 4.10 (b), (c)* and *(d)* increase the magnification of these particles and in all three instances the topography of the underlying superalloy is moulded around the particle. The conclusion being that the particle was present at each location during the casting process on the external surface of the silica-based ceramic core, was subject to the casting process and then remained embedded in position despite the leach process. This hypothesis suggests that the superalloy has deformed the silica core matrix and been forced to envelop the hard particles which leads to the rough surface finish of the component. These particles were subject to EDS analysis, seen in *Fig. 4.13*, the nickel-based superalloy is from the top of the image with one of the hard particles clearly visible in the bottom centre. The particle appears brightly in the zirconium map and partially within the silicon map. This means that the hard particles within the silica-based ceramic are likely zircon particles added to the core during manufacture to get the physical properties desired. In addition to this the aluminium map shows a clear trace along the interface between core and the superalloy signalling the possible presence of an alumina layer. This layer appears to be relatively consistent when formed adjacent to a hard zircon particle as well as besides the normal silica matrix of the core, showing that the closeness of the zircon particle does not totally impede the formation of the alumina layer. Further analysis took place using a FIB lift-out that enabled high magnification examination of the

interface between core and superalloy as seen in *Fig. 4.14*. The images in *Fig. 4.14* support the conclusion that the oxide formed chemically inhabits space liberated from the ceramic core and that a conversion takes place to transform the silica-based ceramic at the outer surface into an oxide which inhibits further elemental ingress into the core whilst protecting the superalloy from further loss of elements. The superalloy on the RHS of the four images of *Fig. 4.14* has a very clear delineated region that stops and whereby there is no further evidence of the γ/γ' structure past this line. Upon moving into the centre of the images it can be seen that there is a band running parallel with the nickel superalloy which is different from the surrounding silica-matrix and the large zircon particle in the bottom LHS. This band is the oxide layer formed within the surface of the silica-based core as a result of high-temperature chemical interaction. The presence of the zircon particle clearly causes some disruption to the formation of this oxide since there is evidence of porosity within the oxide layer trapped between the particle and the superalloy. The FIB lamellae lift-out was further subjected to TEM-based EDS analysis, *Fig. 4.15*, which clarifies the relative location of elements within the interface region. The silicon map shows high intensity on the LHS of the map within the ceramic core and this diminished moving from right to left across the oxide into the superalloy. This shows that silicon is only present within the core and that there is no apparent build-up of silicon within the superalloy sub-surface region suggesting formation of the oxide occurs at high-temperatures. Next the oxygen map clearly shows intensity within the ceramic core and to a lesser extent within the zircon particle in the bottom LHS. The most intense region of oxygen according to the EDS mapping of *Fig. 4.15* is that within the oxide layer formed at the interface. To further confirm the hypothesis the aluminium map shows a very definitive spike in the same region making it clear that alumina is present at the interface in the as-cast core in-situ condition. Towards the bottom of the alumina layer there is obvious disruption in the continuous nature of the oxide due to the presence of the large zircon particle which is impeding the formation of the oxide in a more continuous fashion as can be seen above within the same image. The additional advantage of the FIB lift-outs is the accurate measurement of the thickness of the alumina layer which is ca 1.5 μm.

Visible in *Fig. 4.10 (d)* are brighter regions on the upper, exposed 'hills' of the undulating surface as opposed to a darker colouration upon the depressions. The SEM images in *Fig. 4.10 (d)* are in backscatter mode suggesting that the oxide formed is still present in the depressed rough portions and that there could be an absence or thinning in the oxide on the upper, exposed portions. The oxide formed at the interface is poor and permeable in places and therefore would offer little protection against volatilisation or sublimation. Using EDS analysis within the SEM, *Fig. 4.12*, the 'top-down' view of the as-cast and as-leached surface shows clear correlation between the EDS map for aluminium and oxygen, helping to support the hypothesis that the most likely oxide to form as a result of chemical interaction during the

casting process is alumina. The next map, nickel, appears to show a relatively high abundance, however it is most likely that the power signal for nickel is the underlying nickel-based superalloy and that the alumina layer is thin enough to permit transmission of strong nickel signals from beneath.

Further to the ‘top-down’ SEM images discussed above are transverse images, in *Fig. 4.11* which further aid understanding of material mechanical interactions during casting and the role of the thin alumina layer. The presence of the large hard particles within the silica-based ceramic core results in the eventual rough surface effect. Clearly seen in *Fig. 4.11 (c)* and (d) is the heavily sintered and dense silica layer surrounding the hard zircon particle which could be detrimental to the eventual removal of the core material using the NaOH leaching process. The leaching process is designed to allow the sodium hydroxide solution to move through the networked porosity of the silica-based core enabling fragmentation and eventual removal the core material prior to the next stage of manufacture. The densely sintered regions within the core immediately adjacent to the superalloy will likely mean that removal of this particular area could simultaneously result in the removal or damage of the fragile and thin alumina layer formed at the interface.

4.4. Residual stress

4.4.1. Results

4.4.1.1. Casting 1 – central position core 1

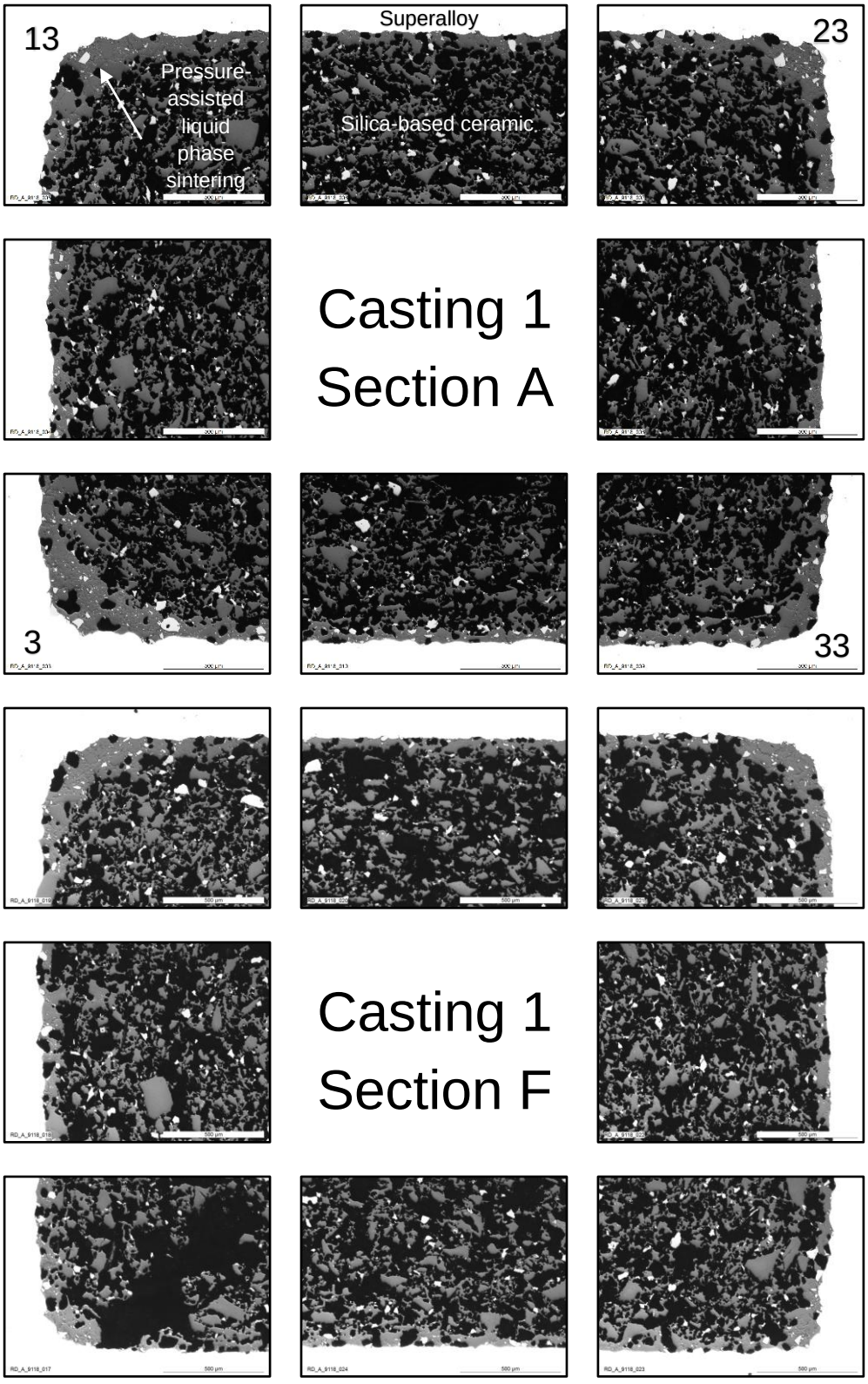

For clarification on core type and location within the mould please see Fig. 4.7 (b)

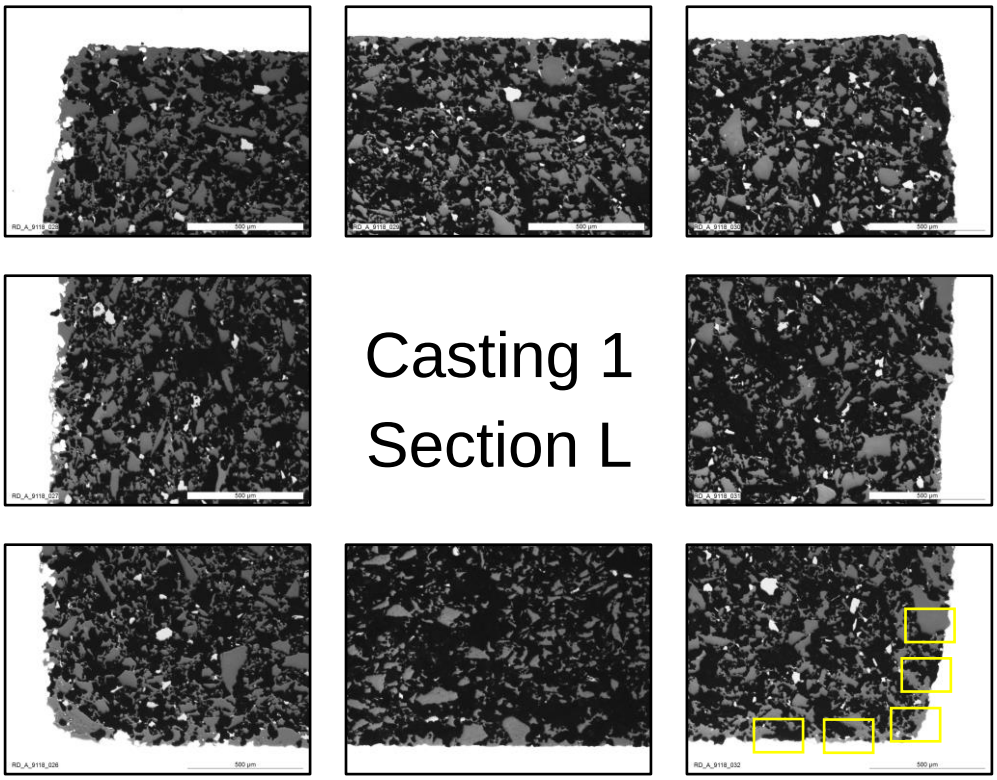

For clarification on core type and location within the mould please see Fig. 4.7 (b)

Fig. 4.16 – optical micrographs showing the silica-based ceramic in-situ within the as-cast nickel superalloy (appears bright white due to contrast) sections A, F and L are shown (top, middle and bottom of casting)

Casting 1 was sectioned into twelve pieces, sections A, F and L are representative of the top, middle and bottom of the casting height of the cuboid respectively. In the optical micrographs there is a clear difference in liquid phase sintering moving from within the ceramic core up to the region that is in intimate contact with the as-cast superalloy. In the micrographs related to section A and F of casting 1 there is an assisted liquid phase sintered region that is light grey in colour (greyscale imagery) and shows far less porosity than within the bulk of the ceramic. This is in spite of the fact that the entire ceramic core at this section height will have experienced the same time at temperature during the high-temperature casting process. Moving to the micrographs for section L of casting 1, these being representative of the bottom of the casting and the first of the mould to solidify. There is an absence of the assisted liquid phase sintering band within the silica-based ceramic and in some instances there appears to be ingress of the superalloy into surface voids of the ceramic which is not seen further up the casting in sections A and F. It is also worth noting that the cross sectional shape exhibited in section L is much closer to the original shape than sections A and F which are far more rounded. Following the inspection at low magnification a series of micrographs were collected at high magnification to accurately measure the assisted liquid phase sintering band from the interface between ceramic and superalloy to the edge of the liquid phase sintering, the results for casting 1 are shown in *Fig. 4.17*.

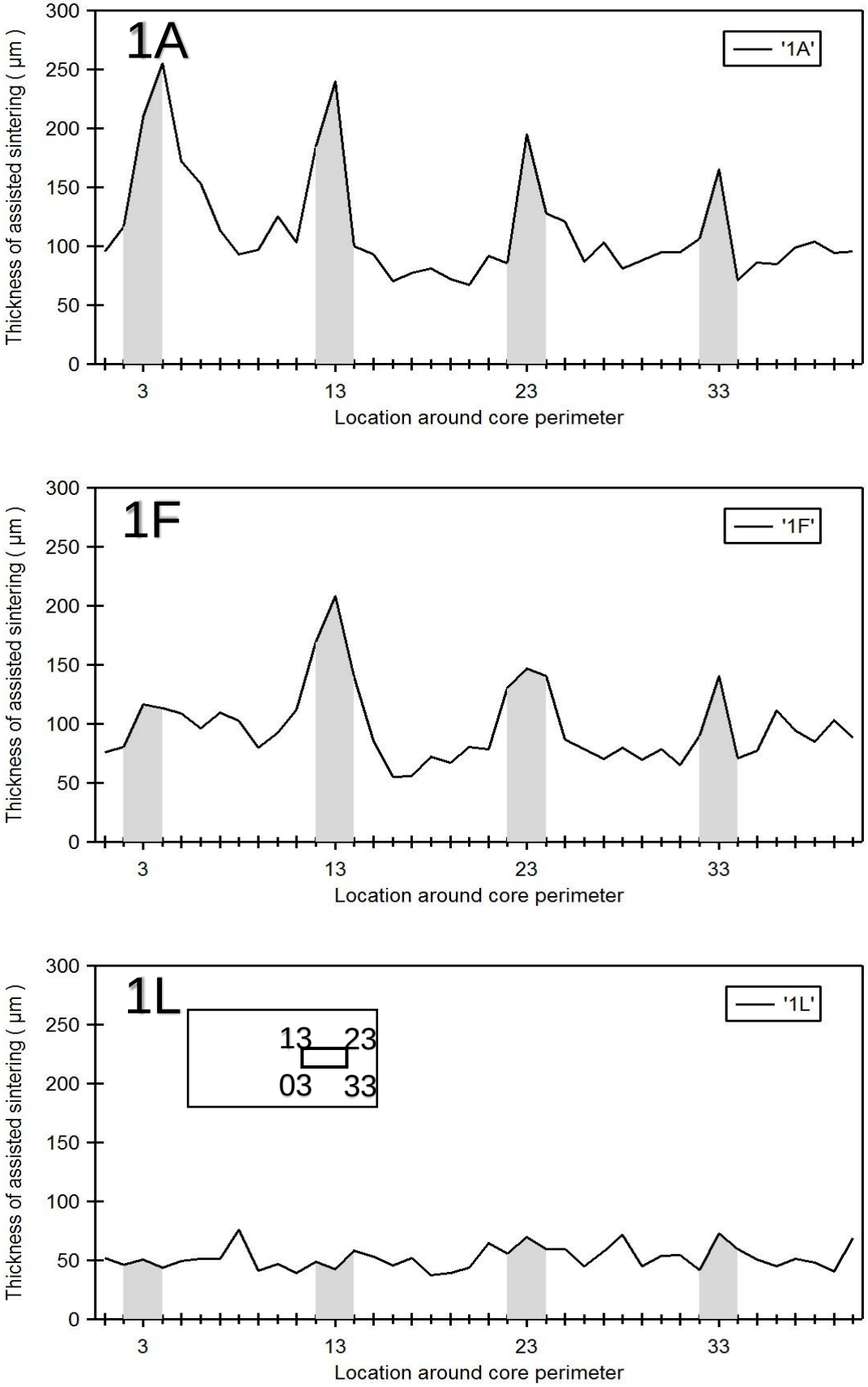

Fig. 4.17 – assisted liquid phase sintering band thickness of casting 1 at sections A, F and L (top, middle and bottom)

Clearly visible in the graphs in *Fig. 4.17* is how the band of assisted liquid phase sintering changes both as result of the spatial location around the circumference of the core and as a function of the height of the casting. Starting with section A of casting 1, there are four clear events that occur around the locations 03, 13, 23 and 33, these being the corners of the cuboidal silica-based ceramic core. This seems to suggest that the band of assisted liquid phase sintering is ca twice as thick as the 'background' liquid phase sintering experienced along the straight edges at this particular section height. Section A of casting 1 was the last region of the cuboid to solidify and was within the hot zone of the Bridgeman casting furnace for the longest period prior to passage through the baffle and subsequent solidification. The thickness of the assisted liquid phase sintering band at the corners of section 1A is ca 200 – 250 μm. In contrast the average thickness of the band along the straight edges (*between* positions 4 and 12, 14 and 22, 24 and 32 and 34 and 40) is ca 100 μm thick at this solidification height. The data collected from section 1F again shows a clear geometry related affect regarding the assisted liquid phase sintering band thickness. Although reduced in severity there is still a small bias towards the corners of the rectangular shape with the thickness at the corners being measured as ca 125 – 200 μm. Again in contrast the straight edges record an average assisted liquid phase sintering of ca 75 μm, less than that experienced at the corners at the same solidification height. Finally moving to section 1L, at the bottom of the casting where the solidification was first to occurring during the withdrawal process, the level of assisted liquid phase sintering is greatly reduced. There is no longer any bias towards to the corners, which are still highlighted in *Fig. 4.17* for clarity but there is clearly no additional liquid phase sintering occurring during the casting at the corners at the very first part of the cuboid shape to solidify. The average thickness of the assisted liquid phase sintering band in 1L is ca 50 μm. A trend has been noted that shows that, disregarding the additional geometry effects of the cuboid shape, the 'background' level of assisted liquid phase sintering changes from 1A at ca 225 μm to 1F which is ca 100 μm and drops down at 1L to ca 50 μm.

4.4.1.2. Casting 2 – central position core 2

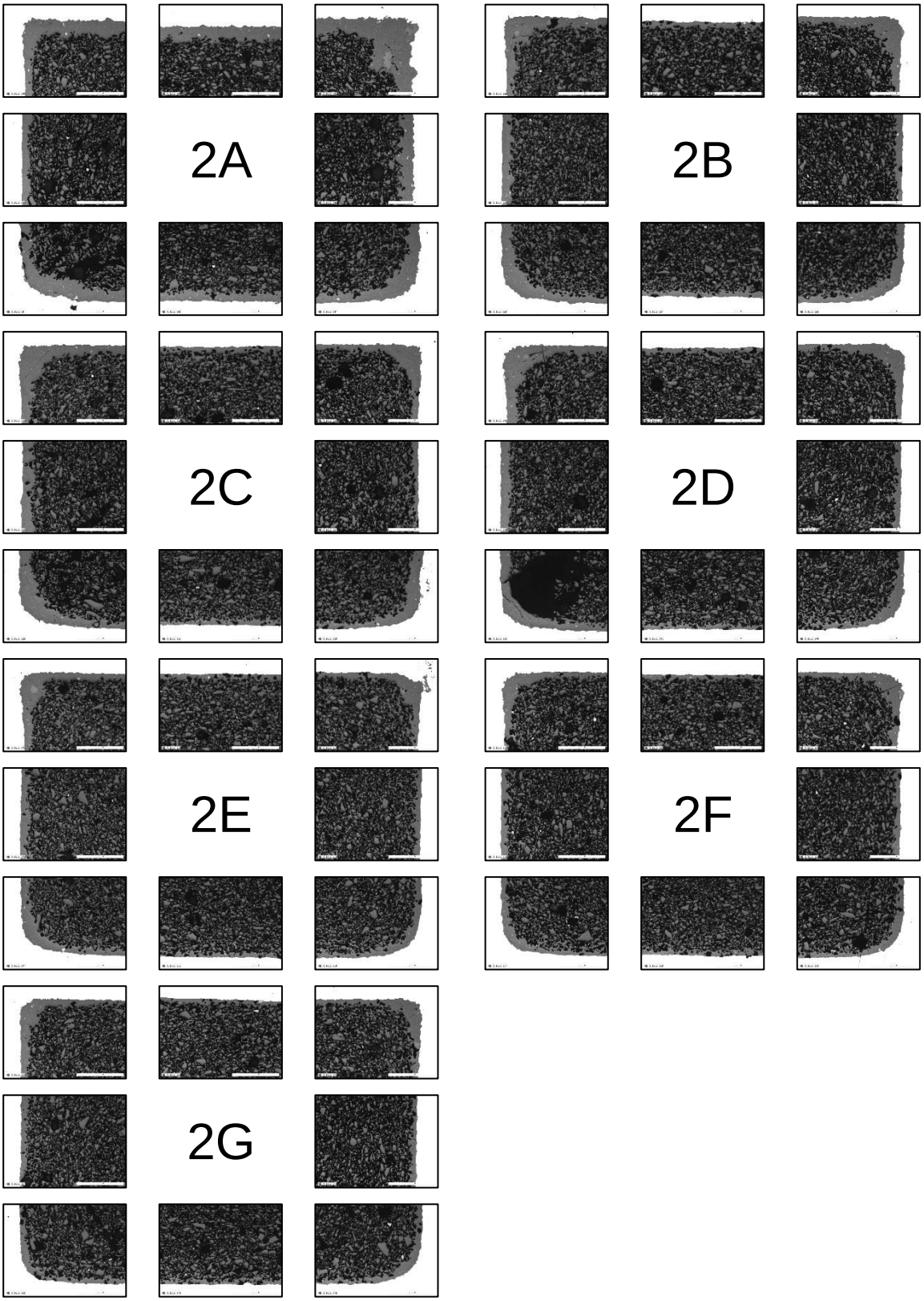

For clarification on core type and location within the mould please see Fig. 4.7 (b)

Fig. 4.18 – optical micrographs showing the silica-based ceramic in-situ within the as-cast nickel superalloy (appears bright white due to contrast) sections A to G of casting 2 are shown

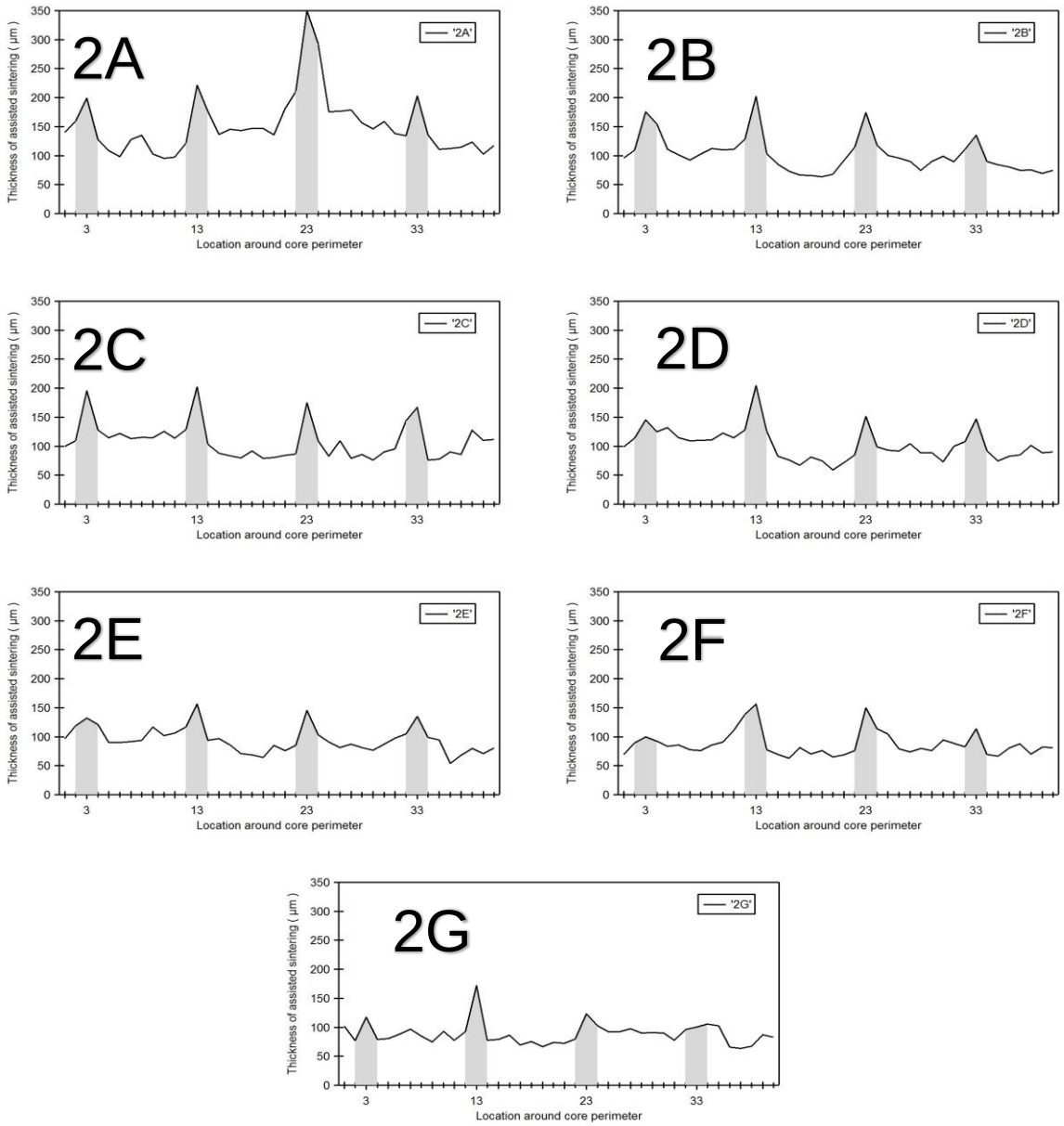

Fig. 4.19 – assisted liquid phase sintering band thickness of casting 2 at sections A through to G

Casting 2, containing the P-35™ core which was shorter than the mould, was sectioned into twelve pieces, with only the top seven, sections A, B, C, D, E, F and G which start at the top of the casting height of the cuboid, containing the ceramic core. The ceramic core used in this casting did not penetrate down the entire length of the casting but a very similar phenomena can be witnessed as seen and explained as in casting 1 above. In the micrographs there is an assisted liquid phase sintered region that is light grey in colour (greyscale imagery) and again shows far less porosity than within the bulk of the ceramic. A series of micrographs were collected at high magnification to accurately measure the assisted liquid phase sintering band from the interface between ceramic and superalloy to the edge of the liquid phase sintering, the results for casting 2 are shown in *Fig. 4.19*.

Again visible in the graphs in *Fig. 4.19* is how the band of assisted liquid phase sintering changes both as result of the spatial location around the circumference of the core and as a function of the height of the casting. The band of assisted liquid phase sintering is ca twice as thick as the 'background' liquid phase sintering experienced along the straight edges at this particular section height. Section A of casting 2 was again the last region of the cuboid to solidify. The thickness of the assisted liquid phase sintering band at the corners of section 2A is ca 200 μm. In contrast the average thickness of the band along the straight edges (*between* positions 4 and 12, 14 and 22, 24 and 32 and 34 and 40) is ca 150 μm thick at this solidification height. The data from sections 2B, 2C, 2D, 2E, 2F and 2G shows a clear geometry related effect regarding the assisted liquid phase sintering band thickness. Although reduced in severity there is still a small bias towards the corners of the rectangular shape. Again in contrast the straight edges consistently record an average assisted liquid phase sintering less than that experienced at the corners at the same solidification height. The previous trend noted in the data from casting 1 has been confirmed, that disregarding the additional geometry effects of the cuboid shape, the 'background' level of assisted liquid phase sintering changes from 2A at ca 125 μm to 2D which is ca 100 μm and drops down at 2G to ca 75 μm.

4.4.1.3. Casting 3 – Offset position core 1

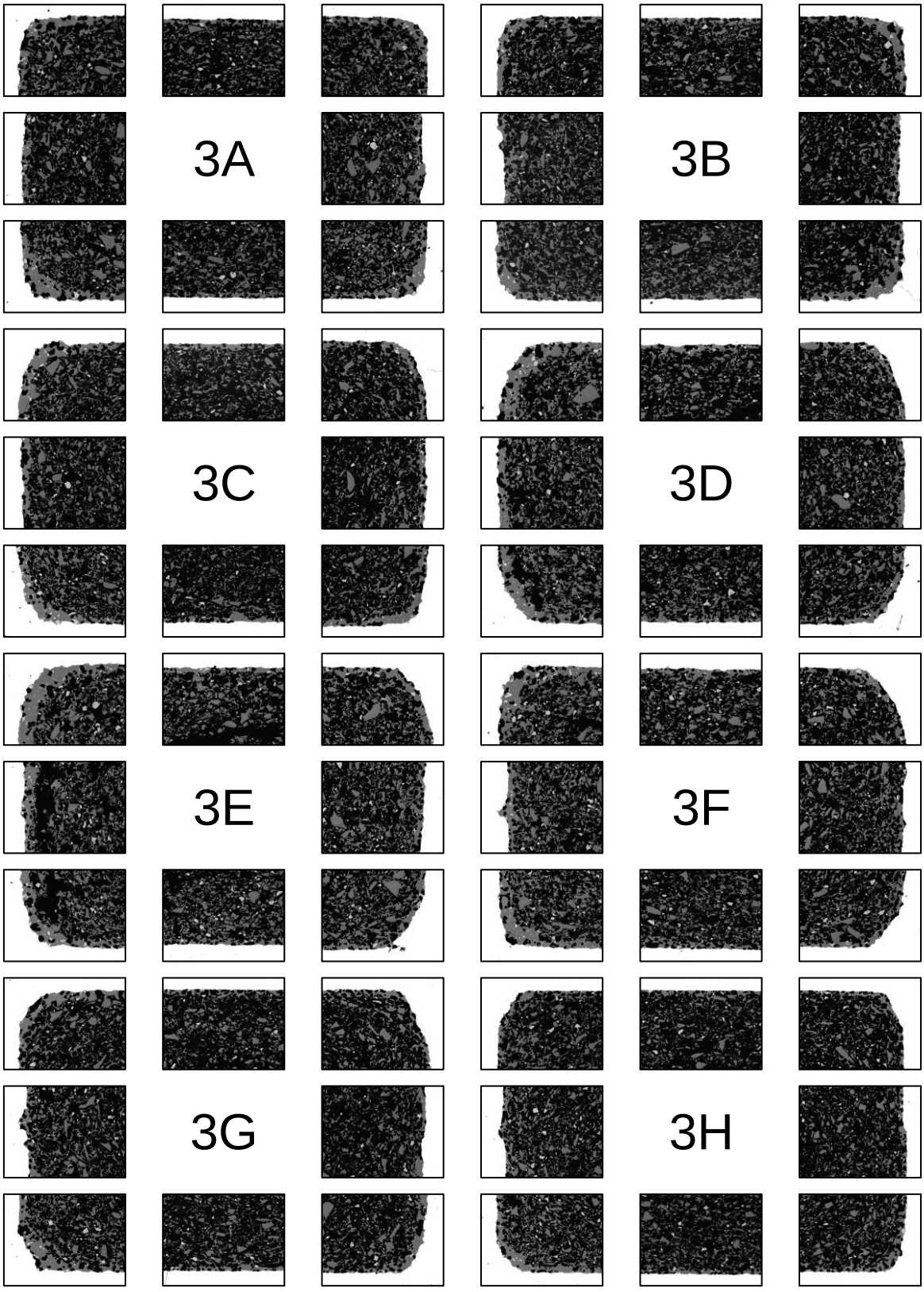

For clarification on core type and location within the mould please see Fig. 4.17 (b)

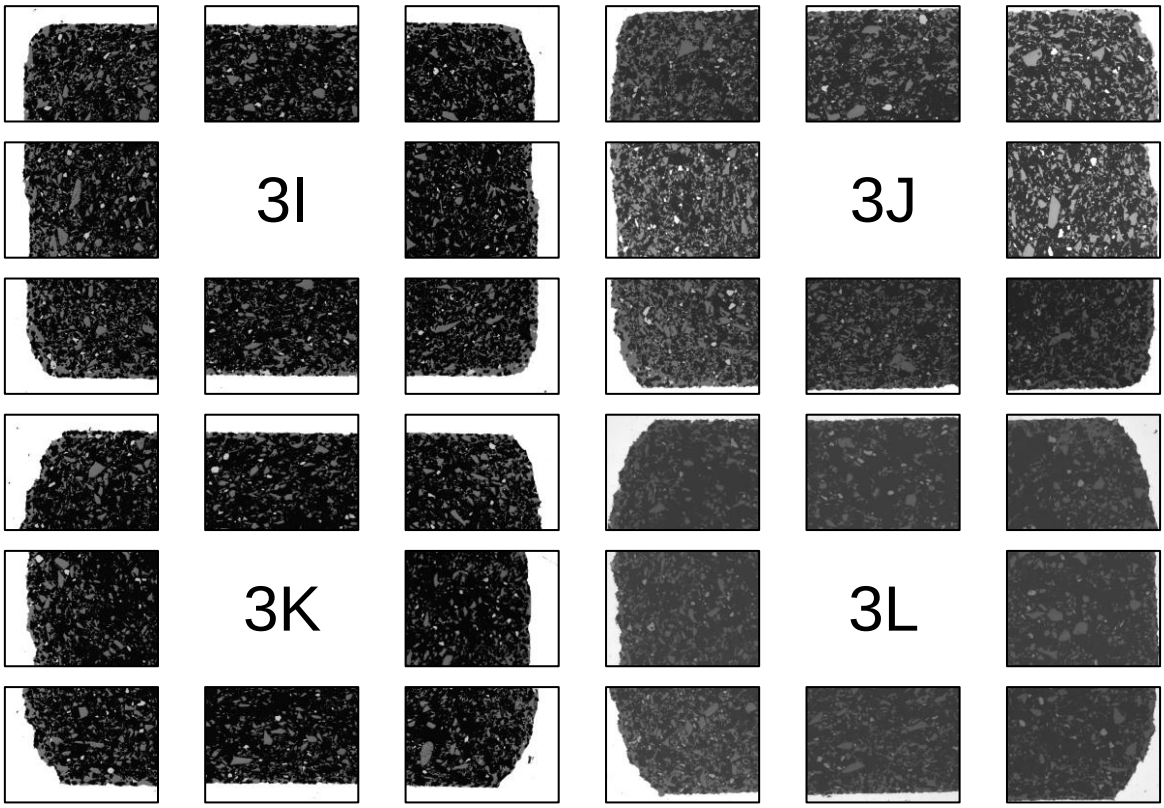

For clarification on core type and location within the mould please see Fig. 4.7 (b)

Fig. 4.20 – optical micrographs showing the silica-based ceramic in-situ within the as-cast nickel superalloy (appears bright white due to contrast) sections A to L of casting 3 are shown

Casting 3, cast using the MD core in the corner of the mould (see *Fig. 4.7 (b)*), was sectioned into twelve pieces, labelled sections 3A, through to 3L with A being the top and L being the bottom of the casting height of the cuboid. As seen before for casting 1 and 2 from the optical micrographs there is a difference in the degree of liquid phase sintering moving from within the core up to the region that is in intimate contact with the as-cast nickel superalloy. In the micrographs (*Fig. 4.20*) there is an assisted liquid phase sintered region that is light grey in colour. The entire ceramic core at each section height will have experienced the same time at temperature during the casting process. As you move down the casting to the micrographs for the lower sections J, K and L of casting 3, representative of the bottom of the casting and the first of the mould to solidify during the DS processing there is a distinct absence of the assisted liquid phase sintering band within the silica-based ceramic. Once again following the visual inspection at low magnification a series of micrographs were collected at high magnification to accurately measure the assisted liquid phase sintering band from the interface between ceramic and superalloy to the edge of the liquid phase sintering, the results for casting 3 are shown in *Fig. 4.21*.

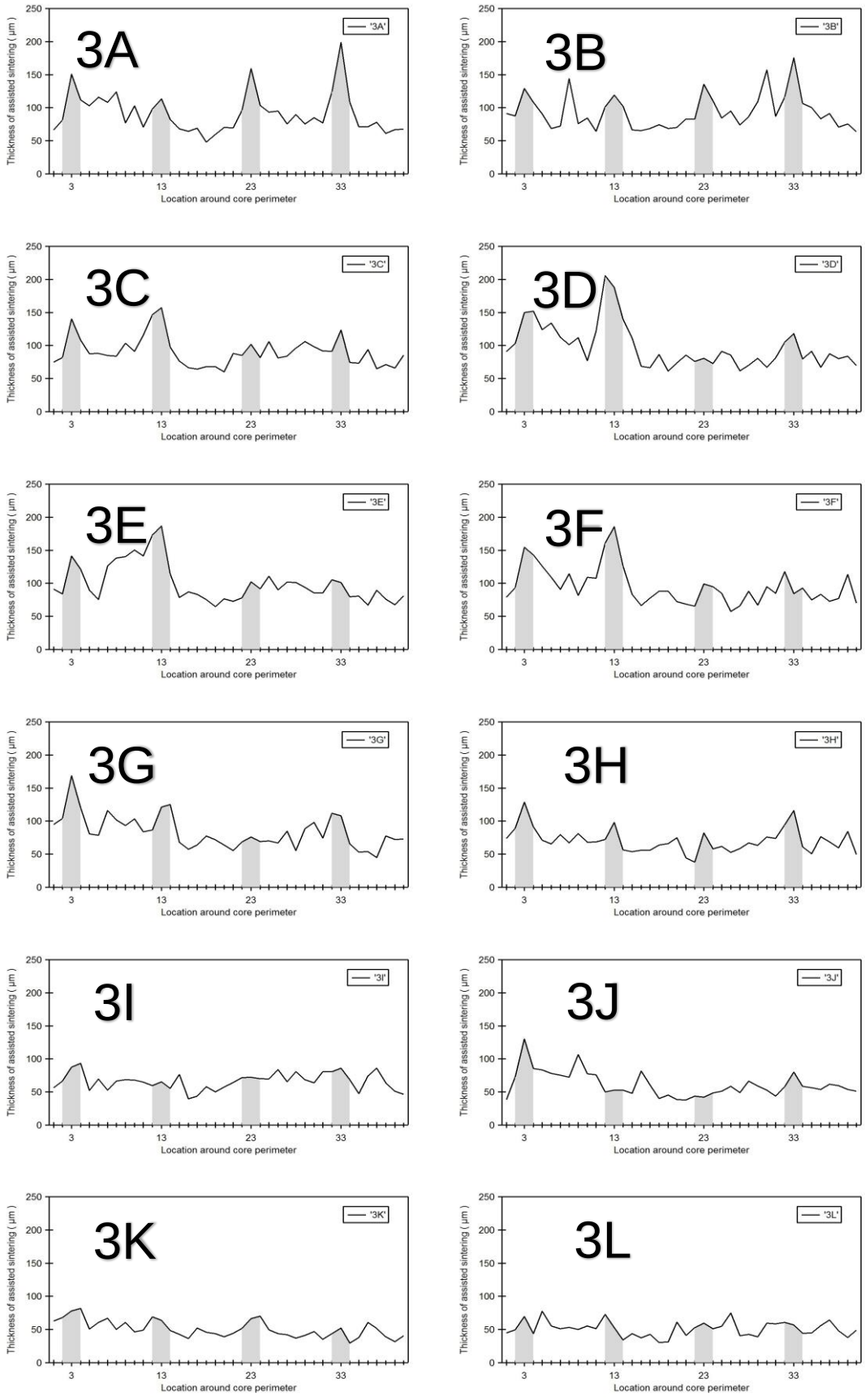

Fig. 4.21 – assisted liquid phase sintering band thickness of casting 3 at sections A through to L

Finally looking at casting 3, the phenomena visible in the graphs in *Fig. 4.21* shows how the band of assisted liquid phase sintering changes both as result of the spatial location around the circumference of the core and as a function of the height of the casting. From section 3A of casting 3 moving down the casting until 3H, the same four intensity events occur around the locations 3, 13, 23 and 33, these being the corners of the cuboidal silica-based ceramic core contained within casting 3. The band of assisted liquid phase sintering is again much thicker, than the 'background' liquid phase sintering experienced along the straight edges at this particular section height. The thickness of the assisted liquid phase sintering band at the corners of section 3A is ca 100 - 200 μm. In contrast the average thickness of the band along the straight edges is ca 100 μm thick at this solidification height. The data from sections 3B, 3C, 3D, 3E, 3F, 3G and 3H again shows a clear geometry related affect regarding the assisted liquid phase sintering band thickness. Again in contrast the straight edges consistently record an average assisted liquid phase sintering less than that experienced at the corners at the same solidification height. The previous trend noted in the data from casting 1 and 2 has been confirmed, that disregarding the additional geometry effects of the cuboid shape, the 'background' level of assisted liquid phase sintering changes from 3A at ca 100 μm to 3F which is ca 75 μm and drops down at 3L to ca 50 μm.

To appreciate the general trends in pressure-assisted liquid phase sintering at the outer reaches of the ceramic core an average was taken of the corner regions, (03, 13, 23 and 33) to yield a geometry affected 'pressure-assisted liquid phase sintering' value for each section of each casting. Furthermore, the remaining data points were averaged to yield a 'background liquid phase sintering' value which represents the effect of liquid phase sintering registered by the remainder of the core along the straight edges and, therefore, without additional geometry effects. *Fig. 4.22* shows the result of this for each casting. All three castings show that on average the geometry affected 'pressure-assisted liquid phase sintering' is greater than the residual level of liquid phase sintering experienced by the straight edges. In addition, all three data sets confirm that upon moving from the top of the casting down to the bottom there is a clear gradient whereby the thickness of the liquid phase sintered band decreases as a function of casting height. Finally all three data sets confirm that moving from the top of the casting to the bottom shows that the discrepancy between the geometry affected corners of 03, 13, 23 and 33 and the remaining data points decreases as shown by the intersecting lines towards sections J, K and L at the bottom of the casting.

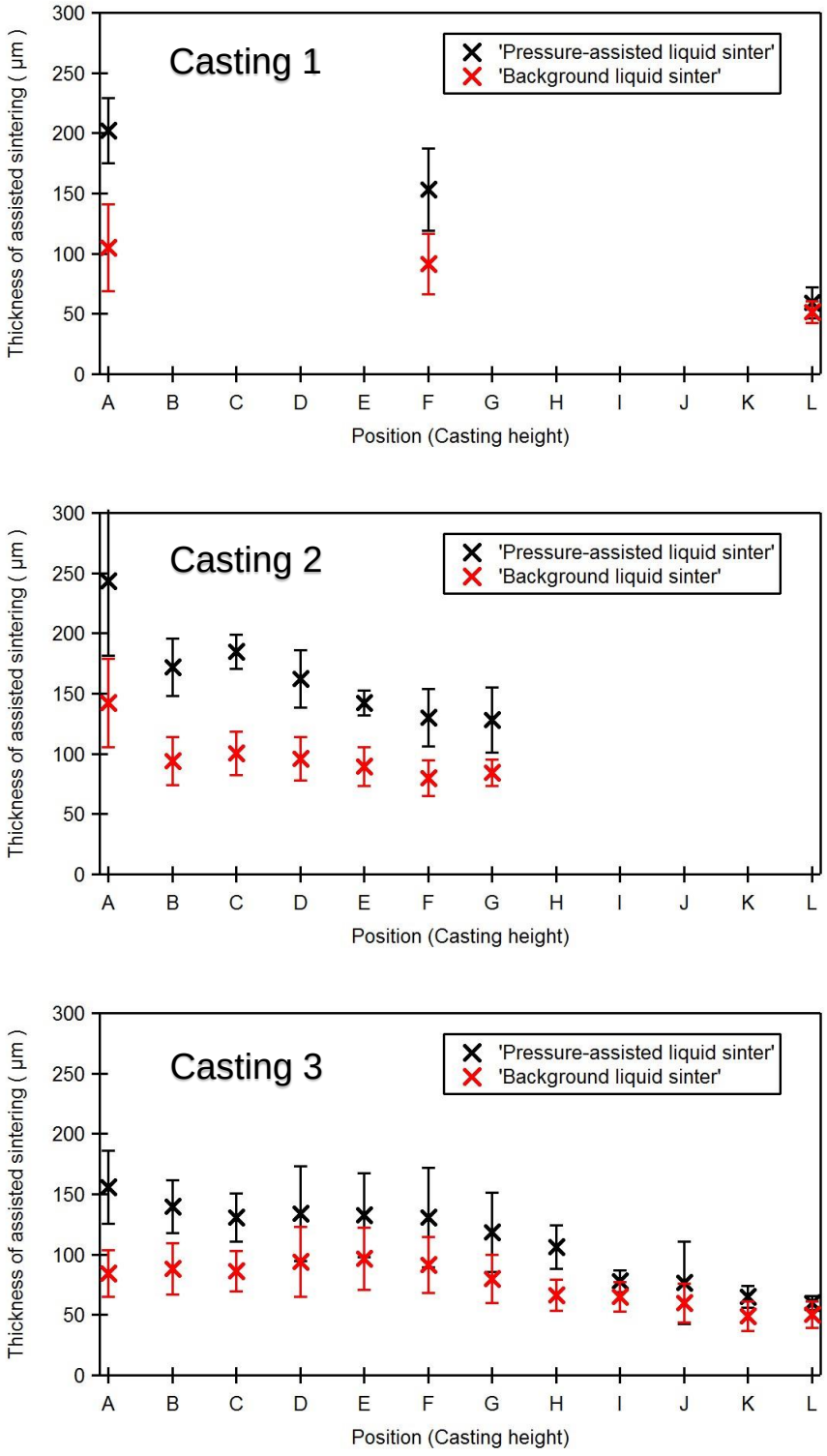

Fig. 4.22 – assisted liquid phase sintering band thickness (average) at (pressure-assisted liquid phase sintering) corners compared to average of the straight (background) edges, castings 1, 2 and 3 at all available section heights

4.4.2. Discussion

During the casting process there are both chemical and physical interactions between the nickel-based superalloy and the casting media, which in this instance is the silica-based ceramic core. The chemical interactions lead to the formation of the thin oxide layer at the interface as discussed in 4.3.1 and 4.3.2 whilst the physical interactions, as seen here, bring about a level of sintering and pressure-assisted sintering within the ceramic core. During the course of this discussion there will be several terms used to describe different levels of liquid phase sintering experienced by the silica-based core, these will be explained here. 'Pressure-assisted liquid phase sintering' is used to describe the accelerated liquid phase sintering of amorphous silica at the corners of the ceramic core as a result of both the high temperatures experienced as well as the compressive forces exerted by the contracting superalloy upon the surface within geometry specific areas that are stress raising features . The level of 'pressure-assisted liquid phase sintering' also varies as a function of casting height as will be shown. The next term, 'background liquid phase sintering', is also used to describe the effect of compressive superalloy forces on the external surface of the ceramic core though now this is in the straight regions, not the corners and therefore geometry effects are no longer in effect. The 'background liquid phase sintering' is similar to the level of assisted-sintering that would be experienced if a cylindrical core was cast within a cylindrical test piece, there would be no stress-raising features present. Finally the term 'bulk liquid phase sintering' is used to describe the sintering which occurs in the centre of the ceramic core only as a result of the high temperatures experienced, thus deep within the core there are no forces present to assist or accelerate the sintering process.

Three casting trials took place during this work, casting 1 was a full height casting using the MD™ core material, casting 2 used the P-35™ core material and finally casting 3 was made using MD™ but had the core placed into the corner of the casting cuboid to exacerbate geometry effects. When examining the microstructure of the ceramic core in-situ after the casting process, in all three cases, it is clear to see that different levels of liquid phase sintering have occurred as a result of the casting height. Using optical micrographs of *Fig. 4.16, 4.18* and *4.20* it can be seen that the internal structure of the core is relatively consistent and features regions of sintered silica as well as porosity. Moving to the edge of the in-situ core it can be seen that the liquid phase sintered silica is now almost continuous and represented as a light grey in the optical micrographs. Finally the white border around the core is the nickel-based superalloy the microstructure of which is not visible since both contrast and brightness have been selected to best observe the ceramic core. In each casting the thickness of both the pressure-assisted liquid phase sintering layer and the background liquid phase sintering layer was measured using optical microscopy to yield the

data seen in graphs of *Fig. 4.17, 4.19* and *4.21*. In all three cases progressing from the top of the casting (A) towards the bottom results in a gradual decrease in the thickness of the pressure-assisted liquid phase sintering band as well as the background liquid phase sintering region. This trend is most clearly seen in *Fig. 4.22* which brings together an average of the data displaying how the thickness changes as a function of casting height in all three castings. The gradient observed has been hypothesised as being a result of differing casting stresses at different heights within the castings. This phenomena will not result from a chemical interaction driven by the hydrostatic pressure of liquid metal since there are clear geometry related features at the corners whereby there are additional levels of liquid phase sintering occurring. If this feature were related to a chemical reaction driven during the period whereby liquid superalloy is in contact with the ceramic prior to freezing then it seems likely the thickness of the sintered band would be equal around the entire perimeter of the core and not reliant on geometrical features. Referring back to *Fig. 4.17, 4.19* and *4.21* it can be observed that there is a discernible difference between the thickness of the liquid phase sintered band in the corners of the core in the 'pressure-assisted liquid phase sintering' region in comparison to the straight edges devoid of stress-raising features, termed the 'background liquid phase sintering' region.

Fig. 4.23 features a schematic detailing the progression of a contracting nickel-based superalloy upon the ceramic core. The initial frame shows a predominantly silica-based ceramic utilising the speckle-pattern and shows individual silica grains as small circles. The zircon particle is represented by a hexagon with the checker-board pattern in the centre of the image, the bottom displays the dark coloured superalloy. As the schematic progresses it can be seen that the superalloy exerts compressive force once freezing begins and this causes the silica to begin to sinter preferentially at the surface as a result of pressure-assisted liquid phase sintering. In the final two frames it can be seen that the amorphous silica begins to compact into the pressure-assisted liquid phase sintering layer immediately adjacent to the nickel-based superalloy and that the zircon particle has been enveloped. The zircon particle is hard and larger than the surrounding silica which means it is not possible for the superalloy to push the particle away or cause it to be compressed in the same way as the silica. The result is that at temperatures of ca 1300°C the superalloy yields and deforms to match the shape of the zircon particle since it is unable to move or crush it. During the subsequent cool down from freezing temperatures the undulating shapes formed are fixed and the zircon particles protruding from the ceramic core into the superalloy remain. As the temperature continues to decrease these protruding points impart plastic deformation into the superalloy as the metal contracts upon it. These points act to focus the force of the compressing superalloy thereby increasing the likelihood of imparting enough plastic deformation in the superalloy before the cool down is complete to generate recrystallisation.

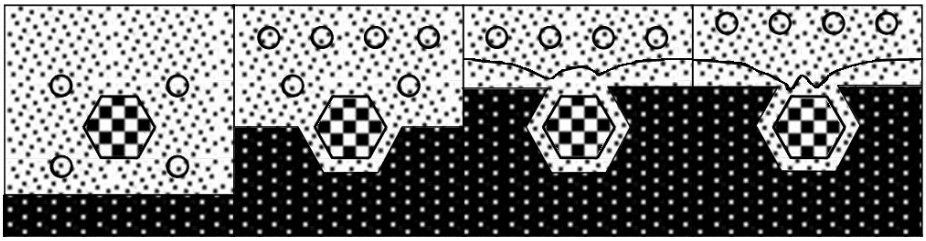

Fig. 4.23 – schematic detailing during the casting process the compressive force imparted by the freezing and contracting nickel superalloy (dark), upon the silica (speckle-pattern) and the zircon particle (checker-board)

Following the casting process and the freezing of the nickel-based superalloy seen in *Fig. 4.23* the cast component receives a core leach operation consisting of a sodium hydroxide solution to dissolve and remove the silica-based core leaving the empty cooling passage cavity. Once successfully leached *Fig. 4.24* aims to explain the next process, the solution heat treatment. For the alloy CMSX-10N a heat treatment with a holding temperature of 1364°C for more than 40+ hours is necessary for solutioning. Due to the locally accumulated plastic deformation during the casting process detailed above the rough as-cast surface could alleviate this strain through recrystallisation of small individual grains. These grains form at the sub-surface and result in high-angle grain boundaries forming between the newly formed recrystallised grains and the single crystal component.

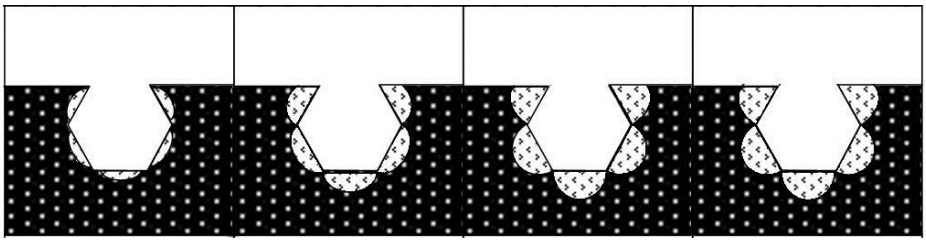

Fig. 4.24 – schematic detailing during the solution heat treatment process, surface undulations left behind as seen in Fig. 4.29 instigate small recrystallised grains

Following the solution heat treatment the recrystallised grains provide grain boundaries necessary for the formation of discontinuous precipitation colonies during the next phase of processing. After quenching from the solution heat treatment at 1364°C the components are exposed to a primary aging treatment at 1150°C in order to correctly grow the γ/γ’ microstructure needed for high temperature service. During this lower temperature treatment *Fig. 4.25* details the growth of DP colonies moving into the superalloy bulk, converting the microstructure into coarsened γ and γ’ and generating what is most likely *P*-phase TCPs.

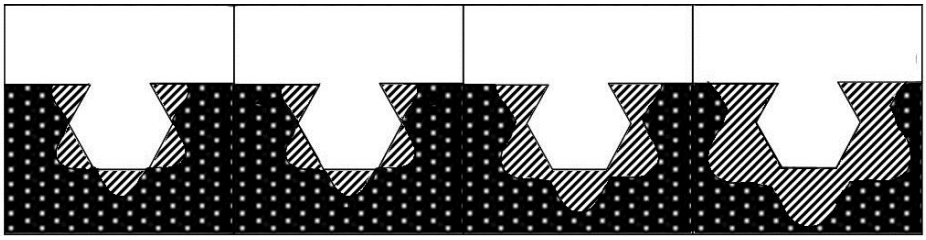

Fig. 4.25 – schematic detailing during the aging heat treatment process, growth of discontinuous precipitation colonies in the sub-surface region

4.5. Conclusion

This chapter has built upon chapter 3 which looked at the surface defect upon the internal surface of a turbine blade. A systematic study of casting the alloy CMSX-10N in bespoke moulds furthered understanding of core / casting interactions that must be accounted for when developing core materials.

1. The as-cast surface formed by the nickel-based superalloy as it presses against the silica-based ceramic core is very rough and features large undulations.
2. The topography of the superalloy is moulded around particles that were present during the casting process within the external surface of the silica-based ceramic core and then remained embedded in position despite the chemical leach process.
3. The superalloy has deformed the silica-based core matrix and been forced to envelop the hard particles which leads to the rough surface finish of the component.
4. EDS compositional analysis of the hard particles appears concentrated in zirconium and silicon. This means that the hard particles within the silica-based ceramic are likely zircon particles added to the core during manufacture to get appropriate physical properties.
5. Aluminium elemental mapping shows a clear trace along the interface between core and the superalloy signalling the presence of an alumina layer. This layer appears to be consistent when formed adjacent to a hard zircon particle as well as besides the normal silica matrix of the core, showing that the closeness of the zircon particle does not totally impede the formation of the alumina layer.
6. The oxide formed chemically inhabits space liberated from the ceramic core and a conversion takes place to transform the silica-based ceramic at the outer surface into an oxide which inhibits further elemental ingress into the core whilst protecting the superalloy from further loss of elements.
7. The presence of the zircon particle causes some disruption to the formation of this oxide since there is evidence of porosity within the oxide layer trapped between the particle and the superalloy.
8. Silicon is only present within the core, as observed using elemental mapping, and there is no build-up of silicon within the superalloy sub-surface region suggesting formation of the oxide occurs at high-temperatures.
9. Brighter regions on the upper, exposed ‘hills’ of the as-cast superalloy undulating surface as opposed to a darker colouration upon the depressions. Backscatter mode images suggest that the oxide formed is still present in the depressed rough portions and that there could be an absence or thinning in the oxide on the upper, exposed portions. The oxide formed at the interface is poor and permeable in places and

therefore would offer little protection against volatilisation or sublimation of nickel or chromium under certain heat treatment furnace conditions

10. ‘Pressure-assisted liquid phase sintering’ is used to describe the accelerated sintering of amorphous silica at the corners of the ceramic core as a result of both the high temperatures experienced as well as the compressive forces exerted by the contracting superalloy upon the surface within geometry specific areas that are stress raising features.
11. The level of ‘pressure-assisted liquid phase sintering’ varies as a function of casting height.
12. ‘Background liquid phase sintering’, is used to describe the effect of compressive superalloy forces on the external surface of the ceramic core though now in the straight regions, not the corners and therefore geometry effects are no longer in effect. The ‘background liquid phase sintering’ is similar to the level of assisted-liquid phase sintering that would be experienced if a cylindrical core was cast within a cylindrical test piece, there would be no stress-raising features present.
13. ‘Bulk liquid phase sintering’ is used to describe the sintering which occurs in the centre of the ceramic core only as a result of the high temperatures experienced, this deep within the core there are no forces present to assist the sintering process.
14. The liquid phase sintering gradient observed is likely a result of differing casting stresses at different heights within the castings. This phenomena will likely not result from a chemical interaction driven by the hydrostatic pressure of liquid metal since there are clear geometry related features at the corners whereby there are additional levels of sintering. If this feature were related to a chemical reaction driven during the period whereby liquid superalloy is in contact with the ceramic prior to freezing then it seems likely the thickness of the sintered band would be equal around the entire perimeter of the core and not reliant on geometrical features.
15. The superalloy exerts compressive force once freezing begins and this causes the silica to begin to sinter preferentially at the surface as a result of pressure-assisted liquid phase sintering. As the amorphous silica begins to compact into the pressure-assisted liquid phase sintering layer the zircon particle can been enveloped. The zircon particle is hard and much larger than the surrounding silica which means it is not possible for the superalloy to push the particle away or cause it to be compressed in the same way as the silica. The result is that at temperatures of ca 1300°C the superalloy must yield and deform to match the shape of the zircon particle since it is unable to move or crush it. During the subsequent cool down from the freezing temperatures the undulating shapes formed are fixed and the zircon particles protruding from the ceramic core into the superalloy remain. As the temperature

continues to decrease these protruding points impart plastic deformation into the superalloy as the metal contracts upon it. These points act to focus the force of the compressing superalloy into a small area thereby increasing the likelihood of imparting enough plastic deformation in the superalloy before the cool down is complete to generate recrystallisation.

16. Following the casting process the cast component receives a core leach operation consisting of a sodium hydroxide solution to dissolve and remove the silica-based core leaving the empty cooling passage cavity. Once successfully leached a solution heat treatment is used. For the alloy CMSX-10N a heat treatment with a holding temperature of 1364°C for more than 40+ hours is necessary for solutioning. Due to the locally accumulated plastic deformation during the casting process the rough as-cast surface could alleviate this strain through recrystallisation of small individual grains. These grains form at the sub-surface and result in high-angle grain boundaries forming between the newly formed recrystallised grains and the rest of the single crystal component.

5. Carburisation – current system

5.1. Introduction

During aluminising of high pressure turbines blades a slurry is used to mask part of the external surface to prevent the deposition in key areas. The procedure of 'stop-off' involves application of slurries to the part via paint brush before drying in a tunnel oven at ca 100°C. These slurries consist of a nickel – chromium – aluminium alloy (M1™) and ceramic powder in a liquid binder, which contains a polymer dissolved in organic solvents that evaporate leaving behind the polymer to hold the paint to the surface. Typically two coats of M1™ 'stop-off' are applied before a final two layers of M7™ 'stop-off', a different composition, are used to cap the surface. These maskants are manufactured by Akron Paints and Varnish (APV) and are bought in for use in the coating facility during aluminising. After processing in the chemical vapour deposition (CVD) rig the internal layers become a powder, which helps removal of the part from the maskant, this transformation is due to the breakdown of the polymer binder at temperatures during the process of 1030°C coupled with a nickel – chromium – aluminium metal powder mixture (M7™) with sufficient ceramic such that it does not sinter. The outer layer forms a harder shell that forms a gas-tight seal and contains the powder during the CVD process.

The undesired result of this system is a sporadic appearance of small carbide precipitates beneath the surface correlating with those regions coated in slurry. These precipitates cannot be tolerated within single-crystal components as it is likely they pose a detriment to the physical properties due to the deviation from the intended microstructure.

Carbon added to an alloy composition prior to casting is distinctly different from the later addition of carbon via surface treatment. Removal of carbon from superalloys enabled the use of tailored heat treatments for effective homogenisation. This work concerns carbon addition during coating processing but much of the literature is not directly comparable, it does however contain information regarding carbide formation in nickel-based superalloys, but usually during casting. Before the introduction of single-crystal casting, superalloys were conventionally cast leading to polycrystalline structures with grain boundaries. Carbide formation upon grain boundaries enabled an increase in high temperature creep properties. The alloy, Mar-M002, features ca 1.7 wt. % hafnium and 0.15% carbon for the purpose of hafnium-carbide formation.[108–110]

5.1.1. Carbide types

There is an array of commonly found carbides within nickel-based superalloys, these include MC, $M_{23}C_6$, M_7C_3 and M_6C, where M stands for a combination of metallic elements with the non-metallic element carbon (C).[108,111] The MC-type carbide usually displays a face centred cubic (NaCl) structure.[108] The types of carbides observed depend upon alloy composition and high-temperature exposure. In general the MC-type carbide is considered stable from 850°C to 950°C, the M_6C carbide is most stable above 1000°C and the $M_{23}C_6$ carbide appears in the 950°C – 1000°C temperature range. Above 1000°C script-like MC carbide decomposes into alternative carbides rapidly.[112,113]

In work by Liu et al. [114] carbon was used in single-crystal alloys to help purify the melt and lend strength to sub-grain boundaries. Castings of large components such as nozzle guide vanes often feature carbon as an insurance, since to guarantee a single-crystal casting of such size is difficult. Liu et al. determines the benefits that MC-type carbides can bestow upon single-crystal castings include providing creep resistance. EDS work by Liu et al. determined that the carbides were rich in two elements, tantalum and titanium. Following a heat treatment, to relieve elemental segregation, Liu et al. found that some of the MC-type carbides had decomposed and formed M_6C carbides, rich in molybdenum, tungsten and chromium, via the following reaction:

$$MC + \gamma \rightarrow M_6C + \gamma'$$

These samples were creep tested to determine the effect of the carbides. At 870°C the decomposition reaction was not activated and the MC-type carbides remained, these carbides were found to contribute to crack initiation. The M_6C carbides had two origins: firstly the decomposition reaction that saw MC-type carbides transform and second the precipitation of M_6C fresh from carbon latent within the crystal structure.[114] The morphology of the M_6C carbides that degrade from MC is irregular whilst the freshly precipitated M_6C carbides feature an octahedral habit with sides of between 400 and 500nm, are coherent and feature an orientation relationship with the superalloy matrix. Liu et al. also determines the existence of $M_{23}C_6$ carbides which form during heat treatments at lower temperatures between 760 and 980°C. These $M_{23}C_6$ carbides form preferentially in the γ channels and could be helpful in providing creep resistance yet their presence removes elements added to the alloy as solid solution strengtheners as well as the element chromium.

5.1.2. Carbide compositions

EDS analysis has revealed that script-like and angular carbides were generally rich in hafnium, tantalum, titanium and tungsten identifying them as MC-type. The occasional presence of other elements (nickel, chromium and cobalt) in the EDS analysis of the smaller particles was attributed to surrounding matrix contribution to the signal.[108] The individual compositions of the MC-type carbides were seen to vary from hafnium-lean (Ti-0.4-Ta-0.35-W-0.2-Hf0.05)C to hafnium-rich (Ti-0.07-Ta-0.12-W-0.06-Hf-0.75)C.[108] The compositions of needle shaped MC-type carbides were found to be tantalum – rich (ca 46 at. %), with niobium (ca 22 at. %) and titanium (ca 11 at. %). Hafnium, molybdenum and nickel concentrations lie around ca 5 at. %. [109,111,112]

Finer carbide particles have been observed within the γ/γ' eutectic and the dendritic regions. These were identified as chromium-rich $M_{23}C_6$.[108,115]

EDS analysis of a cubic phase identified using TEM to be an M_6C carbide was shown to be rich in molybdenum and tungsten.[114] It is claimed that the M_6C appears only when the molybdenum content of nickel- or cobalt- base superalloys exceeds ca 6 to 8 wt % (or its equivalent in tungsten atoms).[111,115]

5.1.3. Orientation relationships

Type	Relationship	Reference
M_6C Cubic	$\{001\}_{M_6C}$ // $\{001\}_{matrix}$ $<001>_{M_6C}$ // $<001>_{matrix}$	114
M_6C Needle phase	$\{110\}_{M_6C}$ // $\{110\}_{matrix}$ $<110>_{M_6C}$ // $<110>_{matrix}$	114
$M_{23}C_6$ Needle phase Alternate Cubic phase, 50 – 500 nm nucleating in the γ channels.	$\{001\}_{M_{23}C_6}$ // $\{001\}_{matrix}$ $<001>_{M_{23}C_6}$ // $<001>_{matrix}$	114
$M_{23}C_6$ carbide (chromium-rich)	$\{100\}_{carbide}$ // $\{100\}_{matrix}$	111

5.1.4. Spatial locations

Cubic shaped carbide precipitates, with a size between 50 and 500 nm, were found to have a strong tendency to nucleate within the γ matrix channels of superalloys with prolonged high-temperature exposure. Discrete $M_{23}C_6$ particles formed within the γ channels may be beneficial to creep properties through blocking dislocation movement but they also withdraw solid solution strengthening elements from the matrix.[116]

Three types of carbides; MC, $M_{23}C_6$ and M_6C were found upon grain boundaries. MC carbides rich in tantalum and titanium are mostly present in the blocky or needle form with finer $M_{23}C_6$ particles present at grain boundaries as well as in γ matrix channels. At the crossing point of two γ channels the $M_{23}C_6$ particles precipitated are larger than those only inside a single γ channel.[116,117] In the interior of grains, precipitation of the secondary $M_{23}C_6$ carbide occurred preferentially on crystal imperfections such as dislocations and stacking faults. Furthermore with increasing aging time the precipitates that nucleated upon the dislocations coarsened and coalesced into chains, while precipitates on the stacking faults grew into a lath shape.[111] Secondary carbides are chromium-rich $M_{23}C_6$ and tungsten-rich M_6C.

There are a number of blocky, primary MC-type carbides precipitated along grain boundaries forming coarse (2 to 10 μm in diameter) as well as elongated tantalum, hafnium, tungsten enriched precipitates within the grain. Fine (0.2 to 0.8 μm in diameter) globular $M_{23}C_6$ carbides were present in the superalloy microstructure after heat treatment. [118,119]

Tantalum and hafnium enriched MC-type carbides predominated within the matrix and chromium – rich $M_{23}C_6$ carbides precipitate preferentially at the periphery of the MC carbides and within the (γ + γ') eutectic at grain boundaries.[118] $M_{23}C_6$ particles are either formed aligning along grain boundaries or isolated to precipitate in globular morphology.[112]

5.1.5. Morphologies

Four tantalum–rich MC-type carbide morphologies were identified; discrete blocky dispersion, well-distributed script-like, needle and nodular.[11,112] Small, spherical carbides were also found to be tantalum – rich and were, therefore, considered to also be MC-type carbides. MC carbides tie up elements such as tantalum, titanium and tungsten, which can have an effect on γ/γ′ lattice misfit and therefore coarsening behaviour.[120]

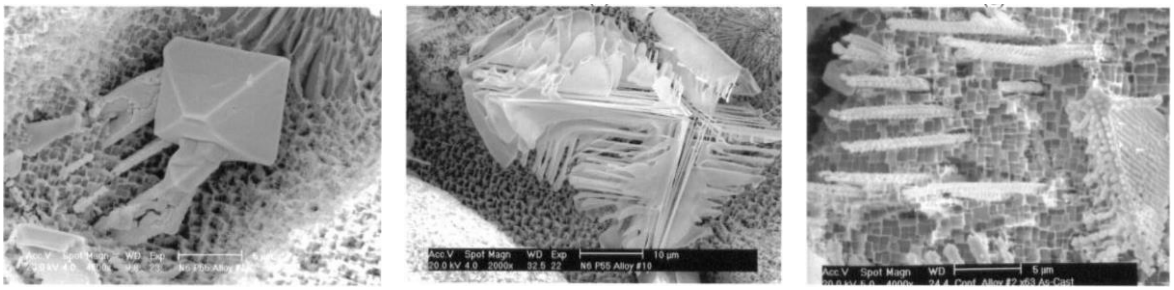

Fig. 5.1 – micrographs of tantalum-rich MC carbide morphologies observed in Rene N5 and N6 based alloys, blocky (a), script (b) and nodular (c) [11]

5.1.5.1. Blocky

The blocky MC precipitates have a larger misfit with the matrix than the needle MC carbides. The larger lattice misfit produces higher interface energy per unit area due to strain energy. There is no doubt that large misfit energy tends to reduce the surface area of a precipitate.[109] For the same volume, blocky MC-type carbides have a smaller surface area than needle-shaped carbides. Hence, the MC-type carbides tend to be blocky to reduce their total interface energy.[109]

5.1.5.2. Octahedral

The octahedron-shape is a leading carbide morphology, and is considered by some to be the 'master' carbide. At slow carbide growth rates, these carbides grow as layers on the faceted surface to maintain the equilibrium octahedron shape. The octahedron with {111} faces is the equilibrium carbide shape due to a minimum interface energy.[109]

5.1.5.3. Acicular

In addition a needle-like phase is found which is inclined at an angle of 45° to the [001] direction. EDS analysis shows that this acicular phase is rich in tungsten and molybdenum, so its morphology and composition indicate a TCP phase however, electron diffraction and chemical analyses prove that the needle-like phase is M_6C carbide precipitate. Careful examination of the needle-like particles on various sections of the specimens shows that they are platelets, parallel to {110} planes of the matrix, which are aligned to 45° to [001] orientation.[114]

5.1.5.4. Platelets

Studies of intragranular carbides showed that $M_{23}C_6$ carbides precipitated as platelets on {111} planes of the matrix.[112,121]

5.1.5.5. Rods

M_7C_3 carbide is in the form of rods or irregular aggregates.[111]

5.1.6. Internal structure

Some carbides were observed to have inner cores that etched differently yielding a central region with an optically different colour, additionally this region displayed darker (lower Z) contrast than the surrounding material in the SEM under backscatter mode.[119] EDS spectra suggests these cores are carbo-nitrides, or more specifically (TiTa)CN. This phase is consistently observed at the cores of the MC-type carbides, it is concluded that it must form at higher temperatures during the solidification process than the MC.[119] Further evidence of these titanium – rich MC-type carbides growing on Ti(CN) was identified in XRD spectra of particles chemically extracted from the superalloy material but again these were not detected as discrete particles with the TEM or SEM, supporting the conclusion that Ti(CN) (or the similar (Ti-0.5-W-0.5)C) exists as particles within the larger MC-type carbides and that in this work the formation of the 'core' without the subsequent outer layers is not observed.[108,122,123]

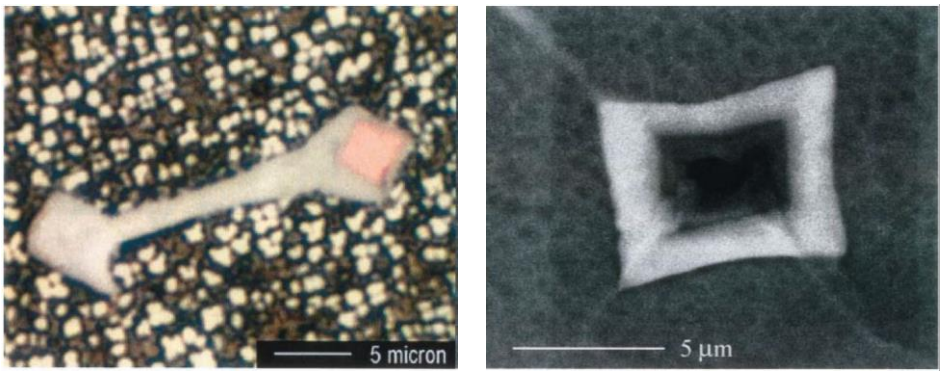

Fig. 5.2 – Colour light optical micrograph showing an 'orange' core in the MC-type carbide of the alloy IN738 (a) and SEM-BSE of one of the MC-type carbides containing a dark, low Z phase in the central core [108,122,123]

The existence of the prior nitride or carbo-nitride has a very strong effect on the nucleation and growth behaviour of the subsequent carbide. When the size of nitride or carbo-nitride particles exceeds a critical carbide nucleation size, MC-type carbides begin to grow on their surface and envelop them. Therefore, the newly precipitated nitride or carbonitride core within the carbide remains very small and cannot be detected by techniques including EPMA.[109] Final proof of this phenomena is that a carbide edge composition has been seen to differ from the carbide centre composition. The carbide edge contains less titanium, but is enriched with hafnium, while tungsten and tantalum contents often remain constant through the entire carbide.[109]

5.2. Experimental

5.2.1. Methodology

This investigation examined one design of high pressure turbine blade, referred to as blade Y, at various stages during manufacture and coating application, as detailed in *Fig. 5.5*. Blade Y, cast from CMSX-4, which was subject to various coating deposition techniques including platinum plating, vapour aluminising and TBC application through EB-PVD. Blade Y displayed a precipitate-rich band in the superalloy sub-surface region typically extending from the external surface to a depth of ca 100 – 200 µm deep. This feature, observed following vapour phase aluminising, detrimentally affected production yield since this new feature was unknown and potentially harmful.

Fig. 5.3 – macro images detailing research and development chemical vapour deposition furnace used in this work, outer bell retort (a), inner reaction vessel / retort (b), gas flow and furnace control (c), rig setup (d)

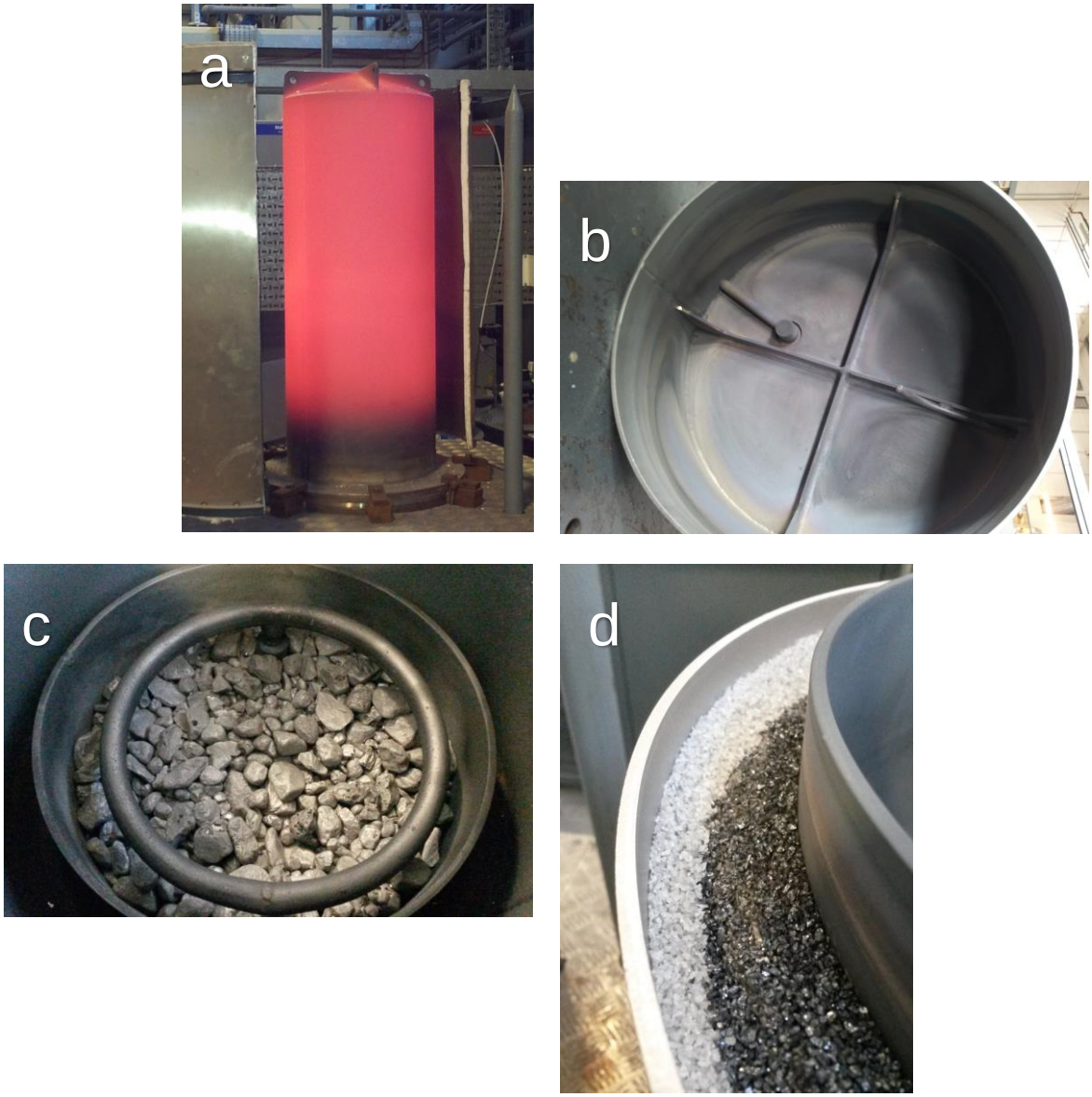

Fig. 5.4 – macro images providing further detail regarding CVD rig, outer retort immediately following a high temperature aluminising run (a), upturned lid of the inner retort / reaction vessel showing thermocouple inlet (b), inside base of the inner retort showing aluminising chips plus halide activator beneath inert gas distribution manifold (c), inner retort torturous gas seal with 20 mesh alumina– note discolouration following reaction (d)

It was therefore necessary to determine which materials came into contact with blade Y components during this process and how the precipitates form. Aluminising in this instance was carried out using the above-the-pack method, this is where chromium-aluminium chips are placed within the inner retort and coated in a small layer of aluminising activator, in this instance AlF_3. This set-up is seen in *Fig. 5.4 (c)* where the chips are sat beneath the inert gas distribution manifold which blasts the chips during the high-temperature process to aid circulation and agitation of the aluminising vapour cloud formed. This vapour cloud envelops the test pieces or components which are situated above the chips on racking or specifically designed tooling.

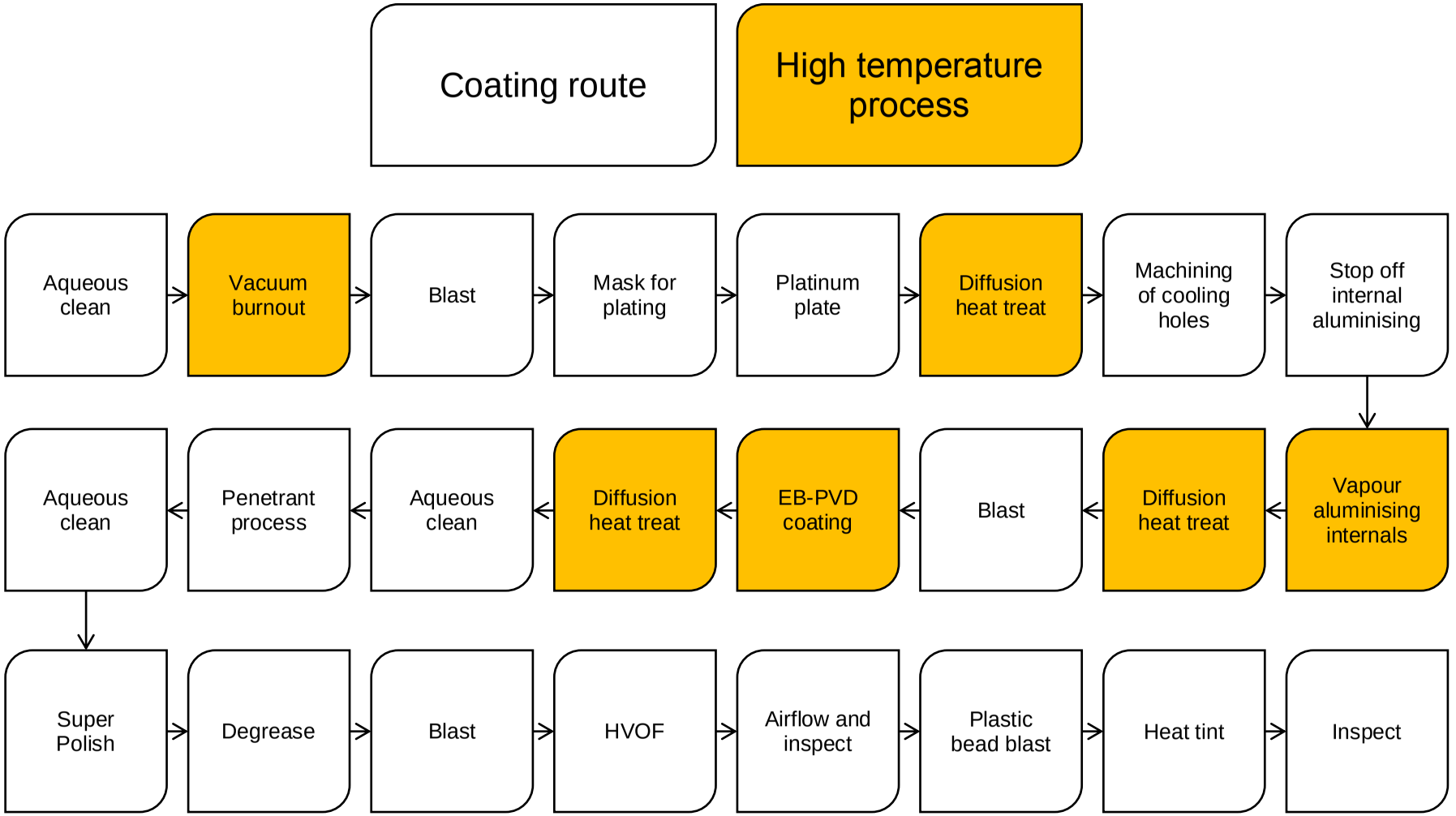

Fig. 5.5 –coating processing for a single-crystal turbine blade

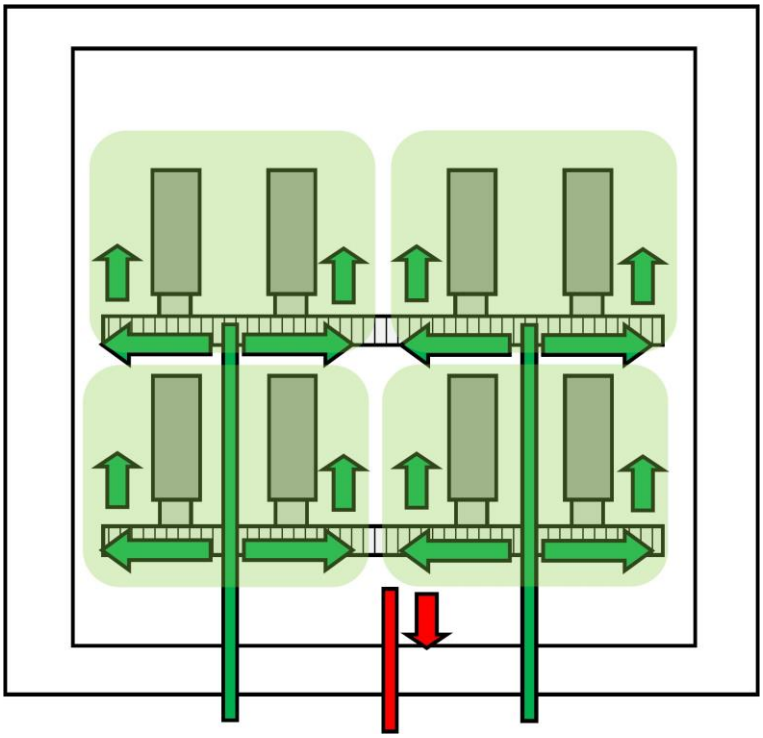

Fig. 5.6 – schematic detailing approximate location of turbine blades (dark grey) upon tooling suspended above the aluminising chips (striped trays). Green tube and arrows indicate argon gas flow into the retort, lifting aluminising vapours from the chips (striped trays) to envelop the parts. Green translucent boxes represent the aluminising vapour surrounding the parts. Red arrow and pipe indicates gas flow to exhaust.

Fig. 5.6 shows how blades are situated above the aluminising chips and how inert gas flows are used to circulate aluminising vapour generated at high-temperatures. *Fig. 5.7* details the thermal profile used in an 'extended' six hour high temperature aluminising run.

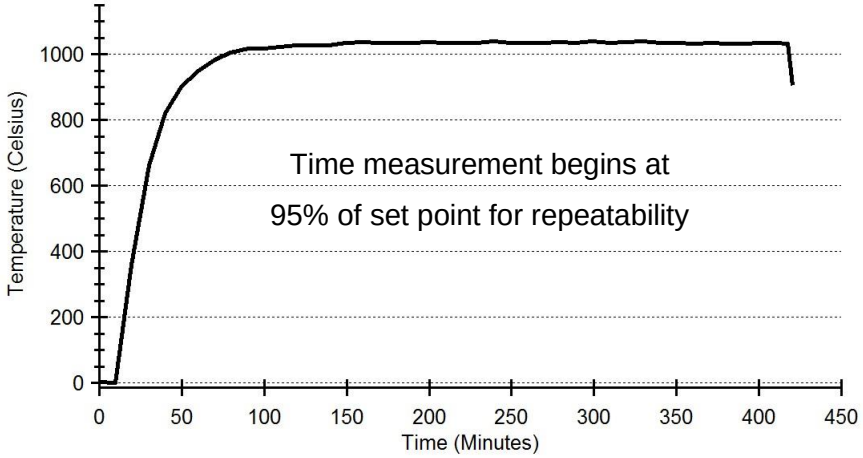

Fig. 5.7 – time / temperature profile taken from internal thermocouple upon the R+D CVD rig. A rapid climb in temperature is seen before a hold for 6 hours at 1030°C.

5.2.2. Microstructural characterisation

5.2.2.1. Metallographic preparation

Specimens were sectioned transverse to the blade long axis in order to provide an 'in-plane' view of the precipitate-rich band. Unless otherwise stated specimens were examined in the polished state and received no further etching or electropolishing treatments.

Cutting

Cut-off machine	Met – prep Cut-off wheels
Discotom – 5	Type FES or 2HA

Mounting – Met-prep conducto-mount

Grinding – (Direction of grinding is same-direction rotation)

Step	SiC grit paper + quantity	Lubricant	Force (N) – single 50mm samples	Time (s)	RPM
1	120 (2)	Water	35	120	150
2	180 (2)	Water	35	120	150
3	220 (2)	Water	35	120	150
4	320 (2)	Water	35	120	150
5	1000 (2)	Water	35	120	150
6	2400 (2)	Water	35	120	150
7	4000 (2)	Water	35	120	150

Polishing – (Direction of polishing is same-direction rotation)

Step	Abrasive	Cloth	Lubricant	Force (N) – single 50mm samples	Time (s)	RPM
1	1µm diamond	MD Nap	'Green'	35	360	150
2	0.04 µm OPS	MD Chem	Water	35	60	150

5.2.2.2. Optical microscopy

Olympus AX70 Provis optical microscope. Image capture system was Imagic. Magnifications used include, 5x, 10x, 20x, 50x and 100x. (*Not all displayed*)

5.2.2.3. Scanning electron microscopy

SEM images were taken at 15 or 20 kV using either a field emission gun (FEG), a FEI Nova NanoSEM FEG, a tungsten filament, Jeol XL30.

5.2.2.4. Energy dispersive spectroscopy

Jeol XL30 fitted with an EDS detector, running Aztec software from Oxford instruments

5.3. Results

5.3.1. Optical microscopy – sub-surface location

Optical microscope images using bright field illumination, *Fig. 5.8,* show the presence of the carbide-rich layer beneath the external surface of a fully manufactured high-pressure turbine blade. *Fig. 5.8 (a)* is a lower magnification image displaying the thermal barrier coating at the top, with the platinum bond coat beneath this and finally the underlying substrate nickel-based superalloy, CMSX-4, at the bottom. It is within the CMSX-4 that many tiny carbides have precipitated during the manufacturing process. *Fig. 5.8 (b)* and *(c)* increases the magnification and pinpoint carbides can be seen in greater detail with clear patterns visible in the relative placement of the precipitates within the pre-existing superalloy microstructure. These 'pinpoint carbides' are most akin to what the literature refers to as blocky morphology, only much smaller. Further inspection using the optical microscope reveals these carbides to be present only within the ca 150 µm thick sub-surface band shown in *Fig. 5.8* and are not to be located anywhere within the superalloy bulk.

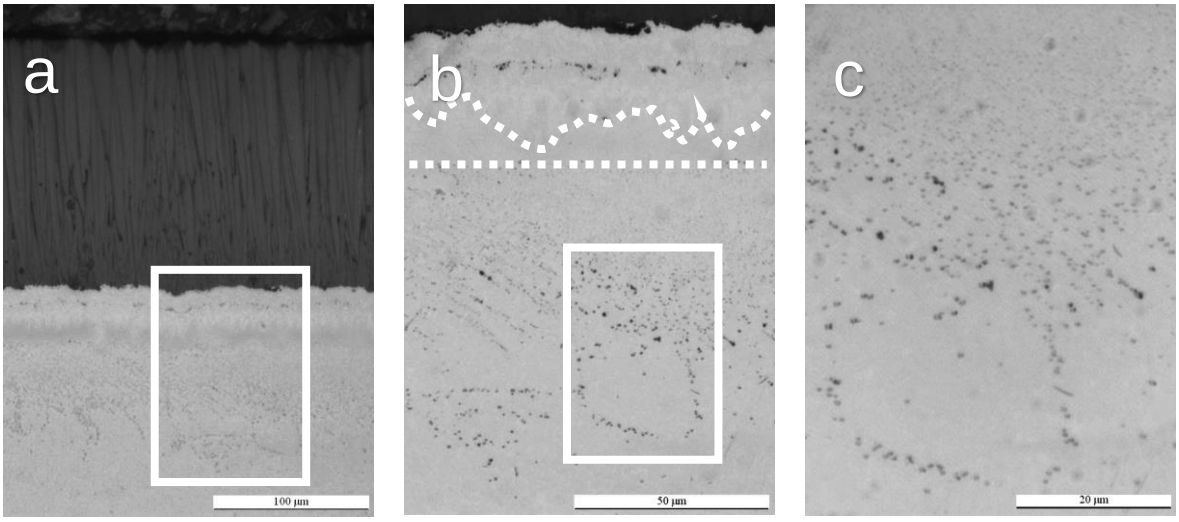

Fig. 5.8 – carbide-rich band present sub-surface, overview including TBC layer (a), higher magnification images (b) and (c)

Also visible within the optical images of *Fig. 5.8* is a carbide denuded region immediately beneath the diffused platinum layer and subsequent diffusion zone at the top of *Fig. 5.8 (b)*. There is a small, ca 25 µm, gap between what is termed the 'grit-line' which denotes the original surface of the component prior to platinum plating, and the onset of the carbide-rich layer. The final observation visible using the optical microscope is the apparent carbide size gradient within *Fig. 5.8 (c)*. Starting at the top of *Fig. 5.8 (c)* the carbides appear at their smallest, then, traversing into the substrate the carbides become less numerous but larger in size. Finally, upon reaching the bottom of *Fig. 5.8 (c)* the carbides are all but gone with only those largest precipitates located in regions of preferential growth being present.

5.3.2. Optical microscopy – proof of origin

To determine the origin of carbon for the sub-surface precipitation test buttons of CMSX-4 were partially coated in maskant ‘stop-off’ and exposed to an above-the-chips aluminising process. *Fig. 5.9* shows optical microscope images taken using dark-field illumination to better observe the presence and quantity of pinpoint carbides. *Fig. 5.9 (a)* shows the region of the button that was fully exposed to the aluminising atmosphere of the chemical vapour deposition rig and at the upper surface a ca 25 µm thick coating can be observed, it appears bright under these optical image capture conditions. There are no carbides observed beneath the aluminising coating deposition. *Fig. 5.9 (b)* moves further along the partially masked button to a region that despite having been covered with the maskant ‘stop-off’ has experienced the phenomena known as ‘bleed’. Bleed occurs when the maskant is not fully adhered to the surface of the component and aluminising vapour is able to chemically deposit, at a reduced rate, upon the poorly protected surface. Bleed is most commonly found at the edge of a masked region. In *Fig. 5.9 (b)* both the aluminising and carburising phenomena can be observed.

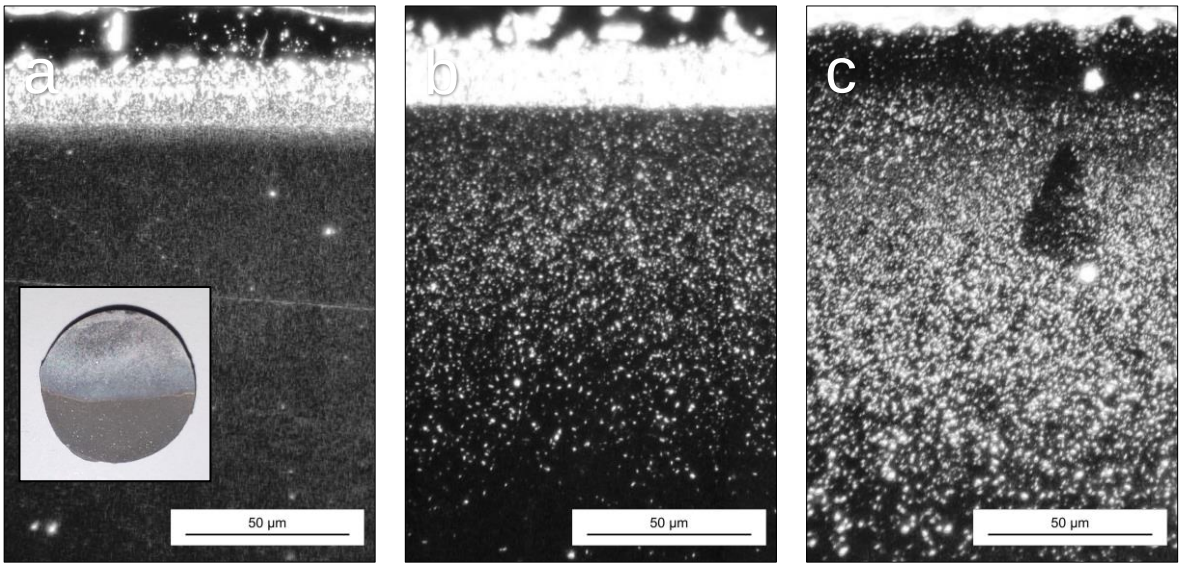

Fig. 5.9 – no carbides visible beneath aluminised layer (a), moderate carbide-rich band present sub-surface in the ‘bleed’ zone (b), severe carbide-rich band beneath wholly masked region (c), test button (insert)

Fig. 5.9 (c) is an optical micrograph detailing the density and thickness of the carbide-rich layer beneath fully adhered maskant. In this region there has been no opportunity for the deposition of aluminium since the surface was protected from the aluminising atmosphere by the well-adhered maskant upon the surface. As a result, the substrate CMSX-4 has precipitated a fully dense and thick band of carbides which strongly supports the maskant as being worthy of further investigation. The dark band at the top of *Fig. 5.9 (c)* features very small pinpoint carbides that are difficult to observe at this magnification.

In this experiment the maskant was applied to a CMSX-4 button before being placed within a vacuum furnace and subjected to a comparable heat treatment cycle to emulate the thermal conditions found within the aluminising chemical vapour deposition rig. As can be seen in *Fig. 5.10* removing the aluminising atmosphere of predominantly argon and replacing it with a vacuum results in a very thin layer of carbides was formed which was sparsely populated.

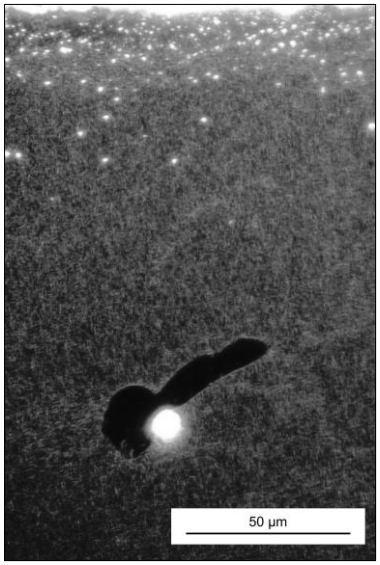

Fig. 5.10 - carbide-poor band beneath wholly masked region which has undergone thermal exposure in the vacuum furnace

5.3.3. Infrared spectroscopy

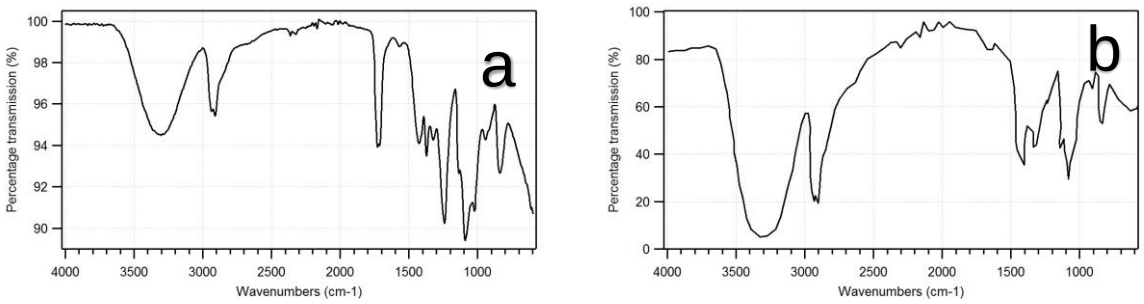

Fig. 5.11 – infrared spectroscopy results of the binder B-100 used to form the maskant M1™, proof of the presence of PVA (a), PVA catalogue reference (b)

Fig. 5.11 details the IR spectra taken of the B-100 binder used to form the maskant M1™ used in this work. After removing solvents the B-100 residue was analysed and found to contain almost exclusively PVA, poly vinyl alcohol.

5.3.4. Energy dispersive spectroscopy – powders

To better understand the relative makeup of the metal powders used within the maskants for the aluminising process a series of EDS point scans were undertaken. *Fig. 5.12* displays the BSE image which indicates the locations from where data was collected for the powder material designated M1™ used in intimate contact with the part to be protected. Spectrum 12 was a singular spectrum used to investigate the oxide-like filler material discovered as part of the powder mixture. Spectrum 12 shows that the filler material is accurately identified as alumina (Al_2O_3), this relatively inert material finds use in reducing the activity of the metallic constituents and hindering the sintering of individual metallic particles together. Spectra 1 to 10, 13, 14 and 15 are individual spectra taken from the metallic constituents of the maskant powder, they were averaged to give the most accurate reading regarding the elemental composition of the powdered metal alloy. The results for M1™ are as follows, nickel ca 62 at. %, chromium ca 2 at. % and aluminium ca 36 at. %. This composition is favoured to enable a material that partially sinters to form an impermeable barrier layer to resist the passage of aluminising vapour to the surface. The addition of the alumina is likely to encourage only partial sintering and enable removal of the maskant post aluminising.

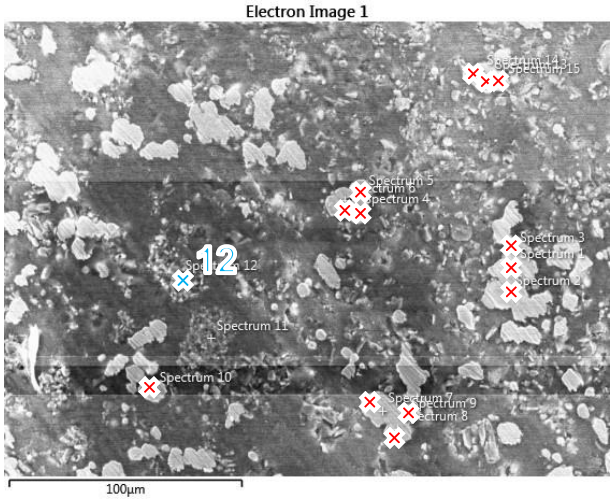

Wt. %	Ni	Cr	Al	O
Spectrum 12	-	-	55.8	44.2
Spectrum 1 – 10, 13, 14 and 15 (average)	77.4	2.3	20.3	-

At. %	Ni	Cr	Al	O
Spectrum 12	-	-	42.8	57.2
Spectrum 1 – 10, 13, 14 and 15 (average)	62.4	2.1	35.5	-

Fig. 5.12 – M1™ elemental compositions identified above in weight and atomic pct

5.3.5. Scanning electron microscopy – carbides

Scanning electron microscopy backscatter (SEM-BSE) images show how the sub-surface carbide layer is formed (*Fig. 5.13*). Backscatter mode provides clear elemental contrast between the darker γ/γ' microstructure and the bright white carbide precipitates enriched in heavy elements. At the top of *Fig. 5.13 (a)* the diffused platinum layer can be observed immediately above the carbide-denuded region before the onset of the carbide-rich layer. As you descend from the top of the carbide-rich layer in *Fig. 5.13 (a)* the densely packed carbides begin to thin and eventually carbides are clearly seen having formed on energetically favourable paths through the pre-formed γ/γ' microstructure of the nickel-based superalloy CMSX-4. By the halfway point in *Fig. 5.13 (a)* the carbides appear to have formed in straight lines with the orientation dictated by the underlying superalloy microstructure. *Fig. 5.13 (b)* further displays the presence of densely packed carbides though, in this instance, the morphology has changed from the familiar pinpoint carbides to an alternative platelet structure which appears to favour a variety of growth orientations relative to the underlying superalloy substrate. *Fig. 5.13 (c)* again displays the nominal arrangement of carbides within the sub-surface layer, this time without additional ordering into straight lines or with additional pathways of preferential formation. There is a continuous layer of carbides with a size gradient starting with the most numerous, very smallest, precipitates at the uppermost surface but upon moving to the bottom of the band the carbides are at their largest.

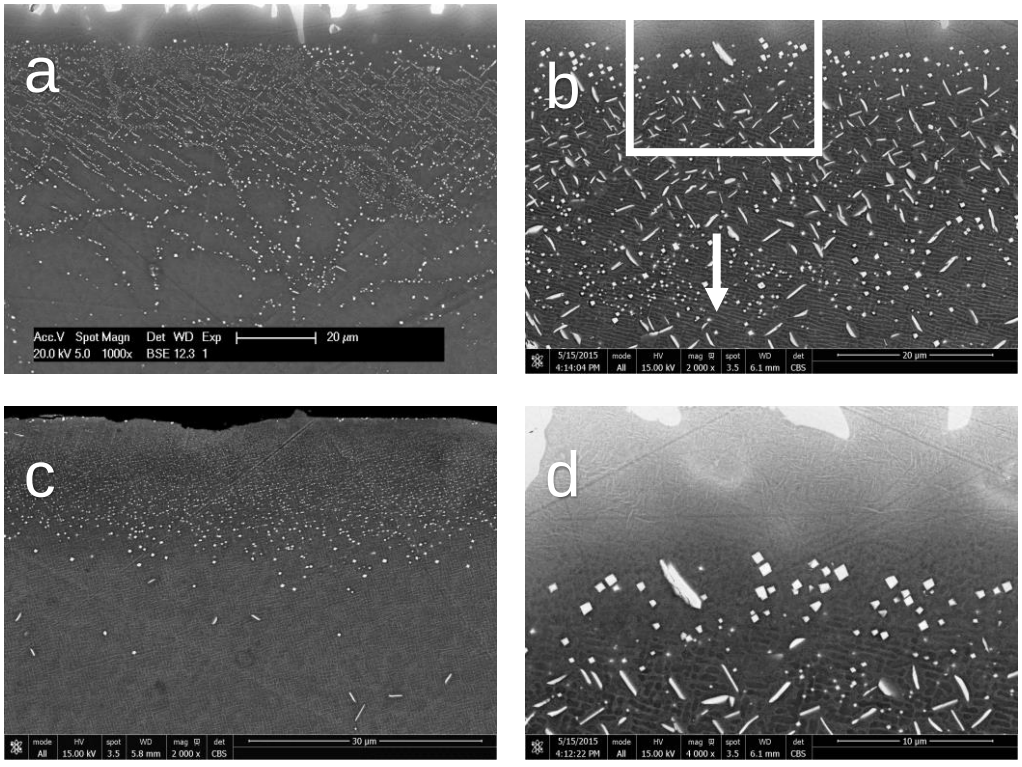

Fig. 5.13 – SEM-BSE micrographs of sub-surface carbides focussing on, residual segregation affects placement (a), possible orientation relationship (b), clear size gradient (c) and carbide denuded zone (d)

This size/quantity phenomena has been noted in most observations, firstly the size gradient with the smallest carbides at the top and the largest at the bottom closest to the substrate and secondly the preferential formation of the most carbides at the uppermost region of the carbide-rich layer with fewer observable carbides towards the bottom of the layer.

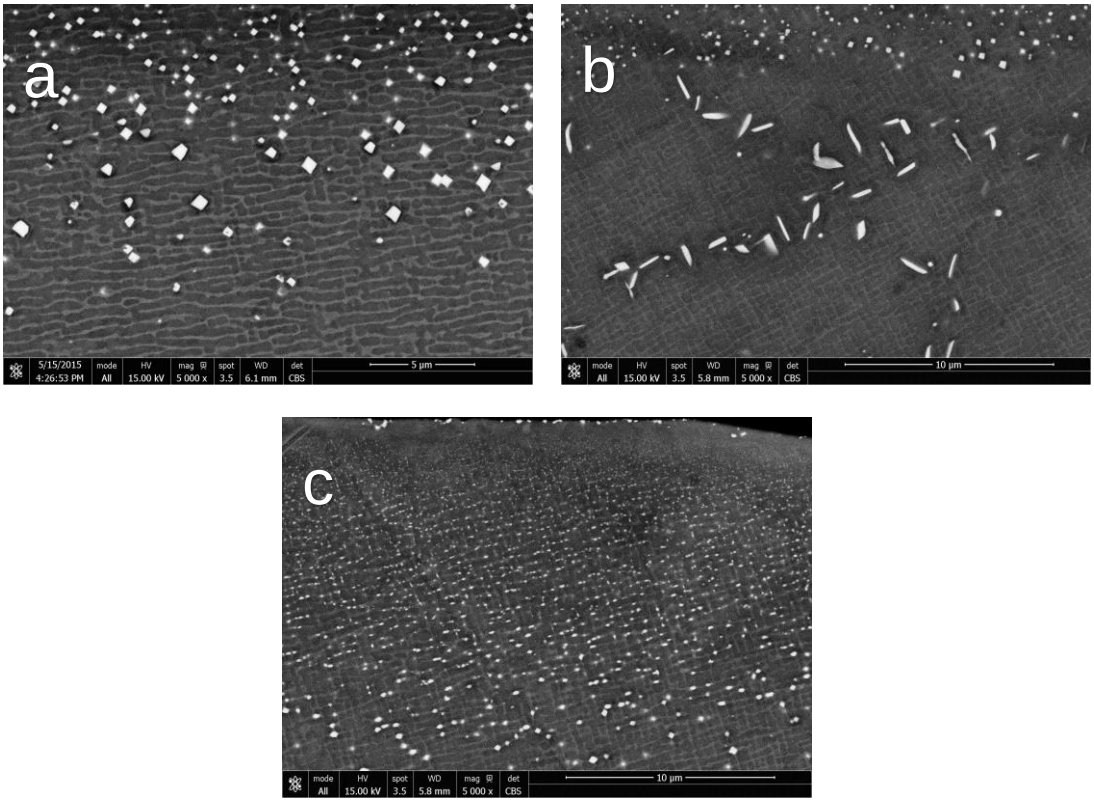

Fig. 5.14 – SEM-BSE micrographs of sub-surface carbides focussing on, larger more defined carbides (a), thin platelet carbides within prescribed pathway (b), densely packed pinpoint carbides (c)

Fig. 5.14 shows further SEM-BSE images of the carbide-rich layer with additional emphasis on the varied morphologies of carbides formed and their relative location within the superalloy microstructure. *Fig. 5.14 (a)* focusses upon what has been described as the nominal pinpoint carbides which are most frequently seen and vary in both size and quantity depending upon depth from the outermost surface into the bulk substrate. *Fig. 5.14 (b)* shows the second carbide morphology of platelets and how in this particular SEM image the precipitates have formed within specific regions of the superalloy microstructure which appear aligned along what are known as ‘river-lines’, they are surrounded by γ’ since they have taken all of the local heavy elements and denuded the immediate region, since the matrix is still a single crystal the individual precipitates have similar orientations to one another. *Fig. 5.14 (c)* displays the densely packed pinpoint carbides.

Fig. 5.15 shows high magnification SEM-BSE images regarding preferential carbide formation within the superalloy microstructure. *Fig. 5.15 (a)* shows pinpoint carbides forming in a chain orientated to the direction of the γ channels running through the microstructure.

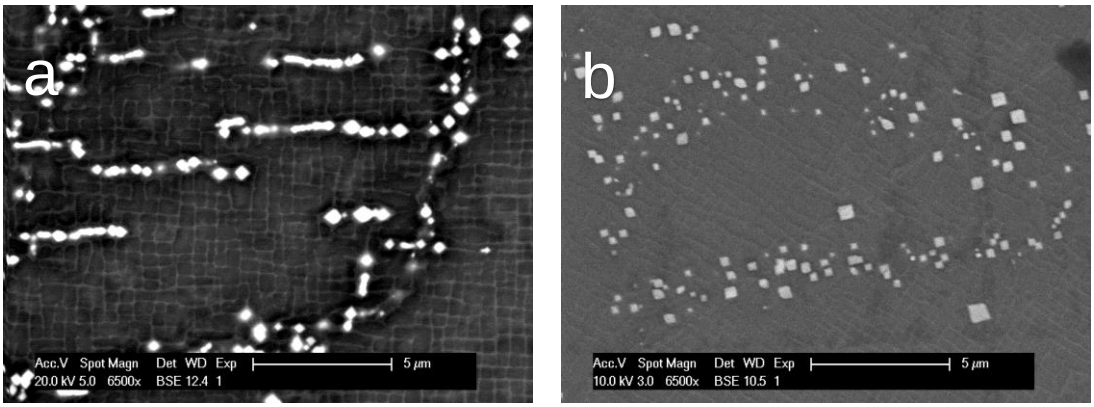

Fig. 5.15 – SEM-BSE micrographs of sub-surface carbides focussing on, small cubic morphology pinpoint carbides sat in chains within the γ channels (a), more pinpoint carbides displaying clear preferential formation patterns in nominally the same underlying superalloy microstructure (b)

This observation in *Fig. 5.15 (a)* is immediately adjacent to a second alternative observation on the RHS of *Fig. 5.15 (a)* which is a collection of carbide precipitates which are again aligned. Despite these carbides forming closely together they appear to be individual precipitates that have formed adjacent to one another and not an interconnected network. *Fig. 5.15 (b)* shows extensive preferential formation of carbides within the superalloy microstructure with no clear distinguishing features to discern why carbides have formed preferentially in the circular region and not at the centre of the feature. Both *Fig. 5.15 (a)* and *(b)* provide the first evidence of how these cubic pinpoint carbides are themselves orientated within the γ/γ' microstructure with the four vertices pointing along the γ channels. This orientation is consistent with all cubic pinpoint carbides displaying this rotation with regards to the superalloy microstructure without exception, the largest carbides enable the easiest observation of this phenomena.

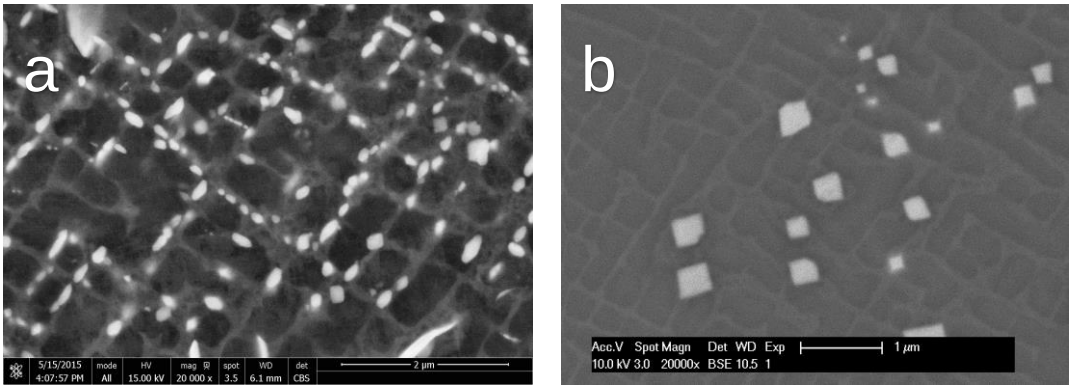

Fig. 5.16 – SEM-BSE micrographs of small proto-carbide morphology within the γ channels (a), pinpoint carbides displaying preferential orientation relationships with superalloy microstructure (b)

Fig. 5.16 provides further clarification on the relative positioning of these pinpoint carbide precipitates within the γ/γ' microstructure. *Fig. 5.16 (a)* at a magnification of 20,000 times shows how the smallest proto-carbides, forming close to the external surface of the test piece are more globular in shape having not grown to the point where the full morphology is displayed, these elongated globules appear to sit within the γ channels and are confirmed as being individual precipitates and not an interconnected network. *Fig. 5.16 (b)* shows the less numerous carbides at a greater depth within the nickel-based superalloy. These less numerous pinpoint carbides are larger in size and have developed further having reached the limit of the γ channel they have begun to consume surrounding material including both the γ and γ' phase. Upon further growth the characteristic cubic nature of the precipitates begins to develop.

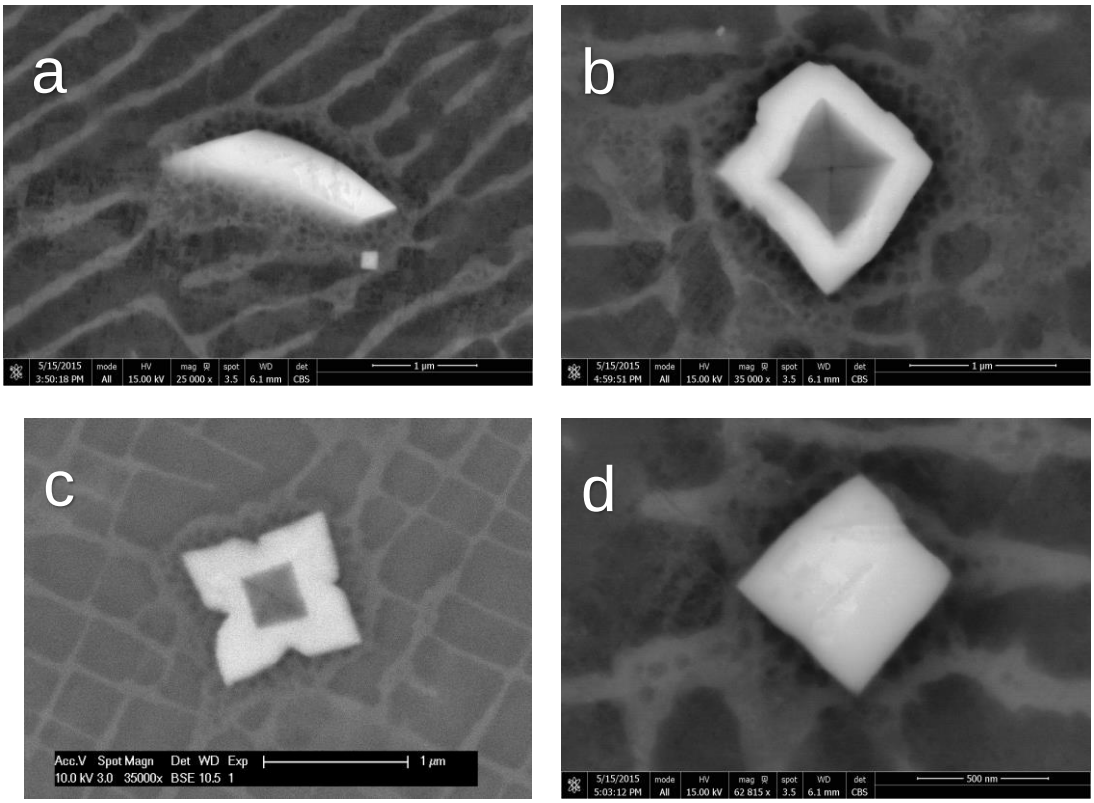

Fig. 5.17 – SEM-BSE micrographs of sub-surface carbides focussing on, platelet carbides (a), pinpoint carbides displaying internal structure (b), further internal structure as well as evidence of arm growth (c), cubic morphology (d)

Fig. 5.17 shows a series of carbides at high magnification using SEM-BSE. *Fig. 5.17 (a)* shows a platelet carbide which has formed in a region of γ/γ' microstructure which has undergone rafting. Of note is that the γ/γ' microstructure halo immediately surrounding the carbide has been thoroughly disrupted as the carbide has grown and removed heavy elements from the surrounding structure. The γ is more apparent and the remaining γ' is small (ca 10 nm) and globular. The platelet carbide appears to sit within the microstructure

protruding at an angle suggesting an orientation relationship with the γ/γ’ matrix. *Fig. 5.17 (b)* shows a well-developed pinpoint carbide which appears to feature two distinct zones. The first central zone appears to be roughly cubic in plane but features a distinct cross shape at its core. This darker region under BSE conditions suggest a carbide core that consists of lighter elements and in three dimensions is likely to resemble an octahedral crystal habit. The second outer shell zone is much brighter under BSE conditions indicating a higher concentration in the heavier elements that have been absorbed by the growing carbide from the surrounding matrix during growth. This second outer shell layer appears to have grown from the inner core and is likely to have precipitated from it. Again the surrounding γ/γ’ microstructure halo has been disrupted as elements have been preferentially absorbed by the growing carbide leaving the miniscule globular γ/γ’ to surround the pinpoint carbide. *Fig. 5.17 (c)* shows another well-developed pinpoint carbide. There are many similarities to the precipitate seen in *Fig. 5.17 (b)* however there is additional evidence of growth from the vertices of the original cubic carbide. Once the carbide had reached its full shape in order to continue growth the preferred orientation was to develop in a dendritic fashion growing from the vertices and create this ‘flower’ or four-pointed star arrangement. This particular carbide shape is unusual but provides insight in how these precipitates develop and continue to grow. *Fig. 5.17 (d)* shows one final high magnification image of a pinpoint carbide, this time the precipitate appears outwardly to be a solid, single phase precipitate and it is not possible to determine whether this particular carbide was instigated in the same manner, by an octahedral carbide of a different elemental constitution. This carbide also features a surrounding halo of disrupted γ/γ’ microstructure, though in this instance to a slightly lesser extent.

5.3.6. Energy dispersive spectroscopy – carbide mapping

Following SEM analysis a carbide was selected for non-quantitative elemental mapping to better understand the relative concentration and distribution of elements both within and around the carbide. As *Fig. 5.18* shows a number of elements are absent from the carbide. The elemental map for nickel and aluminium show clear voids suggesting no incorporation within the precipitate structure, these elements are not ready carbide formers. The maps for chromium and cobalt show an interesting effect which seems to support these elements not being incorporated into the carbide but being concentrated within the disrupted γ/γ' microstructure halo which sits on all sides of the carbide. This observation is acceptable for cobalt yet chromium is usually well known as an able carbide former. The elemental maps for molybdenum, tantalum, titanium and carbon all show strong correlation at the centre of the image and are the likely ingredients of the well-developed pinpoint carbide precipitate examined. The titanium map is the most noteworthy, the concentration of titanium being most heavily concentrated at the carbide core, falling in potency at edges and vertices.

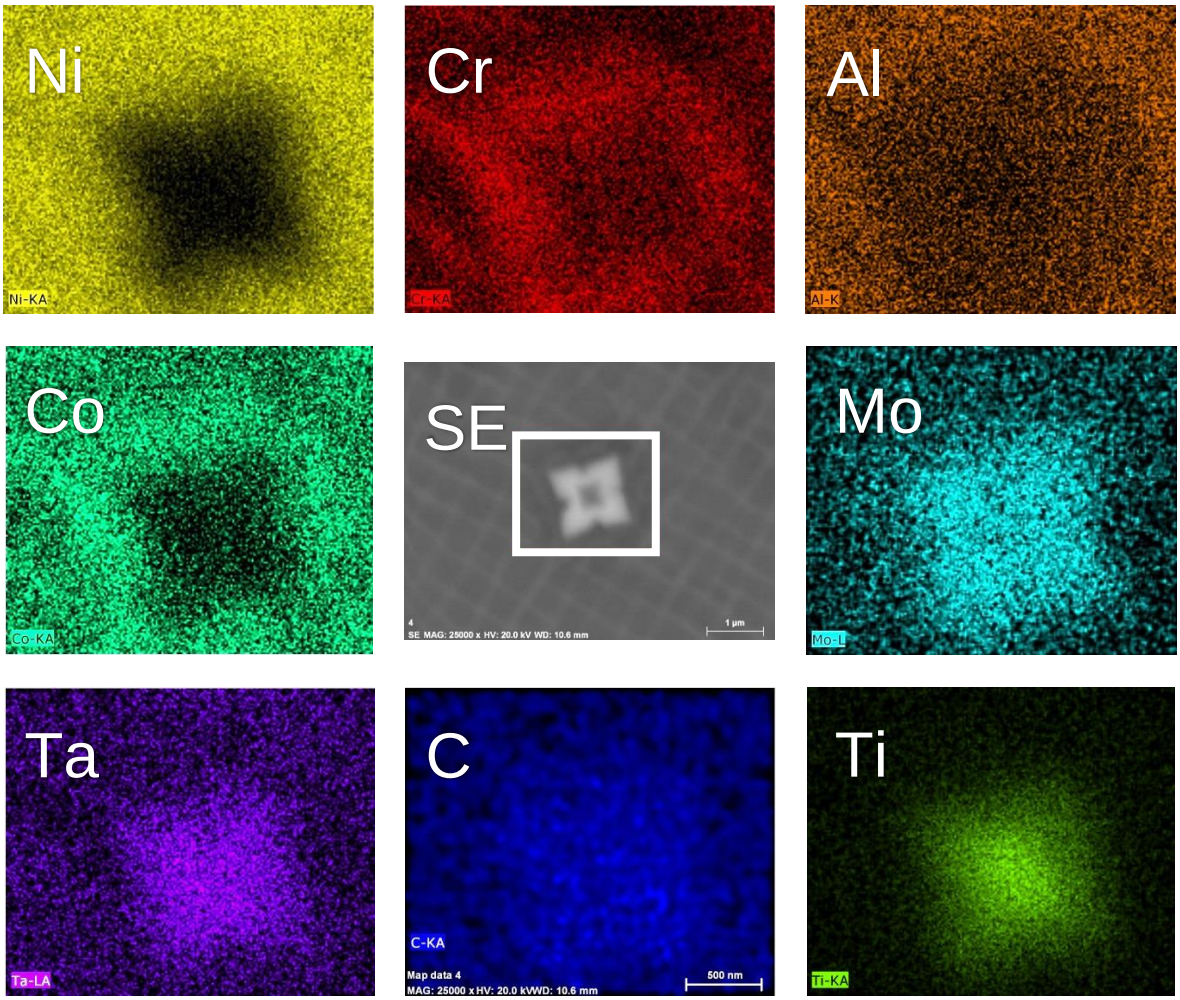

Fig. 5.18 – EDS qualitative mapping of well-developed pinpoint carbide with internal structure

5.3.7. Energy dispersive spectroscopy – carbide quantitative mapping

Further to the elemental mapping of 5.3.6 a grid of individual point scans was conducted upon a carbide (*Fig. 5.19*), using EDS to enable the generation of a quantitative map which would provide more information regarding relative placement and concentration of elements.

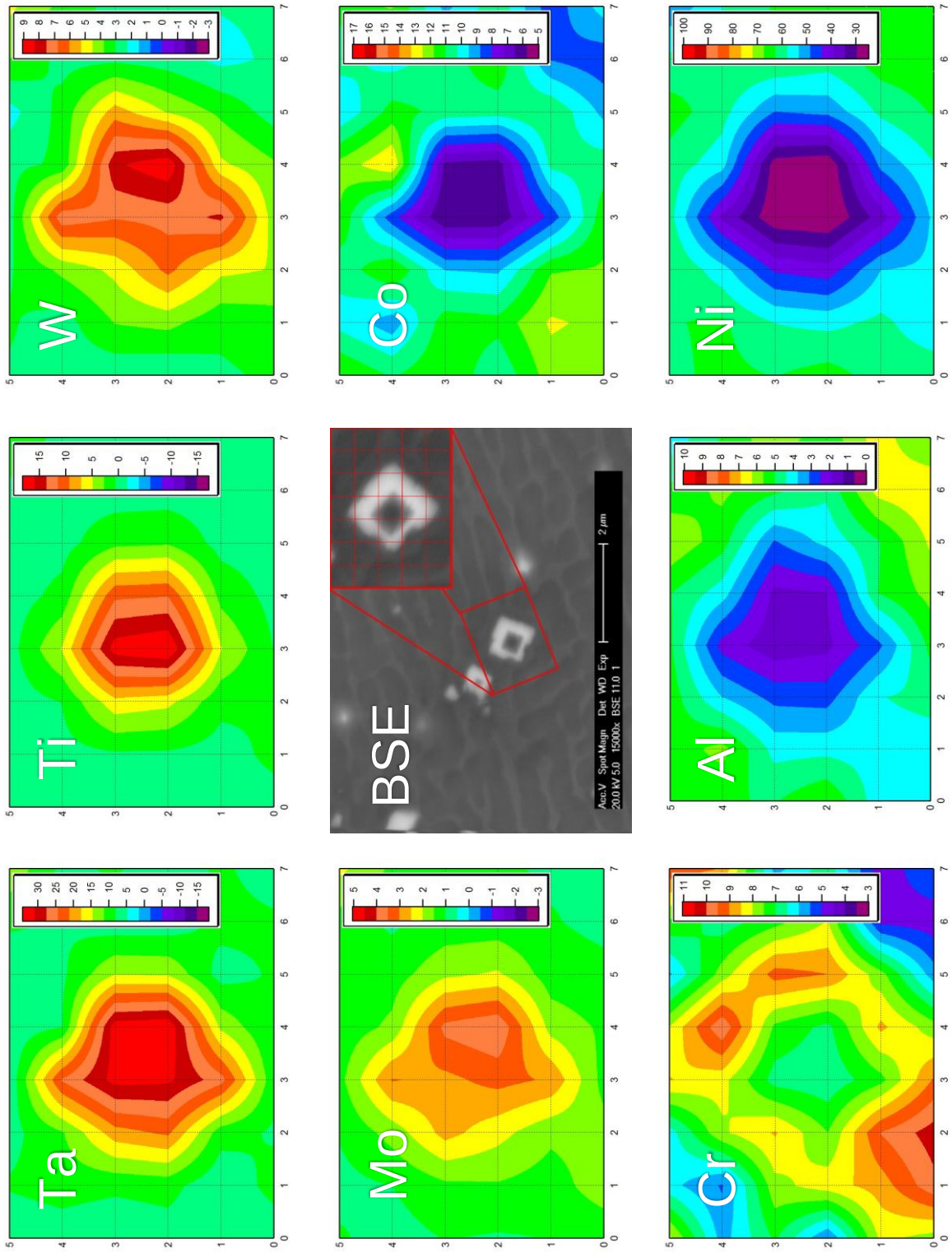

Fig. 5.19 – EDS quantitative mapping of well-developed pinpoint carbide with internal structure

Fig. 5.19 displays maps detailing the elements that both form the carbide and that have been displaced by the precipitates formation. Of the carbide-forming elements; tantalum, titanium, tungsten and molybdenum it is the tantalum that is the most concentrated. The tantalum map clearly shows heavy concentration, ca 25-30 wt. %, within the entire carbide precipitate. This is complimented by the titanium map which at its peak shows a concentration of ca 15 wt. %. Titanium is of particular interest since its concentration appears to be focussed more to the left hand side of the carbide than the right hand side. At this point it is important to note that the carbide analysed via the grid point method is displayed at the centre of *Fig. 5.19* and can be seen to consist of the same two zones, the inner dark core and the outer bright white shell zone described and discussed regarding *Fig. 5.17 (b)*. Of the four most centrally located data points tantalum registers equally likely suggesting that both the central core and the outer shell are made predominately of this element. Titanium appears to be focussed more upon the left hand side which suggests that titanium is more the element of choice for the initial carbide growth potentially forming the inner core octahedral structure before there is a shift towards an alternative favoured carbide chemistry. To expand on this point both the tungsten and molybdenum maps show a favourable increase in concentration on the right hand side of the carbide structure where the data is likely more heavily influenced by the bright white outer shell zone. The maps for the elements nickel, aluminium and cobalt mirror the results from the non-qualitative mapping and display a void whereby these elements have been displaced. Finally the map for chromium is especially interesting, it appears to show a higher concentration in the halo region surrounding the carbide and only slight decreases on the standard background concentration of CMSX-4. This suggests that some chromium is potentially partially incorporated within the carbide but that some chromium has been displaced and relegated to the surrounding region to sit within the disrupted γ/γ’ microstructure halo.

5.3.8. Transmission electron microscopy

To compliment the elemental mapping of 5.3.6 and quantitative mapping of 5.3.7 a TEM liftout was performed upon a carbide containing sample (*Fig. 5.20*), using TEM-based EDS to enable the generation of a high magnification series of elemental maps which provide information regarding the exact placement of elements both in and around the carbides.

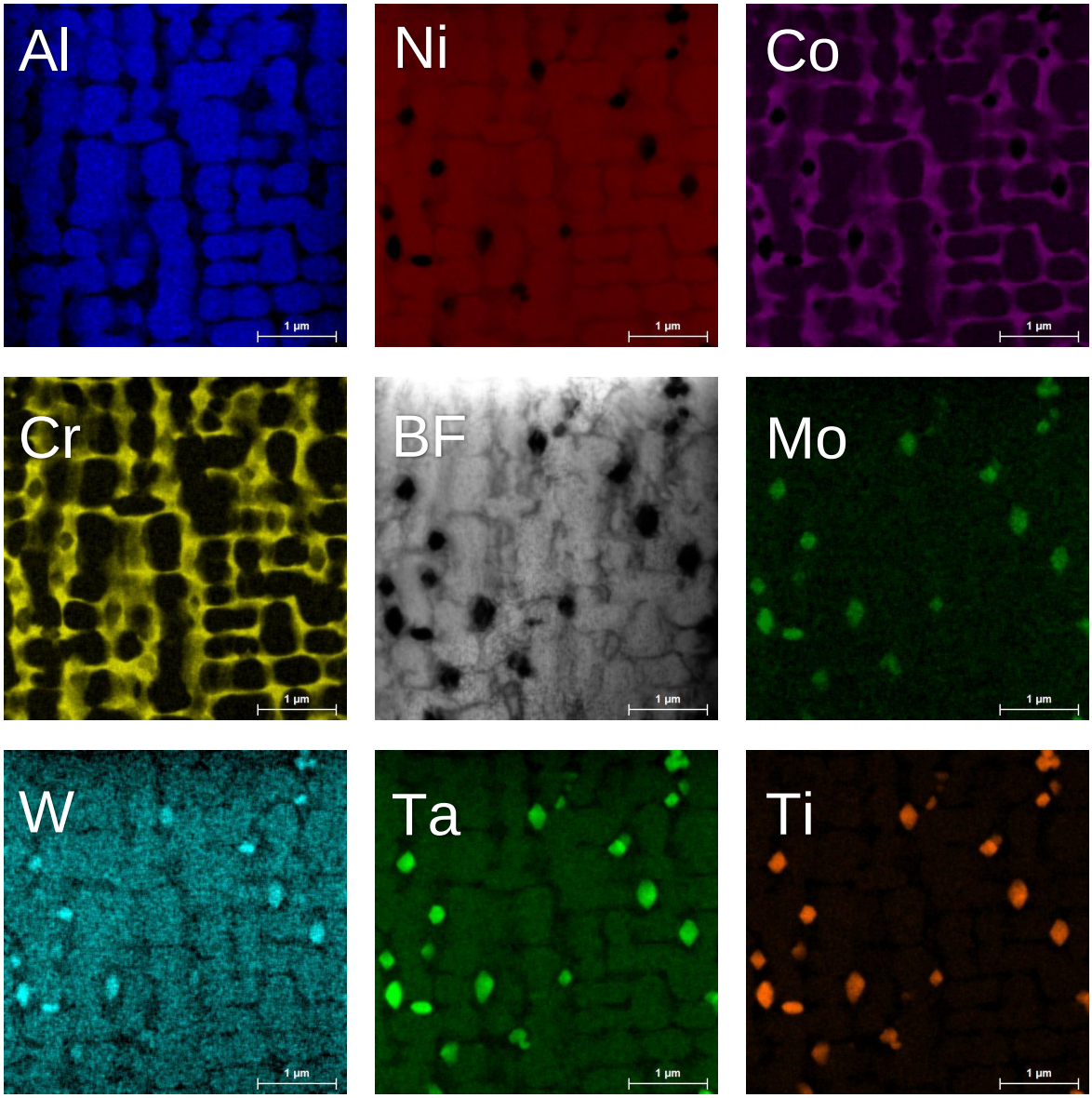

Fig. 5.20 – TEM elemental mapping of pinpoint carbides

5.4. Discussion

5.4.1. Process outline

Turbine blades which undergo the aluminising process require masking before deposition to actively select which parts of the component are coated. A high pressure turbine blade aerofoil will receive an aluminising coating but does not require coating upon the firtree root. Aluminising the firtree would be detrimental and unnecessary. Due to the 'stop-off' maskant material being a proprietary composition work was undertaken to determine the identity of the carbon polymer chain, this was found to be Poly Vinyl Acetate (PVA) (*Fig. 5.11*). In a paper by Voorhees et al. [124] the thermal degradation of polymers are examined. Voorhees goes on to describe the degradation in two steps, there is the loss of water and small, volatile compounds and then there is the breaking of long alkene chains to form a variety of aromatic compounds.[124,125] Thermo Gravimetric Analysis and Differential Thermal Analysis confirmed that PVA begins thermal degradation at approximately 120°C with an upper limit of 290°C. Eventually the polymer chain began to oxidise and resulted in mass loss at 340°C. Finally, following the oxidation phase the alkene degradation was found to occur at approximately 400°C.

Carbides form during the aluminisation of the blade, specifically in regions masked to avoid coating. The temperature profile of the CVD rig used is displayed in *Fig 5.7*. The PVA, in the maskant is the binder for the slurry system to hold the metal particles together. As the polymer degrades carbon is released and diffuses into the alloy. PVA undergoes rapid thermal degradation between 300 and 500°C during the ramp to CVD processing temperatures, typically featuring an ultimate hold of 1030°C. Carbon adsorbs onto the surface of the alloy and rapidly diffuses through the material via interstitial diffusion. The total average depth of carburisation measured from the surface was ca 110 μm. There is a characteristic carbide free band adjacent to the surface. An attempt to reproduce the effect by annealing under vacuum for the same time and temperature led to different results. The level of carburisation was greatly reduced as seen in *Fig 5.10* with an average depth of ca 25 μm and no carbide free band at the surface.

When the expected penetration depth, x, of the carbides at the aluminising temperature of 1030ºC is calculated using the simple formula:

$$x = \sqrt{Dt}$$

D is the diffusion coefficient for carbon in nickel and t is the annealing time of 6 hours, the result was surprising. Using a value of D = 4.4x10 $^{-7}$ cm^2 s^{-1} [126] for the diffusion coefficient at 1030ºC and t = 21,600 s this gives a depth in excess of 1 mm whereas even in the worst case the measured value is 1/5 of this. Thus the surprise is not so much that carbides form but that there is so little observed. Furthermore in a vacuum the depth is 1/20 of that

calculated. This suggests that carbon is not present at the surface throughout the entire anneal and that carburisation occurs during a brief period whilst the PVA is degrading and is removed by the pumping system but before the carbon diffuses away from the superalloy surface. This would be consistent with the observation that the much greater carburisation is observed during annealing under pressure of argon or hydrogen than under vacuum. Assuming a depth of 50 μm consistent with the vacuum anneal this suggests a dwell time on the surface of ca 60 s in vacuum, and using 200 μm, of 15 minutes in argon at an isothermal temperature of 1030°C.

The carbide free band seen during carbide formation under positive pressure is also interesting: there is no band when the vacuum furnace is used to heat the test piece. This evidence suggests that after the evaporation of PVA and diffusion of carbon into the specimen the process reverses and the carbon evaporates by backward diffusion towards the surface. The resulting carbide zone will be the superposition of the initial carbon ingress followed by the decarburisation. This is complicated by the formation of the carbides that clearly take a finite time to grow from the super-saturation of carbon. The initial distribution should follow an error function with a maximum value determined by the solubility of carbon in nickel at 1030°C. Carbides grow from the dissolved carbon and are thus more resistant to de-carburisation. Once the carbon on the surface has gone, the carbon content drops from the surface to produce a maximum dissolved carbon concentration a short distance from the surface. In the case of the testing in gases this produces rather more carbides, deeper in the material, than the vacuum tests; specifically, a carbide free band with the peak density of carbides formed at a depth of between ca 50 and 70 μm and a total depth of ca 110 μm. The exact distribution is complicated to calculate mainly because the visible trace left depends on how fast the carbides nucleate and grow.

Several scenarios regarding carbon ingress have been identified and explored using finite difference methods. Assuming carbon influx begins at 500°C there is a 25 minute window before 900°C is reached which has been taken to be the temperature where carbides begin to precipitate. Depending upon when the amount of carbon is reduced at the surface will define when movement of dissolved carbon will begin to flow both out of the alloy and into the material itself. *Fig. 5.21* shows the three scenarios explored and the 20 minute influx of carbon coupled with 5 minutes of diffusion is the closest to the depth of carburisation seen in *Fig 5.8 (a).* This approach was taken since it is difficult to determine when carbon levels are diluted and ingress stops.

5.4.2. Calculations

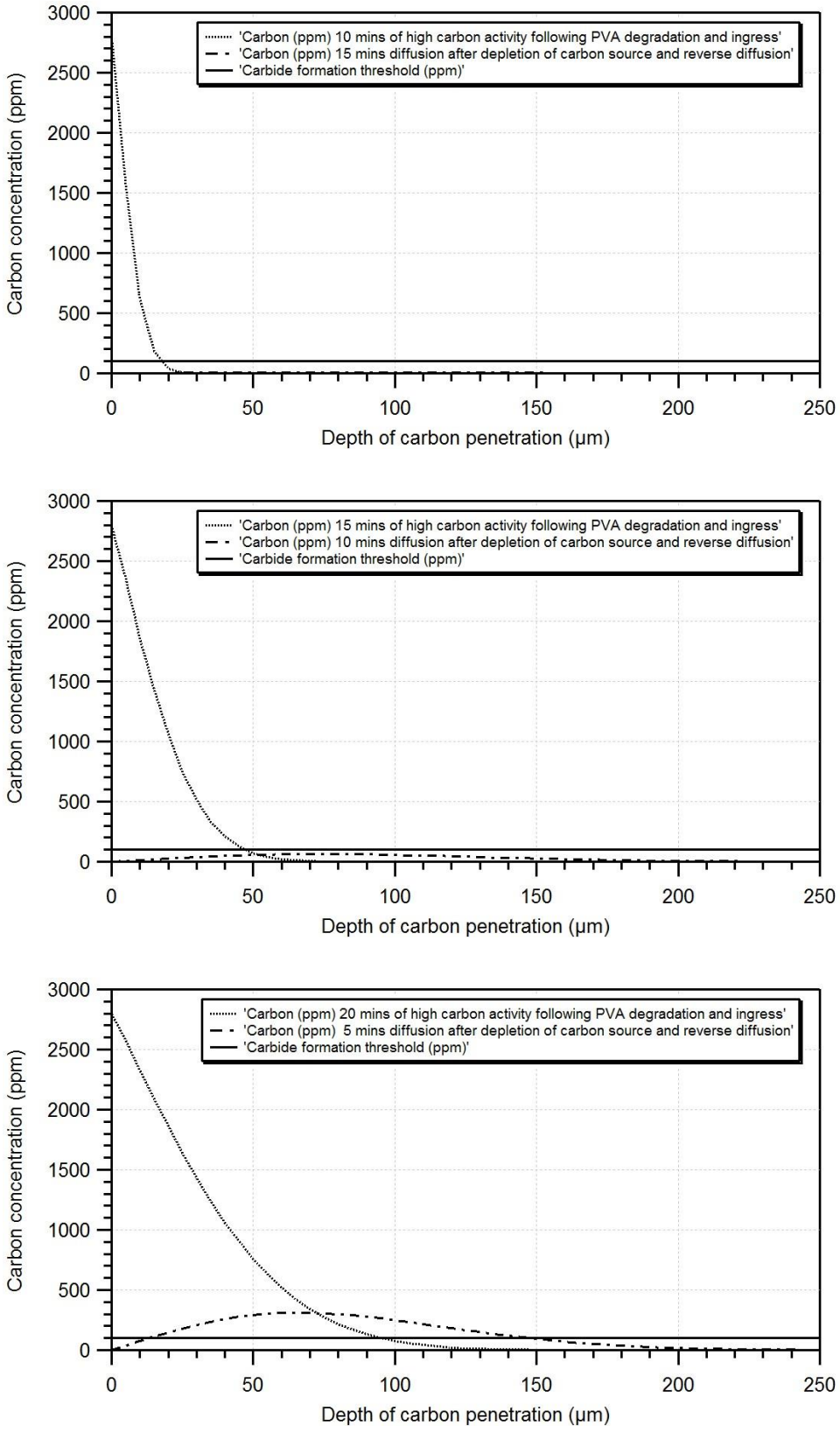

Fig. 5.21 – results of finite difference calculations regarding sub-surface concentration of carbon within the superalloy CMSX-4 during the aluminising process

After examining the thermal traces of the aluminising process observed in the experimental of this chapter there were three scenarios outlined regarding the availability of free carbon to move dynamically through the superalloy matrix and begin the process of sub-surface carbide formation *(Fig. 5.21)*. Once the scenario was outlined a finite difference equation was created and using an excel spreadsheet this simple calculation provides an approximate idea of the amount of carbon available in this subsurface region during the aluminising ramp to the holding temperature of 1030°C. Assumptions included for this calculation include the maximum carbon concentration of 3000 ppm, based on solubility limits for a nickel-based superalloy and a threshold of only 100 ppm necessary for the formation of carbides once the appropriate temperature is reached. In this scenario the starting temperature for the diffusion model was 500°C since beneath this temperature the carbon is likely still contained within the hydrocarbon chains of the PVA molecules and unavailable to begin interstitial diffusion through the superalloy matrix. The upper threshold for the model is the temperature 900°C above which the presence of carbon in the sub-surface region in concentrations above the stated 100 ppm will in all likelihood lead to the formation of the carbides previously explored. The diffusion coefficient used for this work was taken from research which measured how rapidly carbon diffused through pure nickel.[126] The research and development CVD rig available for this work has a relatively rapid climb to holding temperature and therefore only takes ca 25 minutes to climb from 500°C to 900°C before eventually plateauing and then holding at 1030°C. The three scenarios therefore include a period of what is termed ‘high carbon activity’, this being the period of time passing before the concentration of carbon freed from the PVA molecules external to the superalloy drops to a level that no longer supports the active diffusion gradient which leads to ingress into the alloy from outside. Following this ‘high carbon activity’ period there is time available for the carbon that has collected in this sub-surface region to diffuse back out of the alloy or deeper into the bulk where its concentration is too low to form additional precipitates. In the first scenario after 10 minutes of high carbon activity there is an additional 15 minutes of increasing temperature conditions in which the collected carbon can diffuse away. Scenario 1 is presented in *Fig. 5.21 (a)* and shows that in this instance the small amount of carbon is reduced to practically zero through the additional time at temperature. Scenario 2 is 15 minutes of ‘high carbon activity’ followed by the remaining 10 minutes of diffusion time to displace the carbon that has collected, this is shown in *Fig. 5.21 (b)*. This second scenario, though closer, is still not able to retain enough carbon close to the surface following the high temperature diffusion period to trigger the instigation of carbide precipitation. The third scenario proposes that there is sufficiently high levels of carbon available externally to the superalloy that for a 20 minute period from crossing the 500°C threshold that carbon is actively moving into the superalloy substrate.

Therefore the remaining 5 minutes is used to diffuse this carbon away yet when the 900°C upper threshold is crossed there is still sufficiently high levels of carbon to suggest that carburisation is indeed likely. This third scenario is presented in *Fig. 5.21 (c)* and shows that a region starting from 0 μm (i.e. the external surface) to a depth of ca 150 μm this concentration of carbon at 900°C is likely to provide conditions that enable the formation of carbides within the sub-surface region.

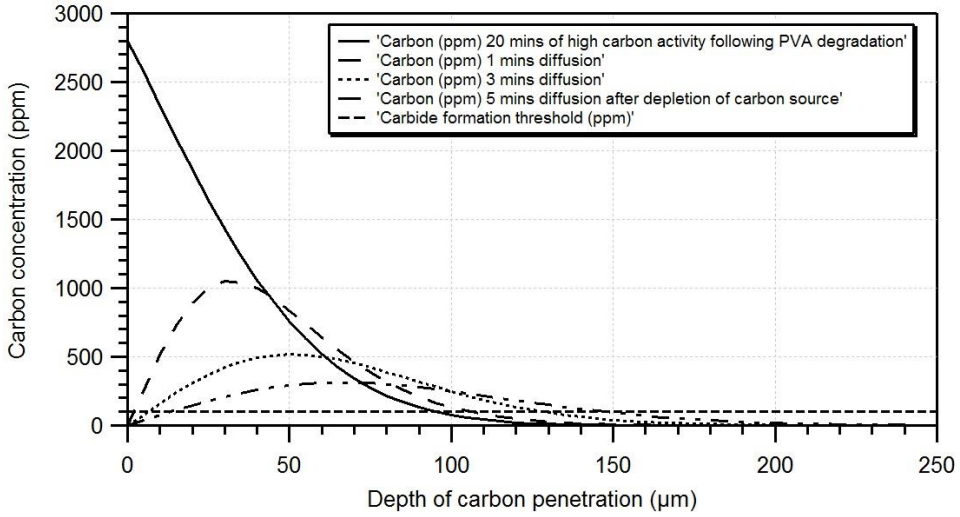

Fig. 5.22 – results of finite difference calculations regarding sub-surface concentration of carbon within the superalloy CMSX-4 during the aluminising process, scenario 3 – 20 minutes high activity and 5 minutes of diffusion time

Building upon the premise discussed regarding diffusion of carbon through the nickel superalloy the *Fig. 5.22* graph shows how the diffusion profile looks after 20 minutes of 'high carbon activity' and how this transforms once the source of carbon is removed. The additional diffusion traces at 1 and 3 minutes aid in displaying how the carbon begins to dissipate very rapidly into the nickel-based substrate and after 5 additional minutes the CVD rig will have reached 900°C which was estimated to be the approximate precipitation temperature of the carbides investigated during this work.

5.4.3. Types of carbide

Carbides observed in this research are found to adopt a number of different morphologies, growth is limited by the formation in the solid state superalloy as opposed to during solidification. The first carbides morphology is that of the ‘proto-carbides’ and these can be seen to form in the gamma channels which are rich in molybdenum and tantalum, see *Fig. 5.16 (a). Fig. 5.23* shows schematically how these very small carbides initiate within the gamma channels immediately beneath the external surface, they are numerous and it is likely that the high quantities results in slower growth since there is a finite concentration of carbon available for subsequent carbide growth.

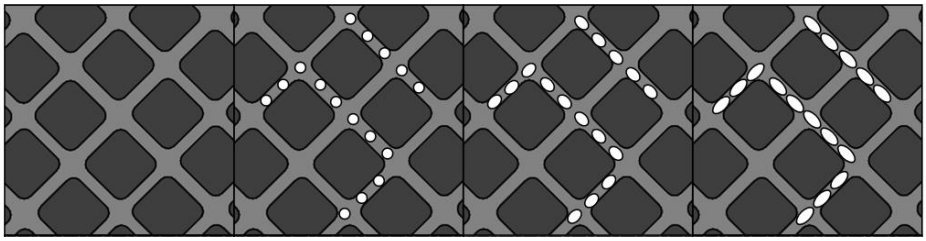

Fig. 5.23 – schematic detailing growth of small proto-carbides within γ channels close to the substrate external surface, see Fig. 5.13 (c)

Fig. 5.14 (a), 5.15 (b) and 5.16 (b) show two types of carbides, pinpoint and platelet, that display a further level of spatial ordering, deeper into the bulk, displaying strings of carbides which likely correspond to residual segregation remaining following solution heat treatment. Despite solutioning ‘river-lines’ of formerly interdendritic regions are retained after heat treatment, these are enriched in titanium and tantalum, key carbide forming elements. In addition these gamma rich seams are likely heavily concentrated in dislocations. These dislocations are possible initiation points for various carbides morphologies and likely lower the energy requirements for carbide initiation therefore enabling preferential formation in these chains. *Fig. 5.24* details a schematic representation show how these ‘river-lines’ within the γ/γ’ microstructure exist as seams, they twist and wind through the material without posing particular threat, they are not grain boundaries. Despite this the seam acts as a preferential formation point for these precipitates, in this instance the platelet carbides are shown, as opposed to the otherwise uniform surrounding γ/γ’ superalloy.

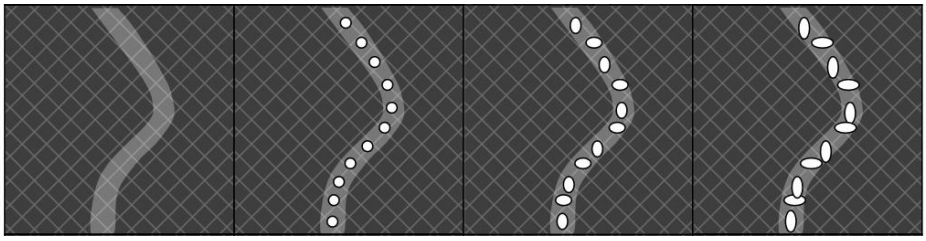

Fig. 5.24 – schematic detailing growth of platelet carbides within low energy pathways, see Fig. 5.13 (b) and 5.14 (a)

A third carbide variant is detailed in *Fig. 5.13 (b)* and its morphology is that of thin platelets that appear oriented at ca 45° to the surrounding γ/γ' superalloy. An almost identical micrograph to that displayed in *Fig. 5.13 (b)* was printed and the author proceeded to manually colour the carbides depending upon the relative orientation to best highlight the families of carbides. This image is displayed in *Fig. 5.25* below.

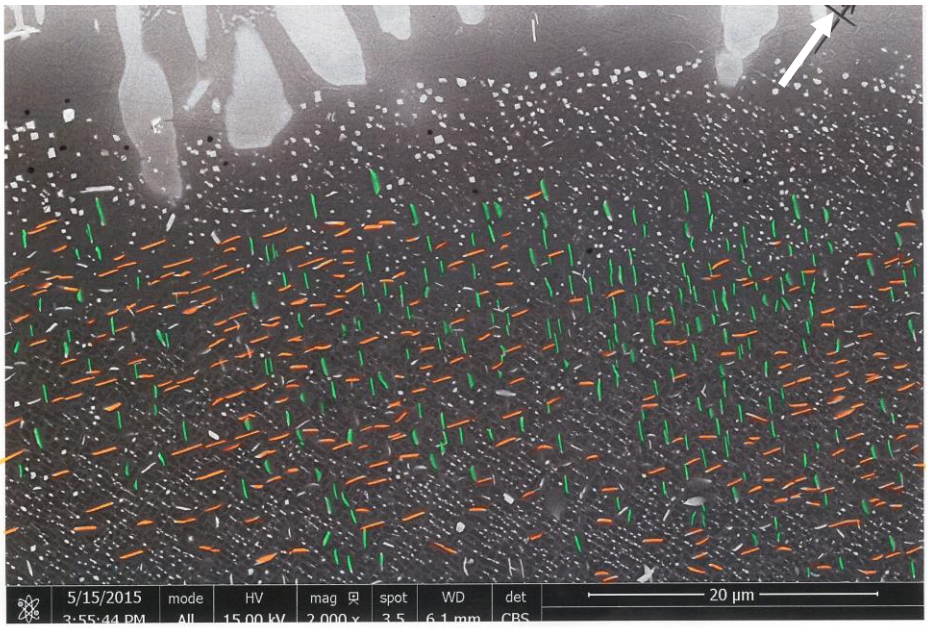

Fig. 5.25 –manually modified SEM-BSE image of platelet carbides, see Fig. 5.12 (b) and 5.12 (d)

Fig. 5.25 clearly shows two different families of the same platelet carbide variant. Both appear to be orientated at ca 45° to the surrounding γ/γ' superalloy but if 0° is expressed as the superalloy [100] orientation then the orange carbides would be at -45° and the green would be at +45°. Since the surrounding γ/γ' superalloy is rather small at this magnification a small white arrow has been placed orientate the reader as to the [100] direction. Therefore these 2D slices through platelet carbides means that they likely inhabit the (111) plane.

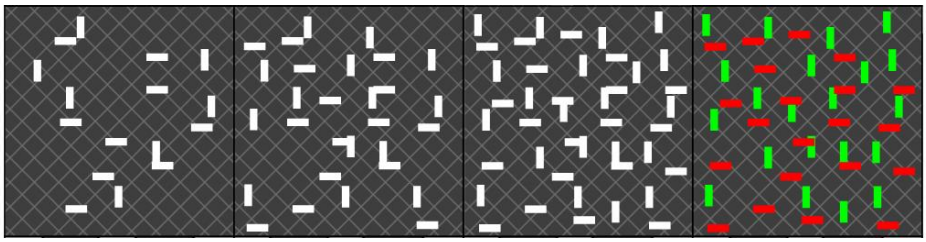

Fig. 5.26 – schematic detailing growth of platelet carbides within pre-existing γ/γ' microstructure with clear orientation relationship, see Fig. 5.13 (b)

Fig. 5.26 details a schematic of how these platelet carbides may have formed in the superalloy microstructure and how their orientation to the surrounding γ/γ' superalloy may appear at first somewhat random but upon segregating into different families the correlation is clearer to see.

The final carbide variant explored is that of the advanced larger carbide found at the bottom of the carbide-enriched band. They are often cubic in nature and examples are seen in *Fig. 5.13 (c), 5.14 (a), 5.15 (a) and (b), 5.16 (b) as well as 5.17 (b), (c) and (d).* These carbides form within the γ channels once again, being closest to the bottom of the carbide region they are far less numerous yet larger in size, often measuring ca 500 nm across. These carbides display a clear orientation relationship with the surrounding γ/γ' superalloy with the vertices of the cube pointing along the gamma channels, *Fig. 5.16 (b)*. These cubic carbides have on occasion been discovered with an interesting core exposed, example of which are seen in *Fig. 5.17 (b) and (c).* These carbides were examined using EDS, the results are seen in *Fig. 5.18 and 5.19*. The carbides appear to have formed in two stages, with a darker (SEM-BSE Z contrast) inner core which features an octahedral habit. This inner core is likely to be a titanium-based carbo nitride which was first to form in the gamma channel. Next the brighter white (Z contrast) carbide layer formed and is likely a molybdenum, tantalum MC-type carbide which forms the now familiar cubic morphology. The relevant nickel and aluminium maps show a clear void since these elements are not strong carbide formers. Interestingly the cobalt map shows a void in the centre and a potential halo effect around the carbide in the disrupted surrounding γ/γ' superalloy, as seen most clearly in *Fig. 5.17 (c)*. This halo effect is also displayed by the chromium elemental map which is unusual since chromium is a keen carbide former.

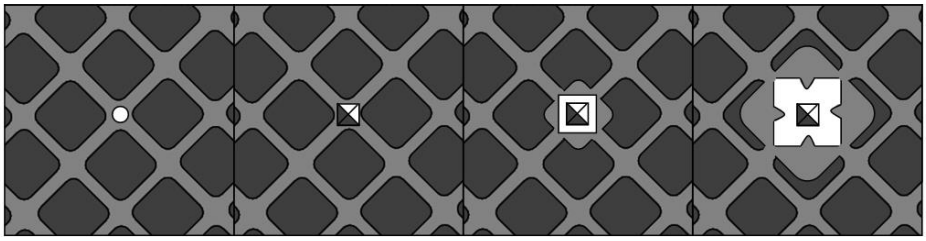

Fig. 5.27 – schematic detailing growth of cubic carbides within pre-existing γ/γ' microstructure with clear orientation relationship and darker Z core, see Fig. 5.16 (b) and (c)

Further growth of this carbide variant can be observed in *Fig. 5.17 (c)* and schematically above in *Fig. 5.27*. This four-pointed star shape is clearly displaying how upon reaching a critical threshold size the cubic morphology can no longer be sustained and in order to continue growth arms emerge from the vertices which enables a more dendritic style. This carbide is unusual but displays the kind of next step that this form of carbide might take given a longer growth period.

5.5. Conclusion

This work has used a range of characterisation techniques to determine the origin of these small precipitates which exist in a very specific sub-surface region of nickel-based superalloys following masking and aluminising conditions. The following conclusions are drawn regarding the process of inadvertent carburisation and the likely identity of the carbides elemental constituents:

1. The maskant material was identified using infrared spectroscopy to determine the carbon polymer chain, this was found to be Poly Vinyl Acetate (PVA)
2. The carbides form during the aluminisation of the blade, but specifically in regions masked to avoid coating, making it definitive that it was a masking-related issue.
3. As the polymer degrades during the ramp to aluminising deposition temperatures the carbon released diffuses into the alloy to form the sub-surface carbides.
4. Carbon is not present at the surface throughout the entire anneal and the carburisation occurs during a brief period whilst the PVA is degrading and is removed by the pumping system but before the carbon diffuses away from the superalloy surface.
5. Assuming carbon influx begins at 500°C there is an approximately 25 minute window before 900°C is reached which has been taken to be the temperature where carbides begin to precipitate. Depending upon when the amount of carbon is reduced at the surface will define when movement of dissolved carbon will begin to flow both out of the alloy
6. A 20 minute influx of carbon coupled with 5 minutes of diffusion is the closest to the depth of carburisation seen.
7. A calculation provides an approximate idea of the amount of carbon available in this sub-surface region during the aluminising ramp to the holding temperature of 1030°C. Assumptions include:
    - Maximum carbon concentration of 3000 ppm, based on solubility limits for a nickel-based superalloy
    - Threshold of only 100 ppm necessary for the formation of carbides once the appropriate temperature is reached
    - Starting temperature for the diffusion model was 500°C since beneath this temperature the carbon is likely still contained within the hydrocarbon chains
    - Upper threshold for the model is the temperature 900°C above which the presence of carbon in the sub-surface region in concentrations above the stated 100 ppm will in all likelihood lead to the formation of the carbides previously explored.

8. Carbides observed in this research are found to adopt a number of different morphologies, growth is limited by their formation in the solid state superalloy as opposed to those that are commonly found in carbon-containing earlier alloys that form during solidification.
9. The first carbide morphology highlighted is that of the ‘proto-carbides’ and these can be seen to form in the γ channels which are rich in molybdenum and tantalum.
10. Pinpoint and platelet carbides display a further level of spatial ordering, deeper into the bulk, displaying strings of carbides which likely correspond to residual segregation remaining following solution heat treatment. Despite solutioning ‘river-lines’ of formerly interdendritic regions are retained after heat treatment, these are enriched in titanium and tantalum, key carbide forming elements. In addition these γ rich seams are likely heavily concentrated in dislocations. These dislocations are possible initiation points for various carbides morphologies and likely lower the energy requirements for carbide initiation therefore enabling preferential formation in these chains.
11. A fourth carbide variant is that of thin platelets that appear oriented at ca 45° to the surrounding γ/γ’ superalloy. These exist in two different families of the same platelet carbide variant. Both appear to be orientated at ca 45° to the surrounding γ/γ’ superalloy but if 0° is expressed as the superalloy [100] orientation then the one group of carbides would be at -45° and the other would be at +45°. These platelet carbides likely inhabit the (111) plane.
12. The final carbide variant explored is that of the advanced larger carbide found at the bottom of the carbide-enriched band. They are often cubic in appearance and found within the γ channels once again and often measure ca 500 nm across.
13. These carbides display a clear orientation relationship with the surrounding γ/γ’ superalloy with the vertices of the cube pointing along the gamma channels. These cubic carbides have on occasion been discovered with an interesting core exposed. These carbides were examined using EDS and appear to have formed in two stages, with a darker (SEM-BSE Z contrast) inner core featuring an octahedral habit. This inner core is likely to be a titanium-based carbo nitride which was first to form in the γ channel. Next the brighter white (Z contrast) carbide layer formed and is likely a molybdenum, tantalum MC-type carbide which forms the now familiar cubic morphology.

6. Carburisation – surface treatments and solutions

6.1. Introduction

This chapter follows directly from the work covered previously in chapter 5. In chapter 5 the phenomena of inadvertent carburisation during the above-the-pack aluminising process was discussed and the source of this carbon was revealed. The work that follows in chapter 6 discusses the impact of varying the aluminising parameters in an attempt to better understand what can be done to affect carbide growth and precipitation whilst still masking part of the superalloy surface, this strand has the added complication of still ensuring adequate aluminising results that provide a turbine component with the necessary protection for high-temperature service. Then the role of grit blasting procedures used to prepare a surface for coating deposition are explored, with the impact that this process has upon the nickel-based superalloy substrate when exposed to post-coating diffusion heat treatments. Finally chapter 6 covers the full turbine blade environmental protection process cycle where specimens are coated with electroplated platinum which is then diffused before a subsequent aluminising process is used to create a plat-aluminide bond coat.

6.2. Experimental

The carburising phenomena is linked to aluminising processing conditions and a series of alternative temperatures were used to determine the impact upon carburisation levels as well as the thickness and aluminium content of the resulting aluminide. *Fig. 6.1* shows the thermal profile of eight aluminising CVD runs the results of which are in section 6.3. In *Fig. 6.1* it can be seen that the lower temperature runs reached the set point faster and therefore appear shorter in duration, in fact the time allowed for deposition is the same in all instances, 3 hours, and this is measured from when the CVD rig reaches 95% of the furnace set point. The 95% of set point was chosen to provide a standard method of timing aluminising runs.

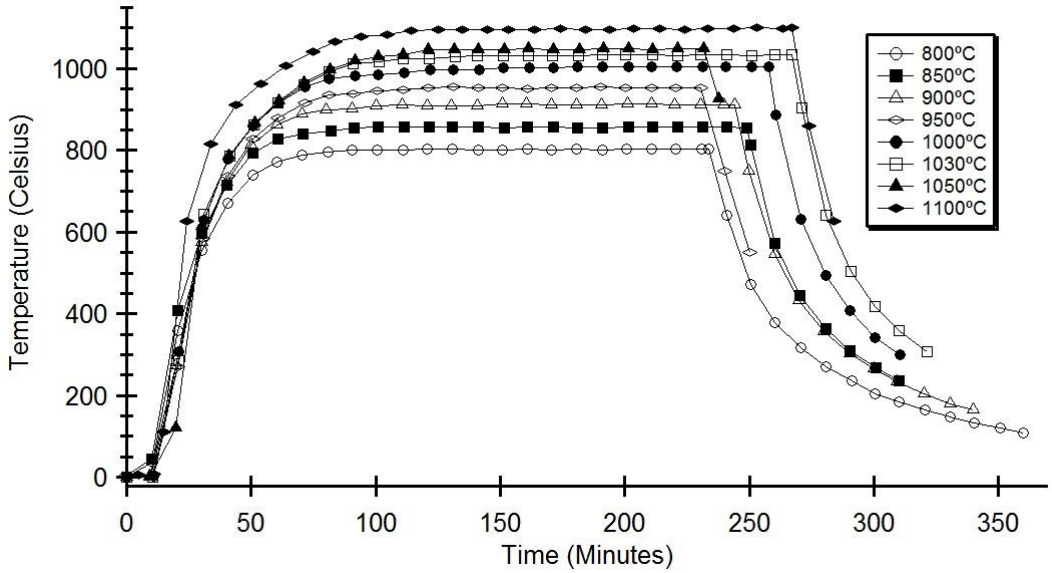

Fig. 6.1 – aluminising CVD run thermal profiles; 800°C, 850°C, 900°C, 950°C, 1000°C, 1030°C, 1050°C, 1100°C, all for a hold time at temperature of ca 3 hours

In addition to different thermal profiles a number of special trials were conducted to explore potential approaches to mitigate carburisation. *Fig. 6.2 (a)* shows the thermal trace for a ramp to 1030°C and then after only 5 minutes at temperature the furnace was removed and the standard cool down commenced. *Fig. 6.2 (b)* shows how altering when the furnace was brought up to temperature affects the ramp rate to 1030°C. *Fig. 6.2 (c)* displays the interrupted climb experiment which introduced a 1 hour hold at 700°C on the ramp to a 3 hour 1030°C aluminising run. *Fig. 6.2 (d)* is the thermal profile for a 'standard' 6 hour hold at 1030°C. In all of these trials samples were taken and analysed to determine the effect on carbide precipitation as well as the thickness and microstructural appearance of the deposited aluminide coating. For completeness, results were collected in these trials for both CMSX-4 and CMSX-10N. However, since carburisation was first observed in CMSX-4 and for succinctness, similar results for CMSX-10N are in the appendix.

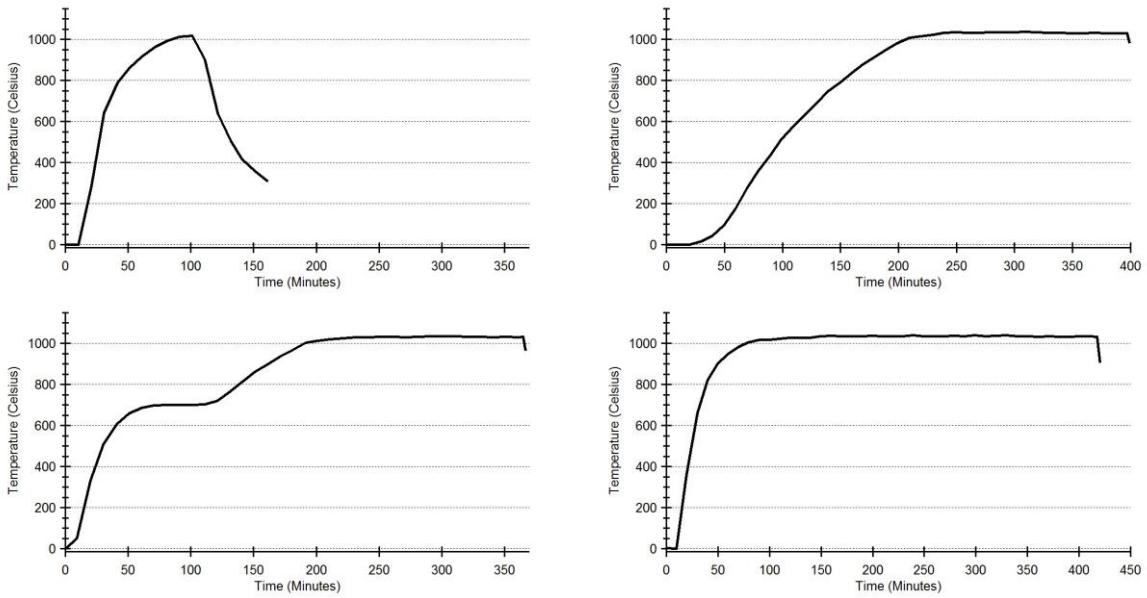

Fig. 6.2 – aluminising CVD run thermal profiles; 5 minute hold at 1030°C (a), slow climb rate to holding set point of 1030°C (b), interrupted climb, intermediate hold at 700°C for 1 hour before 3 hour hold at 1030°C (c), 'extended' 6 hour hold at 1030°C (d)

6.2.1. Grinding

Fig. 6.3 – macro photograph showing nickel-based superalloys CMSX-4 and CMSX-10N test bars or 'pins' before blasting

Material for these trials was obtained from the Precision Casting Facility, Rolls Royce plc in Derby, UK. Small cylindrical bars were used with a diameter of ca 9mm, with a length of ca 60mm and with a defined [001] orientation. The bars represented the alloy CMSX-4 and CMSX-10N. All test pieces were in a fully solutioned state and had experienced the primary age heat treatment, this is representative of the state of these materials as they enter the coating phase of turbine blade manufacture. *Fig. 6.3* shows a collection of these 'pins' which after collection were subject to a machining operation that ground the external surface to a uniform smooth surface finish. In doing so the rough as-cast surface was removed. This was crucial since the following operations varied the surface treatments experienced and it was imperative to have confidence that it was the subsequent operations that had resulted in the changes, as opposed to a pre-existing defect in the surface from casting.

6.2.2. Grit blasting

Fig. 6.4 – macro photograph showing nickel-based superalloys CMSX-4 and CMSX-10N test bars or 'pins' temporarily protected using masking tape (a) and after an array of grit blasting parameters were applied and the masking subsequently removed (b)

As results progressed regarding the source of carburisation it became apparent that the author would need to better understand the role of surface roughness, grit blasting parameters and the effect of a subsequent heat treatment upon the alloy CMSX-4. Early results (*not shown*) appeared confusing with both small TCPs and pinpoint carbides discovered. As a result this series of trials was undertaken to qualify under which circumstances various surface related microstructural coarsening and precipitation transformations take place to better distinguish them from the formation of carbides. Some pins shown in *Fig. 6.4* were subsequently sectioned to observe the post-blast microstructure and the remaining material was heat treated using a VFE vacuum furnace under a partial pressure of argon to mimic the thermal profile experienced within the CVD rig, i.e. 6 hours at 1030°C. The post-blast and post-heat treated microstructure was then examined and the results are discussed in section 6.4.1. *Table. 6.1* shows the blasting media and parameters used and whether SEM images are included within the main chapter (6) or have been placed within the appendix for succinctness.

	CMSX-4			CMSX-10N		
	15 PSI	30 PSI	45 PSI	15 PSI	30 PSI	45 PSI
220 mesh	✓	✓	✓	✓	✓	✓
60 mesh	✓	✓	✓	✓	✓	✓
20 mesh	✓	✓	✓	✓	✓	✓

Table. 6.1 – blasting media and parameters used, tick indicates trial was carried out, green indicates SEM-BSE images can be found in the results section of chapter 6, red indicates results were similar and have therefore been moved to the appendix

6.2.3. Platinum plating

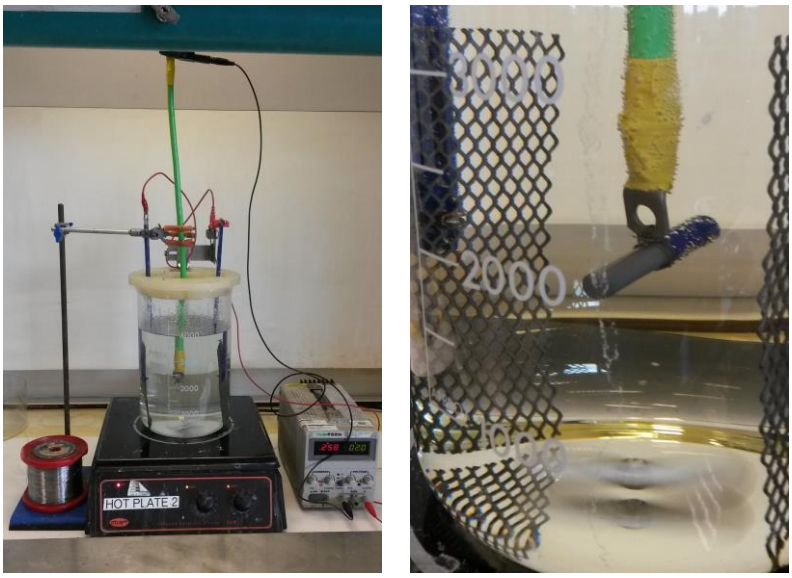

Fig. 6.5 – macro photograph showing experimental set-up, electrochemical platinum plating using constant current (a), close up photograph of masked test pin affixed to copper cable, suspended between anodes (b)

In keeping with standard high pressure blade manufacture the next set of trials demanded similarly grit blasted pins to be subject to electrochemical deposition of platinum upon the surface. Once plated the pins are subject to a 1 hour 1100°C heat treatment within a VFE vacuum furnace under partial pressure argon to diffuse the platinum and superalloy together. *Fig. 6.5* shows photographs of the experimental set-up in the laboratory, each pin was individually plated within the platinum plating solution. Care was taken to ensure that the plating maskant was applied in such a way as to yield four separate conditions, bearing in mind that there were two different surface conditions upon each pin. Therefore the pins following plating and diffusion consisted of the following conditions; grit blasted only, grit blasted with diffused platinum plating, ground smooth surface with platinum plating and ground smooth only. Using this methodology it was possible to ensure that any surface changes were associated with the blasting trials and not a prior feature from casting.

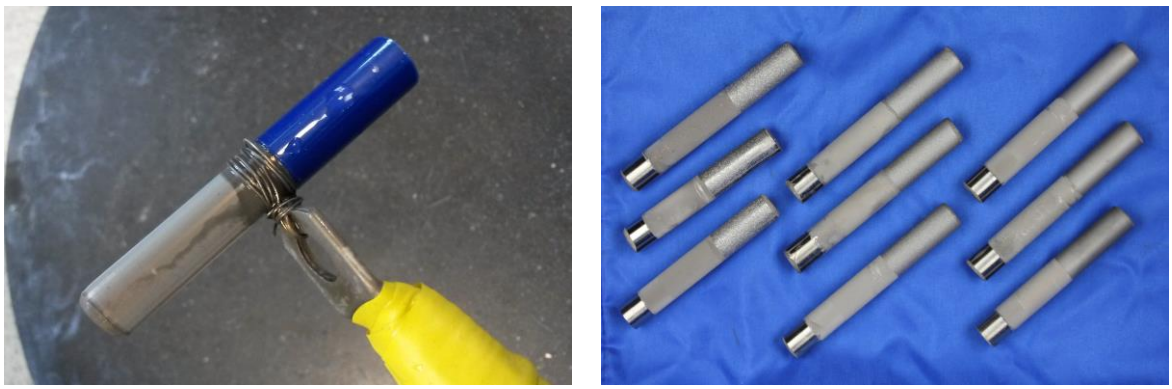

Fig. 6.6 – macro photograph showing platinum plated pin (a), all 9 CMSX-4 pins post blast and post plate (b)

Table 6.2 shows the parameters regarding grit blasting and subsequent platinum plating and diffusion heat treatment. The results of this trial can be found in section *6.5.1.*

CMSX-4

	15 PSI				30 PSI				45 PSI			
	GB	GB PP	G PP	G	GB	GB PP	G PP	G	GB	GB PP	G PP	G
220 mesh	✓	✓	✓	✓	✓	✓	✓	✓	✓	✓	✓	✓
60 mesh	✓	✓	✓	✓	✓	✓	✓	✓	✓	✓	✓	✓
20 mesh	✓	✓	✓	✓	✓	✓	✓	✓	✓	✓	✓	✓

Table. 6.2 – blasting media and parameters used, tick indicates trial was carried out, green indicates SEM-BSE images can be found in the results section of chapter 6, red indicates results were similar and have therefore been moved to the appendix, GB = Grit Blast, GB PP = Grit Blast Platinum Plate, G PP = Ground Platinum Plate and G = Ground surface finish

The following list details specific platinum plating conditions used during this work:

- Temperature ca 85 °C
- pH ca 8.5
- Initial constant current of 1 A for 30 seconds
- Dialled back constant current of 300 mA for 2 hours
- Current standard platinum plating solution used at Rolls-Royce Plc. suppliers

6.2.4. Aluminising

The aluminising process is inadvertently responsible for the carburisation explored in chapter 5. Using CVD equipment aluminising was carried out with various thermal profiles detailed earlier, test pins were subject to deposition as can be seen in *Fig. 6.7*.

Fig. 6.7 – macro photographs showing test pins placed upon tooling within the aluminising CVD rig (a), 2 examples of CMSX-4 pins post aluminising (b) (note their blue steel colouration and the maskant layer)

In addition to the thermal variation of the aluminising parameters a second series of special trials were carried out. This involved the following; use of M1™ maskant powder without carbon-containing binder, use of various thicknesses of the maskant M1™ (thin, medium and thick) and also the use of pure commercially available PVA glue in intimate contact with the surface of the nickel-based superalloy, prior to M1™ maskant application. Fig. 6.8 shows the special trials and how they were assembled within the CVD rig.

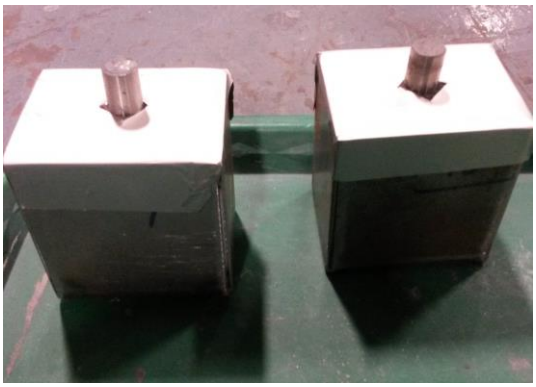

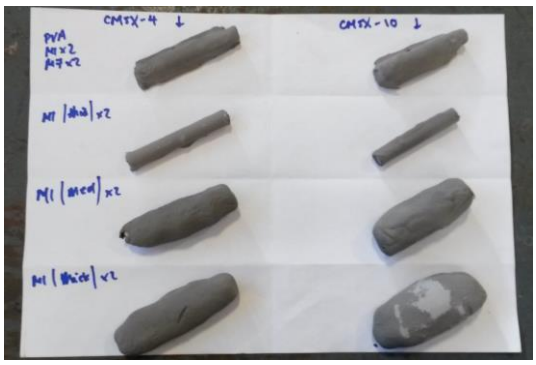

Special trials
M1 'thin' – slurry mass ca 5g
M1 'medium' – putty mass ca 50g
M1 'thick' – putty mass ca 60g

all maskants where applied to test bars measuring ca 65mm long with a diameter of ca 9mm

Fig. 6.8 – macro photographs showing test pins for special carburising trials, two pins are pressed into M1™ maskant powder without addition of binder, the steel boxes are topped with nickel tape (a), special aluminising run, specimens placed in reaction vessel (b), coated test pins for special trials (c)

Table 6.3 shows the relevant special trials. The results of this trial can be found at the end of section *6.3.1.*

	CMSX-4					CMSX-10N				
	M1™ thin	M1™ med	M1™ thick	Box of M1™	PVA	M1™ thin	M1™ med	M1™ thick	Box of M1™	PVA
Ground smooth finish	✓	✓	✓	✓	✓	✓	✓	✓	✓	✓

Table. 6.3 – special trials, tick indicates trial was carried out, green indicates SEM-BSE images can be found in the results section of chapter 6, red indicates results were similar and have been moved to the appendix

6.2.5. Vacuum furnace

Both aluminising and platinum plating operations require a post-coating high temperature diffusion heat treatment to aid diffusion kinetics and merge the coating with the substrate or actively select the desired phase. *Fig. 6.9* shows photographs detailing test pins before and after diffusion heat treatment at 1100°C for 1 hour following the aluminising process.

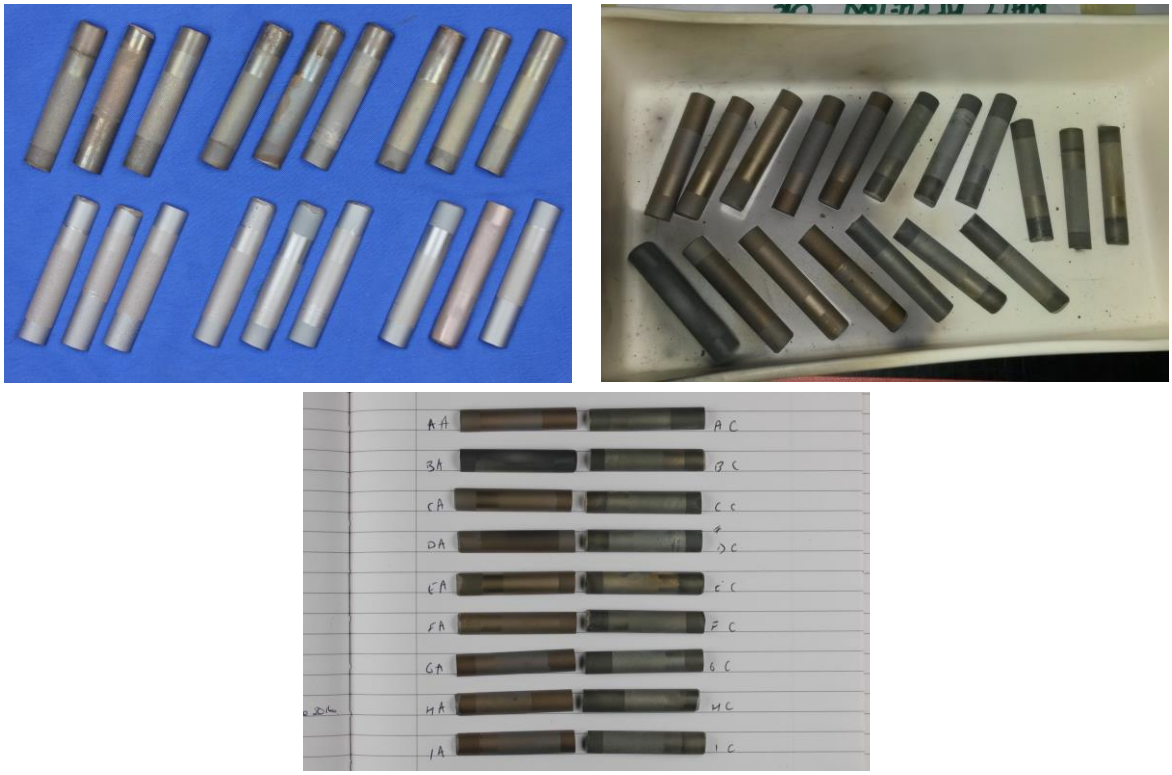

Fig. 6.9 – CMSX-4 test pins after reaction within CVD rig, top row have been blasted, platinum plated and then carburised, bottom row have been blasted, platinum plated and aluminised (a), same test pins receiving post-aluminising heat treatment (b) and same test pins post heat treatment displayed side by side aluminised on LHS and carburised on RHS (c) flow chart of chapter 6 (d)

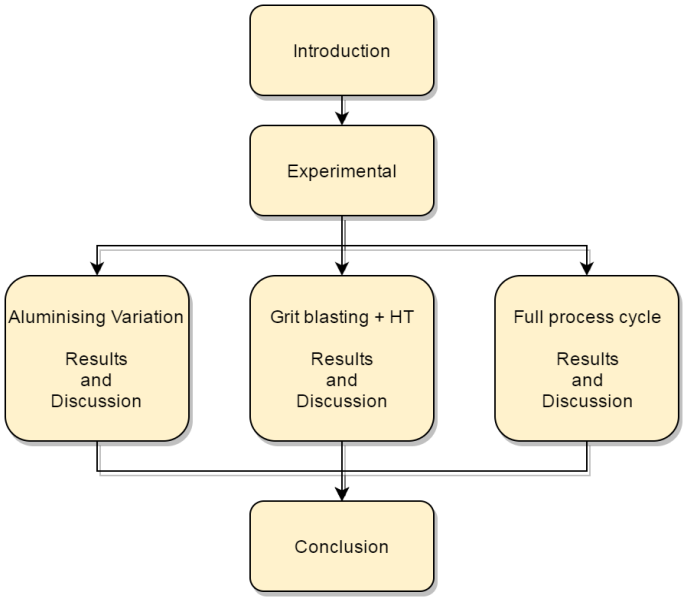

6.3. Aluminising variation

6.3.1. Results

6.3.1.1. Scanning electron microscopy

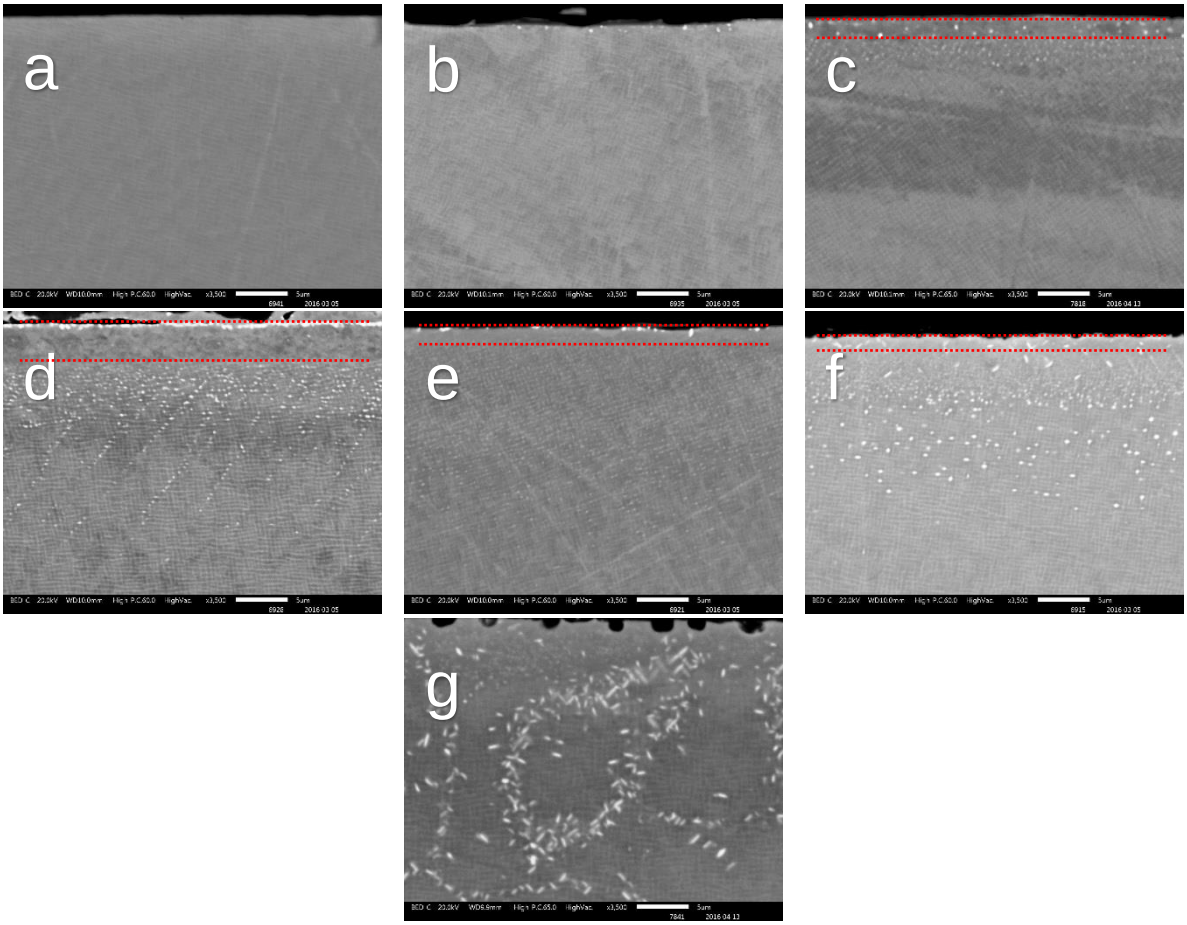

Fig. 6.10 – carburisation results from temperature variation trials upon the alloy CMSX-4, 800°C (a), 850°C (b), 900°C (c), 950°C (d), 1000°C (e), 1050°C (f), 1100°C (g)

Fig. 6.10 shows a series of scanning electron microscope images under backscatter conditions (SEM-BSE). The micrographs detail whether carburisation was present following maskant application and subsequent aluminising upon the alloy CMSX-4. The micrographs in *Fig. 6.10 (a)* and *(b)* showing the results of a 3 hour exposure at temperatures of 800°C and 850°C show practically no presence of carbides in the sub-surface region. *Fig. 6.10 (c), (d)* and *(e)* show the sub-surface region after 3 hour thermal exposures within the CVD rig of 900°C, 950°C and 1000°C. In these micrographs there are clearly visible bands of small carbide precipitates that appear at a layer starting at the outer surface and persisting to a depth of ca 15 µm. The micrographs in *Fig. 6.10 (f)* and *(g)* show the results of the 1050°C and 1100°C temperature 3 hour exposures. These two micrographs show extensive levels of carburisation in terms of quantity and depth. In addition there is an alloy enrichment / depletion effect associated with high-temperature interaction between the metal powder and the substrate, it is difficult to quantify but is often present and ca 2 – 5 µm in thickness.

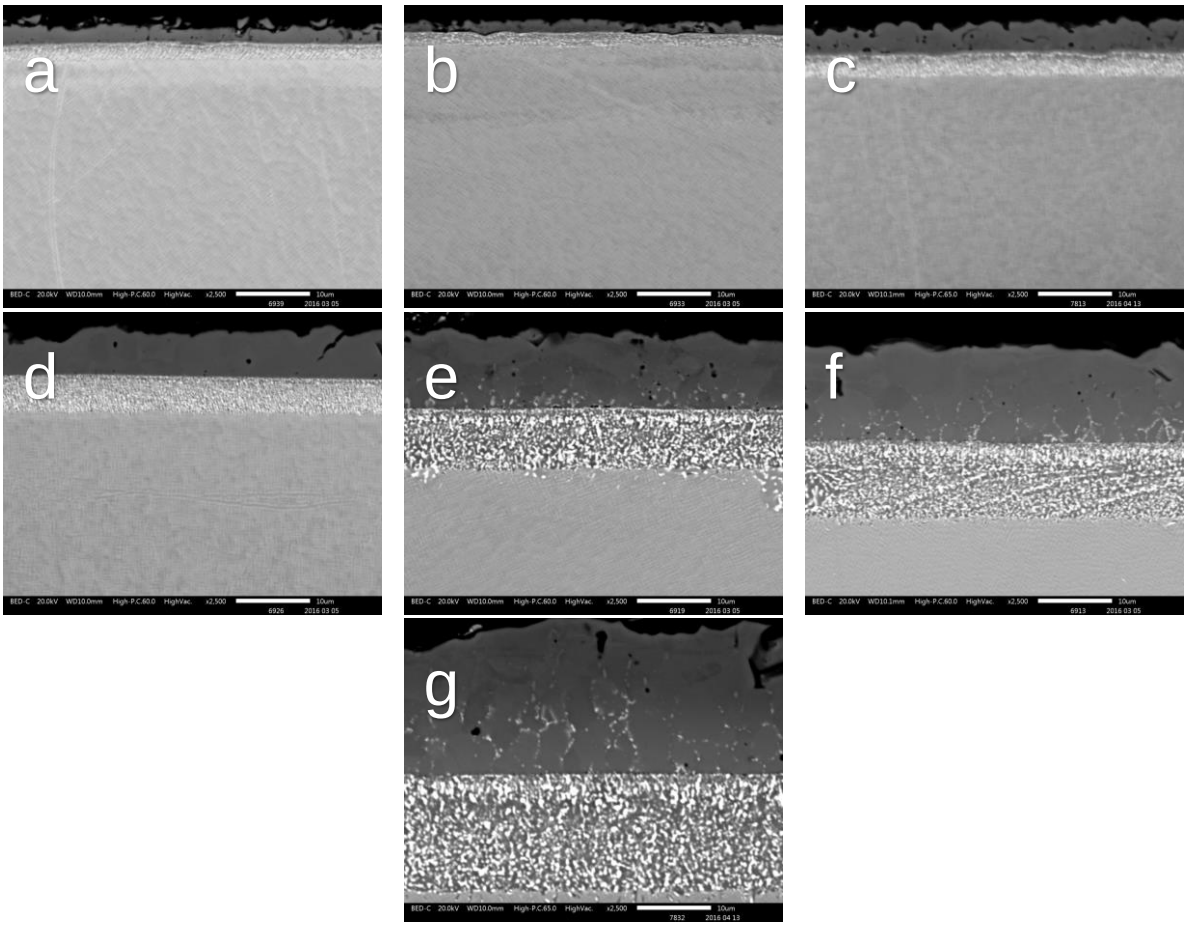

Fig. 6.11 – vapour phase aluminising results from temperature variation trials upon the alloy CMSX-4, 800°C (a), 850°C (b), 900°C (c), 950°C (d), 1000°C (e), 1050°C (f), 1100°C (g)

It is vital to understand the impact of lower temperatures on the formation of carbide precipitates (*Fig. 6.10)* and also upon the formation of the β-aluminide layer, in this instance upon CMSX-4. *Fig. 6.11* shows a series of SEM-BSE micrographs detailing the thickness of the deposited aluminium enriched layer plus the interdiffusion zone at the interface between the coating and the substrate, the heat treated SEM micrographs can be found in the appendix. *Fig. 6.11 (a), (b)* and *(c)* detail the temperatures 800°C, 850°C and 900°C after 3 hours of exposure respectively, they clearly show a thin, incomplete deposition during aluminising. The coating in these cases is ca 3 – 6 µm in thickness and shows frequent gaps in substrate surface coverage. *Fig. 6.11 (d)* shows the 3 hour run at a static temperature of 950°C which shows an even coating deposited with a thickness of ca 8 µm. *Fig. 6.11 (e)* and *(f)* show an aluminide coating that is most akin to that seen as a 'production-standard', these coatings were formed at 1000°C and 1050°C respectively after 3 hours of exposure. The β-NiAl coating thickness in these trials is ca 10 – 15 µm, without porosity or inclusions and with a moderately thick interdiffusion zone beneath the coating. The micrograph in *Fig. 6.11 (g)* shows a sample aluminised at a temperature of 1100°C for a period of 3 hours. This coating is thick, with a β layer approaching 25 µm and a total coating thickness of ca 50 µm.

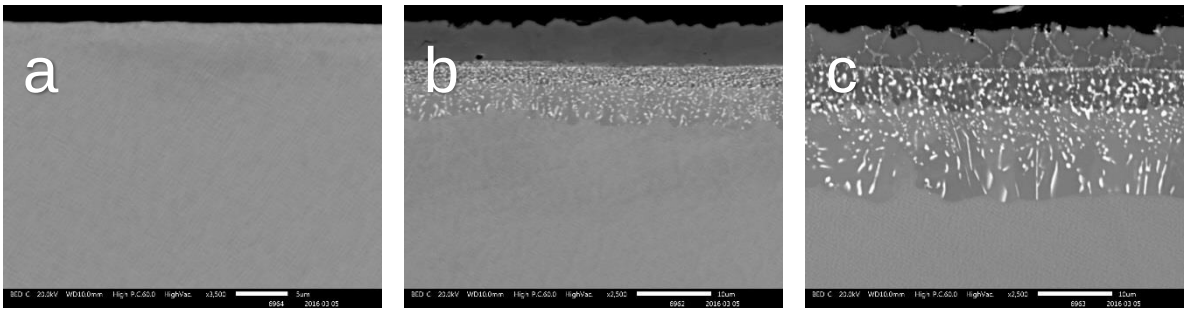

Fig. 6.12 – carburising and vapour phase aluminising results from rapid 5 minute hold time trials upon the alloy CMSX-4, carburised (a), aluminised 'green' (b), aluminised HT'd (c)

A trial was used to determine the impact, on carburisation and aluminising, of a standard ramp to temperature followed by a brief 5 minute hold at 1030°C followed by the normal retort cool down in air. *Fig. 6.12 (a)* shows that there is no evidence of carburisation following the 5 minute hold at temperature indicating that a longer period of time is necessary to enable carbide precipitation. *Fig. 6.12 (b)* shows the aluminising that has already occurred during the final part of the ramp to temperature and after 5 minutes at 1030°C. *Fig. 6.12 (c)* shows the result of the standard post aluminising heat treatment of 1 hour at 1100°C in a vacuum furnace under a partial pressure of argon. The thickness of the beta layer is slightly reduced and there has been extensive SRZ formation in the alloy beneath the coating.

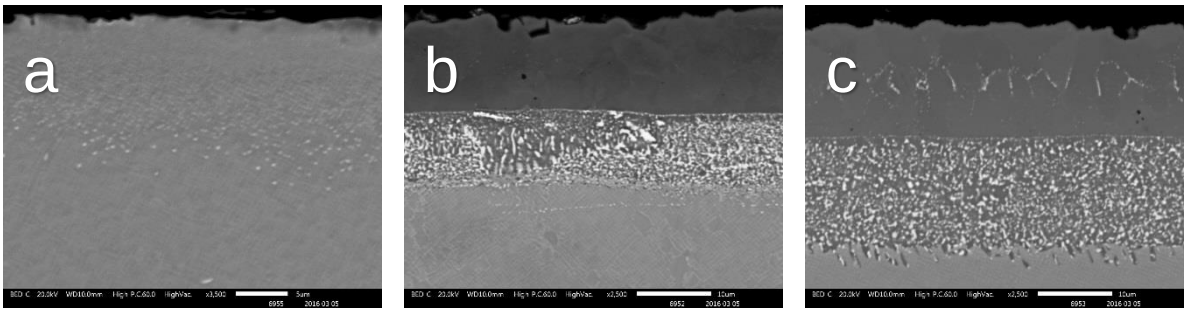

Fig. 6.13 – carburising and vapour phase aluminising results from interrupted climb 700°C hold for 1 hour trials upon the alloy CMSX-4, carburised (a), aluminised 'green' (b), aluminised HT'd (c)

A trial was undertaken introducing a hold during the ramp up to the hold temperature of 1030°C in an attempt to remove enough carbon prior to reaching temperatures known to precipitate carbides in the sub-surface region. The furnace was used to bring the CVD retort to 700°C before holding for a period of 1 hour. Once complete the furnace was ramped up to 1030°C for the standard 3 hour exposure time. *Fig. 6.13 (a)* shows that result of this 700°C prior hold was unsuccessful, and the formation of a densely populated carbide sub-surface layer was seen. *Fig. 6.13 (b)* shows the microstructure of the deposited aluminising layer following this trial, the thickness and structure appear to have been unaffected by the 700°C hold. *Fig. 6.13 (c)* shows the same aluminised CMSX-4 post diffusion heat treat, the microstructure, thickness and coating quality all appear unaffected by the 700°C ramp hold.

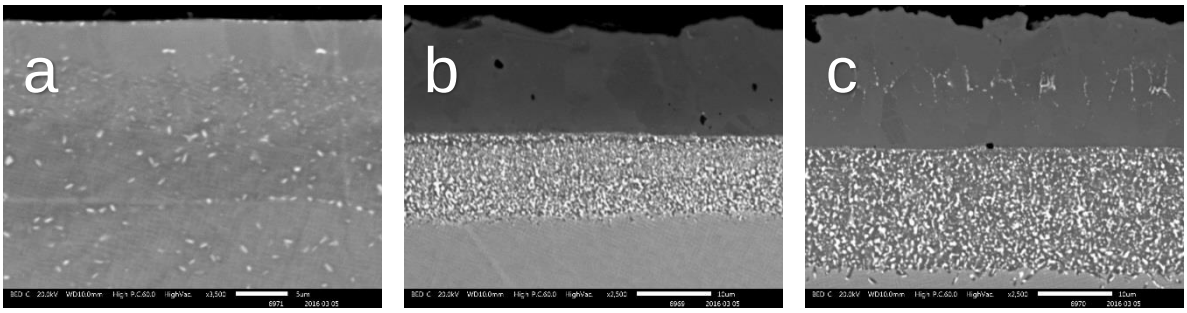

Fig. 6.14 – carburising and vapour phase aluminising results from slow climb trials upon the alloy CMSX-4, carburised (a), aluminised 'green' (b), aluminised HT'd (c)

Under standard practice the furnace used with the CVD rig is permitted to climb up to temperature before being placed over the reaction retort. This process means that once in position there is a short ramp up to the holding temperature of 1030°C due to the low thermal load. In an attempt to alter the rate of carburisation the furnace was placed into position on the CVD before the heating elements were switched on, this meant that the CVD retort would experience a far slower ramp up to the deposition temperature and thus perhaps alter the level of carbides and also the rate of aluminising deposition. *Fig. 6.14 (a)* shows the depth and quantity of pinpoint carbides within the sub-surface region of the alloy CMSX-4 as a result of the slow climb trial. There is again, a high level of carburisation present. *Fig. 6.14 (b)* shows the CMSX-4 aluminised layer in its 'green' state, this being in the as-deposited pre-heat treated condition. The layer is especially thick considering the time at the ultimate hold temperature of 1030°C was still only 3 hours in length. This suggests that the slow climb rate has permitted a boost to the thickness of the coating. *Fig. 6.14 (c)* shows the CMSX-4 aluminised surface post heat treatment, the layer is especially thick.

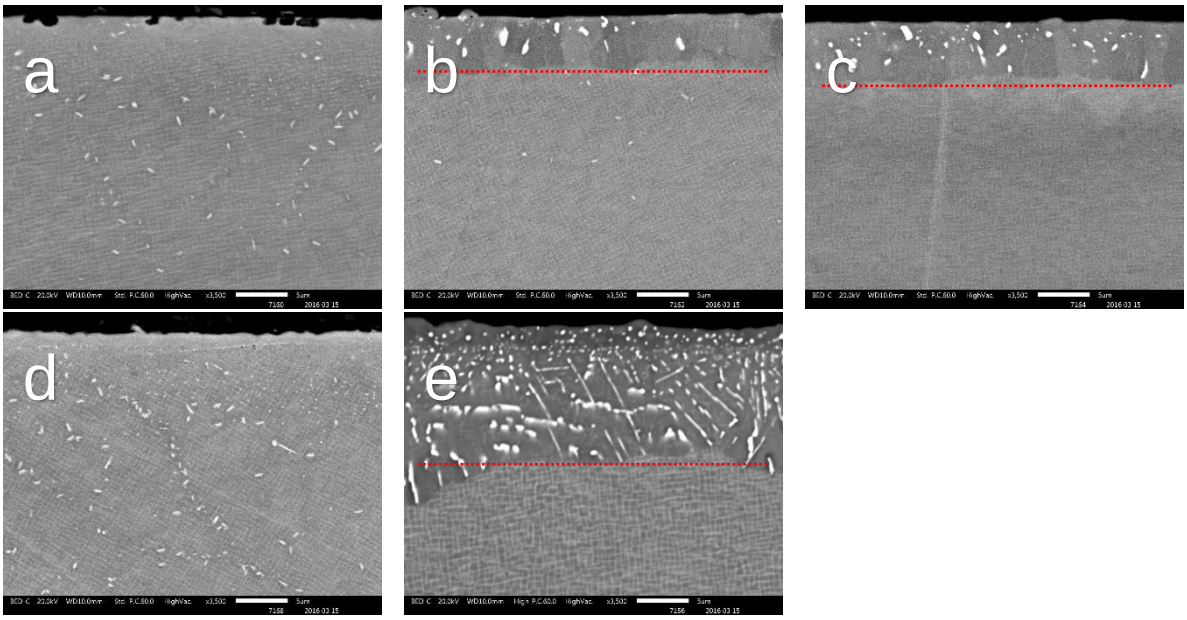

Fig. 6.15 – carburising results from 5 special trials upon the alloy CMSX-4, thin M1™ (a), medium M1™ (b), thick M1™ (c), PVA parting layer (d), steel box filled with M1™ metal powder only and topped with M7™ (e)

A series of 5 special trials were undertaken to look at additional interactions between the underlying substrate and maskant media used during the aluminising process. *Fig. 6.15 (a), (b) and (c)* show the results of applying the maskant M1™ when combined with PVA-based binder system to the surface of the alloy CMSX-4. Different amounts of the slurry mixture were used with a 'standard' thin layer applied to the alloy in the first instance followed by a medium and then a thick application. The relative thickness and weight of slurry matter applied to the superalloy is covered in more detail in the experimental section of this chapter. *Fig. 6.15 (a)* shows the 'normal' level of carburisation that is associated with this particular maskant material when used during the aluminising process. *Fig. 6.15 (b)* shows the results of the medium thickness of maskant slurry applied, there are very few carbides to be observed however there is a ca 10 μm thick sub-surface layer consisting of the alloy enrichment / depletion effect. This region features γ/γ' coarsening associated with discontinuous coarsening of the pre-existing microstructure as well the precipitation of various TCP phases. *Fig. 6.15 (c)* shows the results of a thick application of the M1™ maskant and again displays no carbides but an unusually thick layer of alloy enrichment / depletion. *Fig. 6.15 (d)* shows an SEM micrograph of the sub-surface carbides formed when a thin layer of commercially available PVA glue was applied to the surface between the first M1™ layer and the substrate. This microstructure also displays a 'standard' level of carburisation in terms of depth and quantity of carbides. The micrograph in *Fig. 6.15 (e)* shows the result of placing a CMSX-4 test bar into the pure M1™ metal powder without any of the additional PVA-based binder. This bar was protected from the aluminising atmosphere yet has sustained extensive levels of SRZ, suggesting that local chemistry changes, most likely chromium enrichment was responsible for this sub-surface feature.

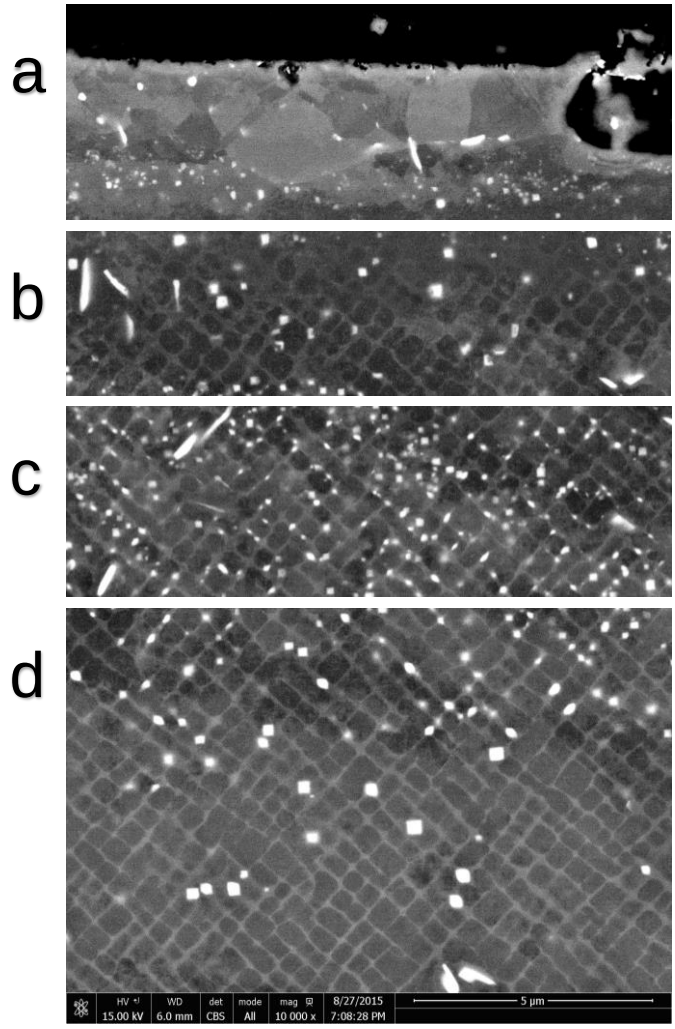

Fig. 6.16 – SEM micrographs ground smooth surface finish CMSX-4 carburised sub-surface region, uppermost (a), middle-upper (b), middle-lower (c) and bottom (d)

Using high magnification SEM-BSE a series of micrographs were taken providing additional detail of the sub-surface microstructure of the carburised alloy CMSX-4*. Fig. 6.16 (a)* displays the uppermost portion of the carburised surface. There is a region ca 3 µm which appears brighter under BSE conditions, this is the portion of the superalloy which has experienced alloy enrichment/depletion effects associated with the transfer of material between the M1™ maskant and the superalloy CMSX-4. The region clearly consists of recrystallised grains of differing sizes and a few sporadic TCP precipitates. *Fig. 6.16 (b) and (c)* show the middle region of the carburised zone. The γ/γ' microstructure is still clearly visible though there is a strong presence of small pin point carbides that appears to reside mainly within the gamma channels of the superalloy microstructure. These carbides are small and numerous. *Fig. 6.16 (d)* shows the threshold between the carbide-rich region and the unaffected superalloy substrate. The carbides are less frequent here and are some of the largest pinpoint carbides observed. The regular cubic appearance of the carbides is visible as well as the common orientation with the γ/γ'.

6.3.1.2. Coating thickness measurements and Energy dispersive x-ray – composition

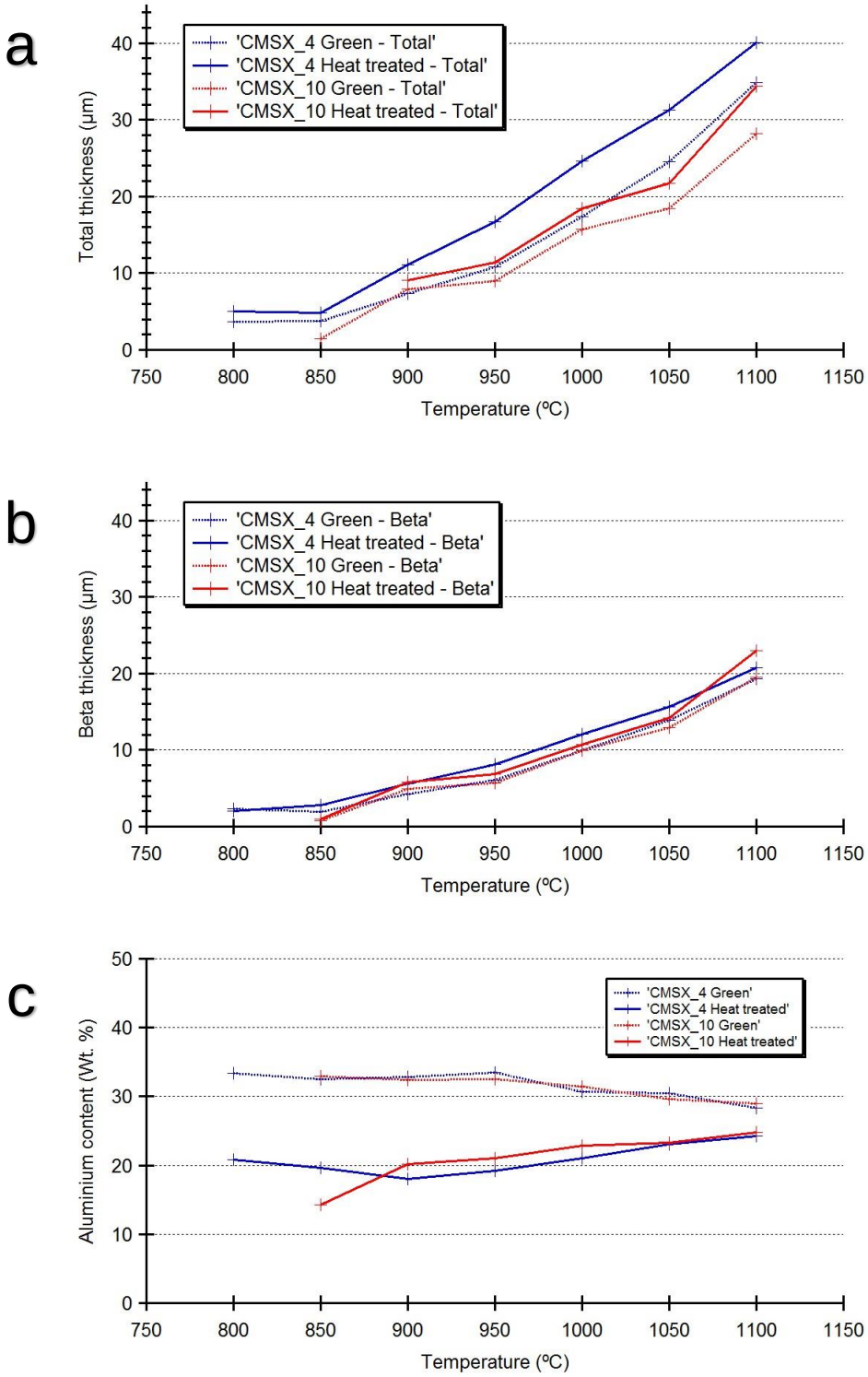

Fig. 6.17 – coating thickness and energy dispersive x ray results from aluminising temperature variation trials, total aluminising thickness (a), beta-phase layer thickness (b) and aluminium concentration in wt. % (c)

Determining the thickness and aluminium content of an aluminide coating is essential to ensuring that the coating is sufficient to provide protection to a nickel-based superalloy component within the gas turbine engine. SEM was used to accurately measure the total thickness of the aluminide coating upon the alloys CMSX-4 and CMSX-10N after the thermal exposure trials both post-aluminising and post-diffusion heat treatment as shown in *Fig. 6.17 (a)*. The aluminide total thickness is measured from the external surface to the bottom of the interdiffusion zone which finishes at the interface between the coating and the underlying substrate. This graph shows that at low temperatures the aluminium activity is too low to provide sufficient aluminium to the surface of the nickel-based superalloy immersed within the CVD retort. Temperatures of 800°C, 850°C and 900°C are all insufficient to deposit what is considered to be a minimum thickness of the coating system. 3 hour holds at the temperatures 950°C, 1000°C, 1050°C and 1100°C then display coating thicknesses of ca 15 µm, 20 µm, 25 µm and 32 µm respectively. CMSX-4 appears to show a marginally thicker coating post-heat treatment than CMSX-10N.

Further measurements were conducted to measure the β-phase layer thickness, this being measured between the external surface and the uppermost interface of the interdiffusion zone. This region is the aluminium-enriched coating system that provides protection from the oxidising environment. The 3 hour thermal holds of 800, 850 and 900 all produce beta thicknesses of ca 0 – 5 µm which is less than the standard, capable aluminide would be. Thermal holds of 950°C, 1000°C, 1050°C and 1100°C show beta thicknesses of ca 8 µm, 10 µm, 14 µm and 20 µm respectively. All four traces of *Fig. 6.16 (b)* show very similar thicknesses of beta-layer, with no discrepancy between the alloys CMSX-4 and CMSX-10N in the ‘green’ state or in the post-diffusion state.

Using EDS area scans elemental composition values were obtained for the aluminide coatings deposited upon the alloys CMSX-4 and CMSX-10N as a results of the temperature variation trials. *Fig. 6.17 (c)* shows that despite the large thickness variations measured that the wt. % of aluminium within the aluminide coating is relatively consistent with the average ‘green’ measurement being ca 30 wt. %. The average post-aluminising heat treatment concentration of aluminium was ca 20 wt. %. This concentration of aluminium was consistent in both of the alloys tested, CMSX-4 and CMSX-10N. Moving to the higher temperatures of 1000°C, 1050°C and 1100°C for the standard 3 hour hold shows an intercept between the ‘green’ state aluminium concentration and the post-heat treatment level.

6.3.2. Discussion

A series of trials were undertaken to understand the conditions required to generate inadvertent carburisation during the aluminising process. Simultaneously test pieces were used to affirm any procedural changes to the aluminising process and the potential impact upon the thickness and therefore capability of the deposited aluminide.

Fig. 6.10 displays a series of SEM-BSE micrographs showing the impact of various temperature trials upon the appearance of sub-surface carbides within the alloy CMSX-4. For each temperature trial a 3 hour hold at the peak temperature was utilised as well as the 'standard' climb and cooling rate as seen in the experimental section of this chapter. The micrographs in *Fig. 6.10 (a) and (b)* show that the temperatures 800°C and 850°C are insufficient to induce the formation of carbides. This lack of carbides is positive however as can be observed in *Fig. 6.11 (a) and (b)* the thickness of the deposited aluminide is very thin and will not protect the surface of a nickel-based superalloy component. *Fig. 6.10 (c), (d) and (e)* show the impact of aluminising temperatures of 900°C, 950°C and 1000°C upon the sub-surface carbides formation respectively. The SEM-BSE micrographs clearly show that a small, relatively narrow band of carbides is present in the sub-surface layer. This supports earlier work that ca 900°C is an appropriate threshold temperature under which the likelihood of observing carbides is low and that if a process is carried out at temperatures in excess of this, carbides are likely. Turning to the complimentary images in *Fig. 6.11 (c), (d) and (e)* it can be observed that the above-the-pack aluminising process is still not effective at 900°C and 950°C. The aluminide coating microstructure in *Fig. 6.11 (e)* is approaching the thickness and visual appearance associated with a commercial and effective protective system. Unfortunately as observed in *Fig. 6.10 (e)* the level of carburisation that already appears at this temperature makes it impossible to alter the aluminide coating to eradicate the possibility of forming sub-surface carbides. The carbides within the sub-surface region of *Fig. 6.10 (f) and (g)* represent what is obtained through using temperatures of 1050°C and 1100°C respectively. Unsurprisingly the use of higher temperatures results in the formation of a densely packed carbide layer in the sub-surface which makes these temperatures inappropriate for use. The final two micrographs of *Fig. 6.11 (f) and (g)* show the thickness and appearance of the resulting aluminide layer from the 1050°C and 1100°C runs. At 1050°C the aluminide appears to be of moderate thickness and of a microstructure consistent with what is used on components today.

Fig. 6.16 shows a series of graphs that plot the measured thickness of the total aluminide, the beta layer and also the aluminium content, in wt. %, of the time – temperature trials discussed so far. *Fig. 6.16 (a)* shows the total aluminide thickness dependent upon temperature for both CMSX-4 and CMSX-10N, in the 'green' just aluminised state as well as

the post-heat treated state. The total thickness is measured from the external surface of the aluminide layer to the bottom of the interdiffusion zone which then transitions into the underlying substrate. There is a small difference between the alloys with CMSX-4 registering a slightly thicker deposited layer in the heat treated state. The thickness climbs with temperature from 850°C to 1100°C which features a maximum post-heat treated thickness of ca 40 µm upon CMSX-4 and 35 µm upon CMSX-10N. Interestingly the β thickness plotted against temperature shows no difference between the alloys and no difference between the green state and the heat treated state. For a constant deposition time the β thickness is only dependent upon the deposition temperature used, rising linearly with temperature from ca 5 µm at 900°C and to ca 20 µm at 1100°C. *Fig. 6.16 (c)* shows the aluminium content of the β phase against aluminisation temperature. The aluminium content is relatively consistent from 800°C to 950°C with a 'green' state measurement of ca 32 wt.% and a post diffusion reading of ca 20 wt. %. Once past 950°C the 'green' state aluminium content begins to drop with each temperature increment indicating that the aluminium is no longer being deposited at the same concentration though this is linked to much thicker coating at these temperatures. Additionally the higher the temperature used to deposit the aluminide the less difference is observed between the 'green' state aluminium concentration and the heat treated state, this is a result of the fact that at higher temperatures the aluminium is already in the β-phase and there is no further diffusion that can occur during the post-aluminising heat treatment.

Further to the CMSX-4 work a complimentary set of test pieces were created from the 3rd generation alloy CMSX-10N and subject to the same time-temperature aluminising variation. Results for carburisation and aluminising were largely similar to that found for CMSX-4 with 900°C being a similar threshold below which carbides were not present and above which carbides were frequently observed (*Appendix*). The sensitivity to aluminising temperature is very apparent, although there is an additional complication regarding this particular alloy; CMSX-10N appears to be unsuitable for straight aluminising upon the bare alloy. This was found when the alloy consistently generated regions of deeply penetrating secondary reaction zone (SRZ) beneath the aluminide formed at all temperatures of 950°C and above.

Further to the time-temperature trials above a series of special aluminising runs were designed to answer specific questions. *Fig. 6.12* details the impact of a standard climb to a holding temperature of 1030°C followed by only 5 minutes at temperature before the furnace was removed and the reaction vessel allowed to cool. The results show that no carbides are visible in either alloy, CMSX-4 or CMSX-10N after such a short period of time at temperature. Furthermore the aluminising results show that although an appreciable thickness of aluminide has been deposited in the ramp to temperature, a significant hold is still essential to deliver a fully formed thick effective coating. CMSX-4 and CMSX-10N show substantial SRZ formation beneath the interdiffusion zone in the post-heat treated state.

A complimentary trial was conducted and the results are shown in *Fig. 6.13*. In this work an additional hold was introduced at 700°C for a period of 1 hour before resuming the climb to 1030°C for an isothermal of 3 hours. The results show that far from enabling the carbon to diffuse away and dissipate, the interrupted climb in fact made the sub-surface carbide layer worse and even more densely packed *(Fig. 6.13 (a)*). The deposited aluminide coating upon CMSX-4 (*Fig. 6.13 (b) and (c)*) appears not to have been detrimentally affected by the temporary hold at 700°C. CMSX-10N again displays consistent and detrimental generation of an SRZ. This heavily carburised layer demonstrates this approach does not work. *Fig. 6.14 (a)* shows the results of a slow climb to 1030 for 3 hours, this approach fails to limit carbide formation and a densely packed sub-surface carbide layer is formed again. Aluminising seen in *Fig. 6.14 (b) and (c)* appears thick and microstructurally consistent. This is a result of a slower ramp enabling a greater period of time for aluminide deposition.

The results of a special series of trials are shown in *Fig. 6.15*. They focus on potential changes to the application of the M1™ maskant material to control carburisation. *Fig. 6.15 (a)* shows the impact of a 'standard' thin M1™ application and a region of densely packed carbides is clearly visible. *Fig. 6.15 (b) and (c)* shows what occurs within the sub-surface region of the alloy CMSX-4 upon a medium and thick application of the same maskant material with the carbon containing binder. What is immediately visible in *Fig. 6.15 (b) and (c)* is that there are practically no carbides and yet there is a ca 5 µm thick layer of alloy enrichment / depletion occurring. This layer is usually enriched in the element nickel, since this is the primary component of the maskant, as a result additional elements like chromium and aluminium appear lower due to the extra nickel that has diffused into the surface This seems to suggest that if an especially thick layer of normal M1™ maskant is applied then carbon is more likely to remain outside the alloy and not diffuse through to form carbides. Instead however there is this band of alloy modification that has occurred as a result of high-temperature interaction between the powdered nickel – chromium – aluminium alloy and the superalloy. This layer appears as a band of γ/γ' coarsening and the precipitation of bright white TCP phases signifying phase instability. Finally, *Fig. 6.15 (d)* shows the result of applying a thin layer of pure commercially available PVA glue to the surface of the superalloy prior to the application of the normal M1™ M7™ nickel foil masking system. The results clearly show that carburisation is featured once again supporting the earlier assessment that a hydrocarbon chain decomposing is the most likely source of the carbon. Finally *Fig. 6.15 (e)* shows what sub-surface effect can be generated by pushing a CMSX-4 bar in the powdered nickel – chromium – aluminium alloy without any carbon binder present. This microstructure features a severe SRZ which is likely generated as a result of the infinite amount of powdered material available to react at the superalloy surface due to the large steel box used to house this reaction.

6.4. Grit blasting and heat treatment

6.4.1. Results

6.4.1.1. Surface roughness measurements

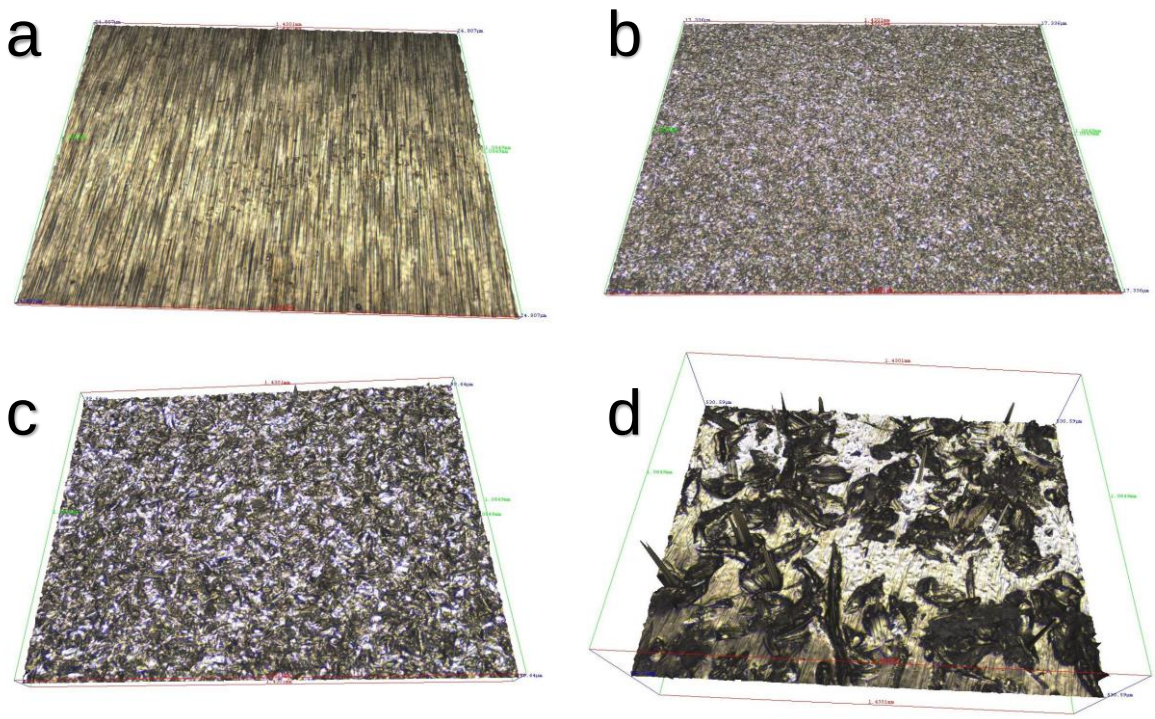

Fig. 6.18 – 3D rendered image, optical micrograph overlay upon measured roughness 3D representation, ground smooth surface finish (a), 220 mesh alumina blast at 15 PSI (b), 60 mesh alumina blast at 15 PSI (c) and 20 mesh alumina blast at 15 PSI (d)

To better understand the formation of precipitates in the sub-surface region of nickel-based superalloys it was necessary to distinguish which conditions would give rise to carbides and which would generate small TCPs. These two phenomena could easily be confused, therefore a series of grit blasting trials were undertaken to explore these features. *Fig. 6.18* shows 4 images, representative of those taken using the Alicona surface roughness measuring system. *Fig. 6.18 (a)* shows the comparatively smooth surface finish generated using surface machining techniques. This machining was used to ensure all superalloy specimens were in an identical nominal state before further testing was carried out, this also meant that surface defects and anomalies were removed to prevent contamination. *Fig. 6.18 (b)* shows a grit blasted surface using 15 PSI blasting pressure and 220 mesh alumina grit as the blasting media. Similarly *Fig. 6.18 (c)* shows the surface following a 15 PSI blast using 60 mesh alumina and *Fig. 6.18 (d)* is representative of a 15 PSI blast with 20 mesh alumina. *Fig. 6.18 (d)* shows that at low blasting pressures there is incomplete coverage and the as-machined striations can be observed upon the untouched surface between impact craters.

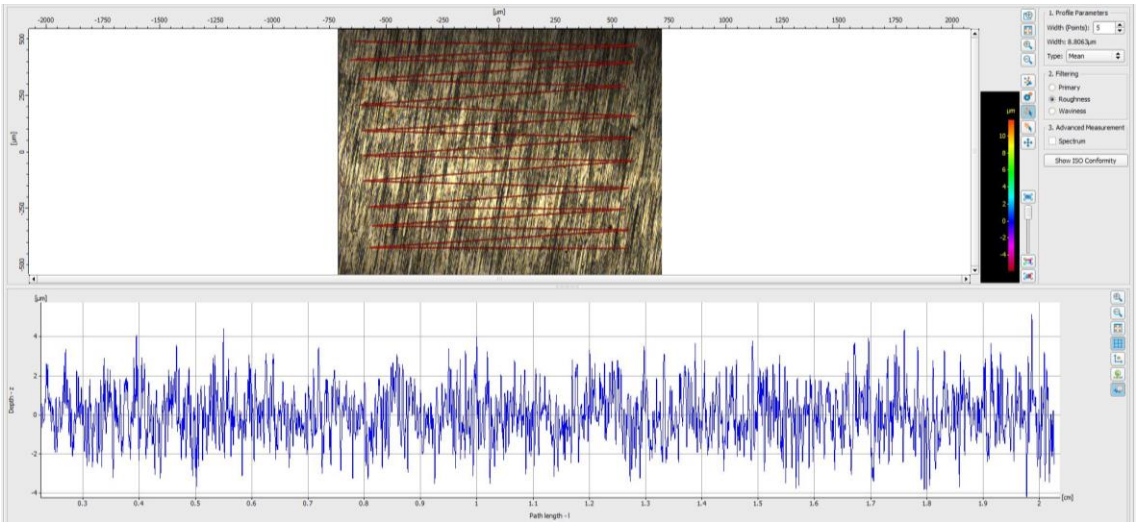

Fig. 6.19 – optical micrograph with line of data collection presented with roughness profile displayed beneath, ground smooth surface finish with no abrasive alumina blast

Once an image is captured using the Alicona system a line scan can be performed which interprets the surface undulations and generates a surface roughness profile which is representative. The red line seen in *Fig. 6.19* is the scan path and the blue spectra shown at the bottom is indicative of the kind of surface roughness trace generated. This data can be then be displayed as an Ra, Rz or Rq value depending upon application and preference.

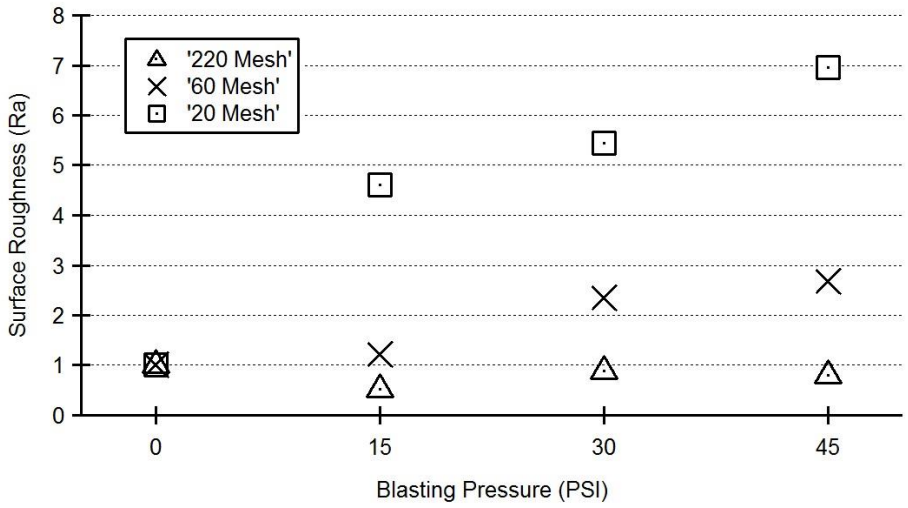

Fig. 6.20 – Alicona data for effect of blasting upon the alloy CMSX-4 for resulting surface roughness, graph shows blasting pressure versus surface roughness in Ra using three different sizes of alumina mesh

Fig. 6.20 shows a graph detailing collated data of grit blasting upon the alloy CMSX-4. The 220 mesh alumina grit blast at 15, 30 and 45 PSI shows a ‘smoother’ surface finish than the original ground surface with an Ra of ca 1.0. Using 60 mesh alumina media at 15, 30 and 45 PSI generates surface roughness of Ra of 1.2, 2.4 and 2.8 respectively. Using 20 mesh alumina at 15, 30 and 45 PSI yielded roughness in Ra of 4.7, 5.4 and 7.0 respectively.

6.4.1.2. Scanning electron microscopy

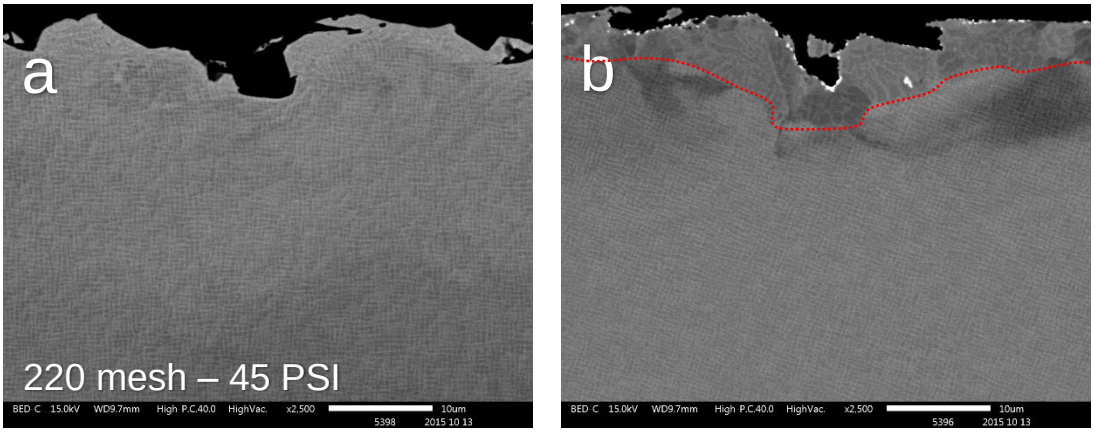

Fig. 6.21 – SEM micrographs effect of grit blasting CMSX-4 with 220 mesh alumina grit at 45 PSI, post-blast (a), post-heat treatment (b)

Following grit blasting the nickel-based superalloy, in this instance CMSX-4, was sectioned and subject to metallurgical preparation before being imaged using an SEM. The remaining material was subject to a heat treatment to mimic the thermal profile experienced during aluminising. This thermal treatment was conducted within a VFE vacuum furnace under a partial pressure of argon. Once heat treated the sample was examined using the same SEM-BSE technique. This set of trial attempted to determine whether the level of plastic deformation and stress imparted to the nickel-based superalloy via grit blasting was sufficient to induce the precipitation of potentially deleterious phases during a subsequent high-temperature thermal exposure. *Fig. 6.21 (a)* shows the microstructure at the surface of the test piece of CMSX-4 following a grit blast of 45 PSI blasting pressure using a media of 220 mesh alumina grit. As can be observed there is very little visible deformation of the gamma/gamma prime except within the uppermost 2 – 4 µm. The micrograph to the RHS, *Fig. 6.21 (b)* shows the same grit blasted sample after the 6 hour 1030°C thermal exposure within the vacuum furnace which aimed to mimic the time and temperature experienced within a standard aluminising CVD run. Observed within this micrograph is a region of discontinuous coarsening of the γ/γ' microstructure in the immediate sub-surface region. This layer extends to a depth of ca 5 µm and is not continuous along the surface, its appearance is linked to the appearance of a 'rough' surface indicating the impact of 220 mesh grit during the earlier surface treatment. There are no precipitates within the discontinuous coarsening (DC) region nor were there any indications of recrystallisation since this material was in the aged state and much greater stress is necessary to generate the formation of RX grains.

Fig. 6.22 displays micrographs regarding grit blasting the alloy CMSX-4 with 60 mesh alumina grit at blasting pressures of 15, 30 and 45 PSI.

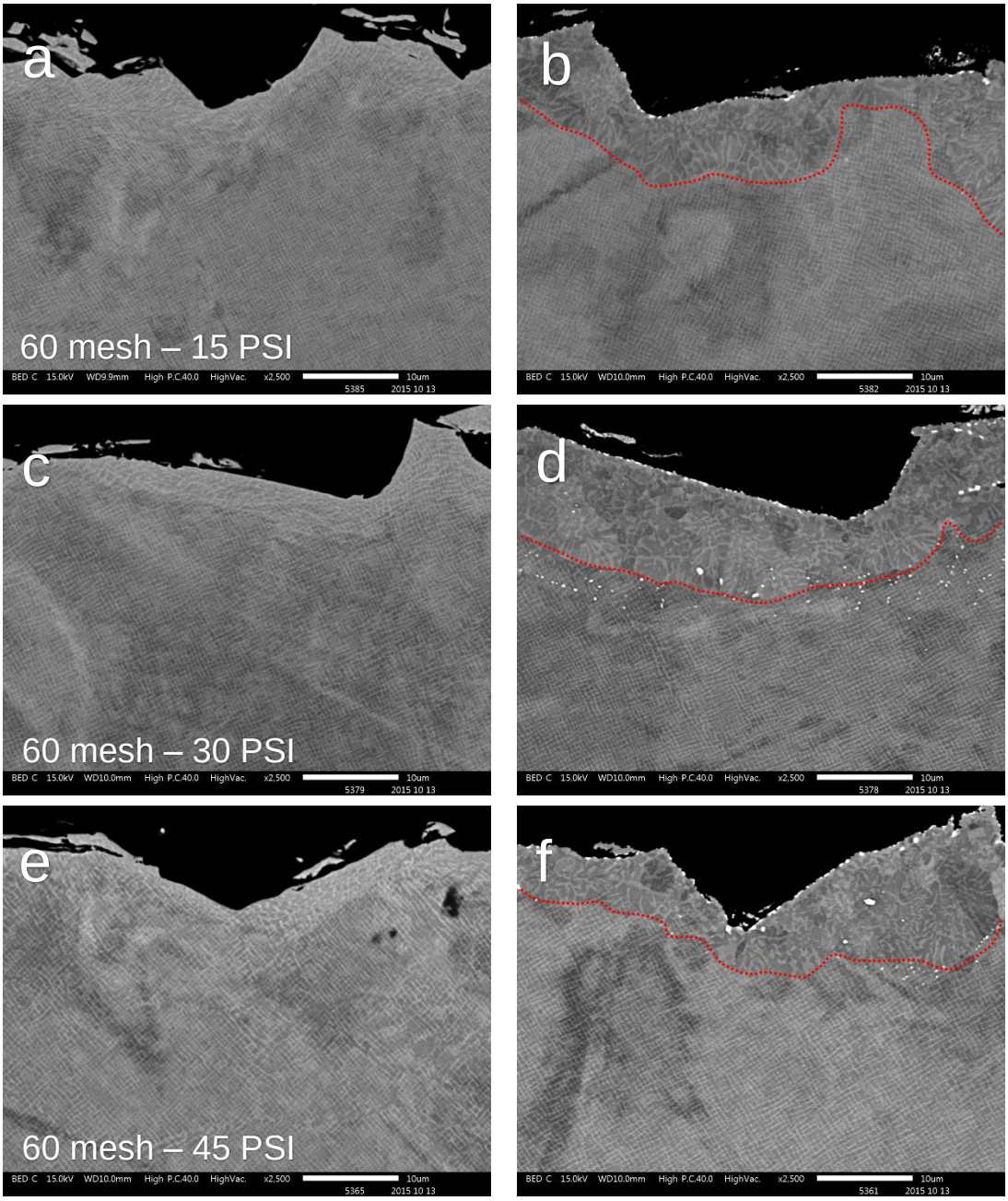

Fig. 6.22 – SEM micrographs effect of grit blasting CMSX-4 with 60 mesh alumina grit at 15, 30 and 45 PSI, post-blast (a, c, e), post-heat treatment (b, d, f)

The images of *Fig. 6.22* show the superalloy microstructure before and after the thermal heat treatment, in all three instances attempts were made to find similarly shaped surface features to best draw parallels. *Fig. 6.22 (a) and (b)* shows the effect of a 60 mesh blast at 15 PSI, the level of microstructural deformation is greater than previously observed and there is clear evidence that post-heat treatment there is the presence of regions of discontinuous coarsening of the γ/γ', this extends from the surface to a depth of ca 10 μm. *Fig. 6.22 (c) and (d)* show the impact of 60 mesh alumina blasting at pressures of 30 PSI. Observations can be made of greater levels of DC as well as a series of small bright precipitates, most likely TCPs, forming immediately beneath this DC layer.

Fig. 6.22 (e) and (f) show the effect of 60 mesh alumina at a blasting pressure of 45 PSI. The effect is similar and sees the generation of a DC gamma/gamma prime microstructure and the precipitation of small TCPs in the alloy immediately beneath the DC region.

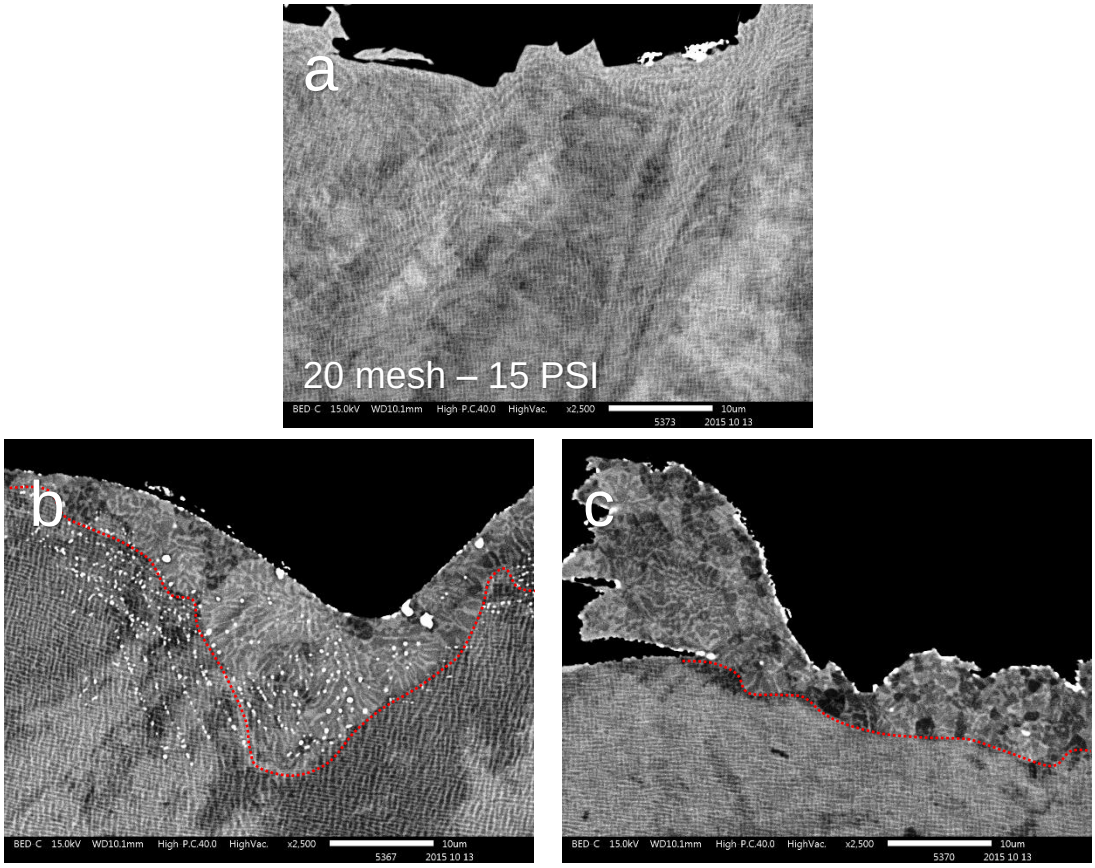

Fig. 6.23 – SEM micrographs effect of grit blasting CMSX-4 with 20 mesh alumina grit at 15 PSI, post-blast (a), post-heat treatment (b and c)

Fig. 6.23 shows SEM-BSE micrographs detailing the impact of 20 mesh alumina grit blast at 15 PSI. *Fig. 6.23 (a)* shows the blasted microstructure and displays moderate plastic deformation and the contortion of the γ/γ' microstructure. It is this deformation which is responsible for further microstructural developments during heat treatment. *Fig. 6.23 (b) and (c)* both show the grit blasted microstructure post-heat treatment, *(b)* shows a region of discontinuous coarsening of the γ/γ' with integrated discontinuous precipitation of TCP phases within the DC region. At its deepest the DC/DP region extends to a depth of ca 20 µm. Further to this region there is an array of TCPs that have precipitated in the superalloy beneath the DC/DP region in delineated patterns. The TCPs observed in *Fig. 6.23 (b)* are small and individual yet form in straight lines. *Fig. 6.23 (c)* shows the same post-heat treated grit blasted surface in another location, this image neatly encapsulates the effect that blasting can have upon the superalloy surface. Part of the surface has received an impact from the 20 mesh grit which lifts the surface, wave-like, this deformed portion is then left upon the surface and experiences severe DC as a result.

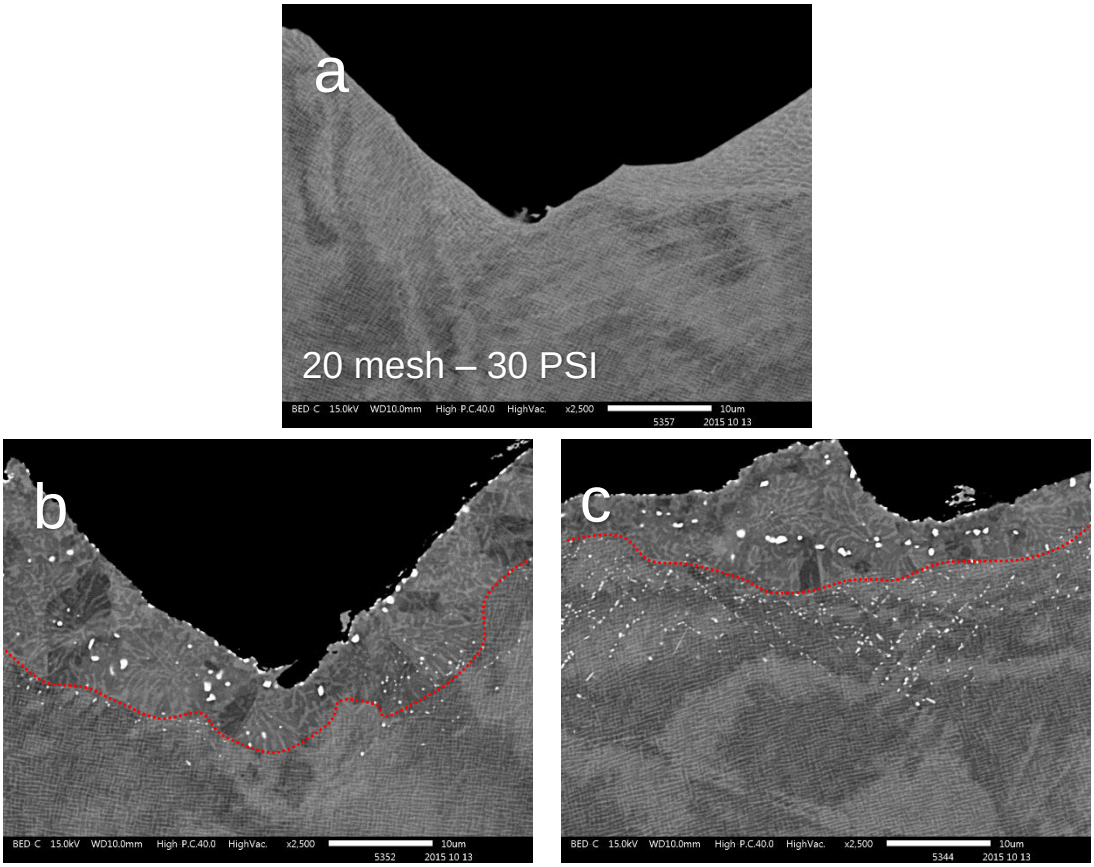

Fig. 6.24 – SEM micrographs effect of grit blasting CMSX-4 with 20 mesh alumina grit at 30 PSI, post-blast (a), post-heat treatment (b and c)

Fig. 6.24 shows SEM-BSE micrographs detailing the impact of 20 mesh alumina grit blast using a pressure of 30 PSI upon the alloy CMSX-4. *Fig. 6.24 (a)* shows the superalloy microstructure post-blasting, the γ/γ' is distorted and plastically deformed by the impact of alumina grit. There are clear lines or bands which cross the SEM-BSE image of *Fig. 6.24 (a)* in the region beneath the more apparent plastically deformed zone at the upper surface. *Fig. 6.24 (b) and (c)* show the same blasted surface following the thermal heat treatment. *Fig. 6.24 (b)* shows extensive discontinuous coarsening and TCP formation both within the DC region and immediately beneath within what appears nominally to be un-affected superalloy. *Fig. 6.24 (c)* shows an additional micrograph of the sub-surface region which features DC, DP and TCP formation, in this case however the TCPs forming beneath the DC region again follow strict linear placement. The total depth of deleterious phases and features is ca 25 – 30 μm.

Fig. 6.25 shows further SEM-BSE images which detail the result of using 20 mesh alumina grit to blast the alloy CMSX-4 at a blasting pressure of 45 PSI. *Fig. 6.25 (a)* shows the post-blasted surface prior to heat treatment. The SEM micrograph clearly details severe plastic deformation and the presence of extraordinarily high levels of dislocations and sub-surface damage.

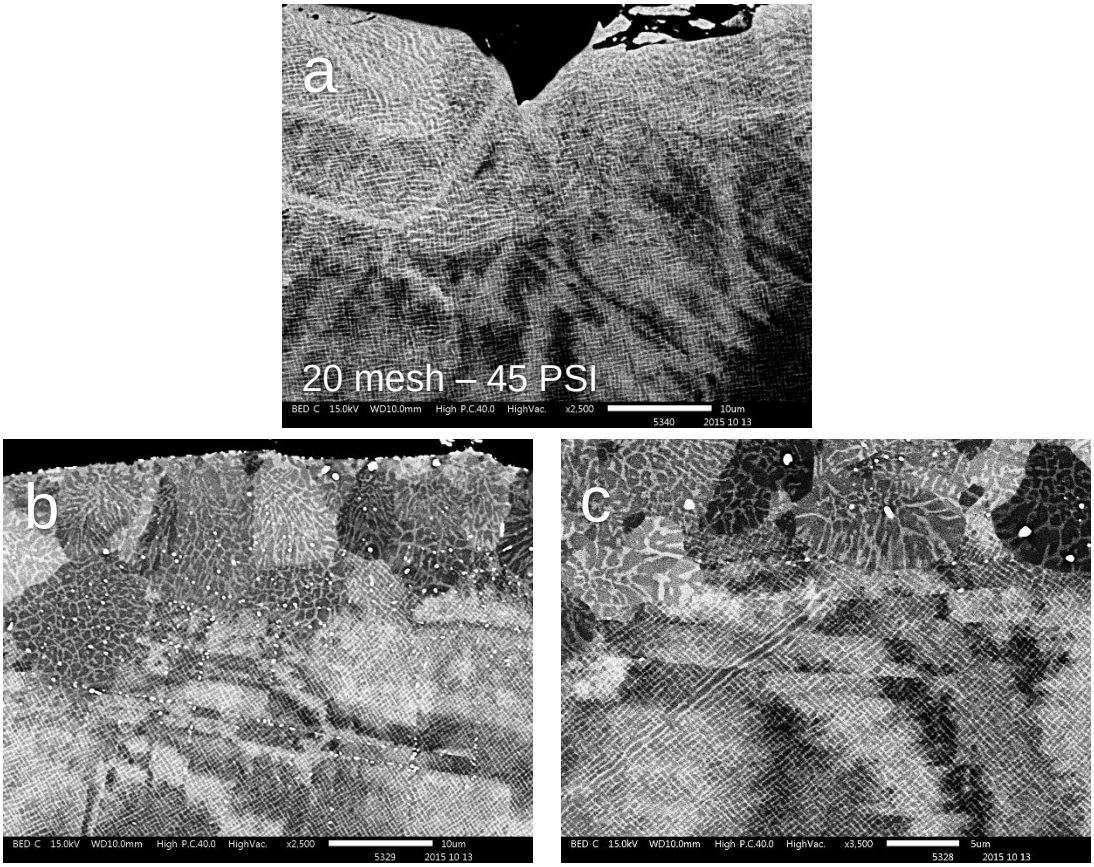

Fig. 6.25 – SEM micrographs effect of grit blasting CMSX-4 with 20 mesh alumina grit at 45 PSI, post-blast (a), post-heat treatment (b and c)

Fig. 6.25 (b) and (c) detail the result of heat treating the aforementioned grit blasted surface. *Fig. 6.25 (b)* shows severe levels of γ/γ' discontinuous coarsening, DP, the precipitation of TCP phases both within the DC/DP region and beneath, again following prescribed straight line routes. In addition to this damage the sub-surface region immediately beneath the outer surface shows clear evidence of recrystallisation. These grains are integrated with the DC/DP region and display as areas of bright or darker contrast which sets each grain apart from the ones either side. *Fig. 6.25 (c)* is at a higher magnification and focusses upon the superalloy immediately beneath the DC/DP region, there are linear features that are parallel to the direction of the surface and are the result of the grit blast impact, in this instance TCPs are not observed to have formed but the feature is otherwise identical to that seen in *Fig. 6.25 (b).*

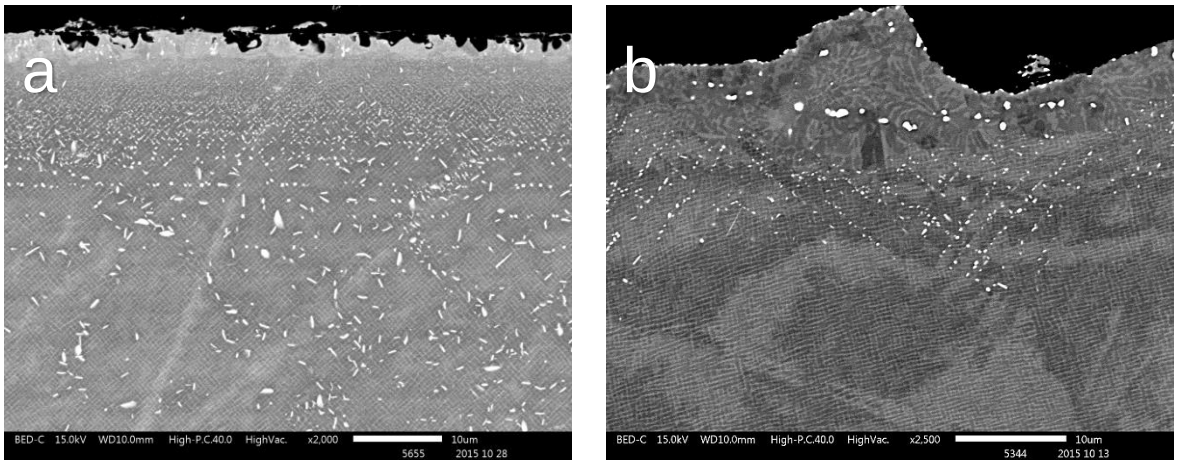

Fig. 6.26 – SEM micrograph ground surface finish carburised sub-surface region upon alloy CMSX-4 (a), an image taken from earlier in this chapter as a good example of the kind of small TCPs that form and can easily be mistaken for carbides (b)

A trial was conducted to determine the average microstructural appearance of the alloy CMSX-4 following interaction with the maskant material M1™ used to protect the superalloy surface during the aluminising process. This maskant was identified in chapter 5 as being the source of carbon for the inadvertent carburisation of the sub-surface layer. These trials were conducted upon the alloy with a machined ground surface finish to prevent conditions that favour the formation of small TCP phases which are easily mistaken for carbides. *Fig. 6.26 (a)* shows the sub-surface microstructure of the alloy CMSX-4 after being masked using the M1™ slurry material and having been subjected to an aluminising run. There is a densely packed layer of pinpoint carbides extending from the alloy surface to a depth of ca 20 μm. This carbide layer then begins to thin out with less carbides being observed but those that exist are larger in size. There is a narrow layer upon the alloy extreme upper surface which is shown as a brighter layer ca 2 – 3 μm in thickness. This layer is a result of alloy enrichment / depletion effects generated by the metal powder component of the maskant M1™ material. Moving further down within the CMSX-4 alloy the carbides change morphology to larger platelet precipitates that appear both randomly within the ‘normal’ γ/γ’ and preferentially along low energy pathways that wind through the microstructure. These pathways have been referred to anecdotally as ‘river-lines’ and are believed to be related to either the ‘memory’ of impinging secondary arm dendrites that have been mostly erased during the solutioning heat treatment or else dislocation networks.

6.4.2. Discussion

The aim of these trials was to explore the impact of grit blasting using different sized alumina media at different blasting pressures upon the alloy CMSX-4 which must often undergo a subsequent heat treatment. This work was used to determine the tendency for the superalloy to form deleterious phases as a result of the deformation and subsequent high temperature exposure to ensure that small carbide precipitates were not being mistaken for equally small TCPs.

Fig. 6.17, 6.18 and 6.19 explore the surface roughness that is generated using alumina grit sized from 220 mesh (ca 60-75µm particle size) up to 60 (ca 250µm) and then finally 20 mesh (ca 850µm) which the largest size of grit used. As can be seen in these images the size of grit is understandably linked to the kind of surface roughness that is generated as a result of the blasting procedure. Interestingly as can be seen in *Fig. 6.19* the 220 mesh blast results in a more homogeneous surface than the original grinding machining operation used to ensure that all test pieces were starting from the same condition. Blasting using 60 or 20 mesh alumina results in an increase in surface roughness, measured using the Ra scale.

Once samples of CMSX-4 were blasted using these procedures they were subject to a heat treatment profile that reflects that experienced during the aluminising CVD run. This means that parts of the blasted specimens were placed within the vacuum furnace and exposed to a 6 hour run at 1030°C under a partial pressure of argon. This was carried out in order to remove the otherwise confusing effects of maskant interaction M1™ or aluminising which also affects the surface.

The results of these trial are observed in *Fig. 6.20, 6.21, 6.22, 6.23 and 6.24*. There is a clear progression in terms the amount of plastic deformation that must be accommodated by the material as the grit size is increased. In *Fig. 6.20 (a)* it can be seen that using 220 mesh at 45 PSI results in very low levels of plastic deformation and it is confined to the surface of the part. Then in *Fig. 6.20 (b)* the subsequently heat treated material can be seen to experience mild discontinuous coarsening of the γ/γ’ which is again confined to the surface and does not extend deeper than ca 4 µm.

Moving up to an alumina grit mesh size of 60 results in a more pronounced effect upon the superalloy surface. *Fig. 6.21 (a), (c) and (e)* show progressively the impact of a 60 mesh grit at 15, 30 and 45 PSI respectively. Clearly visible in these micrographs is a moderate level of sub-surface deformation and precipitate shearing. The γ/γ’ is misshapen as a result of the grit particle impact and the outer surface features deformed grooves. The micrographs in *Fig. 6.21 (b), (d) and (f)* show what happens the grit blasted surface after high temperature exposure. Beneath the still misshapen surface there is very clear evidence of moderate discontinuous coarsening of the γ/γ’ as well as discontinuous precipitation of TCP phases,

most likely P-phase according to literature and the morphology adopted. These TCPs are mostly confined to the region of DC/DP yet can also be observed beneath this layer and appear to precipitate within material that nominally at this magnification appears unaffected by the grit blast, however the formation of these TCPs shows that this is not the case.

The last mesh size to be used in these trials was 20 mesh alumina the results of blasting with a fixed pressure of either 15, 30 or 45 PSI are shown in *Fig. 6.22, 6.23 and 6.24* respectively. The impact of the blast upon the microstructure is observed in *Fig. 6.22 (a)* and there are severe levels of plastic deformation in the sub-surface region and large regions of the γ/γ' microstructure have been warped by the impact. The micrographs in *Fig. 6.22 (b) and (c)* then show what occurs at the surface as a result of the subsequent heat treatment. In the first micrograph there is a region of DC/DP which extends deeply in the substrate. In addition there is widespread TCP formation both confined the DC/DP zone and also beneath. In this instance the region beneath features very small TCPs that have formed in straight lines having being precipitated along a linear slip band that has been generated within the material as a result of the blast and thermal exposure. The second micrograph in *Fig. 6.23 (c)* shows a wave-like structure which emerges from the superalloy and appears to be in the process of falling back upon the material on the LHS of the image. This micrograph very clearly demonstrates that for the nickel-based superalloys the act of grit blasting not only removes material but more importantly churns material around upon the surface without actually removing it. The superalloy microstructure within the wave-form has been obliterated and nothing remains of the original γ/γ'. This illustrates the forces that can be exerted upon the material in highly localised regions as a result of grit blasting.

Fig. 6.23 (a) displays the result of blasting at 30 PSI using 20 mesh alumina. Again the surface has been heavily deformed and the resulting superalloy microstructure undergoes transformation as a result of the heat treatment, these micrographs are seen in *Fig. 6.23 (b) and (c)*. These micrographs show yet more DC/DP regions which extend even deeper into the substrate. In addition there is now a densely packed region of very small TCPs in the substrate microstructure immediately beneath the DC/DP zone.

Finally *Fig. 6.24* shows the most extreme trial results that of the 20 mesh alumina and 45 PSI of blasting pressure. The level of damage that has been imparted into the material using this blasting regime is severe. *Fig. 6.24 (b) and (c)* clearly shows recrystallisation, heavy coarsening of the γ/γ' and the formation of linear features that show frequent TCP formation. This kind of microstructure, whilst formed using extreme conditions, is unacceptable and not suitable for service. In the next section of this chapter a number of further trials are explored and discussed regarding the effect of using platinum plating or aluminising upon the grit blasted surface and the prevalence of defect formation both within the coating microstructure and beneath it.

To finish this section of the chapter a specimen of the original ground smooth CMSX-4 was coated in the M1™ maskant material and exposed to an aluminising run. The purpose of this trial was to provide a direct comparison between the kind of sub-surface precipitates that form within the alloy as a result of the carburisation phenomena as opposed to those formed as a result of plastic deformation and subsequent heat treatment only as already discussed. *Fig. 6.25* shows an SEM-BSE micrograph of the carburised sub-surface. Clearly observed are very small pinpoint carbides that have been previously discussed in chapter 5 as well as the larger more platelet shaped precipitates deeper down. These precipitates are definitely carbides and not TCPs, this has been proven by careful application of maskant materials and the use of materials in the as-machined ground surface finish state, it has not received a grit blast and therefore cannot have generated TCPs in the manner already discussed. The micrographs displayed in *Fig. 6.26* is at a higher magnification but does also show the carburised layer described. This series of images is interesting since it provides evidence of the alloy enrichment/depletion effect that occurs at the extreme outer surface as a result of interaction between the powdered metal alloy component of the maskant and the underlying superalloy. This reaction is separate to the carburisation which can be observed beneath this outer layer. From the shape and morphology of these precipitates featured in *Fig. 6.26* it can again be claimed with confidence that these are small cubic pinpoint carbides and not TCPs.

6.5. Grit blasting, platinum plating and aluminising – full processing cycle

6.5.1. Results

6.5.1.1. Scanning electron microscopy – ground, grit blasted, platinum plated, diffused

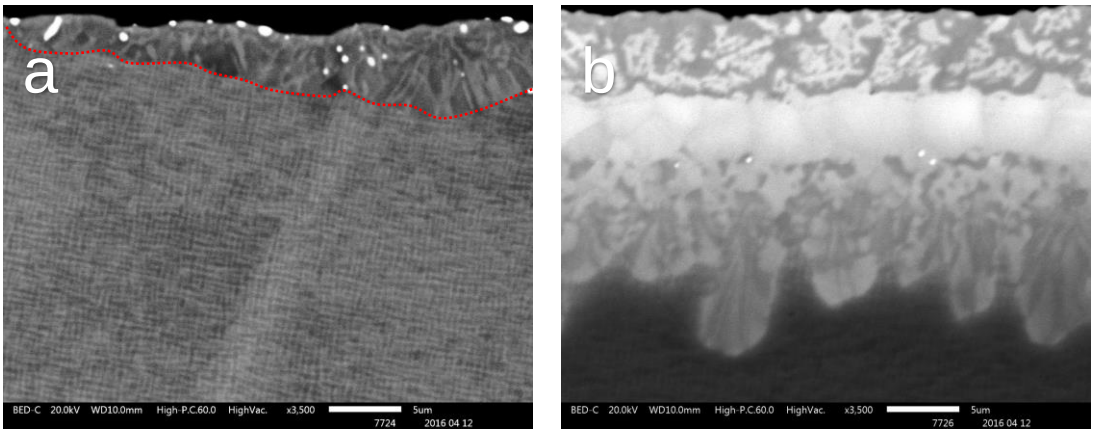

Fig. 6.27 – SEM micrographs ground smooth surface finish CMSX-4 exposed to platinum plating diffusion heat treatment 1 hour 1100°C (a), diffused platinum plating layer upon ground smooth CMSX-4 (b)

A trial was conducted to investigate the effect of grit blasting upon the nickel-based superalloys CMSX-4 and CMSX-10N as well as the impact of subsequent platinum plating and diffusion heat treatment. *Fig. 6.27* details the control sample which featured a machined ground smooth surface finish. This CMSX-4 test piece was then partially coated using electrodeposition of platinum plating and an inert plastic masking tape. This meant that the same test piece received the machining operation and was then 50% coated in platinum. This entire test piece was then subject to the standard platinum diffusion heat treatment of 1 hour at 1100°C in vacuum furnace under a partial pressure of argon. *Fig. 6.27 (a)* compares these two regions of the control sample. The formation of discontinuous coarsening of the γ/γ' and the precipitation of TCPs in the discontinuous precipitation region all immediately beneath the external surface. In *Fig. 6.27 (b)* shows the platinum plated area and shows interdiffusion between the deposited, still separate platinum layer, and the underlying superalloy substrate, in this instance CMSX-4. There is good intermixing in the diffused platinum example and no coarsening of the γ/γ' and no TCP phases.

Once the control microstructure was fully understood a series of grit blasting trials were undertaken. *Fig. 6.28* details the micrographs that show the impact of a constant blasting pressure of 45 PSI and alumina grit blasting media moving from the smallest at 220 mesh to 60 mesh and finally the largest grit at 20 mesh. Then 50% of the superalloy specimen was coated in platinum plating and the entire bar was subject to the diffusion heat treatment.

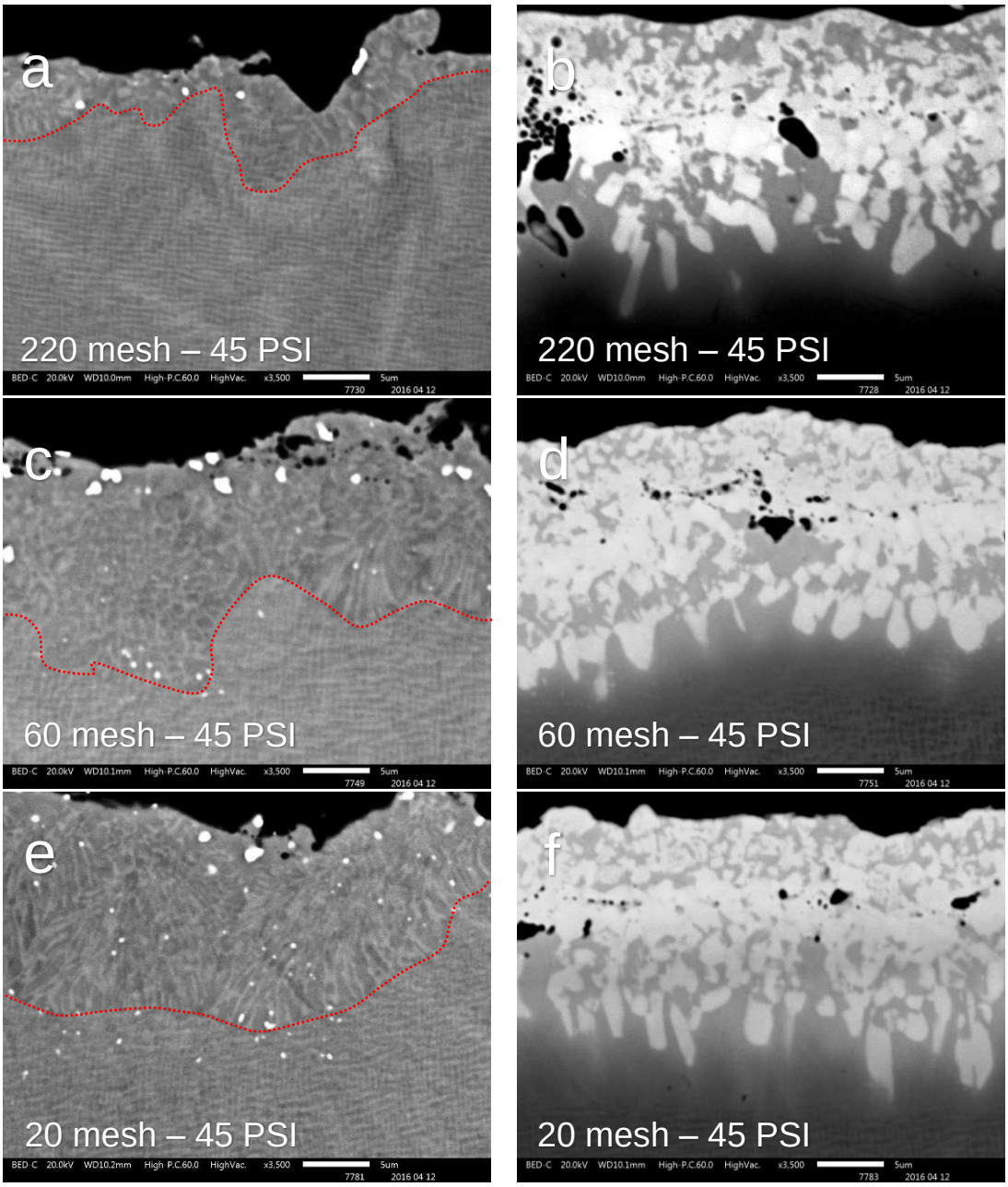

Fig. 6.28 – SEM micrographs grit blasted surface finish CMSX-4 exposed to platinum plating diffusion heat treatment 1 hour 1100°C after 45 PSI blast with 220 mesh alumina (a), 60 mesh (c), 20 mesh (e), diffused platinum plating layer upon grit blasted surface CMSX-4 at 45 PSI with 220 mesh alumina (b), 60 mesh (d) and 20 mesh (f)

Blasting with 220 mesh alumina at 45 PSI and using a subsequent heat treatment yields a narrow band of DC and the precipitation of small, infrequent TCPs (*Fig. 6.28 (a)*). Following platinum plating and diffusion of the blasted surface shows a standard diffused platinum layer, in *Fig. 6.28 (b)* it can be observed that a layer ca 10 µm thick of diffused platinum generates a total layer thickness of 25 µm including the interdiffusion zone. There are frequent black features that appear at the interface between the platinum layer and the

interdiffusion zone which indicates the location of the original interface prior to platinum plating, this is termed the ‘grit-line’.

Increasing the grit size from 220 to 60 mesh and keeping the blasting pressure constant at 45 PSI yields the microstructure observed in *Fig. 6.28 (c).* The depth of DC can been observed to extend to a depth of ca 20 μm and there are frequent TCP precipitates within the coarsened γ/γ’ microstructure. In the platinum plated equivalent the microstructure is nominally the same as previous examples, a grit-line and a nominal diffused platinum layer. There are no precipitates beneath the layer.

Using 20 mesh alumina during the grit blasting meant that additional plastic deformation occurred in the sub-surface region. After subsequent heat treatment a region of DC/DP was generated that penetrated the superalloy to a depth of ca 25 μm. In addition to the coarsening of the γ/γ’ there is a moderate appearance of small TCPs both within the coarsened region and beneath (*Fig. 6.28 (e)*). The application of a platinum layer to this surface resulted in nominally the same diffused platinum plating appearance microstructurally.

6.5.1.2. Scanning electron microscopy – following aluminising, carburising, diffusion

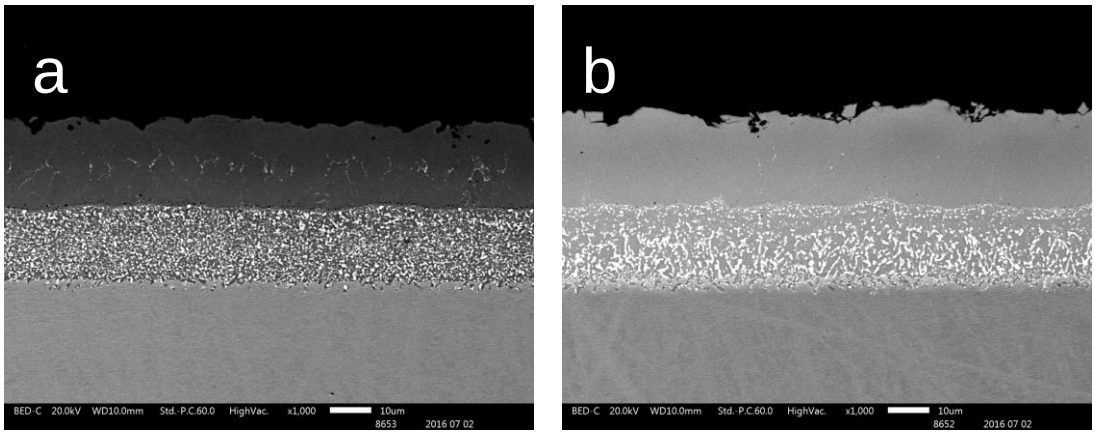

Fig. 6.29 – SEM micrographs ground smooth surface finish CMSX-4 exposed aluminising process 6 hours 1030°C (a), diffused platinum aluminide layer upon ground smooth CMSX-4 (b)

To continue replicating the HP turbine blade manufacturing process for this test pieces the CMSX-4 test bars were subject to partial coating in the M1™ maskant and then subject to an aluminising cycle at 1030°C. This meant that four discrete surface events could be investigated, firstly the effect of either a ground or grit blasted surface upon the formation of a standard aluminide or a platinum-aluminide as shall be shown here as well as the impact of a ground or grit blasted surface upon the impact of inadvertent carburisation during the aluminising cycle upon masked surfaces. *Fig. 6.29 (a)* shows the nominal microstructure of a machined ground surface being aluminised for 6 hours at 1030°C during the above-the-pack process. *Fig. 6.29 (b)* shows the same CMSX-4 which has received a platinum plating layer and subsequent diffusion process prior to the aluminising process. This is a platinum-aluminide coating and as can be seen in both instances there is good, consistent coverage, without gaps in the protective coating and an interdiffusion zone at the interface between the coating and the substrate free of deleterious phase formation in the form of an SRZ. The microstructure of the superalloy CMSX-4 beneath both coatings is completely devoid of carbides, TCPs or DC/DP features.

To continue this set of trials samples of the alloy CMSX-4 were subject to a range of grit blasting parameters. For clarity only the 45 PSI blast pressure images are shown in *Fig. 6.30*. Three different alumina grit sizes were selected, with 220 mesh, 60 mesh and 20 mesh having been used. *Fig. 6.30 (a) and (b)* show the impact of a 220 mesh 45 PSI blast upon the alloy surface prior to aluminising or platinum-aluminide coating formation respectively. The structures are normal and acceptable, they feature the presence of a grit-line as a result of blasting. *Fig. 6.30 (c) and (d)* show the impact of a 60 mesh 45 PSI blast prior to aluminising and platinum-aluminide coating formation respectively. There is sporadic appearance of a discontinuous coarsening / precipitation effect under the interdiffusion zone.

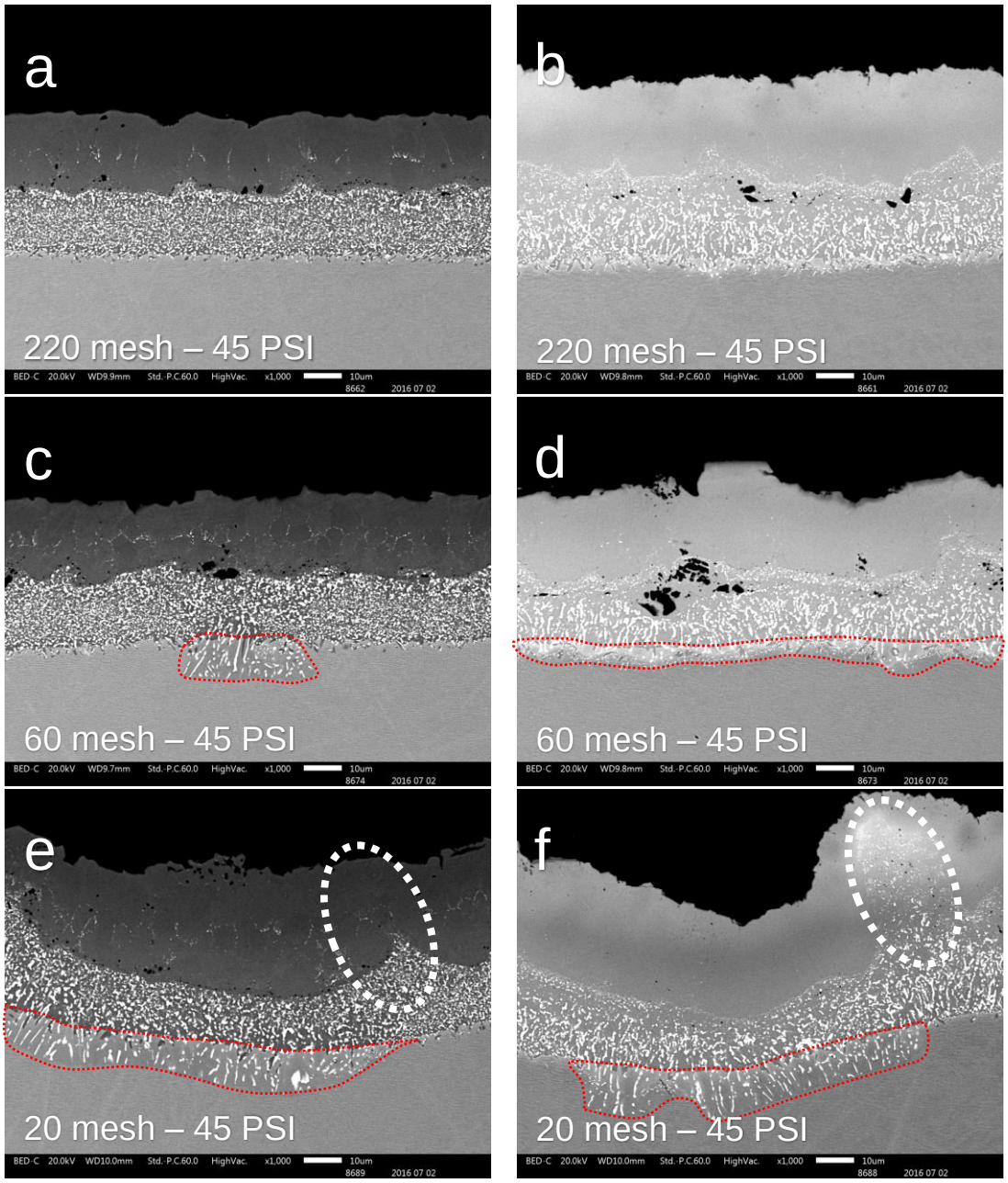

Fig. 6.30 – SEM micrographs grit blasted surface finish CMSX-4 exposed to aluminising and post diffusion heat treatment 1 hour 1100°C after 45 PSI blast with 220 mesh alumina (a), 60 mesh alumina (c), 20 mesh alumina (e), diffused platinum aluminide layer upon grit blasted surface CMSX-4 at 45 PSI with 220 mesh alumina (b), 60 mesh alumina (d) and 20 mesh alumina (f)

Fig. 6.30 (e) and (f) show the result of blasting with 20 mesh alumina at 45 PSI prior to aluminising and platinum-aluminising respectively. There is an undulating surface due to the excessive blasting parameters and beneath the interdiffusion zone in both instances there is consistent secondary reaction zone (SRZ). *Fig. 6.30 (f)* shows that a heavily roughened surface has led to additional platinum being deposited upon the ‘peaks’ and the ‘valleys’ having been potentially poorly plated as a result.

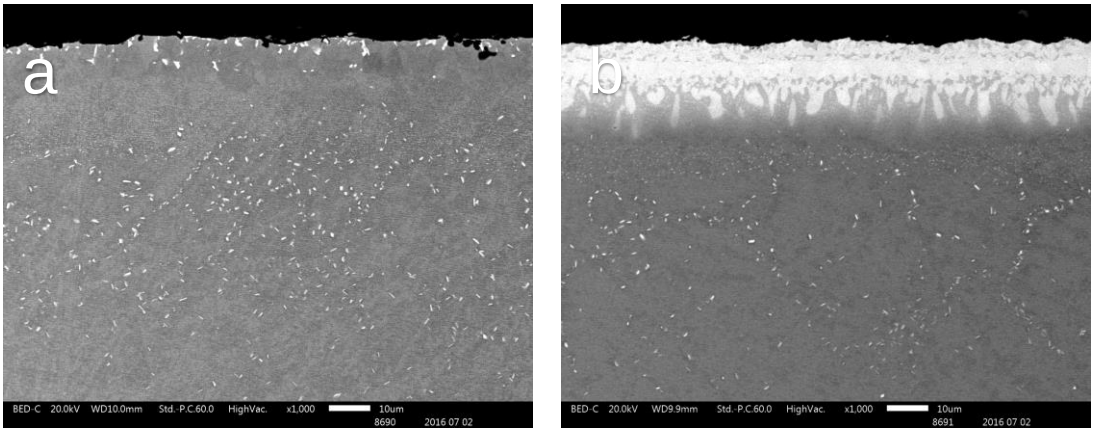

Fig. 6.31 – SEM micrographs ground surface finish CMSX-4 exposed to carburising maskant interaction (a), diffused platinum plating layer upon ground smooth CMSX-4 exposed to carburising maskant interaction (b)

A final trial was conducted to determine the microstructural appearance of the uncoated and platinum plated alloy CMSX-4 following interaction with the maskant material M1™ used to protect the superalloy surface during the aluminising process. These trials were initially conducted upon the alloy with a machined ground surface finish to once again prevent conditions that favour the formation of small TCP phases which are easily mistaken for carbides. *Fig. 6.31 (a)* shows the sub-surface microstructure of CMSX-4 after masking and aluminising. There is a densely packed layer of pinpoint carbides extending from the alloy surface to a depth of ca 50 µm. This carbide layer then begins to thin out but those that exist are larger. There is a narrow layer upon the alloy's extreme upper surface which is shown as a brighter layer ca 5 µm in thickness. This layer is again a result of alloy enrichment/ depletion effects generated by the metal powder component of the maskant M1™.

The same alloy CMSX-4 was platinum plated and was subject to the same trial detailed above, using a machined ground surface finish the test piece was plated before being coated using the M1™ maskant and placed within an aluminising CVD run. *Fig. 6.31 (b)* shows the alloy microstructure in the sub-surface region. There is a carbide-rich region extending from the bottom of the interdiffusion zone to a depth of ca 20 µm, this region is very densely packed with small pinpoint carbides. No small thin band of alloy enrichment/depletion can be observed at the uppermost of the alloy due to the presence of the bright platinum layer deposited upon the surface. There is no observable presence of platelet carbides within the sample yet those larger pinpoint carbides appear to show preferential formation along low energy pathways winding through the pre-existing superalloy gamma/gamma prime microstructure.

To finish this trial samples of CMSX-4 were subject to a range of grit blasting parameters prior to platinum plating and then carburising through maskant interaction *(Fig. 6.32)*.

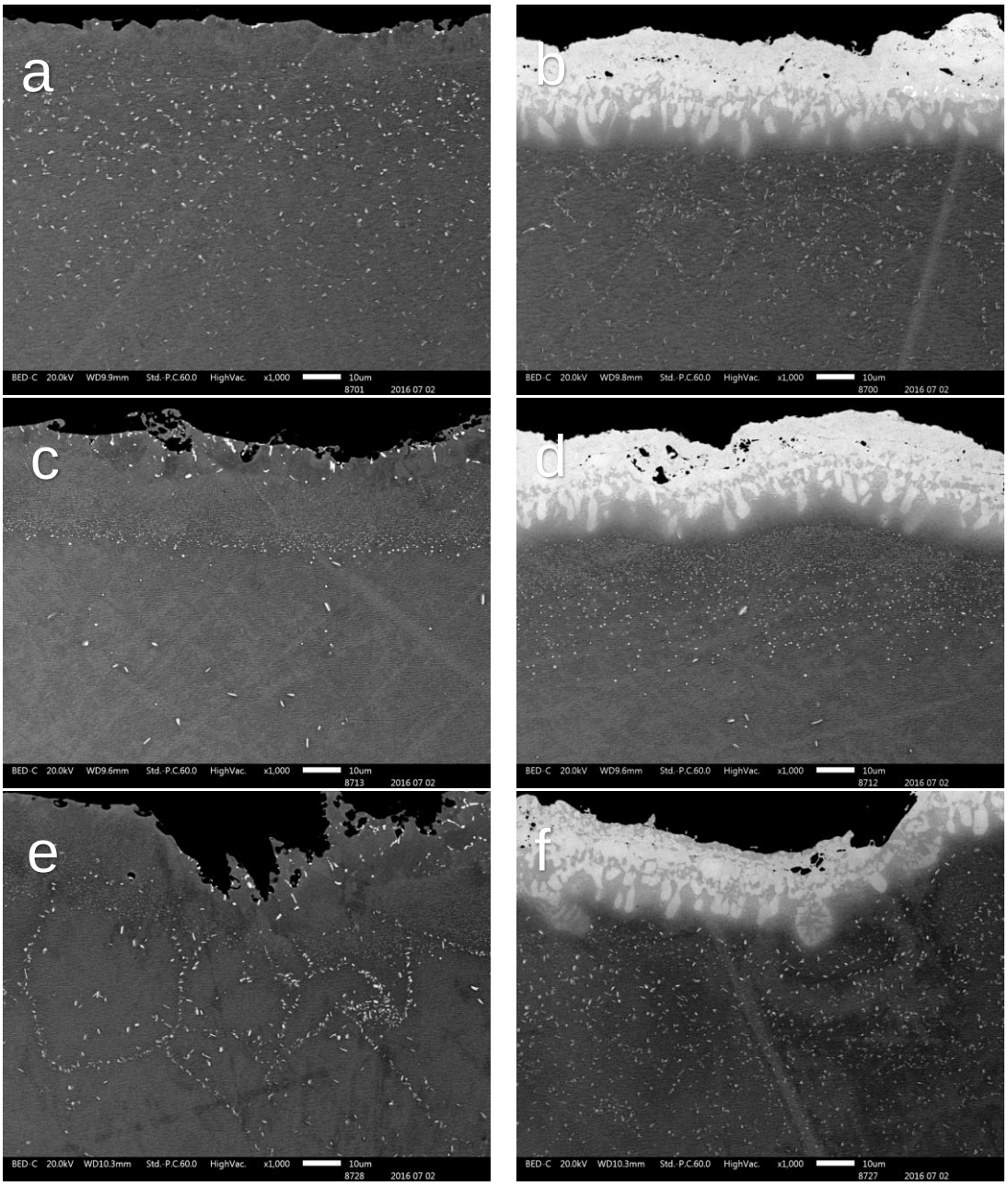

Fig. 6.32 – SEM micrographs grit blasted surface finish CMSX-4 exposed to carburising maskant interaction after 45 PSI blast with 220 mesh alumina (a), 60 mesh alumina (c), 20 mesh alumina (e), diffused platinum aluminide layer upon grit blasted surface CMSX-4 exposed to carburising maskant interaction at 45 PSI with 220 mesh alumina (b), 60 mesh alumina (d) and 20 mesh alumina (f)

For clarity only the 45 PSI blast pressure images are shown in *Fig. 31*. Three different alumina grit sizes were selected, with 220 mesh, 60 mesh and 20 mesh having been used. *Fig. 6.32 (a) and (b)* show the impact of a 220 mesh 45 PSI blast upon the alloy surface prior to carbide formation upon uncoated and platinum plated surfaces respectively. The microstructures both feature densely packed pinpoint carbides extending from the surface into the substrate to a depth of ca 100 µm. *Fig. 6.32 (c) and (d)* shows the impact of a 60 mesh 45 PSI blast prior to carbide formation upon uncoated and platinum plated surfaces

respectively. The microstructures both feature very densely packed pinpoint carbides extending from the surface into the substrate to a depth of ca 30 μm.

Fig. 6.32 (e) and (f) show the result of blasting with 20 mesh alumina at 45 PSI prior to carbide formation upon uncoated and platinum plated surfaces respectively. There is again an undulating surface due to the excessive blasting parameters and both microstructures feature very densely packed pinpoint carbides extending from the surface into the substrate to a depth of ca 100 μm. There is no observable presence of platelet carbides within the sample yet larger carbides appear to show heavy preferential formation along low energy pathways winding through the pre-existing superalloy γ/γ’ microstructure.

6.5.2. Discussion

The experiments outlined in section 6.5 follow on directly from those discussed in section 6.4. The SX alloy CMSX-4 when subject to grit blasting as a preparation for coating deposition can yield small TCPs and region of discontinuous coarsening of the γ/γ'. Further trials were carried out to better understand if and how coating deposition can aid in mitigating or eliminating this unwanted phase formation in the sub-surface region.

Fig. 6.27 shows a ground smooth sample of CMSX-4 that was 50% coated in platinum plating before being exposed to the high-temperature diffusion heat treatment of 1 hour at 1100°C. The heat treatment enables the interdiffusion of the platinum with the superalloy substrate and *Fig. 6.27 (a)* shows the sub-surface microstructure, there is a narrow band of discontinuous coarsening of the γ/γ' and very small TCPs have precipitated within this region. *Fig. 6.27 (b)* shows the platinum plated portion of the same specimen that has also received the post-plating diffusion treatment. There is a clean diffused platinum microstructure, devoid of a grit-line feature as well as notable absence of TCPs or any coarsening beneath the interdiffusion zone. This suggests that the substrate immediately beneath the platinum is rapidly and completely transformed by the diffusing platinum and that the γ/γ' microstructure does not have the opportunity to coarsen or form TCPs.

Moving to grit blasted samples in *Fig. 6.28* it can be observed that increasing the grit size and maintaining a constant blasting pressure of 45 PSI means an increase in the depth of DC/DP and an increased likelihood of small TCP precipitation, in the as-blasted and heat treated surface condition, as was covered in section 6.4. Interestingly *Fig. 6.28 (b), (d) and (f)* clearly confirm that the act of depositing a platinum layer and then subsequently diffusing it into the superalloy surface is capable of consuming and transforming severely blasted γ/γ' surface microstructures without the formation of any visible coarsened microstructural features or TCPs in the sub-surface region. Even in *Fig. 6.28 (f)* where the CMSX-4 surface was blasted using 20 mesh alumina at 45 PSI there are no sub-coating TCPs and the platinum layer and associated interdiffusion zone appears nominally the same as other examples in *Fig. 6.28*, with some minor changes in microstructure. This finding suggests that platinum plating transforms the underlying substrate meaning that moderately grit blasted single crystal nickel-based superalloys can be used for the diffused platinum bond coat. The grit blast does not appear to aid diffusion but has real benefits for adhesion of electro-deposited platinum prior to diffusion heat treatment. Smooth surfaces can often lose deposited platinum as internal stresses causes the coating to rumple and tear.

The next step for these diffused platinum CMSX-4 samples was to be subject to an aluminising run within the CVD rig at 1030°C for 6 hours. *Fig. 6.29* shows the control sample which featured the ground smooth surface finish, *(a)* shows this surface being directly

aluminised and a good deposition of aluminium can be observed. The thickness and microstructural appearance of the aluminide in *Fig. 6.29 (a)* is comparable with production standard coatings. *Fig. 6.29 (b)* shows the same sample but with the additional diffused platinum prior to aluminising. *Fig. 6.29 (b)* shows a good, thick, consistent coating presence and microstructure. In both instances the coating and sub-surface region are devoid of precipitates as well as γ/γ' coarsening anomalies.

Fig. 6.30 displays images of the grit blasted samples following the 1030°C aluminising process as well as the post coating diffusion run in the vacuum furnace of 1100°C for 1 hour. *Fig. 6.30 (a), (c) and (e)* show the grit-blasted surface with the aluminising directly deposited upon the substrate surface. There are three displayed conditions 220 mesh, 60 mesh and 20 mesh alumina grit all at the constant blasting pressure of 45 PSI. *Fig. 6.30 (a) and (b)* show the 220 mesh scenario and as can be observed both the aluminised and plat-aluminised microstructure is unaffected by the blasting process. There are no deleterious phases forming beneath the coating. The main difference between the control in *Fig. 6.29* and this example is a very slightly rougher surface which appears as a gently undulating surface and the presence of a subtle grit-line features which helps to accurately denote the original substrate surface prior to coating deposition, in this way the 220 mesh blast is advantageous. *Fig. 6.30 (c) and (d)* show the aluminide and plat-aluminide deposited upon 60 mesh blasted surface. These micrographs display a sporadic appearance of an SRZ or secondary reaction zone beneath the aluminised surface but there does not appear to be a similar feature beneath the plat-aluminide. Finally in *Fig. 6.30 (e) and (f)* the impact of blasting with 20 mesh alumina at 45 PSI upon the subsequent aluminising and plat-aluminide coating process is shown. In both instances a constant SRZ is seen. This typically extends ca 5 - 10 μm into the underlying bulk superalloy starting at the bottom of the interdiffusion zone. This feature is unacceptable since high-temperature service will lead to rapid growth of these brittle TCP phases. In addition on the RHS of *Fig. 6.30 (f)* the excessive roughness and resulting undulations of the 20 mesh blast means that the platinum plating process can actively deposit more platinum at the 'peaks' and less at the 'valleys' resulting in a far less uniform coating deposition. For accurate coating lifing assessment a good approximation of the average thickness of an oxidation-protective coating is essential to accurately predict life-to-coating exhaustion.

To finish this section of work a series of CMSX-4 samples in various different surface conditions were subject to carburising though interaction between the substrate and the M1™ maskant during the high temperature aluminising process. *Fig. 6.31* shows SEM-BSE micrographs of the control sample in the ground smooth surface condition in both the bare and platinum plated condition. Following maskant interactions it can be observed that sub-

surface carbides form in both instances. *Fig. 6.31 (a)* shows that there is a narrow band of alloy enrichment/depletion at the uppermost 5 μm and then the standard ca 50 – 100 μm of small pinpoint carbides in the sub-surface region. *Fig. 6.31 (b)* shows that the addition of a diffused platinum layer understandably fails to prevent the carbon ingress and that carbides continue to form in the region beneath the outer surface. There are no observable platelet carbides and only some evidence of low energy pathways dictating carbide placement.

Moving to the grit-blasted samples in *Fig. 6.32* the small carbides can be in various arrangements, with very densely packed regions or more of the low energy pathway placement, though crucially all in the pinpoint carbide form. *Fig. 6.32 (a), (c) and (e)* show the carbide sub-surface layer after a 220 mesh, 60 mesh and 20 mesh blast upon bare alloy respectively. *Fig. 6.32 (a)* shows a large number of small pinpoint carbides populating the carburised zone (220 mesh). *Fig. 6.32 (c)* shows a very high number of small carbides immediately beneath the surface (60 mesh). *Fig. 6.32 (e)* shows a high number of carbides that populate both a dense region immediately beneath the outer surface as well as a large number of carbides that have formed upon low energy pathways that are present through the material. Interestingly in *Fig. 6.32 (c) and (e)* an interaction has occurred at the extreme outer surface, this is usually related to the high temperature interaction between the metal powder components of the maskant the substrate alloy. In these two instances there appears more TCPs than usual. This suggests that the aggressive blasting parameters has exacerbated TCP formation. However in all cases, (*Fig. 6.32 (a), (c) and (e)*) there is no real evidence of discontinuous coarsening extending into the bulk microstructure, this suggests that the formation of small pinpoint carbides occurs first and acts to inhibit the coarsening the γ/γ’ microstructure.

All three of these surface conditions, (220 mesh, 60 mesh and 20 mesh blast at 45 PSI), were also exposed to a platinum plating operation with a post-plating diffusion as well as the subsequent masking interactions, these results are displayed in *Fig. 6.32 (b), (d) and (f)*. In all three instances there is a heavy carbide presence immediately beneath the platinum plating coating and the associated interdiffusion zone. In all three cases the carbides do not form in the region of the superalloy that has a high platinum content, there is a clear demarcation, especially in *Fig. 6.32 (d).* The presence of the pinpoint carbides beneath a diffused platinum bond coat do not appear to be particularly detrimental.

6.6. Conclusion

This work has used modern coating techniques to examine the case of inadvertent carburisation during the aluminising process. Techniques used to investigate the coating and precipitation of deleterious phases mainly include SEM and EDS. The following conclusions are drawn regarding the coating microstructure and carbide precipitates formed as a result of this work:

1. A 3 hour hold at the aluminising temperatures of 800°C and 850°C are insufficient to induce the formation of sub-surface carbides. This lack of carbides is positive however as can also be observed the thickness of the deposited aluminide is very thin and will not protect the surface of a nickel-based superalloy component. Aluminising for longer periods to counter this would prove uneconomical.
2. Aluminising temperatures of 900°C, 950°C and 1000°C clearly show that a small, relatively narrow band of carbides is present in the sub-surface layer. This supports earlier work that ca 900°C is an appropriate threshold temperature under which the likelihood of observing carbides is unlikely.
3. The aluminide coating microstructure at 1000°C is approaching the thickness and appearance associated with an effective protective system. Unfortunately as observed the level of carburisation that appears at this temperature makes it unlikely that you would compromise the aluminide coating to eradicate the possibility of forming sub-surface carbides.
4. A special trial conducted, which introduced a hold at 700°C for a period of 1 hour before resuming the climb to 1030°C, showed that far from enabling the carbon to diffuse away and dissipate, the interrupted climb in fact made the sub-surface carbide layer worse and even more densely packed.
5. The result of applying a thin layer of PVA glue to the surface of the superalloy prior to the application of the normal M1™ M7™ nickel foil masking system clearly show that carburisation is featured once again supporting the earlier assessment that a hydrocarbon chain decomposing is the most likely source of the carbon.
6. The 220 mesh blast results in a more homogeneous surface than the original grinding machining operation used to ensure that all test pieces were starting from the same condition. Blasting using 60 or 20 mesh alumina results in an increase in surface roughness, measured using the Ra scale.
7. There is a clear progression in terms the amount of plastic deformation that must be accommodated by the material as the grit size is increased. It can be seen that using 220 mesh at 45 PSI results in very low levels of plastic deformation and it is confined to the surface of the part. The subsequently heat treated material can be seen to

experience mild discontinuous coarsening of the γ/γ’ which is again confined to the surface and does not extend deeper than ca 4 μm.

8. An alumina grit mesh size of 60 results in a more pronounced effect upon the superalloy surface. Clearly visible is a moderate level of sub-surface deformation and precipitate shearing. The γ/γ’ is misshapen as a result of the grit particle impact and the outer surface features deformed grooves. After high temperature exposure beneath the misshapen surface there is very clear evidence of moderate discontinuous coarsening of the γ/γ’ as well as discontinuous precipitation of TCP phases, most likely P-phase. These TCPs are mostly confined to the region of DC/DP yet can also be observed beneath this layer and appear to be precipitating within material that nominally at this magnification appears unaffected by the grit blast, however the formation of these TCPs shows that this is not the case.
9. 20 mesh alumina with a fixed pressure of either 15, 30 or 45 PSI resulted in severe levels of plastic deformation in the sub-surface region and large regions of the γ/γ’ microstructure have been warped by the impact. Subsequent heat treatment leads to regions of DC/DP which extends deeply in the substrate. In addition there is widespread TCP formation both confined the DC/DP zone and also beneath. Micrographs clearly demonstrate that for the nickel-based superalloys the act of grit blasting not only removes material but more importantly churns material around upon the surface without actually removing it.
10. Grinding followed by diffused platinum plating results in a clean diffused platinum microstructure, devoid of a grit-line feature as well as notable absence of TCPs or any coarsening beneath the interdiffusion zone. This suggests that the substrate immediately beneath the platinum is rapidly and completely transformed by the diffusing platinum and that the γ/γ’ microstructure does not have the opportunity to coarsen or form TCPs.
11. The impact of blasting with 20 mesh alumina at 45 PSI upon the subsequent aluminising and plat-aluminide coating process results in a constant SRZ. This typically extends ca 5 - 10 μm into the underlying bulk superalloy starting at the bottom of the interdiffusion zone. This feature is unacceptable since high-temperature service will lead to rapid growth of these brittle TCP phases. In addition the excessive roughness and resulting undulations of the 20 mesh blast means that the platinum plating process can actively deposit more platinum at the ‘peaks’ and less at the ‘valleys’ resulting in a far less uniform coating deposition. For accurate coating lifing assessment a good approximation of the average thickness of an oxidation-protective coating is essential to accurately predict life-to-coating exhaustion.

7. Slurry diffusion aluminising – current system

7.1. Introduction

Slurry coatings form rapidly by combustion reaction synthesis [127,128] and provide a means of increasing the aluminium content at the surface of a nickel-based superalloy component using a temperature below that employed for many diffusion aluminide coatings, the incorporation of the deposited aluminium powder is instead achieved by the localised exothermic reaction with the nickel substrate. Slurry aluminide systems are priced competitively, although when applied with a spray deposition technique they are restricted to line-of-sight applications. Nevertheless, through their usage, it is possible to incorporate additional elements within the aluminium-based coating, most notably silicon, which has shown to be particularly advantageous with respect to hot corrosion.[129]

7.1.1. Combustion synthesis

Self-propagating combustion reaction synthesis benefits from being a simple process with relatively low energy requirements as well as a higher purity of products obtained. The energy-efficient nature occurs because once initiated the process requires no further addition of energy. Higher purity of the products is the consequence of high temperatures associated with the combustion wave and once the reaction begins and the wave is propagating at a steady-state rate, a temperature distribution is established. The schematic in *Fig. 7.1* displays the spatial distributions of parameters; the reaction temperature, the rate of heat generation and the degree of completion of the reaction or conversion, relative to a finite thickness of a combustion wave. The region ahead of the wave is the heat-affected zone over which the temperature increases to the ignition temperature.[130]

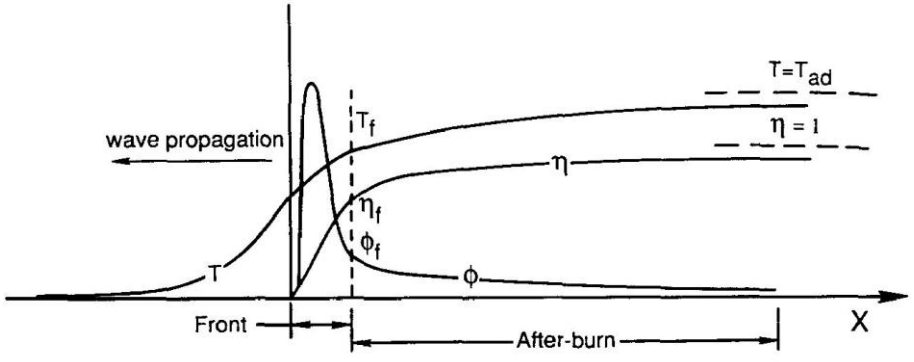

Fig. 7.1 – schematic representation of temperature (T), conversion (η) and rate of heat generation (Φ) in a combustion wave with an after-burn [130]

A combustion reaction quenching method was developed by Fan et al. [131,132] and was used to freeze exothermically reacting powdered aluminium and nickel, the result enabled a step-wise analysis of how the rapid reaction progresses microstructurally. Results demonstrate that aluminium melts before wetting the nickel causing dissolution and subsequent β-NiAl grain precipitation. Fan et al. stated that as the aluminide is created, this being the reaction layer formed at the nickel-aluminium interface, it must subsequently dissolve to further continue the nickel substrate dissolution until exhaustion of the finite aluminium reactant.[131] β-NiAl grains precipitate out initially where the nickel concentration was greatest, this occurring immediately as liquid aluminium contacts the nickel substrate, before eventually precipitating where the aluminium was most highly concentrated.[131,133]

Further work on combustion synthesis by Naiborodenko et al. [127,134–136] found that the metal powder particle size and the ratio of aluminium to nickel powder governed the relative reaction rate and that the propagation of the combustion wave can change from a steady state progression through the compressed powder sample to an oscillating fast-slow combustion due to excess enthalpy which causes a disconnect between the thermal and chemical fronts. Work to better understand the microstructures generated had a combustion reaction of powdered nickel and aluminium water-quenched in order to examine the reaction transformation zone, this was measured across from pure components on one side of the reaction diffusion layer (aluminium and nickel) to pure product (nickel-aluminide) on the other and was found to be ca 20 μm; demarcating the thickness of the chemical reaction zone. The alternatively proposed limiting stage of this reaction type is the rate of diffusion through the reaction product layer [137] as confirmed in research by Aldushin et al.[138] Work by Wong et al. [139] used time-resolved x-ray diffraction to reveal more detail on the fast moving combustion wave front, indicating that there is a delay in the appearance of the final β-NiAl product and that a disordered NiAl meta-phase exists briefly before becoming ordered. Wong's work exemplifies the importance of an 'after-burn' region (see *Fig. 7.1* [130]) that is still hot and reacting after the passage of the initial high-temperature reaction front that sees both liquid aluminium and rapid dissolution of solid nickel superalloy. This work showed that 30 seconds passed by before stable phases begin to form after the liquid formed and meta-stable phases were fleetingly created.[139] Zhu et al. reacted thin foil layers of solid aluminium and nickel and saw evidence indicating the reaction starts as soon as aluminium is completely melted. In this instance there appears to be no reaction before the ignition at aluminium's melting temperature since the heating rate appears constant before the temperature reaches the melting point of aluminium. When the contact between aluminium and nickel is good so that there may be interdiffusion between them during heating, there is some evidence that some reaction may take place before the melting of aluminium. The ignition temperature and the combustion reaction may depend on the heating rate.

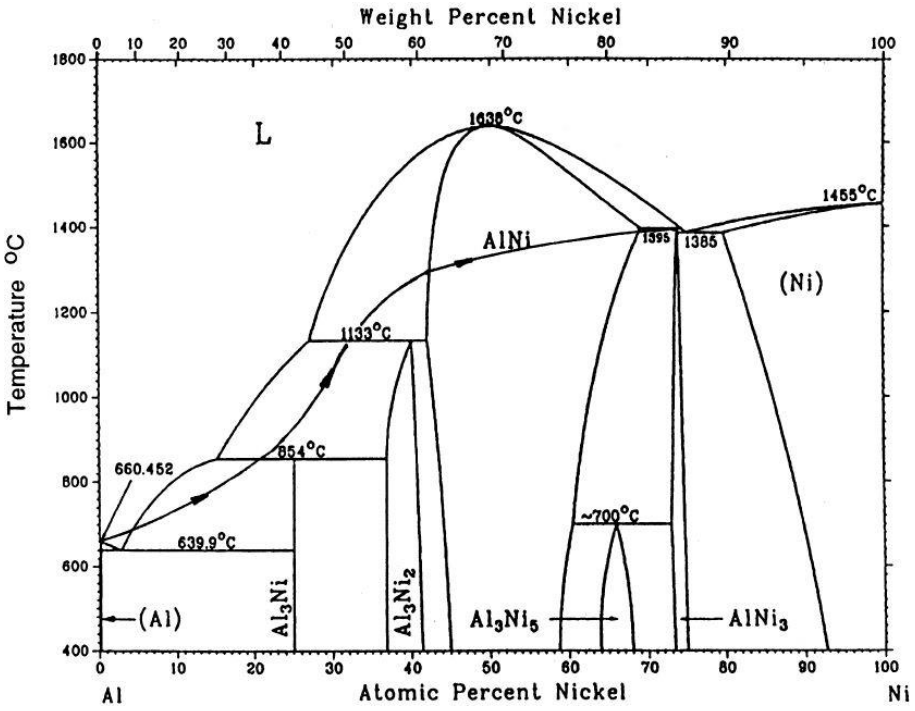

Fig. 7.2 – path of combustion through the Ni-Al phase diagram by Zhu et al. [133]

Zhu et al. divided the reaction into three stages

1. The reaction initiates at the melting point of aluminium. Subsequently nickel dissolves into the molten aluminium to form $NiAl_3$ which is a solid below 854 °C.
2. Then Ni_2Al_3 begins to form between solid nickel and aluminium in the liquid solution in the temperature range between 854 and 1133 °C as a result of exothermically released energy. By the time the temperature reaches 1133 °C, there is evidence of the decomposition of Ni_2Al_3.
3. Finally NiAl begins to form between solid nickel and the aluminium in the liquid solution when the temperature exceeds 1133 °C. The liquid solution begins to disappear and the reaction takes place in the solid state. Aluminium and nickel diffuse in opposite directions and Ni_3Al begins to form in the nickel rich region and spread over the whole specimen. This stage ends with the formation of Ni_3Al near the adiabatic reaction temperature for the completion of combustion.

The path of the reaction is shown (*Fig. 7.2*) by the composition in the middle of the reaction zone at various temperatures sketched in the phase diagram.[140]

Philpot et al. [135] focussed upon the thermal explosion mode of self-propagating high temperature synthesis and the exothermic effects accompanying the reaction between powdered aluminium and nickel. The β-NiAl phase has the highest heat of formation and the highest melting point with values of -58.79 kJ mol^{-1} and 1638 °C respectively. In samples with large temperature increases the sample shape and dimensions changed.

This change was due to the presence of an aluminium rich liquid phase which formed at the Al-$NiAl_3$ eutectic temperature and was a result of the formation of new phases with different lattice parameters. The heat generated by the solid state reaction was found to be a function of powder composition, heating rate and nickel particle size. This heat yielded an observed abrupt rise in temperature and is the consequence of the reaction between solid nickel and a nickel-containing aluminium liquid, the rapid dissolution of nickel then occurs. For samples heated at a slower rate (1 °C min^{-1}) significant amounts of the product phase formed through solid-state reactions compared to samples heated at the higher rate (5 °C min^{-1}) where the reverse is true with most of the product formed through the liquid phase reaction giving rise to higher ΔT. The presence of a liquid phase in powder compacts can lead to a decrease in porosity.

The following physicochemical processes affecting structure formation during combustion synthesis can be identified:

1. Heat transfer from the reaction zone to unreacted particles in the green mixture ahead of the reaction front
2. Phase transitions of solid reactants
3. Formation of eutectic melts and contact melting
4. Melting of reactants
5. Spreading of a molten phase under the action of capillary forces and due to the reduction of surface tension
6. Coalescence of fused particles
7. Gasification of volatile impurities and reactants
8. Chemical reaction with initial product formation
9. Melting of intermediate products
10. *Melt crystallisation upon cooling*
11. *Crystal growth*
12. *Phase transitions in solid products during cooling*
13. *Ordering of the crystal structure*

The first nine processes proceed during the rapid increase in temperature to a maximum at the combustion front and the *last four* take place behind the combustion front with a constant or gradual lowering of temperature.[137,141]

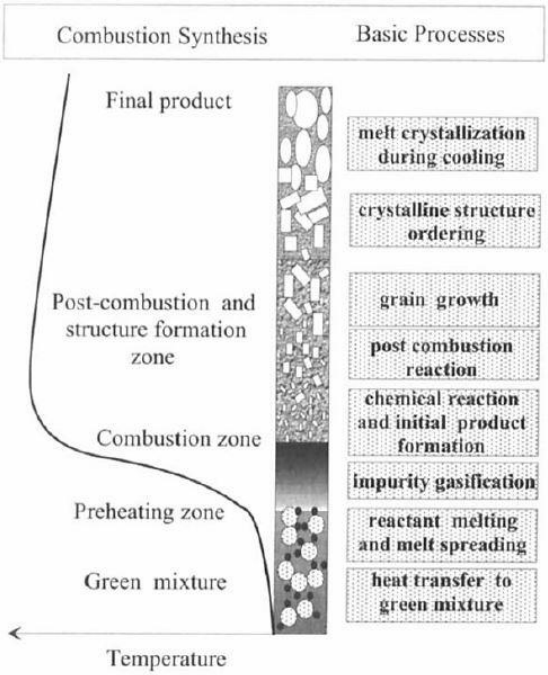

Fig. 7.3 - diagrammatic representation of how the slurry coating forms with understanding from Varma et al. [137]

7.1.2. Slurry coatings

Moving on from literature dealing with more simple powder mixtures of aluminium and nickel to the use of powdered aluminium upon solid nickel superalloy substrates as a means of coating deposition and formation. Thorough investigations by Galetz et al. [142,143] regarding these slurry coating systems yield important points, they concluded that molten aluminium reacts exothermically with the superalloy substrate effectively causing dissolution of the solid nickel to form $NiAl_3$ at the reaction interface.

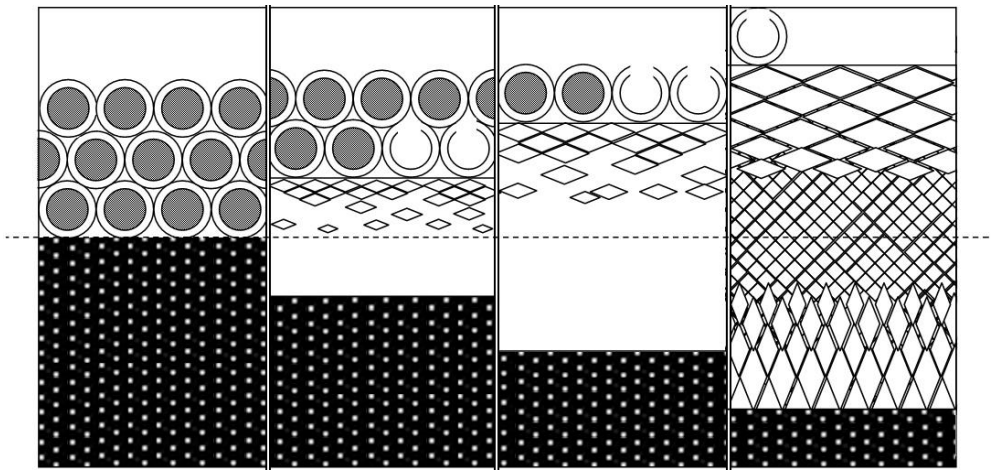

Fig. 7.4 - diagrammatic representation of how the slurry coating forms step-wise from the authors experience and understanding from Galetz et al. [142,143]

Following the current literature, it is the step-wise formation of the slurry aluminide via this mechanism that is the key message of this work. Nickel has a high degree of solubility within liquid aluminium, ranging between 10 and 30 wt. %, dependent upon temperature from 700 to 900 °C respectively.[142] Galetz et al. further explain that the deposited slurry consists of individual aluminium-containing alumina spheres, which crack during heat up, releasing their now liquid contents eventually forming an interconnected network. This molten aluminium reservoir wets the surface of the nickel superalloy and begins the exothermic chemical reaction. This slurry coating formation relies on the availability of aluminium at the nickel superalloy surface, the amount of exothermic reaction heat generated and the rate of that heat loss to the furnace surroundings. These factors must be considered when attempting to create a usable nickel-aluminide coating in this fashion. Also noteworthy is that fact that the formation of such nickel-aluminides is accompanied by an associated volume expansion when compared to the nickel superalloy substrate.[142]

Rasmussen et al. [144–146] explored the formation of β-NiAl and δ-Ni_2Al_3 in slurry aluminide microstructures, as well as the limited solubility of chromium within such phases, this often leads to additional precipitation of phases including, for instance, α-Cr. In thicker applied coatings different horizontal layers were observed traversing the coating from outermost to innermost across the microstructure, these striated bands have been attributed to either an aluminium or nickel enriched β-NiAl phase, located at the top or the bottom of the coating respectively. Additionally Rasmussen et al. make reference to both carbides and nitrides present within the original nickel superalloy substrate that finally reside within the newly formed coating microstructure, these are not chemically involved in the formation and though moved spatially are not dissolved or transformed as a result of the passing reaction front.[144]

Gale et al. [129] observed regions of chromium enrichment ahead of a similar aluminide coating and concluded that chromium was being rejected in front of a growing β-NiAl phase reaction front which consumed the nickel superalloy substrate. Of the chromium-rich precipitates forming some appeared to nucleate directly within the coating matrix, at various points inside β-NiAl grains, these were often randomly orientated, signifying a lack of specific initiation points which may have dictated new phase growth. Alternatively some chromium-rich precipitates were elongated lamellae and observed to form along β-NiAl grain boundaries, these coarse precipitates represent those that had initiated early during coating formation and therefore had the longest time at temperature growing within the coating. If this coating had formed by inward diffusion these coarse chromium-rich phases would lie towards the outermost region of the coating and this spatial distribution is indeed observed.[129]

7.1.3. Functional testing

Work conducted by Kircher et al. [146,147] suggested a link between the chromium content of the superalloy substrate that a slurry aluminide is applied to and the performance of the final coating in high-temperature hot corrosion testing. The reduced chromium concentration within the superalloy, and consequently within the formed coating, diminished the chromium, and in this particular study [146], silicon-rich, lamellar phases. These phases, formed in the outermost region of the coating, were found to be linked to effective corrosion resistance.[146] Protective alumina scales are essential in protecting high temperature materials, and silicon is found to be especially beneficial in coating systems exposed to the high concentrations of sulphur found in engines used in industrial or marine environments. β-NiAl has long been used to inhibit high temperature corrosion in the gas turbine industry because the Al_2O_3 that preferentially forms at high temperatures aids resistance to type 1 and type 2 hot corrosion mechanisms.

A form of inward diffusion is believed to occur in slurry aluminides, like SermaLoy J, which sees the formation of a two phase coating microstructure with a matrix comprising aluminium and nickel and a dispersed phase comprising silicon and chromium. These phases are understood to be β-NiAl and $CrSi_2$. Evidence suggests that cracks forming within the coating microstructure propagate down to the interdiffusion zone and display a 90° turn in order to run parallel with the coating and along the interdiffusion zone.

Post service components show that formerly fine silicides coalesce and coarsen and that the aluminide thickens as a result of high temperature exposure. Analysis has shown that typical amounts of silicon in the outer third of the coating ranges between ca 8 and 10 wt. %. Aluminides with higher than 30 wt. % aluminium content are generally considered to be brittle and this has limited slurry aluminides, which often feature high aluminium contents, to use within the industrial and marine sectors and their application has not found use in the aerospace sector. This distinction is due to the range of both thermal and mechanical loads that a turbine blade must endure during the course of a single flight. Industrial and marine based gas turbine derivatives often seen a different experience that allows the use of the less ductile slurry applied systems.[147]

7.2. Experimental

7.2.1. Methodology

An industry standard chromate-containing silicon-enhanced slurry for aluminising superalloys named IP1041, supplied by Indestructible Paint Ltd, was applied to samples of MarM002. Water-based, the slurry contains phosphates and chromates in addition to powdered aluminium, silicon and thickening agents.

H_2O	$MgHPO_4$	H_3PO_4	CrO_3	SiO_2	Al	Si
Solvent	Additives			Thickener	Powder 6 µm	Powder 10 µm
34.5 %	*3.5 %*	*15.8 %*	*5.7 %*	*2.5 %*	*32.5 %*	*5.5 %*

Table 7.1 – slurry composition prior to deposition upon substrate

Following application via air spray deposition the samples received a bake within an air oven at 350 °C for 60 minutes to dry the slurry upon the surface. The purpose of the bake is to drive away the solvent, aid decomposition of additives used to stabilise the slurry mixture during storage and ultimately to leave only the powder mixture upon the surface ready for diffusion. The samples were then placed within a vacuum furnace for 120 minutes with a holding set point of 870 °C under a partial pressure of argon.

wt. %	Ni	Cr	Al	W	Co	Ti	Ta	Re	Mo
MarM002	Bal	9.0	5.7	10.0	10.0	1.5	2.5	-	-
C263	Bal	20.0	-	-	19.7	2.1	-	-	5.8

Table 7.2 – elemental composition of alloys used in this chapter of work

All of the specimens were placed within the fume hood for 168 hours to allow the sacrificial bisque (quasi-foam) layer to fragment and fall away revealing the final product.

7.2.2. Metallographic examination

Specimens were sectioned transverse to the coated surface in order to provide an 'in-plane' view of the coating microstructure. These were then hot mounted in conducting resin and polished using grinding papers and polishing cloths ending on a colloidal silica polish of 0.04 μm finish. Specimens were examined in the polished state and received no further etching or electropolishing treatments.

7.2.2.1. Scanning electron microscopy

SEM images were taken at 15 or 20 kV using either a field emission gun (FEG), a FEI Nova NanoSEM FEG, a tungsten filament, Jeol XL30 or a thermionic (CeB_6) source, a Phenom ProX.

7.2.2.2. Energy dispersive spectroscopy

Jeol XL30 fitted with EDS detector, running Aztec software from Oxford instruments.

7.2.2.3. Transmission electron microscopy

STEM analysis was performed in a FEI Tecnai F20 operating at 200 kV. The system is equipped with an Oxford instruments XMAXN 80 TLE windowless SDD EDS detector. Images were collected with a bright field (BF) and high angle annular dark field (HAADF) detectors in STEM. EDS spectrum maps were collected using Aztec software then spectra were taken and these were collected for 20 s live time.

Additional TEM analysis was conducted upon a JEOL 200CX operating at 200 kV.

7.2.2.4. X-ray diffraction

X-ray diffraction surface analysis was carried out with a Bruker B3 BB D8 DAVINCI Gen 9 with LynxEye EX position sensitive detector in θ - 2θ mode (using CuKα radiation).

7.2.2.5. Electron back scattered diffraction and Transmission kikuchi diffraction

EBSD and TKD scans were conducted at 30 kV using a FEG source, a FEI Nova NanoSEM FEG running the Bruker EBSD acquisition system. The EBSD data was analysed using the HKL Channel 5 software package distributed by Oxford Instruments.

7.2.3. Focussed ion beam preparation

A dual beam FEI Nova 600 Nanolab focused ion beam (FIB) / FEG scanning electron microscope (FEG–SEM) system was used to prepare site specific TEM samples using an in-situ lift-out procedure. Platinum was deposited using the gas injection system (GIS) over the 40 µm long area of interest, and milling created trenches on either side. The TEM sample was extracted using an Omniprobe micromanipulator and was attached to a Cu grid before final thinning to achieve samples that had similar thickness.

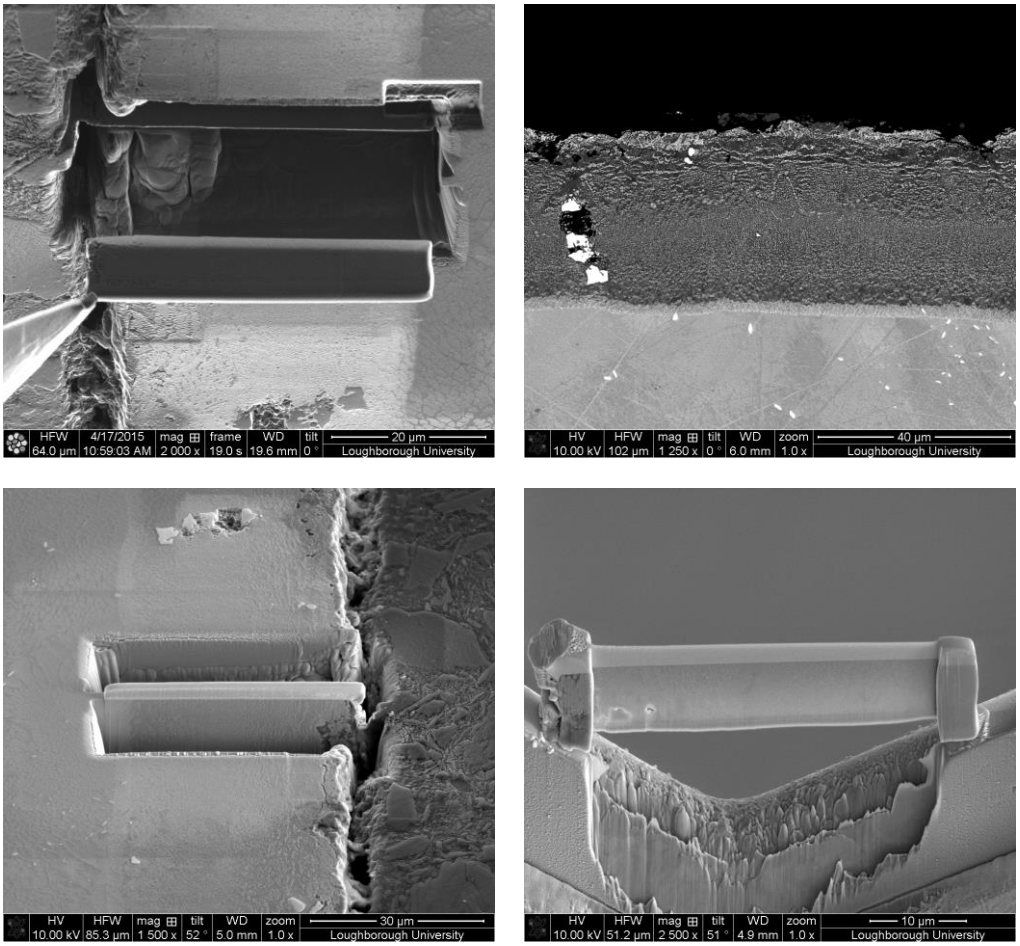

Fig. 7.5 – SEM images detailing the location and process of TEM specimen preparation from the coating IP1041 from the alloy MarM002

Images courtesy of G. West and Z. Zhou

7.3. Results

7.3.1. Scanning electron microscopy

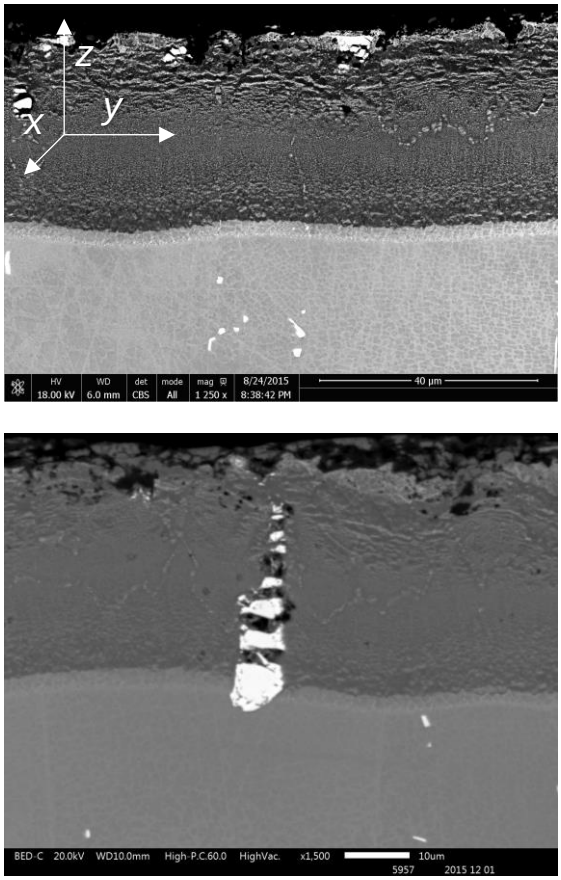

Fig. 7.6 – silicon-enhanced aluminide coating upon MarM002 substrate, nominal appearance (a), containing carbide from original MarM002 substrate (b)

Scanning electron microscope (SEM-BSE) back scatter images (*Fig. 7.6*) show a variable, dual-phase, microstructure within the coating consisting of a darker matrix phase and a lighter, dispersed precipitate phase. Elemental contrast of BS mode suggests the presence of a heavy element within the dispersed precipitate phase. The dispersed phase displays a gradient from coarse to fine going from coating top to bottom, in the *z direction*, before being absent immediately before the narrow interdiffusion zone. In this case of coating upon MarM002 bright regions are seen both within the superalloy bulk and on occasion within the newly formed external coating, these are carbides present from the original microstructure. Further points derived from these SEM-BSE images include the unusually thin interdiffusion zone of ca 2 µm and some sporadic porosity at the extreme outer surface with no porosity presence within the coating itself save that found between the carbide pieces in *Fig. 7.6 (b)*. Traversing the coating in the *y direction* upon the substrate showed little variation in coating thickness or microstructure, *(a) in Fig. 7.6* is representative of this silicon-enhanced slurry aluminide system.

7.3.2. Energy dispersive spectroscopy

A series of EDS line scans were taken parallel with the coating (in the *y direction*), descending stepwise from outermost towards the interdiffusion zone (along the *z direction*) and substrate, the results were averaged per element per line. This method, a 'ladder-scan', averages the dual-phase microstructure into a single result per line to give general elemental trends (*Fig. 7.7*). The approximate spacing between line scans is ca 2.5 µm, the left hand side of each graph starting at zero is the extreme outside of the coating, minus the thin sporadic oxide layer. Traversing the graph from left to right moves across the coating from top to bottom (in the *z direction*) finishing within the bulk microstructure of the parent substrate. The coating upon MarM002 shows a constant aluminium trace and that nickel has a shallow gradient that is highest as the interdiffusion zone is approached. The elements cobalt, chromium and tungsten are almost constant across the coating and exist at lower levels than within the substrate, though there is a slight dip immediately prior to the interdiffusion zone. The silicon trace shows a clear gradient that is highest closest to the external surface that drops away gradually disappearing once the interdiffusion threshold is crossed. The interdiffusion zone itself is low in nickel, features no additional aluminium from the slurry coating and is enriched in tungsten, chromium and cobalt, all of which originate within the substrate only.

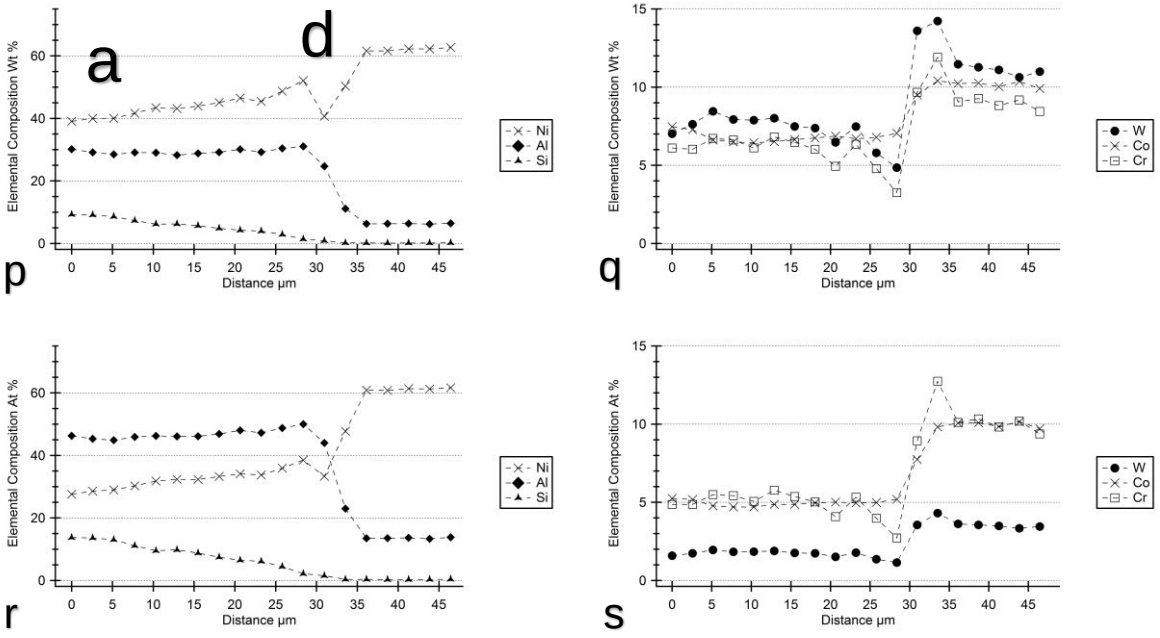

Fig. 7.7 – elemental composition across coating upon MarM002, (p) primary elements in Wt %, (q) secondary elements in Wt %, (r) primary elements in At %, (s) secondary elements in At % locations are referred to in Fig. 7.5

7.3.3. Transmission electron microscopy – images

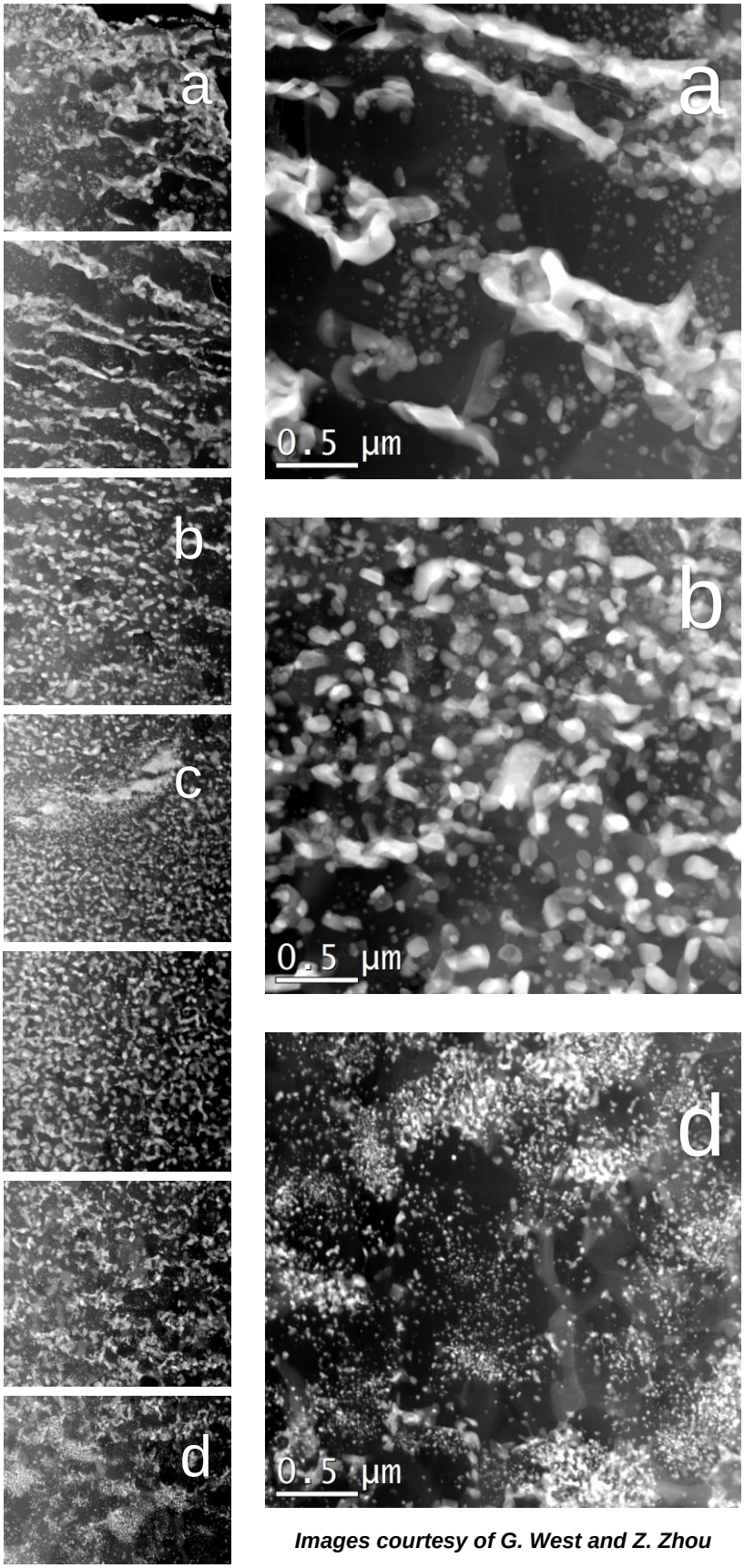

Images courtesy of G. West and Z. Zhou

Fig. 7.8 – TEM micrographs HAADF, at 20,000 times magnification, blow-ups (a), (b) and (d) at 40,000 times

Transmission electron microscope (TEM) images (*Fig. 7.8 and 7.9*) using high angle annular dark field (HAADF) mode distinguishes the matrix phase from the dispersed precipitate which, close to the surface, resides upon the matrix phase grain boundaries. In MarM002 (*Fig. 7.8*) the precipitates which reside sub-surface are confirmed as coarse and run almost parallel with the surface, preferentially growing in the *x* and *y directions*, in three dimensions yielding 'flakes'. Traversing the coating top to bottom in the *z direction* the precipitates obey a gradient, gradually becoming finer until reaching the interdiffusion zone where they exist on the nanometre length scale. At 40,000 times magnification individual matrix grains can be distinguished (*Fig. 7.9*), using the bright field (BF) mode, especially close to the external surface of the coating microstructure (*Fig. 7.9 (a)*). Regarding the dispersed phase only, three distinct bands can be described from coating top to bottom, the top third which displays a coarse elongated nature running parallel with the coating outer surface (*Fig. 7.8 (a)*). The middle third has precipitates that are globular and smaller than previously described (*Fig. 7.8 (b)*). Finally the bottom third has very fine dispersed precipitates that eventually taper away and disappear in the region immediately adjacent to the interdiffusion zone (*Fig. 7.8 (d)*).

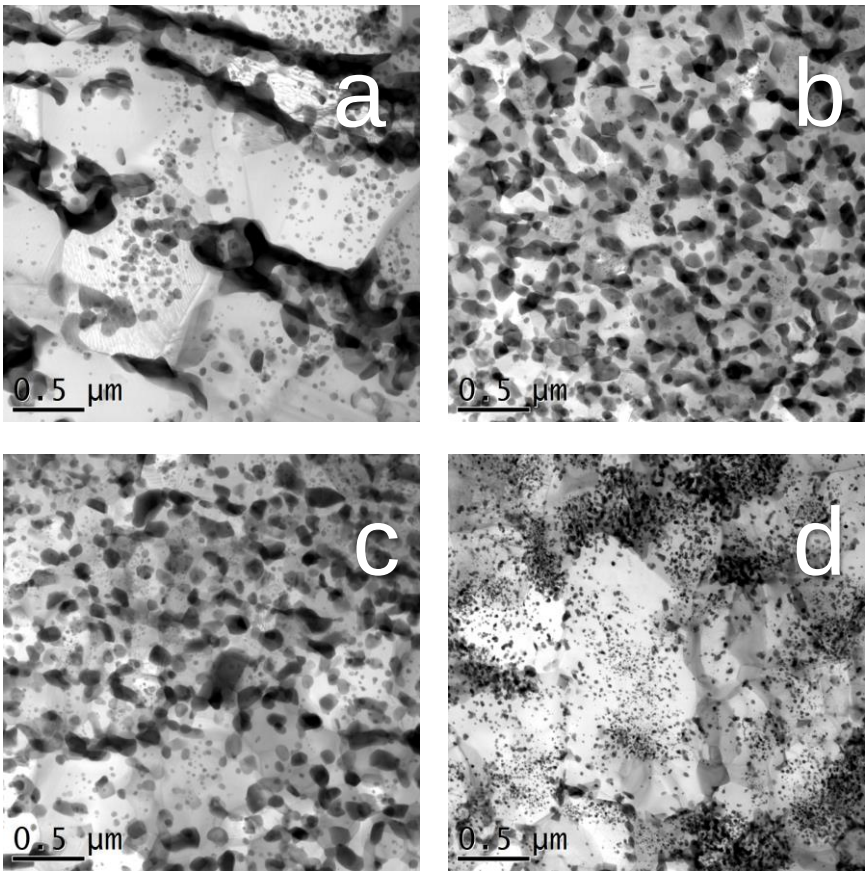

Fig. 7.9 – TEM micrographs BF, coating upon MarM002, blow-ups from Fig. 7.8 are (a), (b), (c) and (d) at 40,000 times

Images courtesy of G. West and Z. Zhou

7.3.4. Transmission electron microscopy – elemental mapping

TEM-based elemental mapping confirmed the two primary phases; the matrix phase consists of the elements aluminium, supplemented from the slurry, as well as cobalt and nickel solely from the substrate, in this case MarM002 (*Fig. 7.10*). The dispersed precipitate phase contains silicon from the slurry, as well as chromium and tungsten from the substrate (*Fig. 7.10*). The presence of tungsten is responsible for giving the precipitate phase its bright appearance under HAADF or SEM-BSE conditions. Close to the external surface, in the uppermost third of the coating the dispersed phase is clear, bright and distinguishable due to its coarse nature (*Fig. 7.10*). The letters *a*, *c* and *d* refer to regions denoted in *Fig. 7.8* at the top, middle and bottom of the coating microstructure.

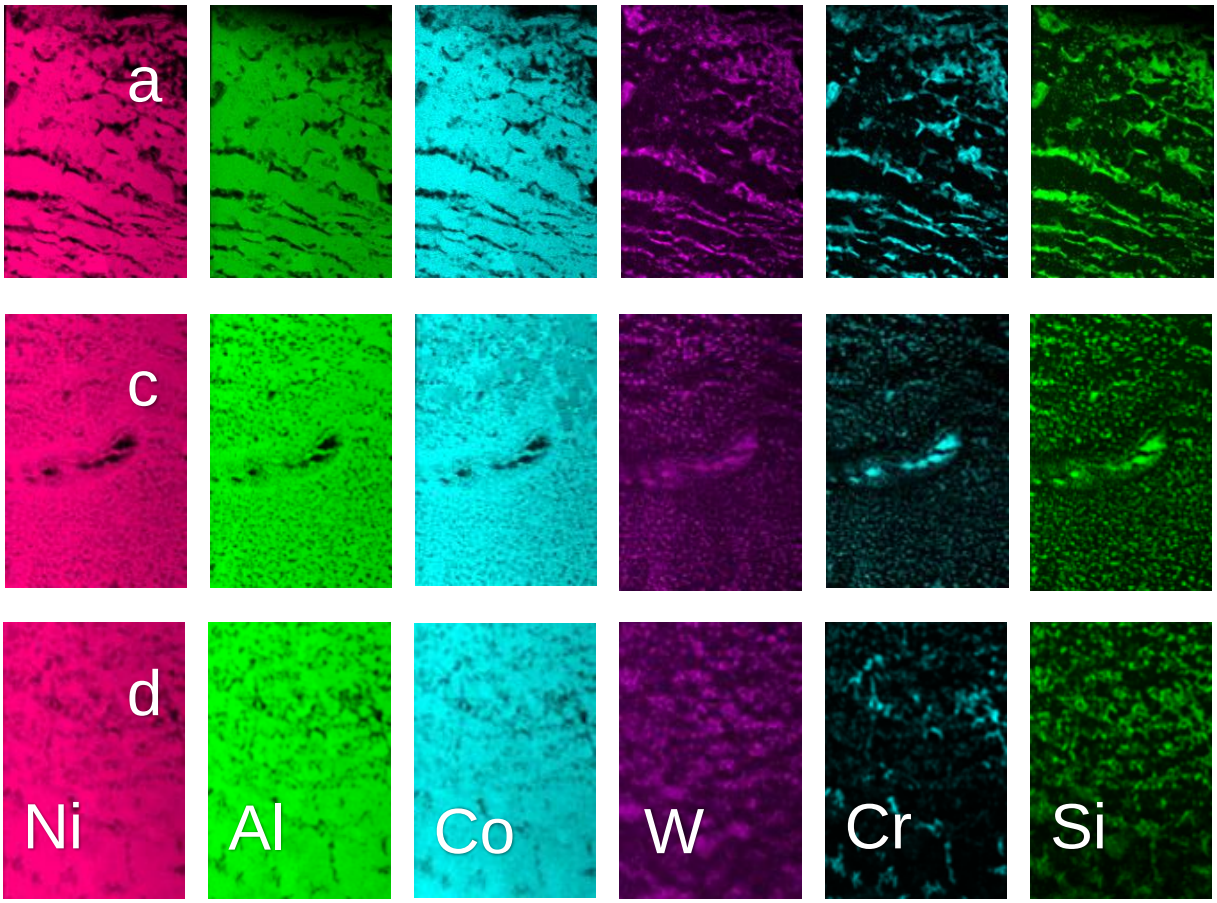

Fig. 7.10 – TEM EDS maps, coating upon MarM002 locations (a), (c) and (d) refer to Fig. 7.8

Images courtesy of G. West and Z. Zhou

7.3.5. Transmission electron microscopy – elemental composition

TEM-based elemental composition work (TEM-EDS) was undertaken to distinguish the matrix from the dispersed precipitate phase (*Fig. 7.11*). Spectrum 1 was drawn within the matrix to minimise the chance of the interaction volume sampling the dispersed precipitate and give a more accurate figure regarding chemical composition. Nickel and aluminium were found to be the main constituents at ca 50 and 32 wt. % respectively and low levels of chromium, cobalt and silicon were also found. Spectrum 2 was similar, though this time drawn to sample data from the dispersed precipitate phase, this being mostly silicon, chromium and tungsten at 12, 29 and 35 wt. % respectively, with low signals also received from nickel, aluminium and cobalt, though this is the nearby matrix caught in the interaction sample volume.

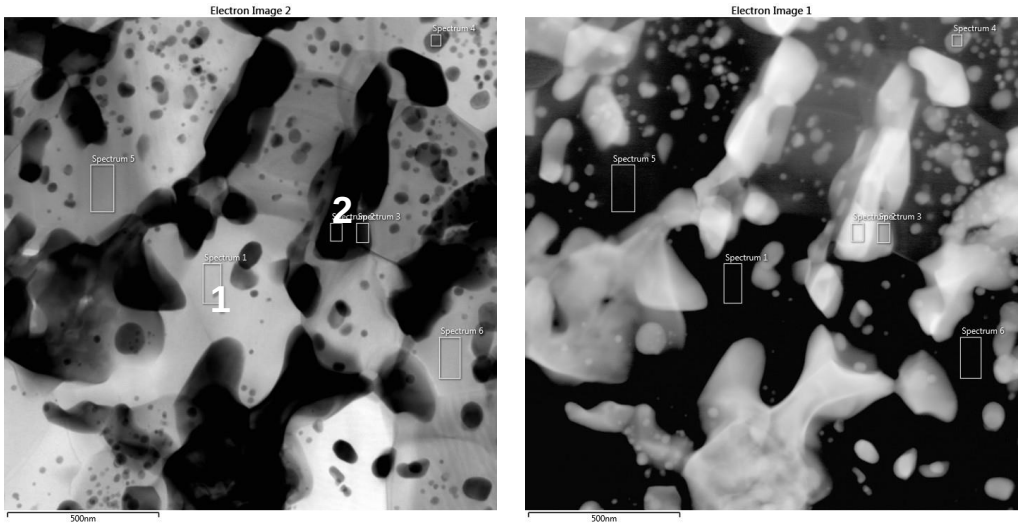

Wt. %	Ni	Al	Si	Ti	Cr	Co	W	Cu
Spectrum 1	50.4	31.8	4.2	-	0.6	9.1	-	4.0
Spectrum 2	9.4	4.1	11.6	0.7	28.5	2.0	35.0	8.8

At. %	Ni	Al	Si	Ti	Cr	Co	W	Cu
Spectrum 1	35.6	48.8	6.2	-	0.5	6.4	-	2.6
Spectrum 2	9.8	9.1	25.1	0.9	33.2	2.1	11.5	8.4

Fig. 7.11 – elemental composition within two separate coating phases upon MarM002, spectrum 1 is within the coating matrix and spectrum 2 is within the dispersed phase. RHS image is TEM micrograph in HAADF mode and LHS is BF mode

– elemental composition within spectrum 1 and 2 identified above in weight and atomic pct.

Images courtesy of G. West and Z. Zhou

7.3.6. X-ray diffraction

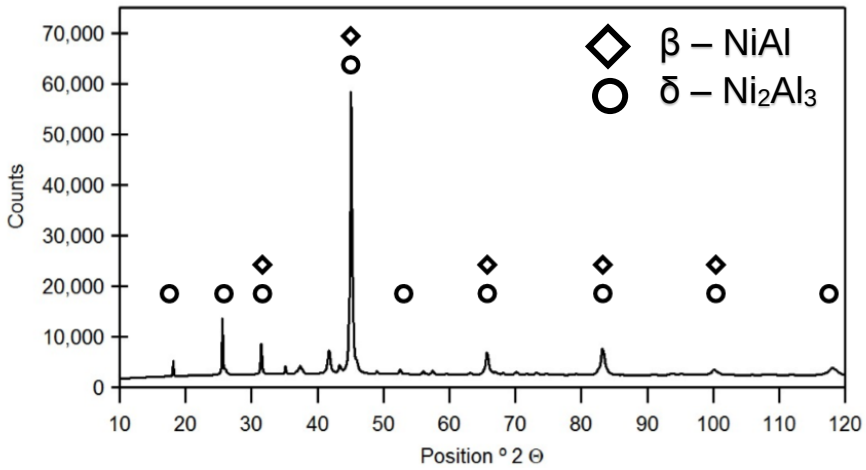

Fig. 7.12 – XRD phase identification of coating upon MarM002

X-ray diffraction (XRD) has been used to better understand the phases found within the coating microstructure after formation (*Fig. 7.12*). A 2.5 by 2.5 mm flat square sample of the MarM002 coated sample was prepared and subjected to XRD analysis. Peaks identified point to both β-NiAl phase as well as δ-Ni_2Al_3 being present using this top-down technique. In addition peaks believed to belong to a $CrSi_2$ phase were also present, though weak in intensity.

7.3.7. Electron back scattered diffraction and transmission kikuchi diffraction

Using electron back scattered diffraction (EBSD) (*Fig. 7.13*) and transmission kikuchi diffraction (TKD) (*Fig. 7.14*) it has been demonstrated that the β-NiAl phase is present throughout the coating on the superalloy substrate. The grain size of the polycrystalline β-NiAl varies according to depth within the coating. In the uppermost third of the coating (*Fig. 7.13 – 1**), the largest grains are seen (ca 2 μm across), elongated in the *x* and *y direction*. Close to the interdiffusion zone, in the bottom coating third, medium sized grains (ca 1 μm) predominate (*Fig. 7.13 just above 3**), now elongated in the *z direction* and smaller in the *x* and *y*. In comparison, β-NiAl grains around the midpoint of the coating are small (< 1 μm) (*Fig. 7.13 – 2**) with no overall order in their relative orientation with many orientations represented in the inverse pole figure (IPF) images (*Fig. 7.13 (q), (r) and (s)*). Local misorientation across the coating increases around the midpoint compared to the top and bottom but is greatest within the interdiffusion zone at the bottom of the coating connecting the substrate (*Fig. 7.13 (t)*). The chromium-silicon dispersed phase is not represented due to the scale of precipitates, both the EBSD and TKD focus upon the β-NiAl phase.

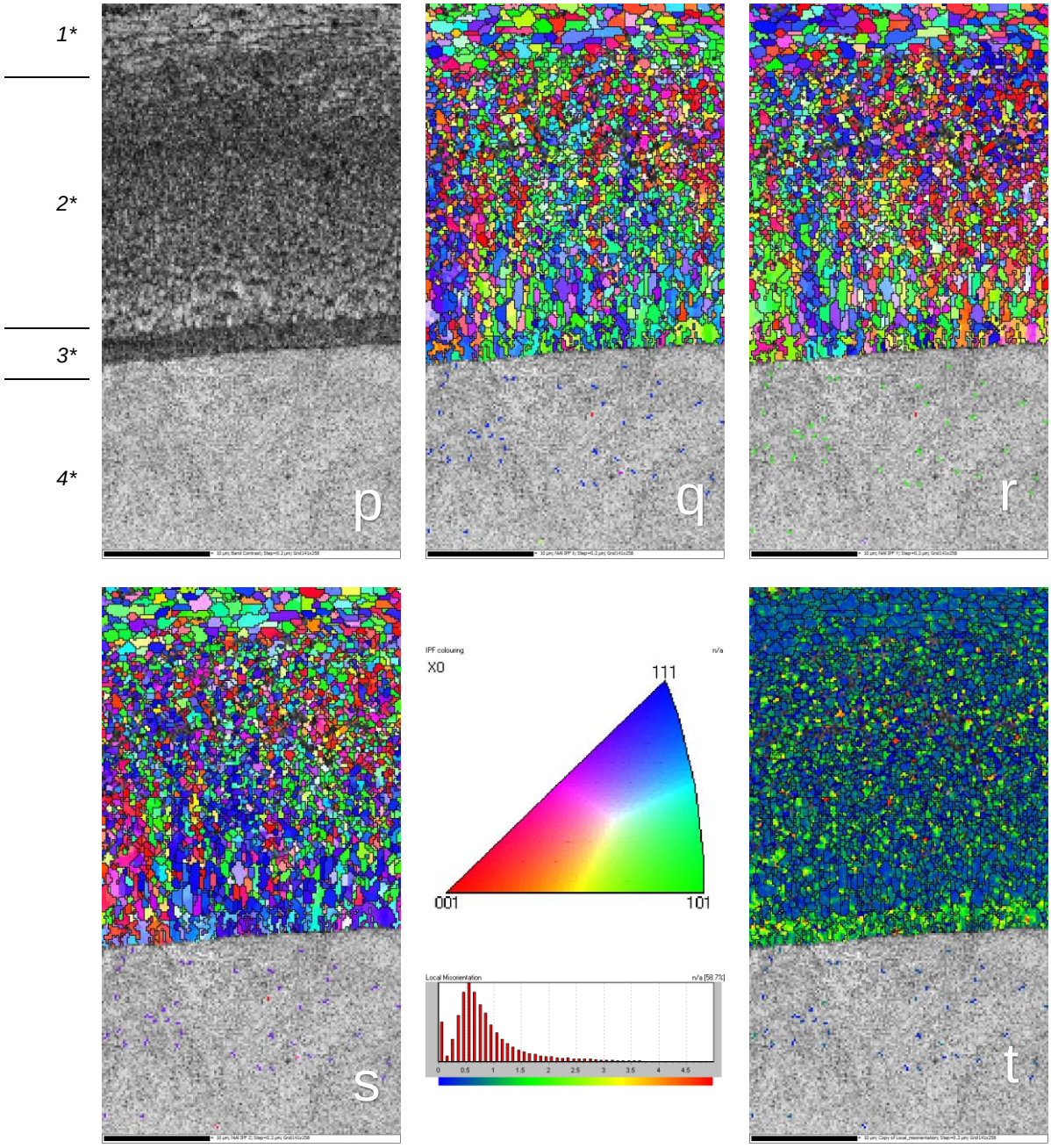

Fig. 7.13 – EBSD of coating upon MarM002, band contrast (p), inverse pole figures in the x (q), y (r) and z orientation (s). Image (t) shows the local misorientation

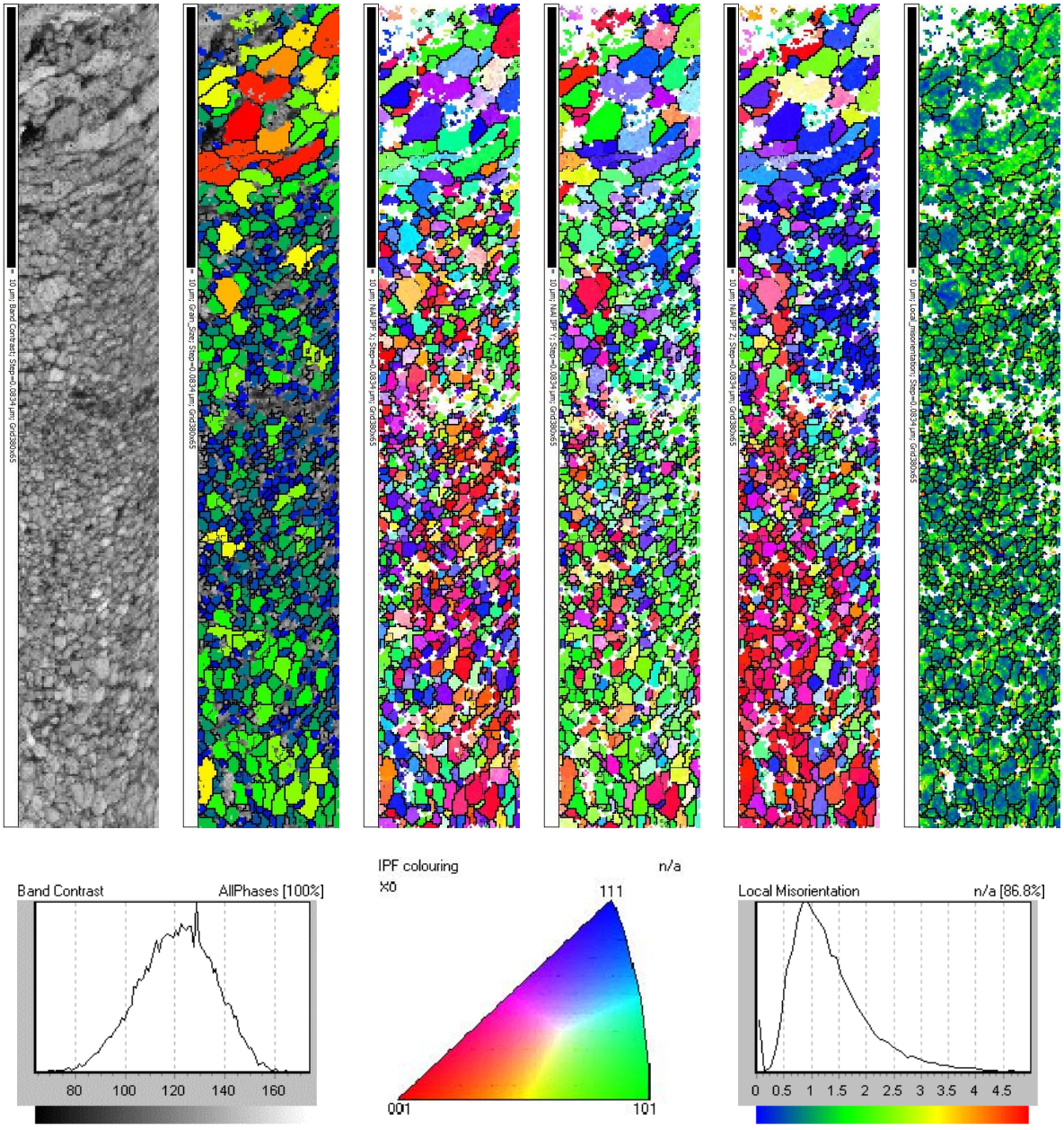

Fig. 7.14 – TKD of coating upon MarM002, image from left to right; band contrast, relative grain size, inverse pole figures in the x, y and z orientations and the final image shows the local misorientation

7.4. Discussion

7.4.1. Coating formation

Slurry deposited aluminides on nickel-base superalloys utilise a unique reaction mechanism as shown by the following results. EDS analysis was conducted using a ladder scan, across the coating, travelling from outside through the coating before crossing the interdiffusion zone, upon the alloy MarM002 (*Fig. 7.7*).

EDS analysis across the coating upon MarM002 (*Fig. 7.7*) reveals that aluminium is homogeneous. In contrast traditional vapour phase aluminising results in a coating that necessitates a subsequent high temperature diffusion heat treatment to ensure high aluminium levels at the extreme outer surface are homogenised throughout the coating and that conversion to the β-NiAl phase is completed throughout. As seen a slurry aluminide formed coating consists of the appropriate β-NiAl phase immediately following the coating process and this is an immediate cost saving on further processing requirements. The coating silicon concentration displays a discernible gradient, it is at its maximum immediately beneath the coating outer surface with ca 8 % Wt, and its composition drops to zero upon crossing the interdiffusion zone into the substrate. The only source of silicon for the coating is applied during the slurry deposition process, nickel-based substrates rarely contain more than a few ppm of silicon within the alloy itself. This gradient in silicon concentration is mirrored by the dispersed precipitate phases coarseness seen using the TEM (*Fig. 7.8*), implying that the silicon within the coating resides predominantly in the dispersed precipitate phase, as opposed to within the β-NiAl coating matrix. The β-NiAl itself is comparatively chemically consistent from surface to interdiffusion zone which further supports this interpretation.

Nickel displays a shallow gradient across the coating, lifting upon approach to the substrate, this being the only source of nickel for the coating. (*Fig. 7.7*) Additional elements such as tungsten, cobalt and chromium are found within the coating microstructure, all of which can only originate from the substrate. (*Fig. 7.7*) The concentration of these additional elements is halved upon incorporation within the coating, compared to original concentrations of the substrate alloy, supporting the hypothesis that the coating formation is accompanied by phase-change driven expansion and a decrease in density of the consumed nickel-based substrate. Elements, such as chromium, have limited solubility within the newly forming β-NiAl coating matrix meaning that, inevitably, the surplus is collected ahead of the reaction front, unwanted by the rapidly growing coating. Gale et al. saw regions of chromium enrichment ahead of the coating in their work and concluded that chromium was indeed being rejected and concentrated in the face of a growing β-NiAl phase reaction front.[129]

Consumption of the original substrate yields a finite population of these additional elements, the extent and span of dissolution being dictated by the amount of aluminium added in slurry form and the concentration of nickel within the substrate. The coating expansion outwards means that the additional elements are spread throughout the coating and the new spatial volume it occupies. The element cobalt is accepted within the nickel-aluminium matrix phase (β-NiAl) whilst tungsten and especially chromium are used to form the silicon containing dispersed precipitate phase. (*Fig. 7.7*) These elements take longer to become incorporated into the forming coating and they become concentrated in the substrate ahead of the reaction front. When the reaction ceases and the heat dissipates, the substrate consumption stops, and the front is left frozen. The nickel gradient across the coating shows that there are two different regimes present, the aluminium rich β-NiAl phase close to the external surface and the nickel-rich β-NiAl phase close to the bottom of the coating and adjacent to the interdiffusion zone.

Slurry coatings are formed by spray deposition at room temperature followed by heat treatment in a furnace under argon or vacuum. The role of the furnace in this formation mechanism is to provide sufficient thermal energy to instigate a self-propagating cascading reaction. Initially the furnace will heat the slurry which at this point is in the green state, i.e. in-situ upon the components surface but as yet unreacted, until the mixture of aluminium and silicon melts upon the surface and then, by capillary action wets the surface of the nickel substrate. Before reaching the final set point of 870 °C this sequence of events will occur, the exothermic intermetallic reaction will begin and drive the temperature of the cascading reaction front much higher much faster. From this point until the dissipation of the released local chemical energy the thermal state of the furnace had a role modifying heat loss from the surface. Following the rapid reaction and local high temperatures the coating system will slowly cool back down to the temperature of the furnace at large, in this scenario 870 °C as aforementioned. During this subsequent time the coating microstructure is undoubtedly still evolving but at a much slower rate since solid state diffusion of chemical species is slow compared to the temporary liquid state that exists during the propagation of the wave front.

Local surface temperatures, once the proportion of nickel has reached critical levels, within the molten aluminium are likely to increase dramatically and aid eventually in the formation of the β-NiAl phase as the matrix for the coating. Formation of the bisque or quasi-foam layer is explained by Galetz et al.[142] and is the remains of alumina shells that formed on the aluminium powder during slurry manufacture. In all trials run during this work a bisque layer was observed to form and was carefully removed to reveal the final coating. This observation was positive confirmation before any other analysis was undertaken that a reaction had taken place and that any variation in the slurry or in the substrate to which the coating was applied did not result in a scenario that failed to produce a coating of this type.

7.4.2. Coating mechanism

Traditional aluminising of nickel-based superalloys is split into two types, the inward growing and the outward growing depending upon the deposition temperature used. Key indicators reveal which coatings are formed in these two ways most notably is the presence of precipitates formed using elements from the substrate and their relative position within the coating microstructure. When regarding outward growth at high activity there are newly grown precipitates found in the uppermost regions of the coating and most importantly because the original interface is close to the new interface between coating and substrate original carbides will have not moved. Original carbides present within the substrate microstructure will reside in the lower reaches of the new coating. Conversely when a coating is grown inwardly at low activity the small carbides close to the original surface find themselves within the middle of the newly formed coating system.

In work by Fan et al. [131,132] a combustion front quenching method was used to freeze the forming microstructure of reacting powdered aluminium and nickel, and, despite this literature being about reacting metal powders and not specifically about slurry coatings, as the author will show there is definitive relevance. Results from Fan et al. demonstrate that aluminium melts before wetting the nickel surface causing dissolution and subsequent β-NiAl grain precipitation. According to Fan et al. [131] as a reaction diffusion layer is formed it must subsequently re-dissolve to continue the nickel dissolution. β-NiAl grains were seen to precipitate out first where the concentration of nickel was greatest, as soon as liquid aluminium contacts, before subsequently forming where aluminium was enriched. In comparing this work with that of Fan et al. [131] some key characteristics are common, the instigation of the reaction upon the melting of aluminium and the start of nickel dissolution. Also common is the idea that β-NiAl will precipitate out where nickel concentrations are high within the molten aluminium upon the surface, though in this work it will be shown that those early forming grains are shifted up and away from the original interface of the substrate due to the formation of new material beneath. A point of disagreement between the work of Fan et al. [131] and this work is that the reaction diffusion layer must subsequently dissolve in order to continue nickel dissolution, since evidence suggests the liquid state has a very short period in which to exist before the heat dissipates and solidification takes place, this evidence being the presence of residual microstructures that survive from the original nickel substrate into the new β-NiAl coating microstructure.

Naiborodenko et al. [134] investigated the gasless combustion of aluminium and nickel powders and in the usual mode of combustion front propagation there is a sharp frontal boundary, consisting of a narrow reaction zone and a high velocity reaction front propagation of several cm s^{-1}.[134] In an unusual case the sharp frontal boundary was absent, the reaction

zone was diffuse and the combustion rate decreased to several mm s^{-1}. Once the front had reached the end of the specimen a reflected front swept back through the material to the centre before being extinguished. This unusual observation was accompanied by a substantial increase in specimen dimensions, electron probe micro analysis and x-ray diffraction saw the presence of not only β-NiAl but also δ-Ni_2Al_3 and free nickel. Naiborodenko [134] states that the deceleration in reaction front velocity is believed to result from a layer of δ-Ni_2Al_3 formed on the surface of the nickel by reactive diffusion. Following this phase growth nickel and the intermediate phases dissolve into the melt which gradually becomes saturated by refractory components. As this change in melt chemistry occurs β-NiAl is able to begin to precipitate and crystallise. Particles are surrounded by a δ-Ni_2Al_3 – β-NiAl layer, effectively forming a semi-permeable barrier through which reactants must traverse. The strongly decelerated combustion mode is related to the change in phase composition of the reaction products, and occurs in systems with several compounds, when the combustion temperature is below the melting points of the intermediate phases.

Thorough work by Galetz et al. [142], specifically regarding slurry coating mechanisms concluded that molten aluminium, at 660 °C, dissolves solid nickel to form $NiAl_3$ at the interface. Nickel has a high degree of solubility within the liquid aluminium, 10 – 30 At. %, increasing with temperature. A network of molten aluminium is formed and this reservoir is made of interconnected spheres of expanding aluminium that cracks the individual thin alumina shells of the powder particles. Coating formation relies on availability of aluminium at the nickel surface, the amount of exothermic heat generated and the loss of that heat to the surroundings. Galetz points out that the formation of such aluminides is accompanied by an associated volume expansion when moving from reactants to products. In this work there are multiple examples of the expansion effect at work in the growth of a new coating, (*Figs. 7.15* and *7.16*) and this is used to explain the rather unusual mechanism of simultaneous dissolution of the nickel substrate and outward growth of the expanding coating system.

The nickel EDS elemental trace in MarM002 (*Fig. 7.7*) displays a drop in concentration across the interdiffusion zone moving from coating to substrate. Simultaneously chromium, tungsten and cobalt concentrations increase supporting that as the cascading reaction front progresses, liberating nickel from the alloy, that these additional elements, especially chromium have limited solubility within the forming β-NiAl phase. Therefore these elements struggle to become incorporated into the forming coating and they become concentrated in the substrate ahead of the reaction front. When the reaction ceases and the heat dissipates the substrate consumption stops and the reaction front is left frozen. The nickel gradient across the coating itself shows that there are two subtly different regimes present, the aluminium rich β-NiAl phase close to the external surface and the nickel-rich β-NiAl phase close to the bottom of the coating and adjacent to the interdiffusion zone. (*Fig. 7.7*)

7.4.3. Order of operations – cascading reaction microstructural proof

During this work it became apparent that an alternative explanation was necessary to describe the order of operations that were occurring during slurry coating formation instead of the traditional inward or outwardly grown aluminide system. To this end in order to better understand the spatial volume that the newly formed coating system occupies, i.e. does it most closely resemble inward or outward aluminising, a masking operation was undertaken upon the alloy C263 with the standard chromate containing slurry aluminide system (*Fig. 7.15*). A temporary maskant was applied to the surface that would block deposition of the air sprayed coating. Following application the maskant was peeled away leaving the coating system in the pre-heat treated friable green state intact upon the remaining surface. This test piece then received the bake and subsequent heat treatment at 870 °C to form the slurry aluminide. The results show that the volume the new coating occupies is ca 50 % inward growth and ca 50 % material growing outwards from the original interface. (*Fig. 7.15*)

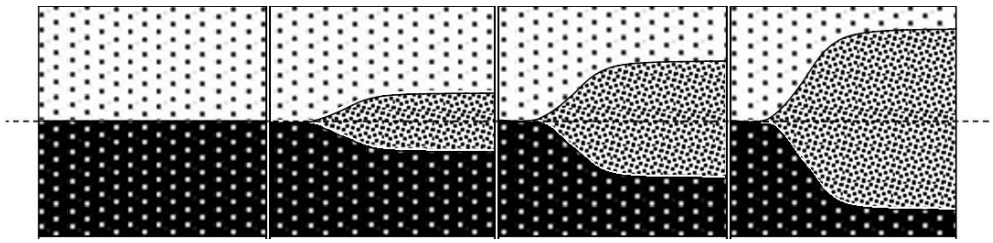

Fig. 7.15 – schematic of coating formation mechanism, masked coating application and relative new coating volume

The slurry coating upon MarM002 yielded an image (*Fig. 7.6 (b)*) that records the formation mechanism frozen within the microstructure. A substrate carbide present sub-surface, ending at the outer surface of the test specimen. Activation of the slurry coating caused the liquid aluminium wetting the surface to dissolve the nickel superalloy around the carbide and proceed through the transformation reaction. The carbide, unable to dissolve or participate in the reaction, is a spectator to the changes around it. The progressive transformation of the nickel superalloy to β-NiAl, through the cascading reaction, sees the matrix crystal structure expanding in volume outwards due to the application to a free surface.

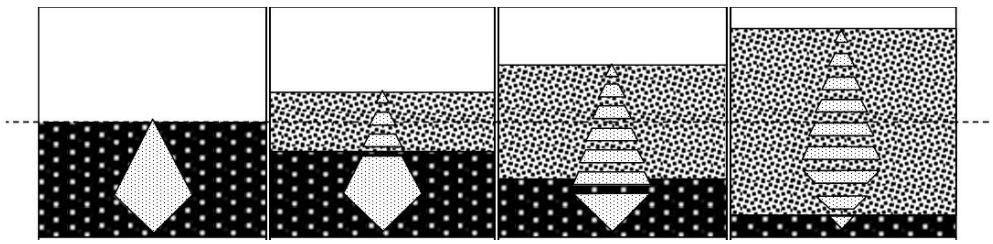

Fig. 7.16 – schematic of coating formation mechanism, the coating upon MarM002 containing a broken carbide seen in Fig. 7.6

As the forming coating expands the carbide is subject to tensile loading whereby the carbide root is held in the, as yet untouched, nickel-based superalloy matrix, beneath the reaction front, and the tip is pulled upwards by the expanding coating. The carbide's fracture toughness is surpassed by the interfacial energy between the carbide and matrix resulting in multiple transverse fractures, perpendicular to the loading direction. This sequential carbide fracture supports the notion of a formation period whereby the amount of carbide encompassed within the new coating increases gradually as the coating expands, eventually fracture occurs, and the reaction front progresses downwards, further down the carbide, before the process repeats. (*Fig. 7.6 (b)* and *7.16*) This cascading reaction front is supported by the stepwise fracture of the carbide before being bodily pushed up and away from the coating that is formed immediately afterwards at the reaction front. This enables the carbide to appear to travel outwards towards the newly formed external surface.

7.4.4. Coating microstructure – NiAl – grain evolution and the cascading reaction

Slurry aluminides like their traditional vapour based analogues make use of a phase rich in nickel and aluminium to provide potent oxidation protection. Of the various nickel-aluminium phases available it is the β-NiAl that provides sufficient aluminium activity as well as thermal capability and ductility at temperature to provide a capable and adherent surface layer to protect the nickel-based system beneath. Traditional pack processing yields the aluminium heavy δ-Ni_2Al_3 phase that requires subsequent heat treatment to redistribute the high aluminium concentration at the surface since too much will result in a brittle material prone to cracking.

X-ray diffraction was carried out using a top down approach where solid samples coated in the slurry aluminide were analysed by passing the incident radiation through the top of the coating before being diffracted back out again. (*Fig. 7.12*) This data supports the presence of both β-NiAl and δ-Ni_2Al_3.

Using FIB lift-outs it was possible to map the relative regions rich in certain elements, determine how many different phases exist and their approximate shape and location within the coating microstructure. Three key maps yield information regarding the matrix phase of the coating, nickel, aluminium and cobalt. (*Fig. 7.10*) All three of these maps closely resemble each other, supporting that for this particular phase, where you find nickel you find both aluminium and cobalt too.

Further to the elemental maps described above a region of the matrix was selected for elemental composition, this provided an average of the elements present within the selected area. This work (*Fig. 7.11*) shows that the matrix consists of ca 35 at. % nickel, ca 49 at. % aluminium and ca 6 at. % cobalt. This phase composition is consistent with the identification of the coating matrix phase as aluminium-rich β-NiAl. The FIB lift-outs used in the TEM

analysis were also used to generate TKD maps to better understand the grain size, orientation and phase identification of the coating. (*Fig. 7.14*) After mapping the matrix phase of the coating, the β-NiAl, the grain size becomes of acute interest. Starting in the uppermost third of the coating the β-NiAl grains appear to be elongated in the *x* and *y coating orientation* and comparatively large (ca 2 μm across), this is likely the first of the β-NiAl to form and has likely had the longest period of time in which to coarsen and grow larger. The middle third of the coating is made up of small (< 1 μm) β-NiAl grains orientated in an array of directions, this is the purest region that sees equiaxed grain growth seeded from many points simultaneously and is allowed to form in this manner due to the uppermost and bottom thirds providing a form of thermal insulation hindering preferential grain growth. The bottom third sees medium sized β-NiAl grains (ca 1 μm) that are elongated in the *z coating* direction, this is a result of both the heat sink provided by the underlying substrate, which is cool in temperature compared to the highly energetic exothermic reaction front, and the seeding effect provided by the still solid substrate. These features provide a heat gradient and a seed point from which crystals can instigate and grow.

Use of electron back scattered diffraction has enabled trends and observations seen in TKD to be confirmed and better understood in the wider context of the coating upon the substrate. Confirmation of the grain size trends explained above are validated in the EBSD scans and the three regions are clearly delineated. (*Fig. 7.13*) Further to the TKD-derived information is that of the local misorientation found across the coating microstructure. In the local misorientation map it can be seen that there are two bands of low level misorientation at the top and bottom of the coating in the regions where grains are larger in size. There is a region in the centre of the coating that has slightly increased misorientation and this correlates with the multitude of small equiaxed grains which formed rapidly and simultaneously. Once the reaction front propagation is established and progressing at a steady state there is little time once the front has passed for growth of large β-NiAl grains. Finally at the bottom of the coating at the interdiffusion zone there is the greatest level of misorientation, this being closely related to stresses found within regions of γ/γ’ rafting with the elongation of the microstructure occurring during reaction front propagation.

7.4.5. Coating microstructure – CrSi – precipitates and the cascading reaction

Slurry applied aluminides are unique compared to their traditional vapour deposited counterparts in that they allow codeposition of extra elements in slurry form that can enhance coating properties, in this instance silicon. The addition of silicon to aluminium-based coatings provides a synergistic effect that promotes the formation of stable, adherent aluminium oxide layers that are quick to form and heal in the event of damage. Early SEM imagery (*Fig. 7.6*) supported the premise of a dual-phase coating microstructure with β-NiAl most likely existing as the coating matrix with a dispersed phase within. Ladder-scan EDS data (*Fig. 7.7*) gave a good general overview of the distribution of elements within the coating microstructure but each line-scan was averaged per element which resulted in an average single value per relative location within the coating. This means that this value is an average of the dual phase microstructure and must be regarded as such. Once FIB samples were lifted from coated samples and examined within the TEM accurate elemental composition data was gathered that meant it was possible to distinguish one phase from another.

HAADF TEM images of the coating upon MarM002 (*Figs. 7.8* and *7.9*) clearly show a distinguishable gradient in the coarseness of the dispersed chromium silicide precipitate phase. Traversing down though the coating from external surface to the interdiffusion zone shows coarse precipitates elongated in the *x* and *y orientation* in the uppermost third of the system, in 3 dimensions these will appear as flakes. Moving down into the middle third sees an array of medium-sized globular precipitates before finally reaching the bottom third of the coating which contains small nanometre-scale versions of the same phase (*Fig. 7.8 (d)*). These Cr-Si dispersed precipitates can form upon grain boundaries of the β-NiAl phase following the matrix solidification (*Fig. 7.9 (a)*), or within grains (*Fig. 7.9 (c)* and *(d)*).

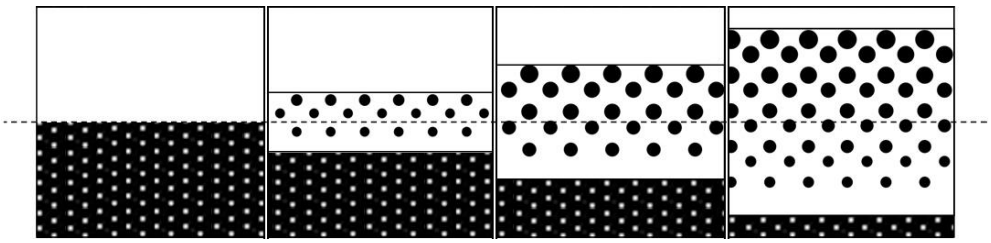

Fig. 7.17 – schematic of coating formation mechanism, showing dispersed phase size gradient seen in Fig. 7.8

The size gradient noted supports the hypothesis that, as the reaction front progresses down and consumes the nickel-based substrate, solid material is ejected up and away from the specimen's original outer surface interface. As the front progresses and fresh liquid aluminium reaches down to continue the exothermic reaction the newly created β-NiAl phase mushy solid is forced outwards and so begins the precipitation of chromium and silicon containing precipitates. Gale et al. [129] said that of the chromium rich precipitates

forming some appeared to nucleate from within the coating matrix, these often being randomly orientated. Some were elongated and seen to form along β-NiAl grain boundaries, coarse precipitates were thought to represent those that had spent the longest period within the coating, which if formed by inward diffusion would lie towards the outside.[129] Disregarding the inward diffusion statement, since a 50/50 split of substrate consumption and new material growth from the original surface, the traits and trends seen in the work by Gale et al. closely resemble what has been seen and examined during the course of this work. The size gradient of the chromium silicide phase suggests that those precipitates lying towards the outermost surface have had the longest time in which to precipitate and see further growth in clear contradiction to the small nm scale precipitates seen further down close to the interdiffusion zone. The fact that there is a clear zone at the base of the coating that sees no chromium silicides whatsoever between the substrate and the coating implies that this region has not seen the required time necessary to yield such phases.

The FIB lift-outs yielded elemental map information regarding the components of the dispersed precipitate phase of the coating; chromium, silicon and tungsten. (*Fig. 7.10*) These elemental maps closely resemble each other, supporting that this dispersed phase is where you find chromium and you will find both silicon and tungsten too.

Further to the maps described above a region of the dispersed phase was selected for elemental composition analysis, this provided an average of the elements present within the selected area. This work (*Fig. 7.10*) shows that the dispersed phase consists of ca 33 at. % chromium, ca 12 at. % tungsten and ca 25 at. % silicon. This phase composition is consistent with the identification of the dispersed precipitate phase as a chrome-silicide enriched with tungsten.

33 at. % Cr	→	47 at. % Cr	64 at. %	
12 at. % W	→	17 at. % W		
25 at. % Si	→	36 at. % Si		
70 at. %				$(Cr,W)_2Si$

7.5. Conclusions

This work has used advanced material characterisation techniques to thoroughly examine the case of slurry aluminides forming upon the nickel-based superalloy MarM002. Techniques include SEM, TEM, XRD, EBSD and TKD. The following conclusions are drawn regarding the coating microstructure formed as a result of this coating method:

1. The concentration of the elements chromium, tungsten and cobalt, from the alloy is halved upon incorporation within the coating, supporting that coating formation is followed by phase expansion and a decrease in density of the consumed nickel-based substrate.
2. The chromium-silicide size gradient, from coating top to bottom, confirms that as the reaction front consumes the nickel-based substrate, solid material is ejected up and away from the specimen. Fresh liquid aluminium reaches down, continues the reaction, and the newly created “mushy” β-NiAl phase, is forced outwards and so begins the precipitation of chromium and silicon containing precipitates.
3. The uppermost β-NiAl grains are elongated in the *x* and *y direction* and large (ca 2 μm across), this is likely the first of the β-NiAl to form and has likely had the longest period of time in which to coarsen and grow larger.
4. Central small (< 1 μm) β-NiAl grains are orientated in an array of directions, this is region sees equiaxed grain growth. The bottom third sees medium sized β-NiAl grains (ca 1 μm) that are elongated in the *z coating direction*, this is a result of the heat sink below and the seeding effect provided by the still solid substrate.
5. The progressive transformation of the nickel alloy to β-NiAl sees the matrix crystal structure expanding in volume outwards, only, due to the coatings application to a free surface.
6. The sequential carbide fracture defines a formation period whereby the amount of carbide encompassed within the new coating increases gradually as it expands, eventually fracture occurs, and the reaction front progresses downwards.

8. Slurry diffusion aluminising – substrate and coating variation

8.1. Introduction

This chapter follows directly from the work covered previously in chapter 7. In chapter 7 the phenomena of slurry aluminising was discussed and what made this process different to more ‘standard’ aluminising practises was revealed. The work that follows in chapter 8 discusses the impact of varying the underlying nickel-based superalloy substrate in an attempt to better understand what can be done to affect coating microstructure whilst keeping the deposited slurry the same. More evidence supporting the hypothesis generated in chapter 7 is explored and similar techniques, such as TEM and TKD have helped to form a more complete picture of depositing slurry aluminides onto nickel-based superalloys. An attempt to tie together the observed microstructural differences to real impacts upon oxidation resistance is also discussed. A greater understanding has been achieved which will help to develop better, more environmentally friendly coatings in the future.

8.2. Experimental

8.2.1. Methodology

An industry standard chromate-containing silicon-enhanced slurry for aluminising superalloys named IP1041, supplied by Indestructible Paint Ltd, was applied to samples of the nickel-based superalloys MarM002, CMSX-10N and IN738. Water-based, the slurry contains phosphates and chromates in addition to powdered aluminium, silicon and thickening agents.

H_2O	$MgHPO_4$	H_3PO_4	CrO_3	SiO_2	Al	Si
Solvent	Additives			Thickener	Powder 6 µm	Powder 10 µm
34.5 %	*3.5 %*	*15.8 %*	*5.7 %*	*2.5 %*	*32.5 %*	*5.5 %*

Table 8.1 – slurry composition prior to deposition upon substrate

Following application via air spray deposition, the samples were baked in air at 350°C for 60 minutes to dry the slurry upon the surface. The purpose of the bake is to drive away the solvent, aid decomposition of additives used to stabilise the slurry mixture during storage and ultimately to leave only the powder mixture upon the surface ready for coating. The samples were then placed within a vacuum furnace for 120 minutes with a holding set point of 870 °C under a partial pressure of argon.

Wt. %	Ni	Cr	Al	W	Co	Ti	Ta	Re	Mo
MarM002	Bal	9.0	5.7	10.0	10.0	1.5	2.5	-	-
IN738	Bal	16.0	3.5	-	8.5	3.5	-	-	-
CMSX-10N	Bal	2.2	5.8	5.5	3.3	-	8.3	6.2	-
CMSX-4	Bal	6.5	5.6	6.4	9.6	1.0	6.5	3	0.6

Table 8.2 – elemental composition prior of alloys used in this work

All of the specimens were placed within the fume hood for 168 hours to allow the sacrificial bisque (quasi-foam) layer to fragment and fall away revealing the final product.

8.2.2. Metallographic examination

Specimens were sectioned transverse to the coated surface in order to provide an 'in-plane' view of the coating microstructure. These were then hot mounted in conducting resin and polished using SiC grinding papers and diamond polishing cloths ending on a colloidal silica polish of 0.04 μm finish. Unless otherwise stated specimens were examined in the polished state and received no further etching or electropolishing treatments.

8.2.2.1. Scanning electron microscopy

SEM images were taken at 15 or 20 kV using either a field emission gun (FEG), a FEI Nova NanoSEM FEG, a tungsten filament, Jeol XL30 or a thermionic (CeB_6) source, a Phenom ProX.

8.2.2.2. Energy dispersive spectroscopy

Jeol XL30 fitted with EDS detector, running Aztec software from Oxford instruments

8.2.2.3. Transmission electron microscopy

STEM analysis was performed in a FEI Tecnai F20 operating at 200 kV. The system is equipped with an Oxford instruments XMAXN 80 TLE windowless SDD EDS detector. Images were collected with a bright field (BF) and high angle annular dark field (HAADF) detectors in STEM. EDS spectrum maps were collected using Aztec software then spectra were taken and these were collected for 20 s live time.

Additional TEM analysis was conducted upon the JEOL 200CX operating at 200 kV.

8.2.2.4. X-ray diffraction

X-ray diffraction surface analysis was carried out with a Bruker B3 BB D8 DAVINCI Gen 9 with LynxEye EX position sensitive detector in θ - 2θ mode (using CuKα radiation).

8.2.2.5. Electron back scattered diffraction and transmission kikuchi diffraction

EBSD and TKD scans were conducted at 30 kV using a FEG source, a FEI Nova NanoSEM FEG running the Bruker EBSD acquisition system. The EBSD data was analysed using the HKL Channel 5 software package distributed by Oxford Instruments.

8.2.3. Focussed ion beam preparation

A dual beam FEI Nova 600 Nanolab focused ion beam (FIB) / FEG scanning electron microscope (FEG–SEM) system was used to prepare site specific TEM samples using an in-situ lift-out procedure. Platinum was deposited using the gas injection system (GIS) over the 40 µm long area of interest, and milling created trenches on either side. The TEM sample was extracted using an Omniprobe micromanipulator and was attached to a Cu grid before final thinning to achieve samples that had similar thickness.

See Chapter 7 for further details.

8.2.4. Oxidation testing

Accelerated furnace cyclic testing (AFCT) was created for the timely assessment of oxidation life and temperature capability of coated and uncoated materials. This is now a standardised test that has been adopted by Rolls-Royce plc. The test involves recoating samples with a measured level of salt at intervals, and repeated thermal exposures at a high temperature in an air furnace followed by cooling to low temperature. The aim of the test is to evaluate the performance of materials under engine representative, oxidation conditions. The salt loading and thermal cycles enhance the rate of attack meaning that the materials systems are less able to repair protective oxides and leads to a breakaway oxidation condition. The AFCT test is sensitive to the following factors which impact oxidation attack rates [148] :

- Temperature
- Cycle frequency
- Salt species applied
- Salt loading applied and the frequency of application
- Sample geometry

The mass of the specimens shall be determined prior to exposure and at each re-coat interval during exposure.

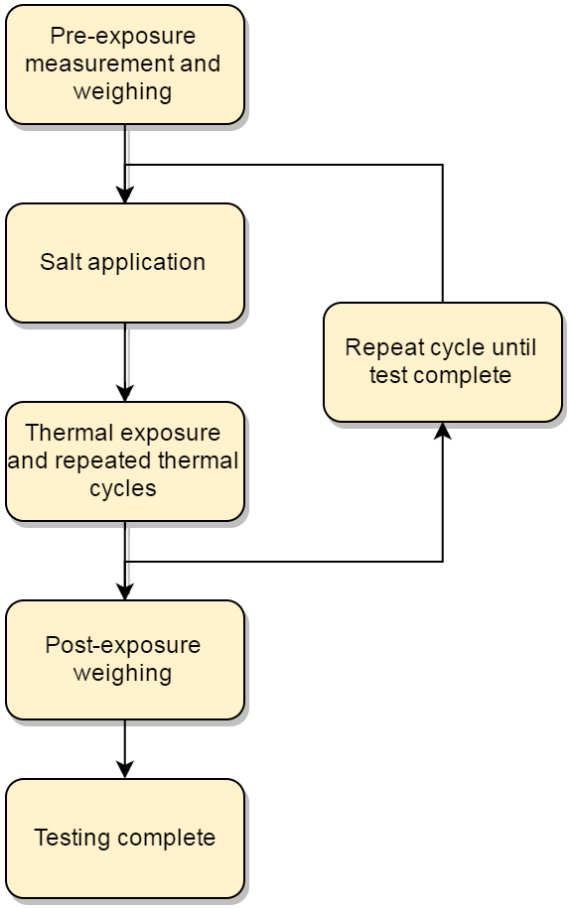

AFCT testing flowchart

Standard test Parameters

The following salt specification, salt loading and recoat interval were used for testing in this work:

- Salt specification - Synthetic seawater to BS 3900-F4
- Salt loading - 0.3 $mg.cm^{-2}$
- Recoat interval - 20 h hot dwell time

Testing procedure:

- Specimens were heated on a hot-plate and allowed to attain the prescribed temperature (typical temperature range – 100-150°C).
- Salt applied to specimens by coating with a number of sprays of salt solution using a spray gun. The following parameters are controlled for standardisation: solution composition, pre-heat temperature of specimen, distance of the spray gun from the specimen, spray gun height, spray time and spray gun air supply pressure.
- Sample rotated, and salt application steps repeated. The spray process must ensure an even distribution of salt over the entire surface.
- Specimen reweighed after spraying to see if required salt load is met.

8.3. Results

8.3.1. Scanning electron microscopy

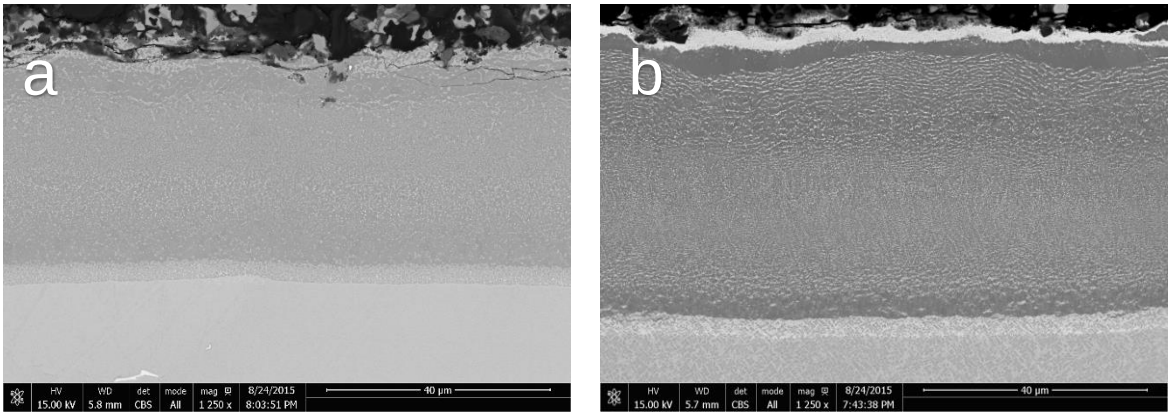

Fig. 8.1 – silicon-enhanced aluminide coating upon IN738 substrate, nominal appearance (a), upon CMSX-10N substrate, nominal appearance (b)

Backscatter scanning electron microscope (SEM-BSE) images of the slurry-deposited aluminide system upon both IN738 and CMSX-10N (*Fig. 8.1*) shows a similar dual-phase coating microstructure to that explored in chapter 7 on the alloy MarM002. The coating comprises a dark matrix phase (β-NiAl) and a lighter, dispersed precipitate phase (Cr_2Si). The size gradient observed in the dispersed phase transitions from coarse to fine within the coating, with it appearing coarse at the top and fine towards the bottom, closest to the unaltered substrate. There is a precipitate denuded zone visible immediately above the ca 5 µm thick interdiffusion zone between superalloy substrate and the formed coating, this observation is akin to that seen using this coating upon the alloy MarM002 discussed in chapter 7. The coating showed little variation in coating thickness or microstructure, the SEM micrographs displayed in *Fig. 8.1* are average representations of this particular slurry-aluminide system upon these two nickel-based superalloys. In *Fig. 8.1 (a)* the microstructure of the IN738 coating appears more chaotic with the dispersed precipitate phase no longer appearing in a ‘patterned’ fashion as observed previously. *Fig. 8.1 (b)* shows the same dispersed precipitate phase, this time within the coating upon CMSX-10N, though in this instance the precipitates are highly ordered with a clear sequential formation, which has resulted in a continuous series of rows of brighter precipitates. The CMSX-10N coating also displays a bright white surface layer on top of the formed coating system and likely suggests a concentration of heavier elements above the coating upper surface.

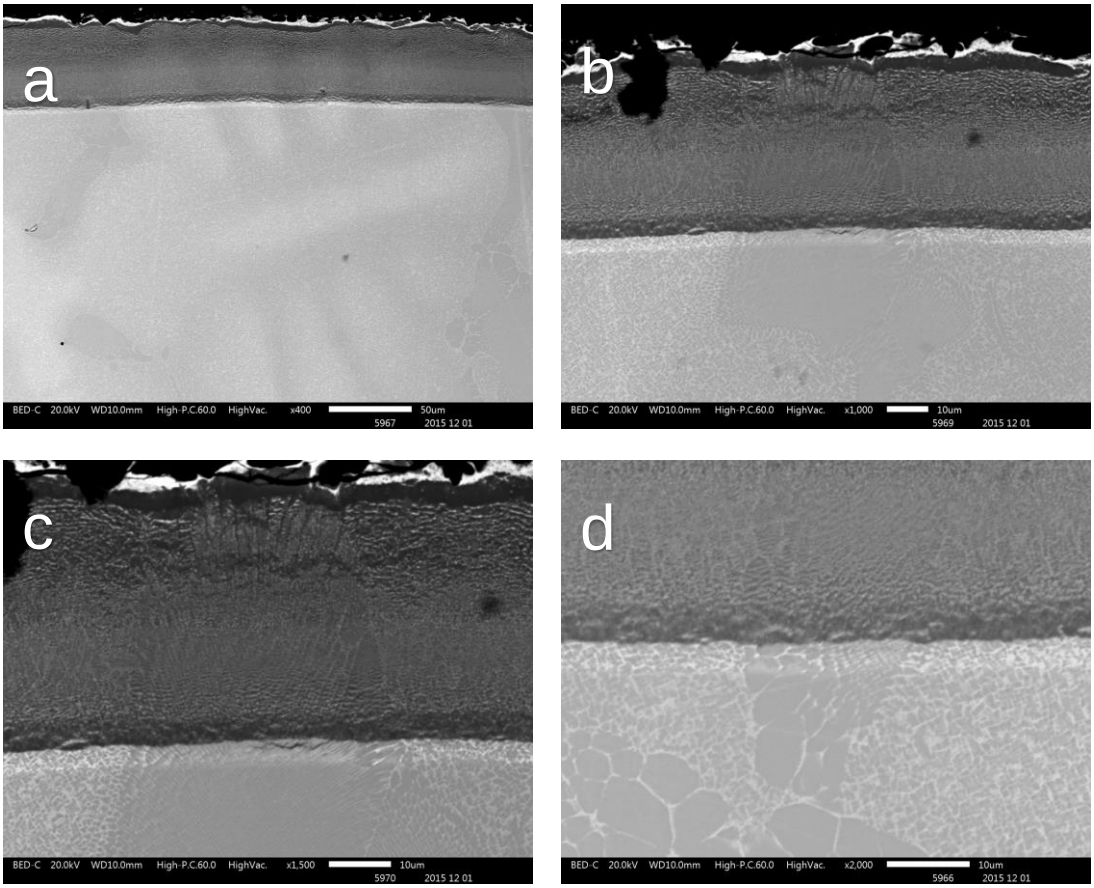

Fig. 8.2 – silicon-enhanced aluminide coating upon CMSX-10N substrate, lower magnification view, note the as-cast dendritic microstructure still clearly visible under BS SEM mode (a), upon CMSX-10N substrate, tip of dendrite within coating microstructure (b and c) high magnification image of interdiffusion zone (d)

Further backscatter scanning electron microscope (SEM-BSE) images of the slurry-deposited aluminide system upon CMSX-10N (*Fig. 8.2*) show important microstructural features which are crucial to understanding slurry-aluminide formation mechanisms. *Fig. 8.2 (a)* is a low magnification image displaying the macro structure present throughout the CMSX-10N specimen which was coated in the un-heat treated condition. Without solution heat treatment the alloy retains its heavily segregated dendritic microstructure, one region of an interdendritic phase is observed in the micrograph. Of particular interest is the positioning of the interdendritic region close to the external surface of the specimen and how the residual segregation phenomena appears to carry through into the slurry aluminide coating. This concept is further explored in *Fig. 8.2 (b) and (c)* where the tip of an IDP region, and its inherent residual segregation, can be observed within the unaltered superalloy substrate, crossing the narrow interdiffusion zone and persisting into the newly-formed aluminide. The tip of the IDP appears to have been elongated, this being most visible in *Fig. 8.2 (c)* where a series of vertical striations appear to disrupt the otherwise complete, yet stretched, memory of the substrate microstructure.

Finally in *Fig. 8.2 (d)* the narrow interdiffusion zone at the interface between the coating and the substrate CMSX-10N is observed and additional evidence of the lingering microstructure is observed. Immediately beneath the interdiffusion zone is segregation in the form of cellular interdendritic phase formation, a result of the solidification process. A faint replica of this cellular pattern is seen immediately above the interdiffusion zone in the same micrograph further supporting previous results of the transmission of a microstructure across the interface and into the newly-formed coating upon the external specimen surface.

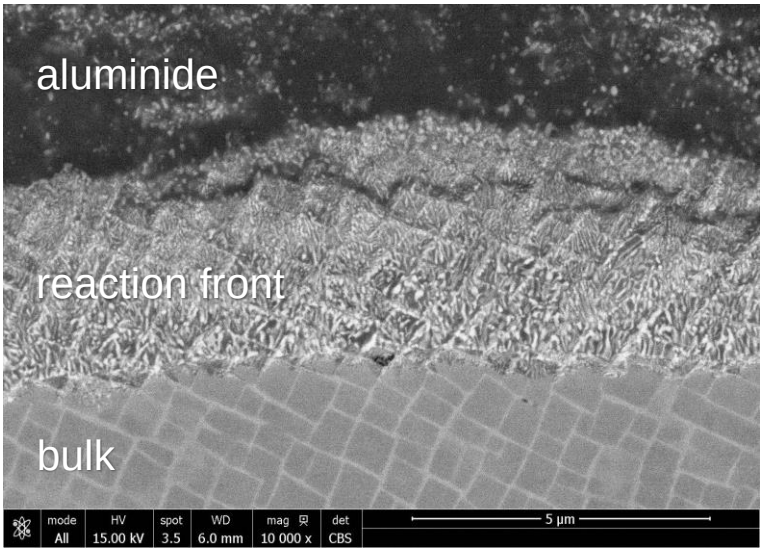

Fig. 8.3 – silicon-enhanced aluminide coating upon CMSX-4 substrate, high magnification image of interdiffusion zone, note the break-away region

In this final SEM-BSE micrograph (*Fig. 8.3*), the same slurry-deposited aluminide coating is formed upon the surface of a CMSX-4 specimen, the high magnification image focusses upon the interdiffusion zone. Of note in *Fig. 8.3* is how the reaction front has been frozen at the interface of the coating and the substrate during the formation mechanism. This pseudo mid-action image neatly encapsulates the narrow chemical reaction front progressing downwards consuming the nickel-based superalloy. In the centre of the image there appears to be a fissure running horizontally from left to right. This fissure appears to suggest a portion of nickel-based superalloy has become disconnected from the substrate at the bottom of the image and the dark colouration proposes that liquid-phase aluminium has seeped into the crevice. This phenomena appears analogous to an iceberg in that a discrete portion of the substrate has been severed from the whole and is moving away from the still-solid substrate enabling fresh liquid to move in behind and again wet the surface. This fissure appears to trace out what was once a γ’ boundary which may shed light on how portions of the material disconnect from the remaining solid.

8.3.2. Energy dispersive spectroscopy

A series of EDS line scans were taken parallel with the coating, this ‘ladder-scan’ averages the dual-phase microstructure into a single result per line to give general elemental trends. The spacing between line scans is ca 2.5 µm, the left hand side of the graph starting at zero is the extreme outside of the coating. Traversing the graph from left to right moves across the coating from outermost to innermost finishing within the bulk microstructure of the superalloy substrate. The coating upon IN738 (*Fig. 8.4 (p) and (r)*) shows a relatively constant aluminium trace and that nickel has a shallow gradient that is highest as the interdiffusion zone is approached and then crossed. The elements cobalt, chromium and tantalum are constant in concentration across the core coating span (*Fig. 8.4 (q) and (s)*) but in the case of chromium displays significantly lower levels than that observed within the substrate, though there is a slight dip immediately prior to the interdiffusion zone. The silicon trace (*Fig. 8.4 (p) and (r)*) shows a gradient that is highest closest to the external surface that drops away gradually, disappearing once the interdiffusion zone is crossed. The interdiffusion zone depleted in nickel, features no additional aluminium from the slurry and is enriched predominantly in chromium, which only originated within the substrate.

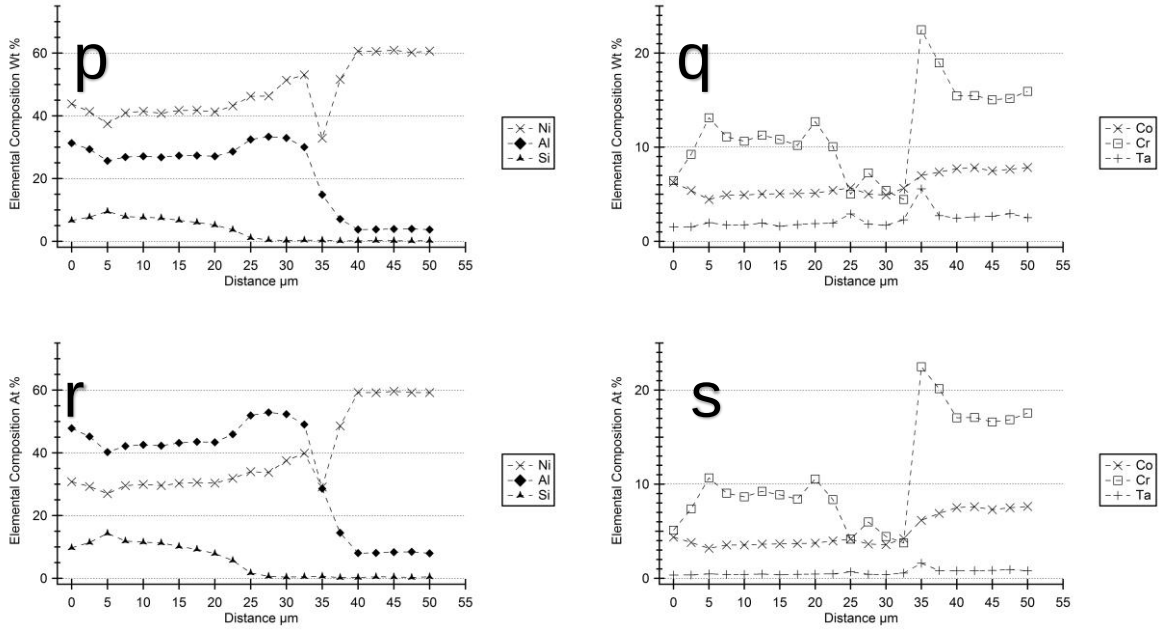

Fig. 8.4 – elemental composition across coating upon IN738, primary elements in Wt % (p), secondary elements in Wt % (q), primary elements in At % (r), secondary elements in At % (s)

The coating upon CMSX-10N (*Fig. 8.5 (p) and (r)*) shows a constant aluminium trace and that nickel has a shallow gradient that is highest as the interdiffusion zone is approached and then crossed. The elements tantalum, tungsten and rhenium are constant in concentration across the coating span (*Fig. 8.5 (q) and (s)*) but display significantly lower concentrations than that observed within the substrate, though there is a slight dip

immediately prior to the interdiffusion zone within the aluminide. The silicon trace (*Fig. 8.5 (p) and (r)*) shows a clear gradient that is highest closest to the external surface that drops away gradually, disappearing once the interdiffusion zone is crossed. The interdiffusion zone depleted in nickel, features no additional aluminium from the slurry coating and is enriched in tantalum, tungsten and rhenium all of which originate only within the substrate.

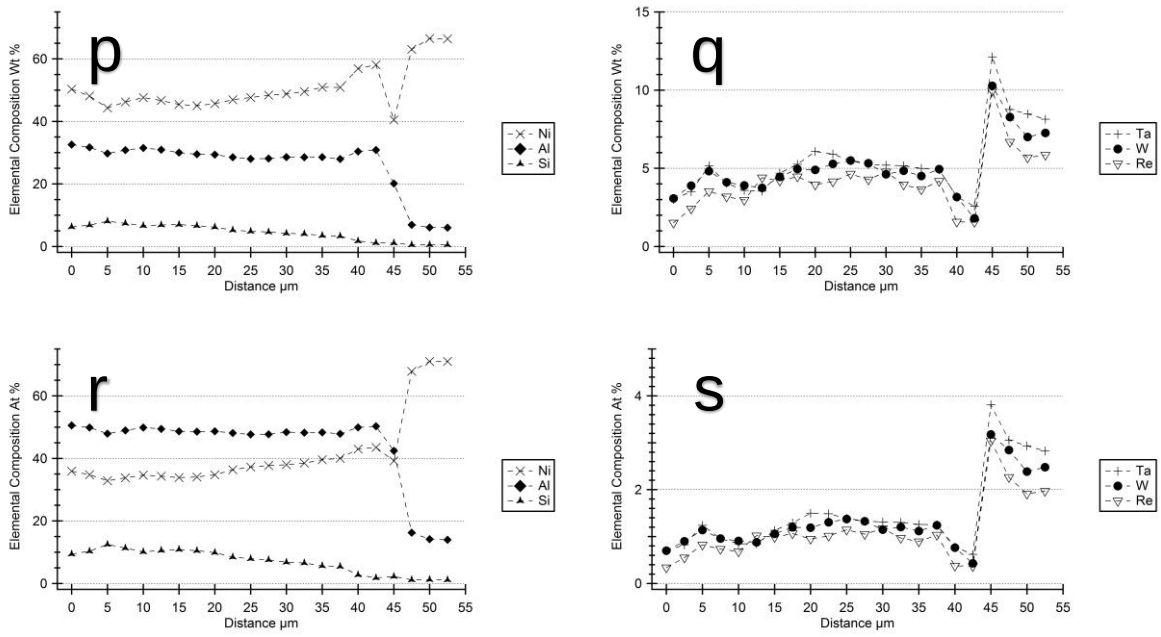

Fig. 8.5 – elemental composition across coating upon CMSX-10N, primary elements in Wt % (p), secondary elements in Wt % (q), primary elements in At % (r), secondary elements in At % (s)

The 'ladder-scans' of *Fig. 8.4* and *8.5* confirm trends observed in chapter 7. The only elements present within the slurry-deposited aluminide that originate from the slurry are aluminium and silicon. Any additional elements within the coating have started from within the nickel substrate, this includes the nickel and any additional elements like tungsten, rhenium and particularly chromium. The dip in elemental concentration immediately above the interdiffusion zone correlates with the precipitate denuded zone noted in section 8.3.1.1 and the SEM micrographs discussed.

8.3.3. Transmission electron microscopy – images

Transmission electron microscope (TEM) images, at 20,000 times magnification, using high angle annular dark field (HAADF) mode distinguish the matrix phase from the dispersed precipitate which, close to the surface, resides upon matrix phase grain boundaries. (*Fig. 8.6*) In CMSX-10N the initial sub-surface precipitates are defined as coarse and run parallel with the surface, preferentially growing in the *x* and *y directions*, yielding 'flakes'. Traversing the coating top to bottom in the *z direction* the precipitates clearly obey a gradient, progressively becoming finer until reaching the denuded zone immediately above the interdiffusion zone where they exist on the nanometre length scale.

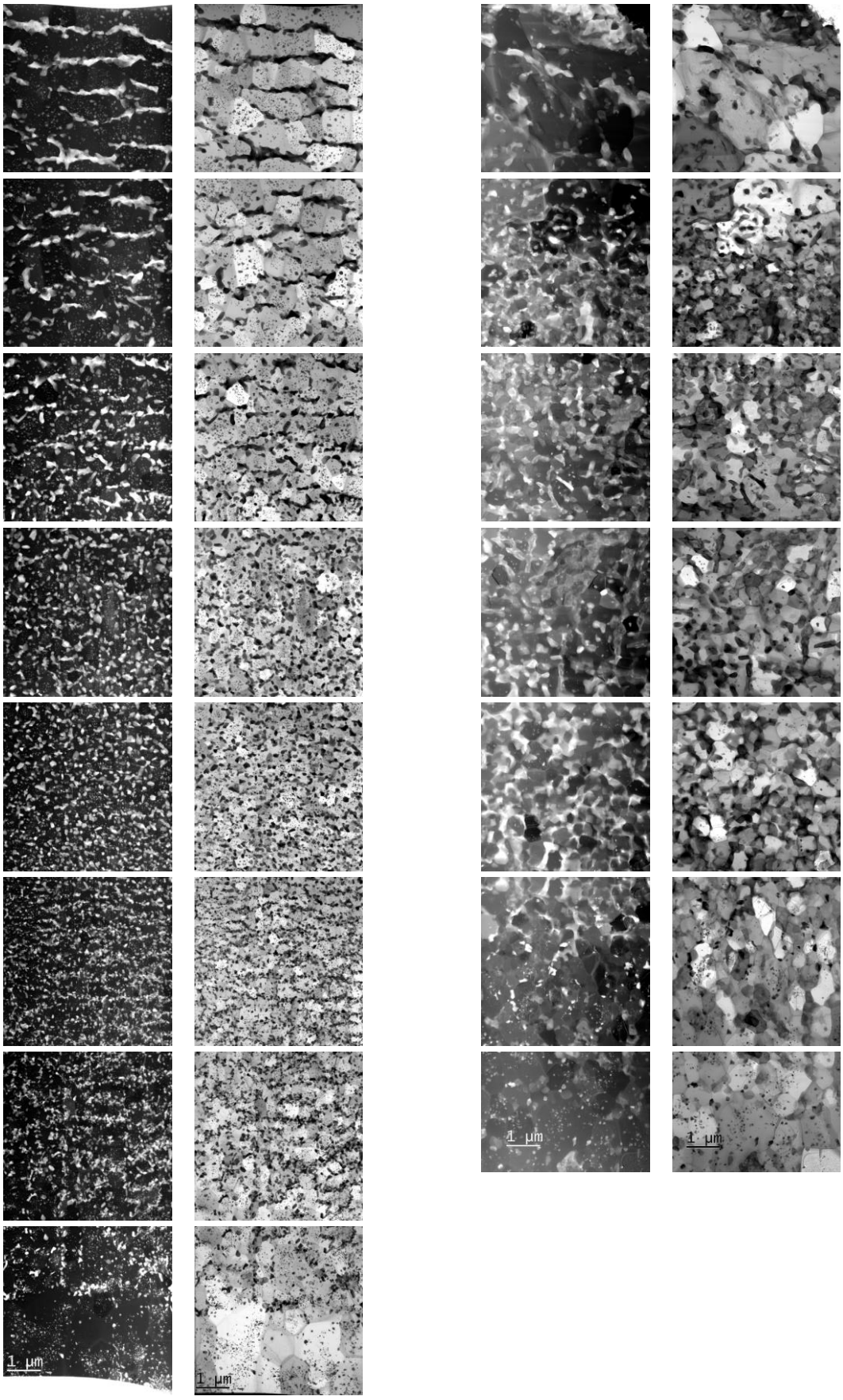

Fig. 8.6 – TEM images HAADF and BF, at 20,000 times magnification, LHS is CMSX-10N and RHS is IN738

Images courtesy of G. West and Z. Zhou

Regarding the dispersed phase three distinct bands can be described from top to bottom, the top third displays a coarse elongated nature (ca 1 – 1.5μm long) running parallel with the coating outer surface. The middle third has precipitates that are globular and smaller than previously described (ca 100nm across). Finally the bottom third has extremely fine dispersed precipitates (ca 10nm across) that eventually taper away and disappear in the denuded region immediately above the interdiffusion zone. Within the TEM micrographs of CMSX-10N in *Fig. 8.6* the trend in the dispersed precipitate phase is abundantly clear, using HAADF mode the contents of the dispersed phase is rich in heavy elements making contrast sufficiently different to clearly delineate the one phase from the other. In *Fig.8.6* on the RHS are the micrographs associated with the coating upon the alloy IN738 and the microstructure although displaying clear correlations with the alternative substrate alloys is more chaotic and difficult to interpret. Of the features that persist are the elongated dispersed precipitate phase at the outmost of the coating in the top third as well as the much smaller precipitates to be observed in the lower third. In addition there is a clear denuded region at the base of the coating and again it is immediately above the interdiffusion zone.

8.3.4. Transmission electron microscopy – elemental mapping

TEM-based elemental mapping (*Fig. 8.7* and *8.8*) confirmed two primary phases within the slurry-deposited aluminide upon CMSX-10N and IN738. The coating matrix phase consists of aluminium, as well as nickel and cobalt solely from the substrate. The dispersed precipitate phase contains silicon from the slurry, as well as chromium and elements like tungsten or titanium that originate from the substrate. Close to the external surface, in the top third the dispersed phase is bright and distinguishable due to its coarse nature.

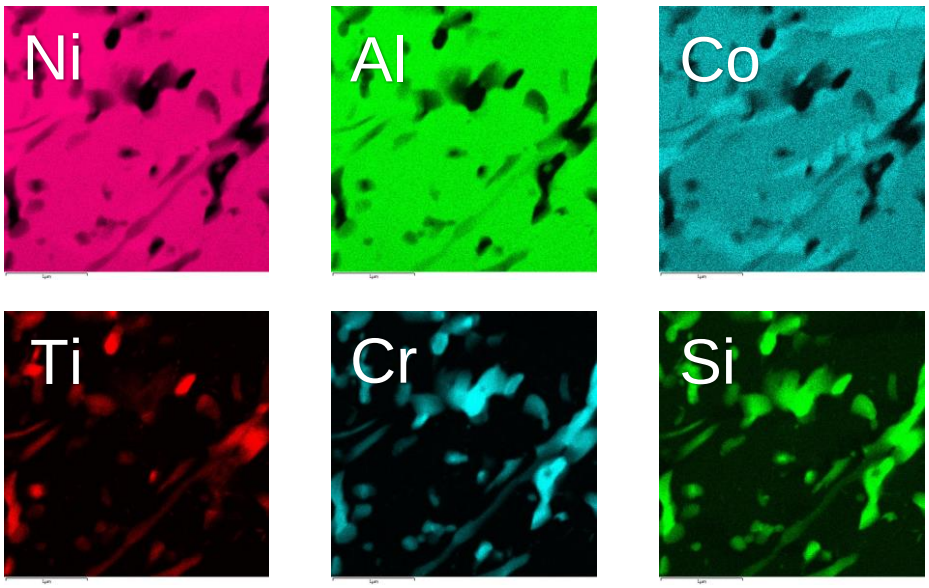

Fig. 8.7 – TEM EDS maps, coating upon IN738

Images courtesy of G. West and Z. Zhou

The coating upon IN738 shown in *Fig. 8.7* clearly shows the chaotic disorganised nature of the dispersed precipitate phase as observed using the titanium, chromium and silicon maps. *Fig. 8.8* showing the coating on CMSX-10N is more organised in nature with the elongated 'flake' precipitates easily recognisable from the upper region of the TEM micrographs.

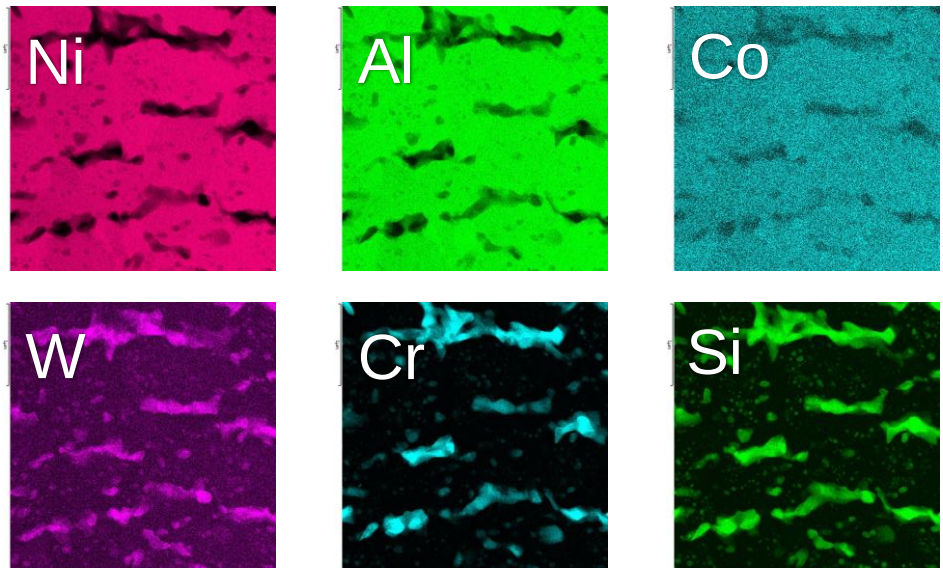

Fig. 8.8 – TEM EDS maps, coating upon CMSX-10N

Images courtesy of G. West and Z. Zhou

8.3.5. Transmission electron microscopy – elemental composition

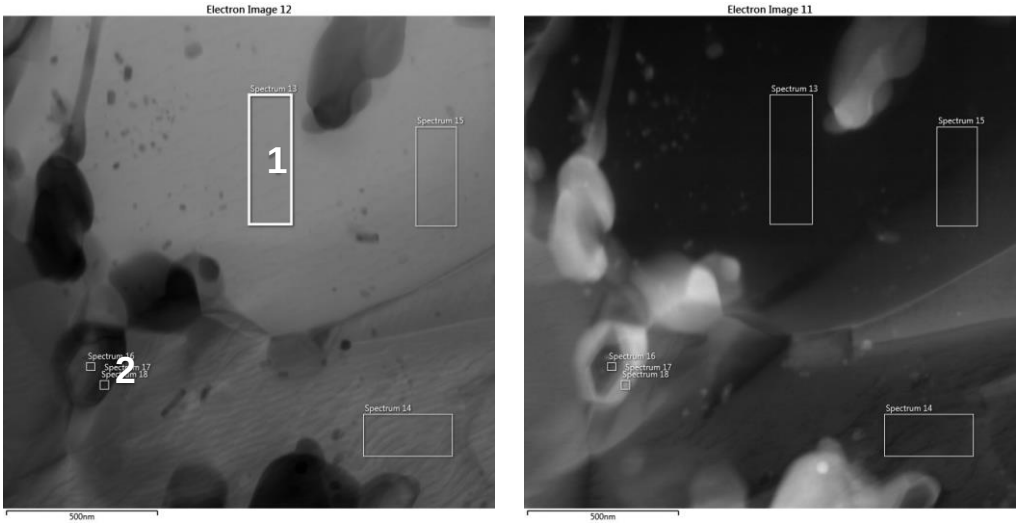

Wt. %	Ni	Al	Si	Ti	Cr	Co	W	Cu	Ta
Spectrum 1	46.0	37.4	3.2	-	0.6	0.8	-	6.0	-
Spectrum 2	0.7	1.7	25.8	20.0	32.9	-	1.2	7.5	4.8

At. %	Ni	Al	Si	Ti	Cr	Co	W	Cu	Ta
Spectrum 1	31.2	55.3	4.6	-	0.5	4.6	-	3.8	-
Spectrum 2	0.5	2.8	40.8	18.6	28.1	-	0.3	5.2	1.2

Fig. 8.9 – elemental composition within two separate coating phases upon IN738, spectrum 1 is within the coating matrix and spectrum 2 is within the dispersed phase. RHS image is TEM micrograph in HAADF mode and LHS is BF mode

– elemental composition within spectrum 1 and 2 identified above in weight and atomic pct.

Images courtesy of G. West and Z. Zhou

Further to the elemental maps of section 8.3.4 a series of quantitative box scans were undertaken using TEM-based EDS to determine the composition of the two primary phases within the coating microstructure. In *Fig. 8.9* the coating is on the alloy IN738 and spectrum 1 was taken from within the matrix phase. Using atomic percent the phase appears to be composed of ca 30% nickel, ca 55% aluminium and ca 5% of silicon and cobalt respectively. This confirms that the phase is predominately a nickel-aluminium phase with some cobalt substituting for nickel to form an approximately stoichiometric mixture. Spectrum 2 consists of data collected from one of the dispersed precipitate phases and using atomic percent is comprised of the following. The dispersed phase is ca 40% silicon, ca 18% titanium and ca 28% chromium. This confirms the elemental mapping seen previously suggesting that the dispersed precipitate consists of a chrome silicide phase with some substitution for readily available elements in the underlying substrate, in this instance titanium.

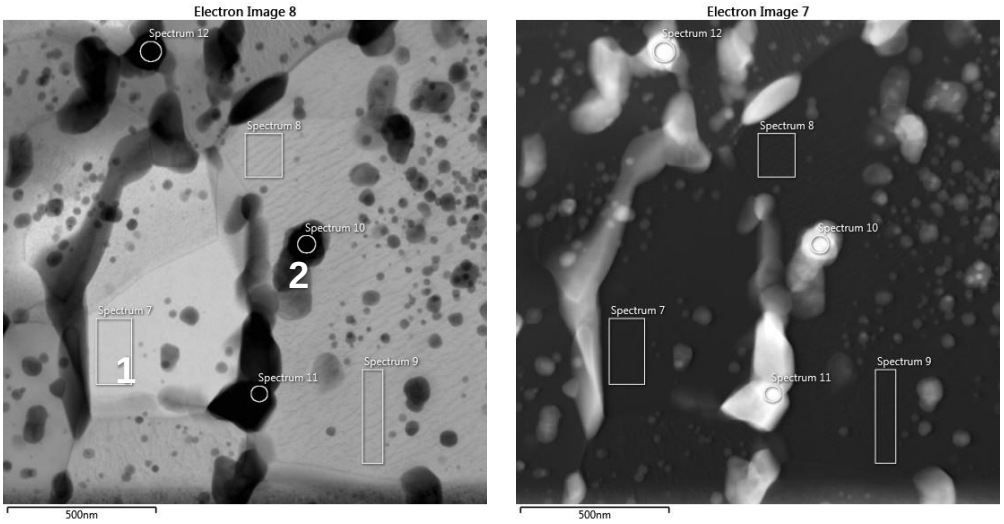

Wt. %	Ni	Al	Si	Ti	Cr	Co	W	Cu	Ta	Re
Spectrum 1	51.5	37.9	4.8	-	0.2	2.2	-	3.2	-	-
Spectrum 2	1.9	6.7	19.3	0.4	7.6	0.3	15.2	9.5	25.5	12.0

At. %	Ni	Al	Si	Ti	Cr	Co	W	Cu	Ta	Re
Spectrum 1	34.4	55.2	6.7	-	0.1	1.4	-	1.9	-	-
Spectrum 2	2.1	15.7	43.4	0.6	9.3	0.3	5.2	9.5	8.9	4.0

Fig. 8.10 – elemental composition within two separate coating phases upon CMSX-10N, spectrum 1 is within the coating matrix and spectrum 2 is within the dispersed phase. RHS image is TEM micrograph in HAADF mode and LHS is BF mode

– elemental composition within spectrum 1 and 2 identified above in weight and atomic pct.

Images courtesy of G. West and Z. Zhou

Further quantitative box scans were undertaken. In *Fig. 8.10* the coating is on the alloy CMSX-10N, spectrum 1 was taken from within the matrix phase. Using atomic percent the phase appears to be composed of ca 34% nickel, ca 55% aluminium and ca 6% of silicon and only ca 1.4% cobalt. This again confirms that the phase is predominately a nickel-aluminium phase with some cobalt substituting for nickel to form an approximately stoichiometric mixture. Silicon present in spectrum 1 is likely residual since silicon has some solubility within the nickel-aluminide phase. Spectrum 2 again consists of data collected from one of the dispersed precipitate phases and confirms that the dispersed precipitate in this instance consists of a silicide phase with substitution for readily available elements in the underlying substrate, in this instance rhenium, tungsten and chromium.

34.4 at. % Ni		55.2 at. % Al		
1.4 at. % Co		6.7 at. % Si		
1.9 at. % Cu				
0.1 at. % Cr				Ni_2Al_3 +
37.8 at. %		61.9 at. %		Al-rich β-NiAl

15.7 at. % Al	→	18 at. % Al	67 at. %	
43.4 at. % Si	→	49 at. % Si		
59.1 at. %				(Al+Si)
9.3 at. % Cr	→	11 at. % Cr	33 at. %	
5.2 at. % W	→	6 at. % W		
8.9 at. % Ta	→	10 at. % Ta		
4.0 at. % Re	→	4.5 at. % Re		
0.6 at. % Ti	→	1.7 at. % Ti		
28.0 at. %			(Cr+W+Ta+Re+Ti)	
87.1 at. %			$(W,Cr_2,Ta)(Si,Al)_2$	

8.3.6. Transmission electron microscopy – diffraction patterns

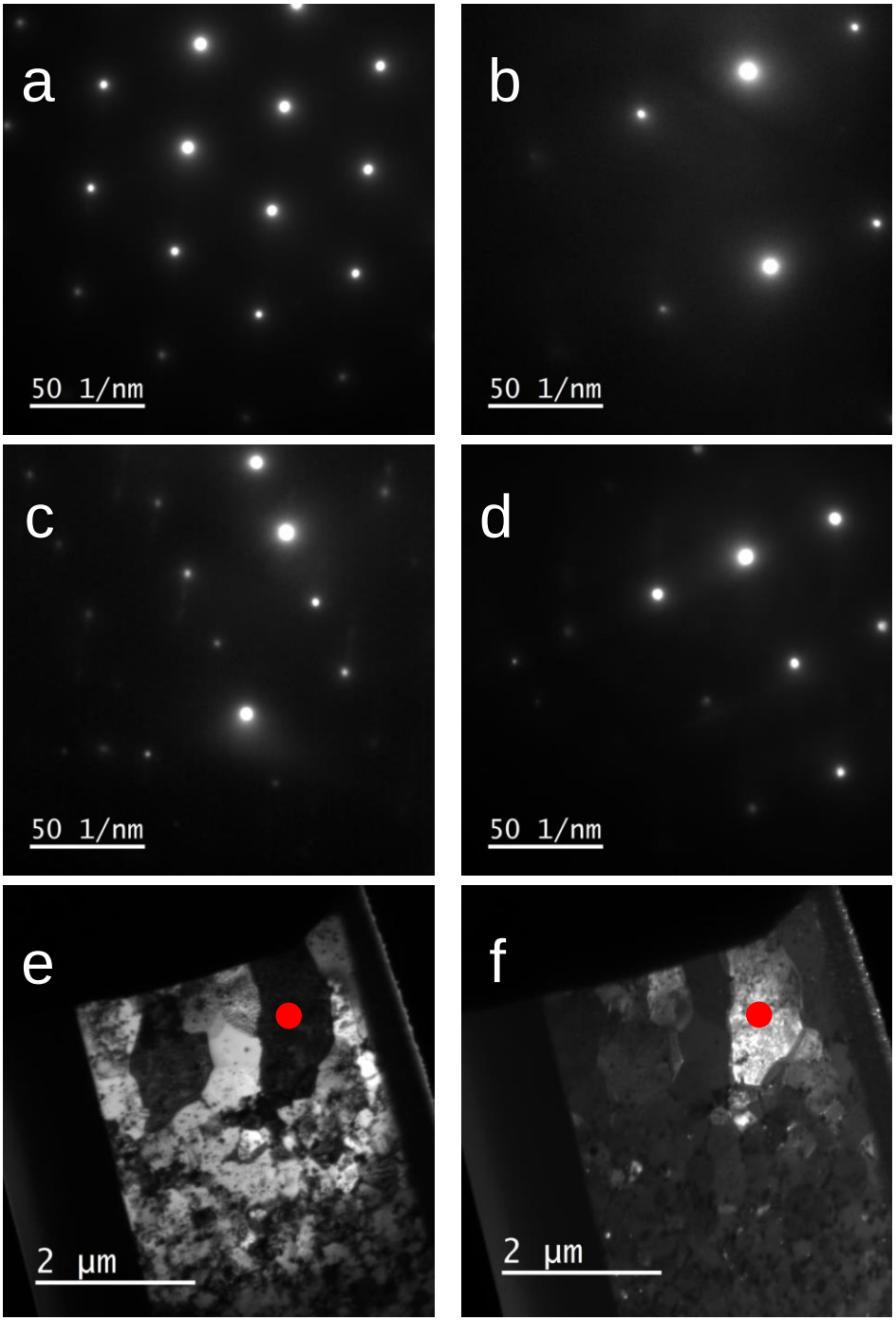

Fig. 8.11 – TEM diffraction patterns, coating upon CMSX-10N confirming presence of β-NiAl*;* [111] *(a),* [113] *(b),* [110] *(c) and* [211] *(d). Images (e) and (f) display the FIB lamella and the grain from which this diffraction data was collected at the bottom of the coating close to the interdiffusion zone with the substrate CMSX-10N*

Images courtesy of S. Lainé

Using TEM it was possible to form diffraction patterns from a single grain of the polycrystalline nickel-aluminide coating upon the alloy CMSX-10N. The images in *Fig. 8.11 (e)* and *(f)* show the grain selected near the base of the coating close to the interdiffusion zone. The diffraction patterns identified confirm that the matrix in this instance was β-NiAl.

8.3.7. Transmission kikuchi diffraction

Using transmission kikuchi diffraction (TKD) it has been confirmed that the β-NiAl phase is present throughout the coating upon the substrates CMSX-10N and IN738 (*Fig. 8.12 and 8.13*). In the coating upon IN738 (*Fig. 8.12*) the grain size of the polycrystalline β-NiAl varies according to depth within the coating. In the uppermost third of the coating, the largest grains are seen (ca 2 μm across), elongated in the *x* and *y direction*. Close to the interdiffusion zone, in the bottom third of the coating, medium sized grains (ca 1 μm) predominate, now elongated in the *z direction* and smaller in the *x* and *y*. β-NiAl grains around the midpoint of the coating are small (< 1 μm) with no overall order in their relative orientation with many orientations represented in the inverse pole figure (IPF) images. Local misorientation across the coating on IN738 (*Fig. 8.11*) is relatively consistent from coating top to bottom.

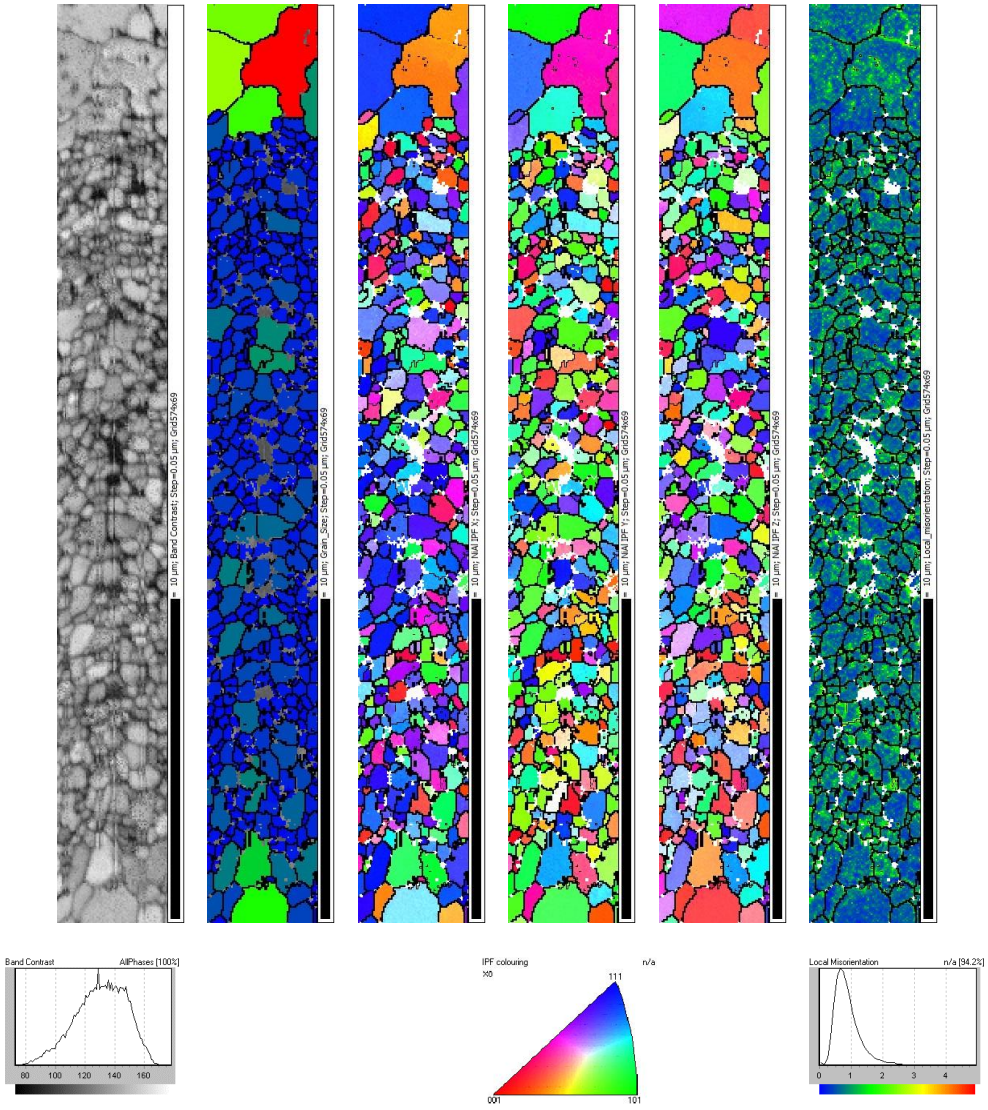

Fig. 8.12 – TKD of coating upon IN738, image from left to right; band contrast, relative grain size, inverse pole figures in the x, y and z orientations and the final image shows the local misorientation

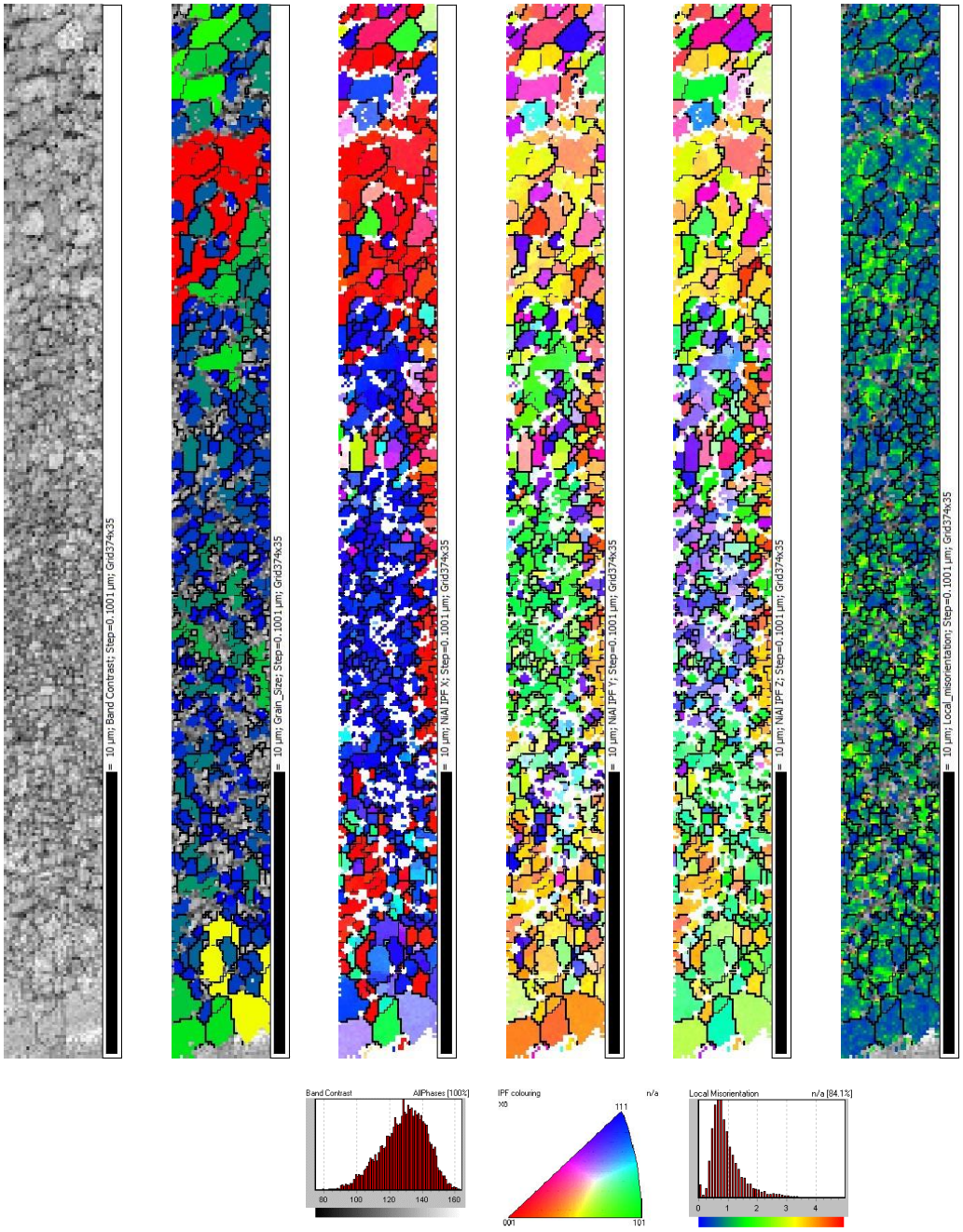

Fig. 8.13 – TKD of coating upon CMSX-10N, image from left to right; band contrast, relative grain size, inverse pole figures in the x, y and z orientations and the final image shows the local misorientation

In the coating upon CMSX-10N (*Fig. 8.13*) the grain size of the polycrystalline β-NiAl varies according to depth within the coating in a similar fashion to the coating on IN738. In the uppermost third of the coating, the largest grains are seen, elongated in the *x* and *y direction*. In the bottom third of the coating, medium sized grains (ca 1 µm) predominate, now elongated in the *z direction*. β-NiAl grains around the midpoint of the coating are small (< 1 µm) again with no overall order in their relative orientation with many orientations represented in the inverse pole figure (IPF) images. Local misorientation across the coating is slightly raised in the middle of the coating but is relatively consistent from top to bottom.

8.3.8. Oxidation testing

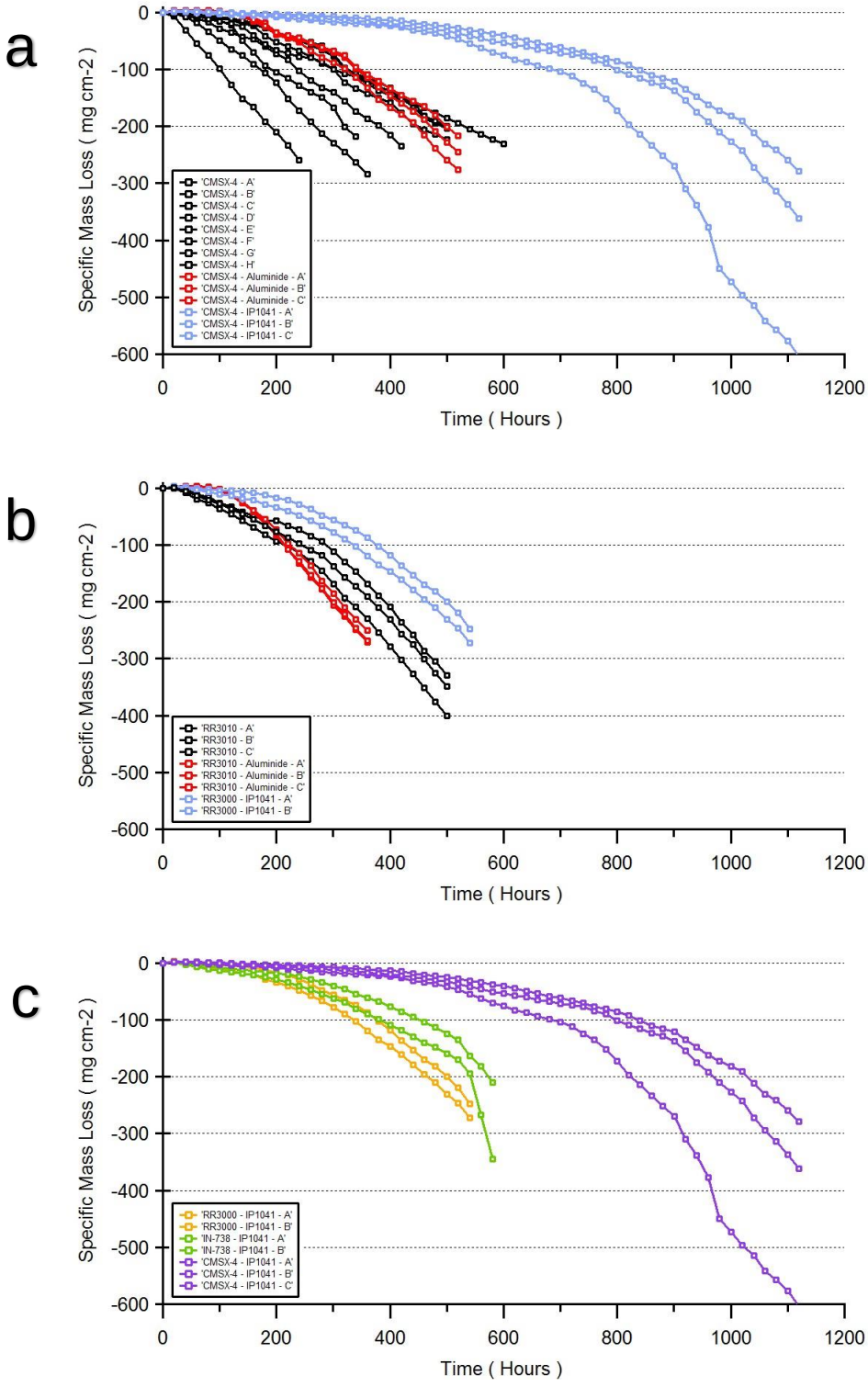

Fig. 8.14 – Oxidation testing 1050°C; the alloy CMSX-4 subject to AFCT testing, BLACK traces are bare alloy, RED is simple vapour aluminising and BLUE is silicon-enhanced slurry aluminide (a), the alloy tested was CMSX-10N and BLACK is bare, RED is simple vapour aluminising and BLUE is silicon-enhanced slurry aluminide (b) and finally the alloys tested are IN738 (GREEN), CMSX-10N (ORANGE) and CMSX-4 (PURPLE) (c)

Data courtesy of G.J.J. Brewster and A.J. Leggett

Accelerated furnace cyclic testing (AFCT) determines how effective oxidation resistant coatings provides rapid data which enables different systems to be compared and rated. *Fig. 8.14 (a)* features data from a series of AFCT tests using the alloy CMSX-4. All black traces show bare uncoated materials subjected to the test and indicate how long in hours it takes before a period of constant rate of specific mass loss is reached. It is important to note that there is only a limited incubation period for bare uncoated CMSX-4 since this form of testing is harsh and designed to yield rapid results, the alloy is unable to form a strong, adherent, impermeable oxide for long before the cyclic nature of the testing results in oxide spallation. All three red traces within *Fig. 8.14 (a)* again regard the substrate alloy CMSX-4 now coated with a comparatively simple vapour phase deposited coating system which provides some protection from the harsh testing conditions. There is now an incubation period resulting in all three red traces being at the top end of what bare CMSX-4 is capable of under certain circumstances. Finally *Fig. 8.14 (a)* features three blue traces which represents three separate specimens coated with the standard chromate containing silicon-enhanced slurry-deposited aluminide. This silicon-enhanced aluminide deposited upon CMSX-4 outperforms the standard aluminide system considerably, in this test, lasting almost twice as long and only undergoing substantial oxidation after a period of ca 600 – 800 hours compared to the ca 300 hours that a ‘normal’ aluminide lasted.

Fig. 8.14 (b) shows the results of similar AFCT testing, this time upon the alloy CMSX-10N. The three black traces within *Fig. 8.14 (b)* show the impact of oxidation upon the bare uncoated alloy and this is comparable to the rate of oxidative attack seen previously upon the alloy CMSX-4. The three red traces represent the same alloy, this time coated with the simple vapour phase aluminising. It can be observed that despite offering a marginal incubation period and protection from the oxidising environment for ca 100 hours after this protection is exhausted the alloy rapidly degrades and rates of oxidative attack match the uncoated samples. Finally the two blue traces show the impact of coating the alloy CMSX-10N with the silicon-enhanced slurry-deposited aluminide. The two blue traces clearly show an improvement in the incubation period and thereby the length of time that the protection lasts when compared to the bare uncoated alloy and the standard aluminising. It is interesting to note that the length of time and additional protection offered by the silicon-enhanced slurry-deposited aluminide is significantly reduced when compared to the exact same coating used upon the alloy CMSX-4 (see results above from *Fig. 8.14 (a)*) and a period of ca 100 hours is gained before full-rate oxidative attack once again occurs.

The traces in *Fig. 8.14 (c)* display the same silicon-enhanced slurry-deposited aluminide upon three different alloys, green is the alloy IN738, orange is CMSX-10N and purple is the substrate alloy CMSX-4. A clear difference is observed regarding the level of protection offered by the exact same coating system deposited upon different substrate alloys.

8.3.9. ThermoCALC

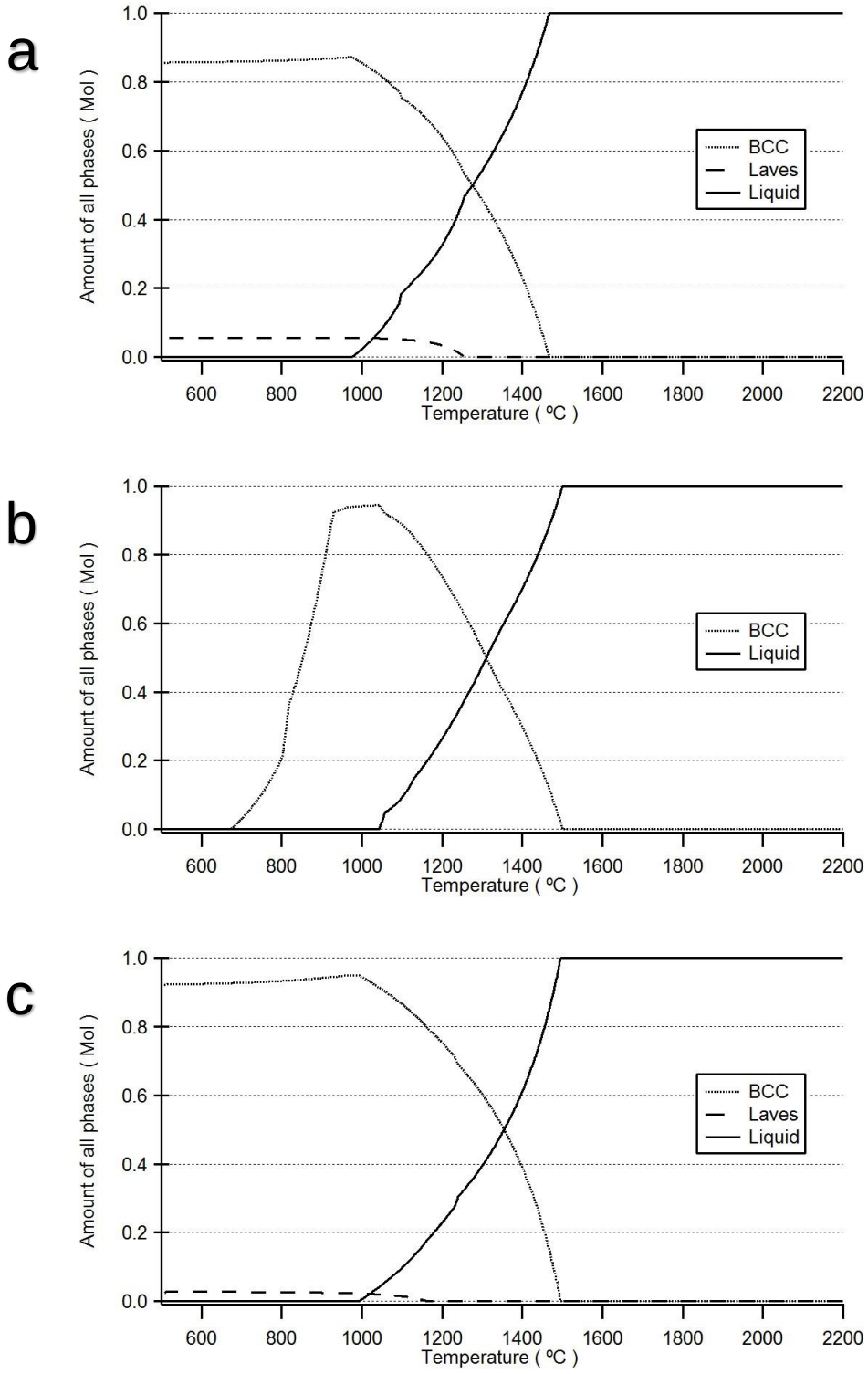

Fig. 8.15 – ThermoCALC results, elemental composition data from EDS results was input for the same silicon-enhanced slurry-deposited aluminide upon different substrate alloys to yield solvus and solidus predictions, the first is the alloy MarM002 from chapter 7 (a), then the alloy IN738 (b) and finally the alloy CMSX-10N (c), some additional phases have been omitted for simplicity

Using an average value for the coating upon the substrate alloys MarM002, IN738 and CMSX-10N taken from the EDS ladder-scans of sections 8.3.1.2 and 8.3.1.2 the composition was input to the thermodynamic software ThermoCALC for predictions of solidus and liquidus values at equilibrium. *Fig. 8.15 (a)* displays the amount of phase versus the temperature plot for the alloy MarM002 mainly discussed in chapter 7. The two traces of interest are the liquid phase and the body-centred cubic phase (BCC) which represents the β-NiAl phase which forms as result of the reaction between the liquid aluminium and the solid nickel-based superalloy. In this instance the coating upon the alloy MarM002 has a solidus of ca 990°C and a liquidus of ca 1450°C. *Fig. 8.15 (b)* shows the ThermoCALC results for the coating upon the substrate alloy IN738 which displays a solidus of ca 1025°C and a liquidus of ca 1500°C. Finally *Fig. 8.15 (c)* displays the ThermoCALC results of the coating upon the alloy CMSX-10N. This ThermoCALC prediction has a solidus of ca 990°C and a liquidus of ca 1500°C. All three instances shown in *Fig. 8.15* make the situation clear that if the slurry coating applied to the alloy in the green state is heat treated at ca 870°C then the aluminium will melt at ca 660°C and the exothermic formation reaction of Ni_2Al_3 in equilibrium with liquid phase aluminium bridges the gap between the 870°C and the minimum melting point of the nickel-aluminide at ca 1000°C and brings about the kind of coating microstructures and features that result from this coating system.

8.4. Discussion

The same silicon-enhanced slurry-deposited aluminide coating system (IP1041) was applied to samples of the alloy MarM002, IN738, CMSX-4 and CMSX-10N to better understand how alternative substrates affected final coating microstructure and therefore performance. The slurry coating, IP1041, applied upon CMSX-10N yielded an image supporting the proposed formation mechanism (*Fig. 8.2 (c)*) outlined previously regarding the cascading reaction front and the generation of exothermic energy through intermetallic phase formation. The premise of this formation mechanism, established in chapter 7, is that liquid aluminium wets the surface of the superalloy before starting an exothermic reaction that slowly consumes the nickel-based substrate converting it to a nickel aluminide with the aluminium supplied by the slurry. The alloy CMSX-10N in the un-heat treated state, prior to solutioning treatment, maintains a highly segregated as-cast microstructure including dendrites and interdendritic phase regions (IDP), the latter containing high levels of aluminium and tantalum. The IDP region extended to the external surface of the original specimen before the addition of the slurry aluminide layer in a similar fashion to the carbide described in chapter 7. The coating microstructure shows the fine cross-hatch structure of the IDP, clearly displaying an expansion effect associated with a rolling sequential dissolution and consumption of nickel downwards, ahead of the outward growth and expansion of the new β-NiAl phase. The volume occupied by the coating is half inward growing and half outward growing however the coating is proposed to be the result of nickel superalloy substrate dissolution followed by outward expansion of the newly formed phases. The IDP residual memory within the final microstructure shows that the coating does not melt as there is minimal mixing of the coating in the *x* and *y directions* which would disrupt any pre-existing structure within the coating. Therefore the high-temperature exothermic reaction must remain confined to the narrow rolling band of the reaction front, this enables the fine filigree IDP pattern to remain intact in spite of the high temperatures experienced. (*Fig. 8.2 (c)*) A schematic of the altering IDP region over the course of the coating formation is shown in *Fig. 8.16.*

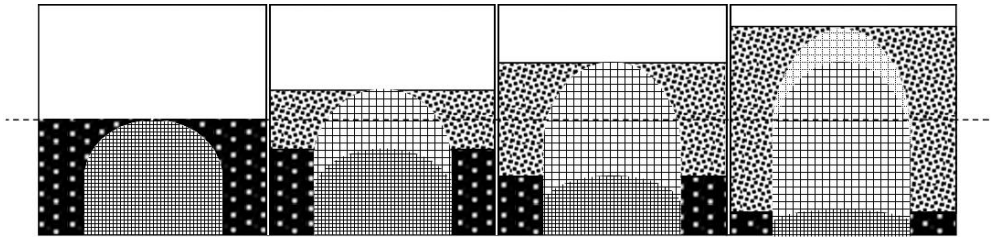

Fig. 8.16 – schematic detailing cascading reaction upon CMSX-10N, dark speckle pattern is dendritic phase, fine grid is interdendritic phase, random speckle pattern is the growing slurry aluminide coating and coarse grid pattern is the stretched interdendritic phase within the slurry coating

Fig. 8.3 displaying the interdiffusion zone at the interface between the slurry aluminide and the substrate CMSX-4 supports the cascading exothermic formation reaction hypothesis established in chapter 7. This SEM micrograph is also represented diagrammatically in the schematic *Fig. 8.17*. This micrograph shows the ca 5 μm interdiffusion zone which appears to actually represent the thickness of the reaction layer that has formed as a result of chemical interaction and intermetallic formation between the liquid phase aluminium delivered by the deposition process and the solid nickel-based superalloy substrate. At the bottom the micrograph in *Fig. 8.3* the γ/γ' microstructure of the CMSX-4 is observed, unaffected by the coating above, it appears normal and representative of this alloy upon entering service. The interdiffusion zone is unusually narrow when compared to other more widely understood aluminide deposition systems and faint residual gamma/gamma prime can be seen within the band itself. This band displays the reaction front frozen upon the reaction ceasing and provides further understanding of how the reaction has progressed to this point. At the top of the interdiffusion zone there is a large section that appears broken away from the solid substrate and a dark fissure is observed. The dark portion at the top of the image (*Fig. 8.3*) represents the nickel-aluminide formed and this is the matrix of the dual-phase coating microstructure. The fissure is dark in appearance because as the intermetallic layer is forming at the interface there is the evolution of thermal energy, this enables portions of the forming intermetallic to become disconnected from the underlying substrate and 'float' away from the surface and continue the nickel dissolution process within the mushy aluminide above. This 'iceberg' like behaviour helps to understand the process of the continuing cascade reaction. Since the reaction between the liquid aluminium and the solid nickel substrate would cease upon initial formation of the intermetallic phase, which from this point would act as an impermeable barrier layer, the only way for the reaction to continue is for fragments of the forming intermetallic layer to disconnect from the surface and move away from the solid surface enabling fresh liquid aluminium to wet the surface of the nickel and so begin again the process of intermetallic formation and nickel dissolution. This cascading process continues indefinitely whilst there is additional liquid aluminium to feed the reaction front, upon depletion of the aluminium reservoir the reaction ceases.

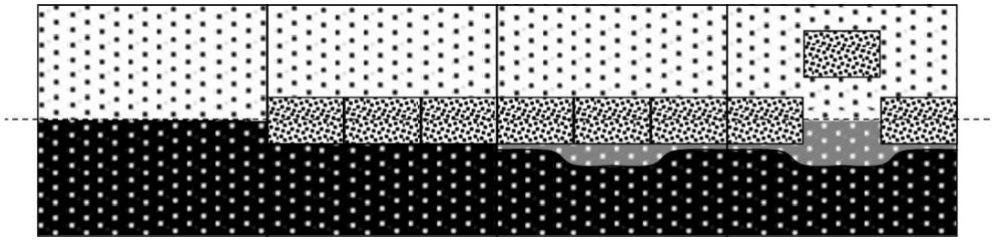

Fig. 8.17 – schematic detailing cascading reaction upon CMSX-4, dark speckle pattern is superalloy, light speckle pattern is the growing slurry aluminide and random speckle pattern is the reaction front

The coating upon IN738 and CMSX-10N was subject to the same FIB lift-out procedure detailed in chapter 7. This process fabricated thin lamella foils for use in both TEM instruments and for use generating TKD maps in the appropriate SEM. *Fig. 8.6* displays the TEM results in both HAADF and BF mode for the coating upon these two alloys. *Fig. 8.6* LHS shows the coating microstructure for the alloy CMSX-10N which features a very clear gradient in the chrome-silicide (Cr-Si) dispersed precipitate phase which appears as bright white precipitates under HAADF conditions. The Cr-Si dispersed phase displays the same size gradient from coarse to fine going from coating top to bottom in the z direction as that previously discovered and discussed upon the alloy MarM002 in chapter 7. This definitive size gradient provides substantial proof regarding the step-wise coating formation mechanism that is concurrent with the cascading reaction believed to occur at the interface. As the coating is formed as a result of nickel dissolution, semi-solid 'mushy' nickel-aluminide emerges from the chemical reaction and fresh liquid aluminium moves down to wet the newly exposed solid nickel-based superalloy in order to continue the intermetallic formation reaction. As this 'mushy' nickel aluminide is formed it is moved outwards from the original point of formation at the interface by the formation of new material beneath it afterwards. As this material is carried up and away from the interface the Cr-Si phase begins to form and the size and shape of these precipitates is dictated by the length of time they are given to grow. For instance, the clear size gradient witnessed in *Fig. 8.6* with regards to the alloy CMSX-10N shows that the material at the outer external portion of the coating has had the longest period of time in which to form the dispersed phase precipitates which results in large, well developed silicon-rich phases which appear to conform to the grain boundaries of the matrix phase, the nickel-aluminide. Moving down the set of images towards the base of the coating the precipitates become smaller rapidly. The precipitates positioned in the middle of the coating have had less time in which to form and develop resulting in smaller more globular shapes. Finally upon moving to the bottom of the TEM images of *Fig. 8.6* show a clear denuded region which features no visible evidence of the formation of the chrome-silicide phase. This region is immediately above the interdiffusion zone which is proposed to be the reaction front frozen as a result of reaction termination. This denuded zone has not experienced the period of time necessary to enable the formation of this dispersed phase being so close the cascading reaction front. The RHS of *Fig. 8.6* details the TEM micrographs of the coating upon the alloy IN738. This alloy is high in chromium and cobalt being an earlier generation nickel alloy and the coating has formed a chaotic microstructure. The coating upon IN738 still consists of a dual-phase structure with the TEM-based EDS of *Fig. 8.7* confirming the matrix as a nickel-aluminide and the dispersed phase as being rich in chromium and silicon. The key features of the coating microstructure are the larger dispersed precipitate phase at the outermost region and a denuded region immediately

above the interdiffusion zone at the bottom. The middle portion of the coating is difficult to discern. There is a presence of medium-sized globular dispersed precipitates but the clear size gradient familiar in the MarM002 and CMSX-10N coatings has been replaced by a disordered structure. This lack of order is likely due to the excess chromium available within the underlying substrate which is forming the Cr-Si phase within the forming coating matrix. In the case of MarM002 and CMSX-10N the alloy chromium levels are lower meaning that the excess of silicon can form a fixed volume fraction determined by the chromium content of chrome-silicides. In this instance the additional silicon is incorporated within the nickel-aluminide matrix since it is soluble within this phase. In the case of IN738 the high chromium levels mean that the population of chrome-silicides can grow to much greater proportions and form the chaotic overstocked microstructure observed in *Fig. 8.6*.

TEM-based EDS work summarised in *Fig. 8.9 and 8.10* confirms the assertion that the matrix of the coating upon both IN738 and CMSX-10N consists of predominately nickel and aluminium with atomic percentages of ca 32 and 55 % respectively. In addition there are low levels of silicon ca 5 % as well as cobalt ca 5 % along with some contamination from the copper grid used in the TEM-foil fabricating process. The dispersed precipitate phase within the coating upon alloy IN738 was found to consist of ca 40 at. % silicon, ca 19 % titanium and ca 28 at % chromium. This supports the premise that the dispersed phase is predominately a chrome-silicide with some substitution from alternative elements within the underlying substrate alloy, in this instance titanium. Finally the dispersed phase found within the coating upon the alloy CMSX-10N contains ca 15 at. % aluminium, ca 43 at. % silicon, ca 9 at. % chromium, ca 5 at. % tungsten and ca 9 at. % tantalum. This confirms that the dispersed phase in the coating upon the alloy CMSX-10N is predominately silicon with chromium, though since the underlying alloy only contains low levels of chromium, there is substantial substitution for elements including tungsten and tantalum, The heavy presence of these elements explains the clear and vivid contrast different between the dispersed precipitate phase and the matrix phase in this coating system under HAADF conditions in the TEM. *Fig. 8.11* displays the TEM diffraction patterns gathered from a single grain of the coating upon the alloy CMSX-10N close to the base of the coating. The DP matched the nickel-aluminide β-NiAl which is the predominant phase in alternative aluminising processes.

To determine the mechanism of coating growth from the perspective of the β-NiAl phase the FIB liftout were used in the TKD method or transmission kikuchi diffraction (*Fig. 8.12 and 8.13*). In both coatings upon IN738 and CMSX-10N there is a size difference within the polycrystalline aluminide structure dependent upon the relative location within the coating system. Closest to the top of the coating the largest beta grains appear followed by a large array of small grains throughout the middle third of the coating. Finally at the bottom of the coating nearest the substrate there are medium sized grains. In addition to the size variation

of the grains, the coating upon MarM002 (chapter 7) and that upon CMSX-10N (*Fig. 8.13*) show what appears to be some correlation between individual grains in the centre of the coating when regarding the inverse pole figures. The figure regarding the x orientation especially in *Fig. 8.13* appears to show a red and blue preference for grains in the middle third of the coating. This could indicate that these grains have influenced one another during the solidification of the coating from the 'mushy' state and that these channels could represent the pathways that liquid aluminium had utilised during the coating growth phase to move material from the top of the coating to feed the chemical reaction occurring at the interface between the coating and the substrate.

Finally to better understand the temperatures attained during slurry aluminising the approximate elemental composition for the coatings was attained from EDS (*Fig. 8.9 and 8.10*), and was input to the thermodynamic software ThermoCALC. *Fig. 8.15* shows the predictions of the equilibrium phase fraction as a function of temperature. MarM002 displays a profile with a melting-freezing window that starts at ca 990 °C and ends with complete melting at ca 1450 °C. The alloy IN738 displays a solidus of ca 1025°C and a liquidus of ca 1500°C. *Fig. 8.15 (c)* displays the ThermoCALC results of the coating upon the alloy CMSX-10N. This ThermoCALC prediction has a solidus of ca 990°C and a liquidus of ca 1500°C. From this we can conclude that the exothermic reaction clearly raises local temperatures above 1000 °C, since the microstructure shows evidence of a 'mushy' state in the history of the coatings formation. This is strong evidence in support of an exothermic reaction since vacuum furnace temperatures do not exceed 870°C, which in themselves would be inadequate to cause melting of the β-NiAl phase.

8.4.1. Substrate chromium variation

Using different nickel-based superalloy substrates with the same slurry coating system enabled exploration of the impact of underlying material on the formation of the coating. Slurry aluminide coatings, more than standard vapour phase aluminides, rely upon substrate compatibility in order to form an effective protection system. This particular research was undertaken to understand the role of hexavalent chromium within the slurry system and whether the initial assumptions regarding the dispersed precipitate phase containing chrome-silicides were justified and to determine the source of the coating chromium.

The choice of different nickel-based superalloys for this project was determined by differing levels of chromium. The lowest chromium level was to be found within the alloy CMSX-10N, a third-generation superalloy with ca 2 wt. % chromium. The medium and highest chromium containing alloys were MarM002 and IN738 with ca 9 wt. % and ca 16 wt. % respectively. All of the alloys were coated with nominally the same slurry-aluminide system and heat treated within a vacuum furnace to instigate the exothermic reaction detailed in chapter 7. Once formed these coating systems were examined using EDS ladder-scans to determine the distribution of elements throughout the coating span from outermost to innermost and across the interdiffusion zone into the underlying superalloy bulk. *Fig. 7.7 (r) and (s)* show the results of the ladder scan across the coating upon MarM002, the chromium level within the coating is ca 5 at. %. The EDS trace for chromium across the interdiffusion zone confirms that the pre-existing chromium level within the underlying substrate was ca 10 at. % meaning that the formation the coating between the liquid aluminium and the solid superalloy has redistributed the original concentration of chromium throughout the newly formed, less dense intermetallic nickel-aluminide. This interpretation is further supported by the atomic % of nickel within the coating upon MarM002 going from a normal of 60 at. % within the superalloy which drops to an average of ca 30 at. % within the coating. The source of nickel for the nickel-aluminide coating is the nickel-superalloy and the additional elements like chromium and cobalt are present in proportions reduced in the same manner supporting the alloy as the source. *Fig. 8.4* and *8.5* display similar ladder-scans this time from the coating upon the alloys IN738 and CMSX-10N respectively. Identical phenomena regarding the underlying concentration of chromium and other minor elemental additions within the substrate alloy and the final coating microstructure have been observed. In the ladder-scan for IN738 the chromium concentration changes from ca 18 at. % in the substrate to ca 9 at. % in the coating. Similarly CMSX-10N features ca 2 at. % of the elements tantalum, tungsten and rhenium within the alloy all of which drop to ca 1 at. % upon incorporation within the final coating microstructure. The correlation between the concentration of elements like nickel and chromium within the substrate and the final coating

aid understanding of coating mechanisms. This correlation between the chromium content of the alloy and the final coating microstructure means that in order to create effective corrosion and oxidation resistant coatings it is imperative that the underlying alloy contain minimum threshold levels of vital elements like chromium and that low level additions to the slurry prior to deposition do not provide a source of chromium for the finished coating as previously speculated.

8.4.2. Oxidation testing

A series of oxidation tests were undertaken at Cranfield University to assess the relative effectiveness of the protective capability of silicon-enhanced slurry aluminides. This set of results shows clearly that in the case of the alloy CMSX-4 the application of such a silicon-enhanced slurry aluminide can provide substantial benefits in the face of an aggressive oxidative test which could provide significant life benefits to such a component/coating combination in a real-world gas turbine engine. The matrix of the silicon-enhanced aluminide IP1041 is similar to the standard vapour phase aluminide, β-NiAl. This finding would strongly suggest that the presence of the chrome-silicide phase within the slurry aluminide coating provides the additional protection enabling the deployment of both chromium and silicon at the surface. Both of these elements have proven ability to form either additional oxides as well as mixed oxides at the surface or to provide a synergistic effect which boosts the rapid formation of strong adherent aluminium oxide at the external surface.

Fig. 8.14 (b) shows the results of similar oxidation testing upon the alloy CMSX-10N with three black traces representing the bare uncoated alloy, the two red traces are the standard aluminising upon the surface and then the two blue traces for the silicon-enhanced slurry aluminide. What is immediately apparent in this graph is that no matter which coating system applied to this alloy, the results are mediocre in terms of the longevity of the oxidative protection. The uncoated alloy lasts ca 150 hours but is immediately beginning to oxidise from the beginning of the test since the base alloy has a chromium level of only 2.2 wt. % and aluminium is 5.8 wt. %. These elements are vital for oxidative and corrosion resistance but are low in 3rd generation nickel-based superalloy to accommodate additional solid solutioning elements like rhenium into the alloy for enhanced creep resistance. Environmental protection was moved from a blade alloy attribute to one to be achieved through coatings and surface treatment. The standard vapour phase aluminising provides a small boost to oxidation resistance and the addition of the silicon-enhanced slurry aluminide is again marginally better. Of most interest in this graph is that the alloy CMSX-10N appears to suffer from poor oxidation resistance in the face of aggressive testing no matter the surface treatment. This suggests that the chrome-silicides within the silicon-enhanced slurry coating does require moderate levels of chromium to exist within the underlying substrate in

order to bolster the coating forming upon the surface. Therefore when applied to a low chromium containing alloy like CMSX-10N there is limited protection that can be offered to the material.

Fig. 8.14 (c) shows the results of oxidation testing for the same silicon-enhanced slurry aluminide system (IP1041) applied to three different alloys. In green are two traces for the coating upon the alloy IN738, in orange the two traces represent the coated alloy CMSX-10N and the three purple traces are the coating upon the alloy CMSX-4. This graph serves to show that the underlying alloy is essential when it comes to the use of slurry aluminide in that two alloys, one high in chromium and one low in chromium perform moderately and the alloy with a level of both chromium and aluminium can form an especially effective barrier against oxidation.

8.5. Conclusion

This work has used advanced material characterisation techniques to thoroughly examine the case of slurry aluminides forming upon the nickel-based superalloys CMSX-10N and IN738. Techniques include SEM, TEM, XRD, EBSD and TKD. The following conclusions are drawn regarding the coating microstructure formed as a result of this coating method:

1. The premise of the cascading formation mechanism is that liquid aluminium wets the surface of the superalloy before starting an exothermic reaction that slowly consumes the nickel-based substrate converting it to a nickel aluminide with the aluminium supplied by the slurry.
2. An IDP region extended to the external surface of the CMSX-10N specimen before the addition of the slurry aluminide layer. The coating microstructure shows the fine cross-hatch structure of the IDP, clearly displaying an expansion effect associated with a rolling sequential dissolution and consumption of nickel downwards, ahead of the outward growth and expansion of the new β-NiAl phase. The volume occupied by the coating is half inward growing and half outward growing however the coating is proposed to be the result of nickel superalloy substrate dissolution followed by outward expansion of the newly formed phases.
3. The IDP residual memory within the final coating microstructure on CMSX-10N shows that the coating does not melt as there is minimal mixing of the coating in the *x* and *y directions* which would disrupt any pre-existing structure within the coating. Therefore the high-temperature exothermic reaction must remain confined to the narrow rolling band of the reaction front, this enables the fine filigree IDP pattern to remain intact in spite of the high temperatures experienced.
4. The interdiffusion zone at the interface between the slurry aluminide and the substrate CMSX-4 supports the cascading exothermic formation reaction hypothesis. Micrographs show the ca 5 μm interdiffusion zone which represents the thickness of the reaction layer that has formed as a result of chemical interaction and intermetallic formation between the liquid phase aluminium delivered by the deposition process and the solid nickel-based superalloy.
5. The interdiffusion zone band displays the reaction front frozen upon the reaction ceasing and provides further understanding of how the reaction has progressed to this point. At the top of the interdiffusion zone there is a section that appears to have broken away from the solid substrate and a dark fissure is observed. The dark portion at the top of the image represents the nickel-aluminide formed and this is the matrix of the dual-phase coating microstructure. The fissure is dark in appearance because as the intermetallic

layer is forming at the interface there is the evolution of thermal energy, this enables portions of the forming intermetallic to become disconnected from the underlying substrate and ‘float’ away from the surface and continue the nickel dissolution process within the mushy aluminide above. This ‘iceberg’ like behaviour helps to understand the process of the continuing cascade reaction.

6. Both HAADF and BF mode TEM images for the coating for the alloy CMSX-10N features a clear gradient in the chrome-silicide (Cr-Si) dispersed precipitate phase which appears as bright white precipitates under HAADF conditions. The Cr-Si dispersed phase displays the same size gradient from coarse to fine going from coating top to bottom in the z direction as that previously discovered and discussed upon the alloy MarM002. This definitive size gradient provides substantial proof regarding the step-wise coating formation mechanism that is concurrent with the cascading reaction believed to occur at the interface.
7. The clear size gradient in the coating upon the alloy CMSX-10N shows that the material at the outer external portion of the coating has had the longest period of time in which to form the dispersed phase precipitates which results in large, well developed silicon phases.
8. In both coatings upon IN738 and CMSX-10N there is a size difference within the polycrystalline aluminide structure dependent upon the relative location within the coating. Closest to the top of the coating the largest beta grains appear followed by a large array of small grains throughout the middle of the coating. Finally at the bottom of the coating there are medium sized grains. The coating upon MarM002 and that upon CMSX-10N show a correlation between individual grains in the centre of the coating when regarding the inverse pole figures. This could indicate that these grains have influenced one another during the solidification of the coating from the ‘mushy’ state and that these channels could represent the pathways that liquid aluminium had utilised during the coating growth phase to feed the chemical reaction occurring at the interface.
9. The chrome-silicides within the silicon-enhanced slurry coating require moderate levels of chromium to exist within the underlying substrate in order to bolster the coating forming upon the surface.
10. The results of oxidation testing for the same silicon-enhanced slurry aluminide system applied to three different alloys are shown. Data serves to show that the underlying alloy is essential when it comes to the use of slurry aluminide in that two alloys, one high in chromium and one low in chromium perform moderately and the alloy with a level of both chromium and aluminium can form an especially effective barrier against oxidation.

9. Overall conclusions

Single crystal turbine blades are investment cast, followed by a complex series of operations including heat treatment, machining, blasting, etching and polishing to produce a product ready for coating. Coating systems examined in this thesis provide environmental protection for turbine components. This thesis sought to examine the root causes of various defects and processing features that render components unsuitable for service. The impact of increasing our understanding of these expensive materials is to increase process yield, and thus lower unit costs

Internal surface melting found on intermediate pressure turbine blades following high-temperature heat-treatment; consisted of a layer enriched in aluminium and tantalum on the surface of the internal cooling passage. This thesis details the systematic investigation of the silica-based ceramic cores used to form the cooling passage to better understand core / casting interactions. The silica-based core displayed assisted sintering at those geometric locations where the nickel-based superalloy exerted a crushing force on the surface due to differential contraction after solidification. The areas affected matched those that later displayed surface melting. This phenomena is clearly related to casting height since the severity of pressure assisted sintering could be mapped and decreased with the height of the casting. Further findings in this thesis include the formation of a thin alumina layer at the interface between the superalloy and the silica-based core, this layer prevents volatilisation or sublimation from the surface of the component during the heat treatment. In the bespoke castings undertaken to further explore this phenomena clear evidence emerged of zircon particles, an integral constituent of the core, pinning the superalloy during the casting process. The result was a rough undulating surface with depressions formed by the hard, immovable zircon particles and peaks where the small silica grains where able to sinter and retreat against the pressure of the superalloy. A theory has been proposed that these zircon particles effectively indent the casting in specific locations at high temperatures. At the top of the casting where more effective stress and strain are experienced, this can translate into local stresses reaching the threshold for inducing recrystallisation during subsequent heat treatment.

High pressure turbine blades coated during the aluminising process have masking applied to those areas that need to be left bare. These masking materials are not inert at the deposition temperatures, leading to the inadvertent carburisation of a sub-surface layer of the blade alloy. Elemental carbon forms as the polymer-based binder thermally degrades during the ramp to aluminising deposition temperatures of ca 1030°C. This highly mobile elemental carbon moves interstitially through the superalloy where its concentration is at its maximum just beneath the surface. The temperature is high enough to enable the

precipitation of carbides before the carbon source is depleted, then very small carbides form in the γ channels. These carbides are detrimental in that they tie up the elements molybdenum, tantalum and tungsten. Very numerous small ‘proto-carbides’ form immediately beneath the surface and inhibit further growth of the larger carbides by depleting the finite carbon source. ‘River-lines’ of elemental segregation can lead to the preferential formation of carbides in strings that wind through the material and alternative morphologies include carbide platelets that sit upon the (111) planes. The final carbide morphology seen was larger and consisted of a two-layer structure, the inner core most likely comprises a titanium-based carbo-nitride whilst the outer layer forms later upon the surface of the core and is composed of molybdenum, tantalum and tungsten. As the carbide forms it denudes the surrounding γ/γ’ of important strengthening elements. Work has been undertaken to better understand the processing parameters which generate these undesired precipitates in an attempt to mitigate their effects.

Slurry aluminide coatings are a cost-effective protective coating widely used in gas turbine engines. In this work, a water-based industry-standard slurry, was air sprayed on three nickel-based superalloys designed for blade applications. The alloys were in an as-cast or solution heat-treated condition, before a diffusion heat treatment was used to form the coating microstructure ready for service operation. Altering the underlying substrate resulted in the formation of markedly different microstructures within the final coating and has implications for in-service corrosion resistance. It was found that the concentration of key elements, such as chromium, tungsten and cobalt are evenly distributed throughout the newly-formed coating, this is a departure from the more traditional inward or outward growing aluminides formed by pack or vapour methods. The formation of the slurry aluminide is accompanied by a volume expansion as the nickel used to form the NiAl intermetallic is extracted from the FCC nickel-based superalloy. The slurry deposited consists predominantly of aluminium and silicon. A clear gradient in grain size for the dispersed silicide phase strongly supports a cascading reaction mechanism that slowly consumes the substrate through the wetting of the surface by liquid aluminium before a rapid surge of exothermic energy causes the newly formed coating to break away from the surface and move up in to the mushy coating above.

Further work

This work has explored three different topics that affect the economic production and manufacture of turbine blades. With regards to the internal melting phenomena on intermediate pressure turbine blades the impact of how the oxide forms as a chemical interaction between the superalloy and the silica-based ceramic is of utmost importance. To better understand which oxides are formed, whether this is impacted by casting height or stresses exerted during casting would benefit the casting community. This oxide layer which forms ideally needs to withstand the chemical leaching process which removes the core and thereby protect the internal surface of the blade from evaporation or volatilisation of elementals from the surface which could contribute to the kind of features seen in this work. If an additional separate layer of ceramic could be deposited upon the surface of the core then a potential barrier to excessive sintering of the core could be prevented though this could have detrimental impacts on the plastic deformation imparted into the superalloy. This kind of balancing of the core requirements must be further explored and developed to best improve the castability of these blades.

The masking of turbine blades for coating processing will undoubtedly be a necessity for the future and furthering the ability of creating inert temporary barriers will be a must. The idea of creating parting layers that reduce the flow of elemental carbon into the sub-surface of the nickel superalloy substrate is an idea that will be explored to ensure that maskants of the future will no longer provide the concentrations of carbon that until now have provided the required amount of carbon for carbide precipitation. Of additional interest would be to better understand how detrimental the impact of these small carbides is and whether they have a significant impact on the mechanical properties of the material within which they exist.

Finally the role of slurry aluminides is important within the marine and industrial gas turbines of the future. Understanding the microstructures formed and the role of the different elements like silicon will aid the paint and slurry formulations of the next generation of coatings. Having the ability to locally aluminise in a cheap manner, without using potentially harmful ingredients, could have great promise for coating all manner of components in gas turbine engines. The ability to co-deposit elements like silicon simultaneously enables the formation of potentially very useful and resilient protective coatings.

Bibliography

1. Rolls-Royce Plc. *The Jet Engine*. (1986).

2. Cumpsty, N. *Jet Propulsion: A Simple Guide To The Aerodynamic and Thermodynamic Design And Performance Of Jet Engines*. (Cambridge University Press, 2003).

3. Spittle, P. Gas turbine technology. *Phys. Educ.* **38,** 504–511 (2003).

4. Wickerson, J. & Whittaker, M. Holistic Gas Turbines Course. *Holist. Gas Turbines Course* (2013).

5. Schafrik, R. & Sprague, R. Saga of Gas Turbine Materials: Part III. *Adv. Mater. Process.* **162,** 27–30 (2004).

6. Williams, J. C. & Starke, E. A. Progress in structural materials for aerospace systems. *Acta Mater.* **51,** 5775–5799 (2003).

7. Reed, R. C. *The Superalloys: Fundamentals and Applications*. (Cambridge University Press, 2006).

8. Betteridge, W. & Shaw, S. W. K. Development of superalloys. *Mater. Sci. Technol.* **3,** 682–694 (1987).

9. Sims, C. T. A History of Superalloy Metallurgy for Superalloy Metallurgists. *Superalloys 1984, TMS* 399–419 (1984).

10. Harris, K. *et al.* Development of Two Rhenium-Containing Superalloys for Single-Crystal Blade and Directionally Solidified Vane Applications in Advanced Turbine Engines. *J. Mater. Eng. Perform.* **2,** 481–487 (1993).

11. Tin, S., Pollock, T. M. & King, W. T. Carbon Additions and Grain Defect Formation in High Refractory Nickel-Base Single Crystal Superalloys. *Superalloys 2000* 201–210 (2000).

12. Versnyder, F. I. & Shank, M. E. The development of columnar grain and single crystal high temperature materials through directional solidification. *Mater. Sci. Eng.* **6,** 213–247 (1970).

13. Ricks, R. A., Porter, A. J. & Ecob, R. C. The growth of gamma prime precipitates in nickel-base superalloys. *Acta Metall.* **31,** 43–53 (1983).

14. Murakumo, T., Koizumi, Y., Kobayashi, K. & Harada, H. Creep Strength of Ni-Base

Single-Crystal Superalloys on the γ/γ' Tie-Line. *Superalloys 2004 (Tenth Int. Symp.* 155–162 (2004).

15. Caron, P. High gamma' Solvus New Generation Nickel-Based Superalloys for Single Crystal Turbine Blade Applications. *Superalloys 2000 (Ninth Int. Symp.* **5,** 737–746 (2000).

16. Cetel, A. D. & Duhl, D. N. Second-Generation Nickel-Base Single Crystal Superalloy. *Superalloys 1988 (Sixth Int. Symp.* 235–244 (1988).

17. Okazaki, M. High-temperature strength of Ni-base superalloy coatings. *Sci. Technol. Adv. Mater.* **2,** 357–366 (2001).

18. Hobbs, R. A., Tin, S., Rae, C. M. F., Broomfield, R. W. & Humphreys, C. J. Solidification characteristics of advanced nickel-base single crystal superalloys. *Superalloys 2004, TMS* 819–825 (2004).

19. Ford, D. A. & Arthey, R. P. Development of single crystal alloys for specific engine applications. *Superalloys 1984 (Fifth Int. Symp.* 115–124 (1984).

20. Goulette, M. J., Spilling, P. D. & Arthey, R. P. Cost Effective Single Crystals. *Trans. Met. Soc. AIME* **117,** 167–176 (1984).

21. Konter, M., Kats, E. & Hofmann, N. A Novel Casting Process for Single Crystal Gas Turbine Components. *Superalloys 2000 (Ninth Int. Symp.* 189–200 (2000).

22. Piearcey, B. & Kear, B. H. Correlation of structure with properties in a directionally solidified nickel-base superalloy. *Trans. AIME* **239,** 1209 (1967).

23. Piearcey, B. & Terkelsen, B. The effect of unidirectional solidification on the properties of cast nickel-base superalloys. *Trans. AIME* **239,** 1143 (1967).

24. Preston, J. & Foster, E. _. *Trans. Intern. Vacuum. Met. Conf,. Am. Vac. Soc.* (1967).

25. Pollock, T. M. & Tin, S. Nickel-Based Superalloys for Advanced Turbine Engines: Chemistry, Microstructure and Properties. *J. Propuls. Power* **22,** 361–374 (2006).

26. Wagner, C. _. *J. Phys. Chem.* **B21,** 25–41 (1933).

27. Birks, N., Meier, G. H. & Pettit, F. S. *Introduction to the High Temperature Oxidation of Metals*. *Engineering* (Cambridge University Press, 2006).

28. Prescott, R. & Graham, M. J. The formation of aluminum oxide scales on high-temperature alloys. *Oxid. Met.* **38,** 233–254 (1992).

29. Stott, F. H., Wood, G. C. & Stringer, J. The influence of alloying elements on the development and maintenance of protective scales. *Oxid. Met.* **44,** 113–145 (1995).

30. Brumm, M. W. & Grabke, H. J. The oxidation behaviour of NiAl-I. Phase transformations in the alumina scale during oxidation of NiAl and NiAl-Cr alloys. *Corros. Sci.* **33,** 1677–1690 (1992).

31. Grabke, H. J. Oxidation of NiAl and FeAl. *Intermetallics* **7,** 1153–1158 (1999).

32. Akhtar, A., Hook, M. S. & Reed, R. C. On the oxidation of the third-generation single-crystal superalloy CMSX-10. *Metall. Mater. Trans. A* **36,** 3001–3017 (2005).

33. Giggins, C. S. & Pettit, F. S. Oxidation of Ni-Cr-Al Alloys Between 1000° and 1200°C. *J. Electrochem. Soc.* **118,** 1782 (1971).

34. Pettit, F. S. Oxidation Mechanisms for Nickel-Aluminum Alloys at Temperatures Between 900° and 1300°C. *Trans. Metall. Soc. AIME* **239,** 1296–1305 (1967).

35. Kear, B. H., Pettit, F. S., Fornwalt, D. E. & Lemaire, L. P. On the transient oxidation of a Ni-15Cr-6Al alloy. *Oxid. Met.* **3,** 557–569 (1971).

36. Sato, A., Moverare, J. J., Hasselqvist, M. & Reed, R. C. On the Oxidation Resistance of Nickel-Based Superalloys. *Adv. Mater. Res.* **278,** 174–179 (2011).

37. Sato, A., Chiu, Y. L. & Reed, R. C. Oxidation of nickel-based single-crystal superalloys for industrial gas turbine applications. *Acta Mater.* **59,** 225–240 (2011).

38. Nicholls, J. R. Advances in Coating Design for High-Performance Gas Turbines. *MRS Bull.* **28,** 659–670 (2003).

39. Goward, G. W. Progress in coatings for gas turbine airfoils. *Surf. Coatings Technol.* **108–109,** 73–79 (1998).

40. Pint, B. A. The role of chemical composition on the oxidation performance of aluminide coatings. *Surf. Coatings Technol.* **188–189,** 71–78 (2004).

41. WING, R. G. & McGILL, I. R. The Protection of Gas Turbine Blades. *Aircr. Eng. Aerosp. Technol.* **53,** 15–21 (1981).

42. Rickerby, D. S. & Winstone, M. R. Coatings for Gas Turbines. *Mater. Manuf. Process.* **7,** 495–526 (1992).

43. Bose, S. *High temperature coatings and oxidation*. (Butterworth-Heinemann, 2011).

44. Smith, A. B., Kempster, A. & Smith, J. Vapour aluminide coating of internal cooling

channels, in turbine blades and vanes. *Surf. Coatings Technol.* **120–121,** 112–117 (1999).

45. Mévrel, R., Duret, C. & Pichoir, R. Pack cementation processes. *Mater. Sci. Technol.* **2,** 201–206 (1986).

46. Wöllmer, S., Zaefferer, S., Göken, M., Mack, T. & Glatzel, U. Characterization of phases of aluminized nickel base superalloys. *Surf. Coatings Technol.* **167,** 83–96 (2003).

47. Hwang, S. L. & Shen, P. Microstructures and crystallographic relationships in aluminized coatings on IN713LC and MAR-M247. *Mater. Sci. Eng.* **94,** 243–250 (1987).

48. Gale, W. F. & King, J. E. A Microstructural Study of Aluminide Surface Coatings on Single Crystal Nickel-Base Superalloy Substrates. *Surf. Modif. Technol. V* **8,** 401 (1992).

49. Tin, S. & Pollock, T. M. Phase instabilities and carbon additions in single-crystal nickel-base superalloys. *Mater. Sci. Eng. A* **348,** 111–121 (2003).

50. Streiff, R. & Boone, D. H. Corrosion resistant modified aluminide coatings. *J. Mater. Eng. Perform.* **22,** 2801–2812 (2013).

51. Tawancy, H. M., Abbas, N. M. & Rhys-Jones, T. N. Role of platinum in aluminide coatings. *Surf. Coatings Technol.* **49,** 1–7 (1991).

52. Tawancy, H. M., Sridhar, N., Tawabini, B. S., Abbas, N. M. & Rhys-Jones, T. N. Thermal stability of a platinum aluminide coating on nickel-based superalloys. *J. Mater. Sci.* **27,** 6463–6474 (1992).

53. Rickerby, D. S. & Wing, R. G. Thermal barrier coating for a superalloy article and a method of application thereof. (1997).

54. Boone, D. H. Physical vapour deposition processes. *Mater. Sci. Technol.* **2,** 220–224 (1986).

55. Padture, N. P. Thermal Barrier Coatings for Gas-Turbine Engine Applications. *Science (80-.).* **296,** 280–284 (2002).

56. Wills, V. A. & McCartney, D. G. A comparative study of solidification features in nickel-base superalloys: microstructural evolution and microsegregation. *Mater. Sci. Eng. A* **145,** 223–232 (1991).

57. D'Souza, N. & Dong, H. B. Solidification path in third-generation Ni-based superalloys, with an emphasis on last stage solidification. *Scr. Mater.* **56,** 41–44 (2007).

58. Pang, H. T. *et al.* Microstructure and solidification sequence of the interdendritic region in a third generation single-crystal nickel-base superalloy. *Metall. Mater. Trans. A Phys. Metall. Mater. Sci.* **40,** 1660–1669 (2009).

59. Rosell-Laclau, E., Durand-Charre, M. & Audier, M. Liquid-solid equilibria in the aluminium-rich corner of the Al-Cr-Ni system. *J. Alloys Compd.* **233,** 246–263 (1996).

60. Caldwell, E. C., Fela, F. J., Fuchs, G. E. & Rene, N. Segregation of Elements in High Refractory Content Single Crystal Nickel Based Superalloys. *Superalloys 2004* 811–818 (2004).

61. Whitesell, H. S. & Overfelt, R. A. Influence of solidification variables on the microstructure, macrosegregation, and porosity of directionally solidified Mar-M247. *Mater. Sci. Eng. A* **318,** 264–276 (2001).

62. Hobbs, R. A., Zhang, L., Rae, C. M. F. & Tin, S. TCP suppression in a ruthenium bearing single-crystal nickel-based superalloy. *JOM* **60,** 37–42 (2008).

63. Rae, C. M. F. & Reed, R. C. The precipitation of topologically close-packed phases in rhenium-containing superalloys. *Acta Mater.* **49,** 4113–4125 (2001).

64. Carter, P., Cox, D. ., Gandin, C. . & Reed, R. . Process modelling of grain selection during the solidification of single crystal superalloy castings. *Mater. Sci. Eng. A* **280,** 233–246 (2000).

65. Brewster, G., Dong, H. B. B., Green, N. R. R. & D'Souza, N. Surface Segregation during Directional Solidification of Ni-Base Superalloys. *Metall. Mater. Trans. B* **39,** 87–93 (2008).

66. Brewster, G. J. J. Solidification and heat-treatment related defects in single crystal nickel-base superalloys - EngD Thesis. (University of Cambridge, 2009).

67. Pang, H. T., Zhang, L., Hobbs, R. A., Stone, H. J. & Rae, C. M. F. Solution Heat Treatment Optimization of Fourth-Generation Single-Crystal Nickel-Base Superalloys. *Metall. Mater. Trans. A* **43,** 3264–3282 (2012).

68. Beddoes, J. Design of solution heat treatments for aerospace alloys. *Can. Metall. Q.* **50,** 215–221 (2011).

69. Caron, P. & Khan, T. Improvement of Creep strength in a nickel-base single-crystal superalloy by heat treatment. *Mater. Sci. Eng.* **61,** 173–184 (1983).

70. Fuchs, G. E. Solution heat treatment response of a third generation single crystal Ni-base superalloy. *Mater. Sci. Eng. A* **300,** 52–60 (2001).

71. Hegde, S. R., Kearsey, R. M. & Beddoes, J. C. Designing homogenization-solution heat treatments for single crystal superalloys. *Mater. Sci. Eng. A* **527,** 5528–5538 (2010).

72. Scarlin, R. B. Discontinuous precipitation in a directionally solidified nickel base alloy. *Scr. Metall.* **10,** 711–715 (1976).

73. Karunaratne, M. S. A., Rae, C. M. F. & Reed, R. C. On the microstructural instability of an experimental nickel-based single-crystal superalloy. *Metall. Mater. Trans. A* **32,** 2409–2421 (2001).

74. Walston, W., Schaeffer, J. & Murphy, W. A new type of microstructural instability in superalloys - SRZ. *Superalloys 1996, TMS* 9–18 (1996).

75. Zambaldi, C., Roters, F., Raabe, D. & Glatzel, U. Modeling and experiments on the indentation deformation and recrystallization of a single-crystal nickel-base superalloy. *Mater. Sci. Eng. A* **454–455,** 433–440 (2007).

76. Manna, I., Pabi, S. K. & Gust, W. Discontinuous reactions in solids. *Int. Mater. Rev.* **46,** 53–91 (2001).

77. Okazaki, M., Hiura, T. & Suzuki, T. Effect of Local Cellular Transformation on Fatigue Small Crack Growth in CMSX-4 and CMSX-2 at High Temperature. *Superalloys 2000, TMS* 505–514 (2000).

78. Nystrom, J. D., Pollock, T. M., Murphy, W. H. & Garg, A. Discontinuous cellular precipitation in a high-refractory nickel-base superalloy. *Metall. Mater. Trans. A* **28,** 2443–2452 (1997).

79. Welton, D. *et al.* Discontinuous Precipitation in Ni-Base Superalloys During Solution Heat Treatment. *Metall. Mater. Trans. A Phys. Metall. Mater. Sci.* **46,** 4298–4315 (2015).

80. Wu, Y. *et al.* Surface recrystallization of a Ni3Al based single crystal superalloy at different annealing temperature and blasting pressure. *Rare Met.* **31,** 209–214 (2012).

81. An, K. & Johnson, D. L. The pressure-assisted master sintering surface. *J. Mater. Sci.* **7,** 4555–4559 (2002).

82. Rahaman, M. N., Jonghe, L. C. & Brook, R. J. Effect of Shear Stress on Sintering. *J. Am. Ceram. Soc.* **69,** 53–58 (1986).

83. Kazemi, A., Faghihi-Sani, M. A. & Alizadeh, H. R. Investigation on cristobalite crystallization in silica-based ceramic cores for investment casting. *J. Eur. Ceram. Soc.* **33,** 3397–3402 (2013).

84. Kazemi, A., Faghihi-Sani, M. A., Nayyeri, M. J., Mohammadi, M. & Hajfathalian, M. Effect of zircon content on chemical and mechanical behavior of silica-based ceramic cores. *Ceram. Int.* **40,** 1093–1098 (2014).

85. Wereszczak, A. A. *et al.* Dimensional changes and creep of silica core ceramics used in investment casting of superalloys. *J. Mater. Sci.* **37,** 4235–4245 (2002).

86. Frye, H., Yasrebi, M. & Sturgis, D. H. Basic ceramic considerations for lost wax processing of high melting alloys. *St. Fe Symp. Techform, PCC Struct. Inc* 101–116 (2000).

87. Pollock, T. M. & Murphy, W. H. The breakdown of single-crystal solidification in high refractory nickel-base alloys. *Metall. Mater. Trans. A* **27,** 1081–1094 (1996).

88. D'Souza, N., Simmonds, S., West, G. D. & Dong, H. B. Role of elemental sublimation during solution heat treatment of Ni-based superalloys. *Metall. Mater. Trans. A Phys. Metall. Mater. Sci.* **44,** 4764–4773 (2013).

89. Simmonds, S. Formation and Avoidance of Surface Defects During Casting and Heat-Treatment of Single-Crystal Nickel- Based Superalloys - PhD Thesis. (2013).

90. Simmonds, S., D'Souza, N., Ryder, K. S. & Dong, H. Analysis of surface scale on the Ni-based superalloy CMSX-10N and proposed mechanism of formation. *IOP Conf. Ser. Mater. Sci. Eng.* **27,** 12038 (2012).

91. Brewster, G., D'Souza, N., Ryder, K. S., Simmonds, S. & Dong, H. B. Mechanism for Formation of Surface Scale during Directional Solidification of Ni-Base Superalloys. *Metall. Mater. Trans. A* **43,** 1288–1302 (2012).

92. D'Souza, N., Welton, D., West, G. D., Edmonds, I. M. & Wang, H. On the Roles of Oxidation and Vaporization in Surface Micro-structural Instability during Solution Heat Treatment of Ni-base Superalloys. *Metall. Mater. Trans. A Phys. Metall. Mater. Sci.* **45,** 5968–5981 (2014).

93. Panwisawas, C. *et al.* Prediction of Plastic Strain for Recrystallisation during Investment Casting of Single Crystal Superalloys. *Superalloys 2012, TMS* 547–556 (2012).

94. Panwisawas, C., Gebelin, J.-C. & Reed, R. C. Analysis of the mechanical deformation

arising from investment casting of directionally solidified nickel-based superalloys. *Mater. Sci. Technol.* **29,** 843–853 (2013).

95. Panwisawas, C., Gebelin, J. C., Warnken, N., Broomfield, R. W. & Reed, R. C. Numerical Modelling of Stress and Strain Evolution during Solidification of a Single Crystal Superalloy. *Adv. Mater. Res.* **278,** 204–209 (2011).

96. Panwisawas, C. *et al.* Prediction of recrystallization in investment cast single-crystal superalloys. *Acta Mater.* **61,** 51–66 (2013).

97. Meng, J., Jin, T., Sun, X. F. & Hu, Z. Q. Surface recrystallization of a single crystal nickel-base superalloy. *Int. J. Miner. Metall. Mater.* **18,** 197–202 (2011).

98. Mathur, H. Recrystallisation in single crystal nickel based Superalloys - PhD Thesis. (2013).

99. Jones, S. & Yuan, C. Advances in shell moulding for investment casting. *J. Mater. Process. Technol.* **135,** 258–265 (2003).

100. Bowen, N. L. & Greig, J. W. The system: Al2O3.SiO2. *J. Am. Ceram. Soc.* **7,** 238–254 (1924).

101. Blander, M. & Pelton, A. D. Thermodynamic analysis of binary liquid silicates and prediction of ternary solution properties by modified quasichemical equations. *Geochim. Cosmochim. Acta* **51,** 85–95 (1987).

102. Chao, C. H. & Lu, H. Y. Optimal Composition of Zircon – Fused Silica Ceramic Cores for Casting Superalloys. *J. Am. Ceram. Soc.* **79,** 773–779 (2002).

103. Zawrah, M. F. & Hamzawy, E. M. A. Effect of cristobalite formation on sinterability, microstructure and properties of glass/ceramic composites. *Ceram. Int.* **28,** 123–130 (2002).

104. Wilson, P. J., Blackburn, S., Greenwood, R. W., Prajapti, B. & Smalley, K. The role of zircon particle size distribution, surface area and contamination on the properties of silica-zircon ceramic materials. *J. Eur. Ceram. Soc.* **31,** 1849–1855 (2011).

105. Zhu, Y. *et al.* Effect of P, S, B and Si on the Solidification Segregation of Inconel 718 Alloy. *Superalloys 718, 625, 706 Var. Deriv. (1994), TMS* 89–98 (1994).

106. Zhu, H. Q. *et al.* Effect of phosphorus on solidification process and segregation of directionally solidified IN738 superalloy. *Metall. Mater. Trans. B* **26,** 831–837 (1995).

107. Holt, R. T. & Wallace, W. Impurities and trace elements in nickel-base superalloys.

Int. Mater. Rev. **21,** 1–24 (1976).

108. Starink, M. J., Cama, H. & Thomson, R. C. MC CARBIDES IN THE Hf CONTAINING Ni BASED SUPERALLOY MarM002. *Scr. Mater.* **38,** 73–80 (1998).

109. Chen, J., Lee, J. ., Jo, C. ., Choe, S. . & Lee, Y. . MC carbide formation in directionally solidified MAR-M247 LC superalloy. *Mater. Sci. Eng. A* **247,** 113–125 (1998).

110. Mihalisin, J. R., Corrigan, J. & Launsbach, M. Some effects of carbon in the production of single crystal superalloy castings. *Superalloys 2004, TMS* 795–800 (2004).

111. Jiang, W. H., Yao, X. D., Guan, H. R. & Hu, Z. Q. Secondary carbide precipitation in a directionally solified cobalt-base superalloy. *Metall. Mater. Trans. A* **30,** 513–520 (1999).

112. Yang, J., Zheng, Q., Sun, X., Guan, H. & Hu, Z. Relative stability of carbides and their effects on the properties of K465 superalloy. *Mater. Sci. Eng. A* **429,** 341–347 (2006).

113. Wang, D., Zhang, J. & Lou, L. H. Formation and stability of nano-scaled M23C6 carbide in a directionally solidified Ni-base superalloy. *Mater. Charact.* **60,** 1517–1521 (2009).

114. Liu, L. R. *et al.* Formation of carbides and their effects on stress rupture of a Ni-base single crystal superalloy. *Mater. Sci. Eng. A* **361,** 191–197 (2003).

115. Weiguo, Z., Lin, L. & Hengzhi, F. Effect of cooling rates on dendrite spacings of directionally solidified DZ125 alloy under high thermal gradient. *Rare Met.* **28,** 11–14 (2009).

116. Liu, L., Sommer, F. & Fu, H. Z. Effect of solidification conditions on MC carbides in a nickel-base superalloy IN 738 LC. *Scr. Metall. Mater.* **30,** 587–591 (1994).

117. Dong, X. *et al.* Microstructure of Carbides at Grain Boundaries in Nickel Based Superalloys. *J. Mater. Sci. Technol.* **28,** 1031–1038 (2012).

118. Szczotok, a & Rodak, K. Microstructural studies of carbides in Mar-M247 nickel-based superalloy. *IOP Conf. Ser. Mater. Sci. Eng.* **35,** 12006 (2012).

119. Lvov, G., Levit, V. I. & Kaufman, M. J. Mechanism of primary MC carbide decomposition in Ni-base superalloys. *Metall. Mater. Trans. A* **35,** 1669–1679 (2004).

120. Wasson, A. J. & Fuchs, G. E. The effect of carbide morphologies on elevated temperature tensile and fatigue behavior of a modified single crystal Ni-base

superalloy. *Superalloys 2008, TMS* 489–497 (2008).

121. Gao, M. & Wei, R. P. Precipitation of intragranular M23C6 carbides in a nickel alloy: Morphology and crystallographic feature. *Scr. Metall. Mater.* **30,** 1009–1014 (1994).

122. Litz, J., Rahmel, A. & Schorr, M. Selective carbide oxidation and internal nitridation of the Ni-base superalloys IN 738 LC and IN 939 in air. *Oxid. Met.* **30,** 95–105 (1988).

123. Cockcroft, S. L., Degawa, T., Mitchell, A., Tripp, D. W. & Schmalz, A. Inclusion Precipitation in Superalloys. *Superalloys 1992, TMS* 577–586 (1992).

124. Voorhees, K. J., Baugh, S. F. & Stevenson, D. N. The thermal degradation of poly(ethylene glycol)/poly(vinyl alcohol) binder in alumina ceramics. *Thermochim. Acta* **274,** 187–207 (1996).

125. Fernández, M. D. & Fernández, M. J. Thermal degradation of copolymers from vinyl acetate and vinyl alcohol. *J. Therm. Anal. Calorim.* **92,** 829–837 (2008).

126. Lander, J. J., Kern, H. E. & Beach, A. L. Solubility and diffusion coefficient of carbon in nickel: Reaction rates of nickel-carbon alloys with barium oxide. *J. Appl. Phys.* **23,** 1305–1309 (1952).

127. Moore, J. J. & Feng, H. J. Combustion synthesis of advanced materials: Part II. Classification, applications and modelling. *Prog. Mater. Sci.* **39,** 275–316 (1995).

128. Moore, J. J. & Feng, H. J. Combustion synthesis of advanced materials: Part I. Reaction parameters. *Prog. Mater. Sci.* **39,** 243–273 (1995).

129. Gale, W. F. & King, J. E. Precipitation of chromium containing phases in aluminide coated nickel-base superalloy single crystals. *J. Mater. Sci.* **28,** 4347–4354 (1993).

130. Munir, Z. A. & Anselmi-Tamburini, U. Self-propagating exothermic reactions: The synthesis of high-temperature materials by combustion. *Mater. Sci. Reports* **3,** 279–365 (1989).

131. Fan, Q., Chai, H. & Jin, Z. Dissolution-precipitation mechanism of self-propagating high-temperature synthesis of mononickel aluminide. *Intermetallics* **9,** 609–619 (2001).

132. Li, Y., Nan, Y. xiong, Guo, W. xiang, Che, H. qing & Fan, Q. cheng. Dissolution-precipitation-decomposition-crystallization mechanism of self-propagating high-temperature synthesis of Al3Ni2. *Intermetallics* **18,** 179–187 (2010).

133. Zhu, P., Li, J. C. M. & Liu, C. T. Reaction mechanism of combustion synthesis of NiAl.

Mater. Sci. Eng. A **329–331,** 57–68 (2002).

134. Naiborodenko, Y. S. & Itin, V. I. Gasless combustion of metal powder mixtures. *Combust. Explos. Shock Waves* **11,** 293–300 (1975).

135. Philpot, K. A., Munir, Z. A. & Holt, J. B. An investigation of the synthesis of nickel aluminides through gasless combustion. *J. Mater. Sci.* **22,** 159–169 (1987).

136. Cahn, R. W. Self- Propagating High-Temperature Synthesis. *Adv. Mater. Res. News* **2,** 314–316 (1990).

137. Varma, A., Rogachev, A. S., Mukasyan, A. S. & Hwang, S. Combustion Synthesis of Advanced Materials: Principles and Applications. *Adv. Chem. Eng.* **24,** 79–226 (1998).

138. Aldushin, A. P., Martem'yanova, T. M., Merzhanov, A. G., Khaikin, B. I. & Shkadinskii, K. G. Autovibrational propagation of the combustion front in heterogeneous condensed media. *Combust. Explos. Shock Waves* **9,** 531–542 (1975).

139. Wong, J. *et al.* Time-Resolved X-ray Diffraction Study of Solid Combustion Reactions. *Science* **249,** 1406–1409 (1990).

140. Zhu, P., Li, J. C. M. & Liu, C. T. Combustion reaction in multilayered nickel and aluminum foils. *Mater. Sci. Eng. A239* – **240,** 532–539 (1997).

141. Dyer, T. S. & Munir, Z. A. The synthesis of nickel aluminides by multilayer self-propagating combustion. *Metall. Mater. Trans. B* **26,** 603–610 (1995).

142. Galetz, M. C. *et al.* The role of combustion synthesis in the formation of slurry aluminization. *Intermetallics* **44,** 8–17 (2014).

143. Montero, X., Galetz, M. C. & Schütze, M. A Novel Type of Environmentally Friendly Slurry Coatings. *JOM, TMS* **67,** 77–86 (2015).

144. Rasmussen, A. J., Agüero, A., Gutierrez, M. & José Landeira Østergård, M. Microstructures of thin and thick slurry aluminide coatings on Inconel 690. *Surf. Coatings Technol.* **202,** 1479–1485 (2008).

145. Shirvani, K., Saremi, M., Nishikata, A. & Tsuru, T. The role of Silicon on Microstructure and High Temperature Performance of Aluminide Coating on Superalloy In-738LC. *Mater. Trans.* **43,** 2622–2628 (2002).

146. Kircher, T. A., McMordie, B. G. & McCarter, A. Performance of a silicon-modified aluminide coating in high temperature hot corrosion test conditions. *Surf. Coatings*

Technol. **68–69,** 32–37 (1994).

147. Berry, D., Meelue, M., McMordie, B. & Kircher, T. Enchancing Performance of Silicon-modified Slurry Aluminides on Turbine Components Operating in Marine E nvironments. *Am. Soc. Mech. Eng.* 1–6 (1995). doi:10.1115/95-GT-359

148. Pahlavanyali, S., Pang, H. T., Li, F., Bagnall, S. & Rae, C. On effect of salt deposits on oxidation behaviour of CMSX-4 above 1000°C. *Mater. Sci. Technol.* **30,** 1890–1898 (2014).

Appendix

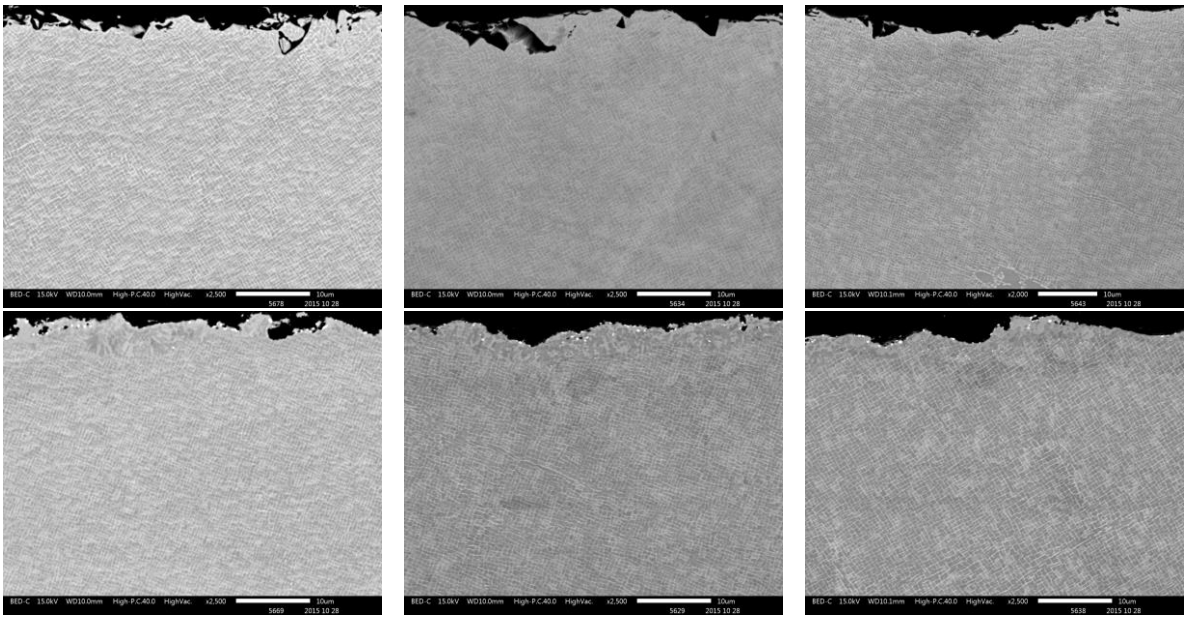

Fig. A1 – CMSX-10N blasted with 220 mesh alumina at 15 PSI (a), at 30 PSI (b) and 45 PSI (c) and then after subsequent heat treatment (d), (e) and (f)

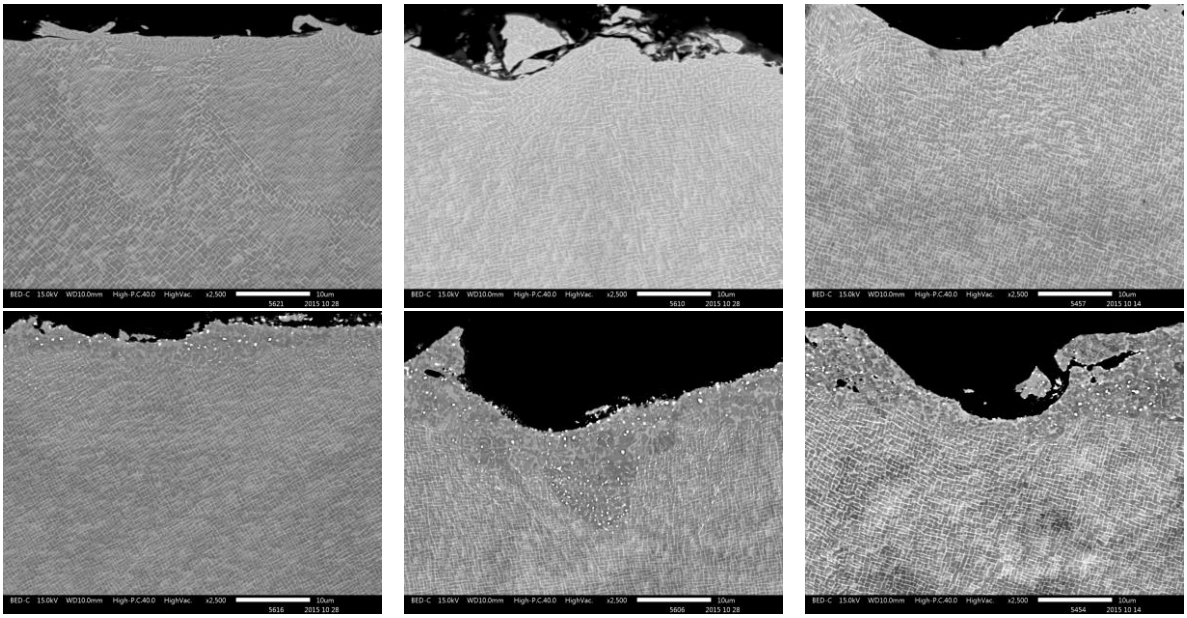

Fig. A2 – CMSX-10N blasted with 60 mesh alumina at 15 PSI (a), at 30 PSI (b) and 45 PSI (c) and then after subsequent heat treatment (d), (e) and (f)

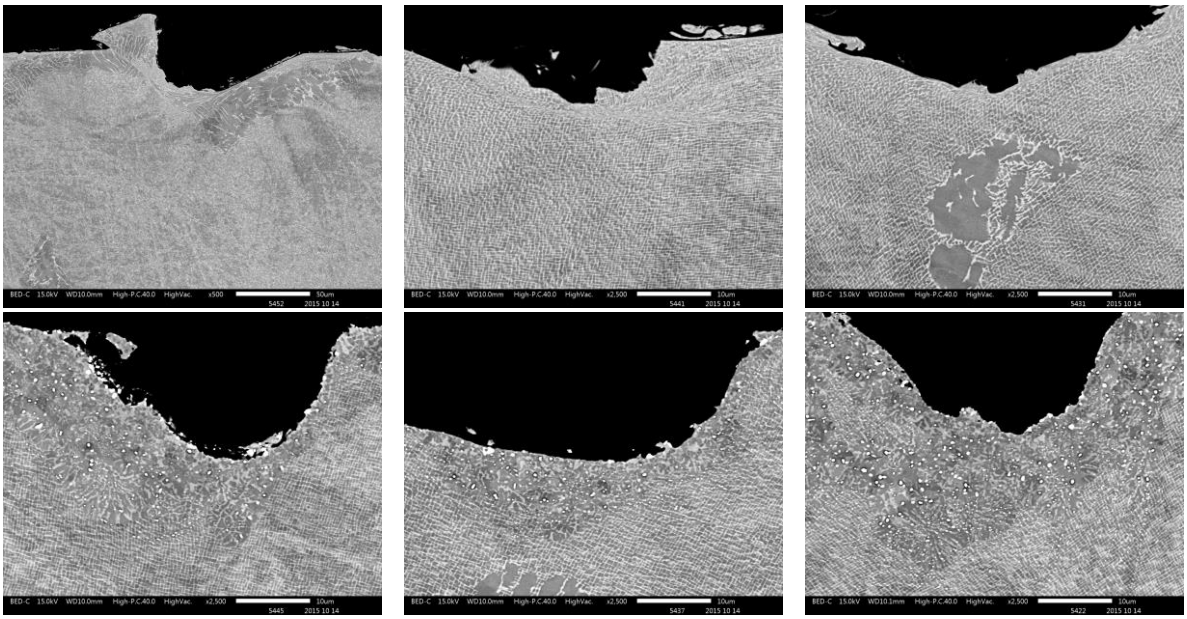

Fig. A3 – CMSX-10N blasted with 20 mesh alumina at 15 PSI (a), at 30 PSI (b) and 45 PSI (c) and then after subsequent heat treatment (d), (e) and (f)

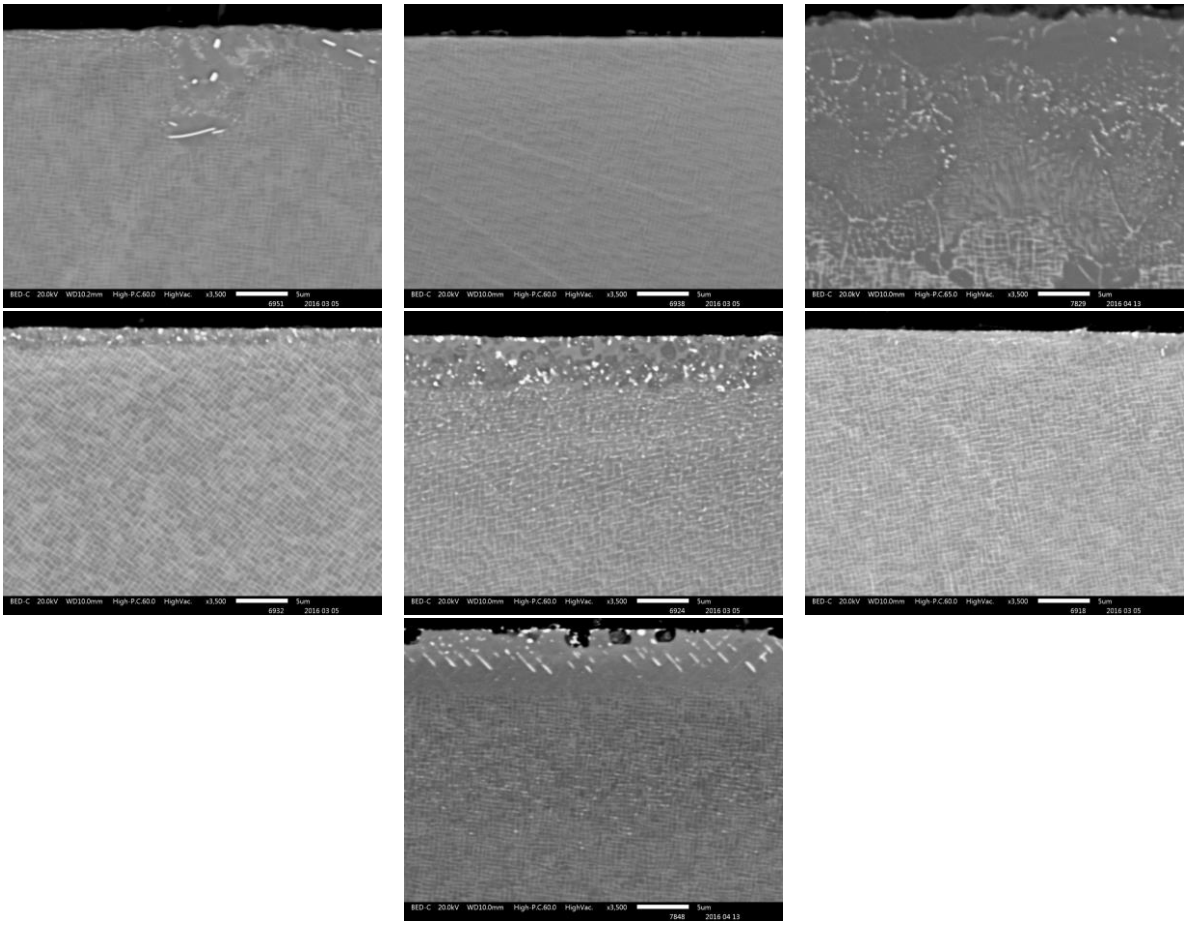

Fig. A4 – carburising results from temperature variation trials upon the alloy CMSX-10N, 800°C (a), 850°C (b), 900°C (c), 950°C (d), 1000°C (e), 1050°C (f), 1100°C (g)

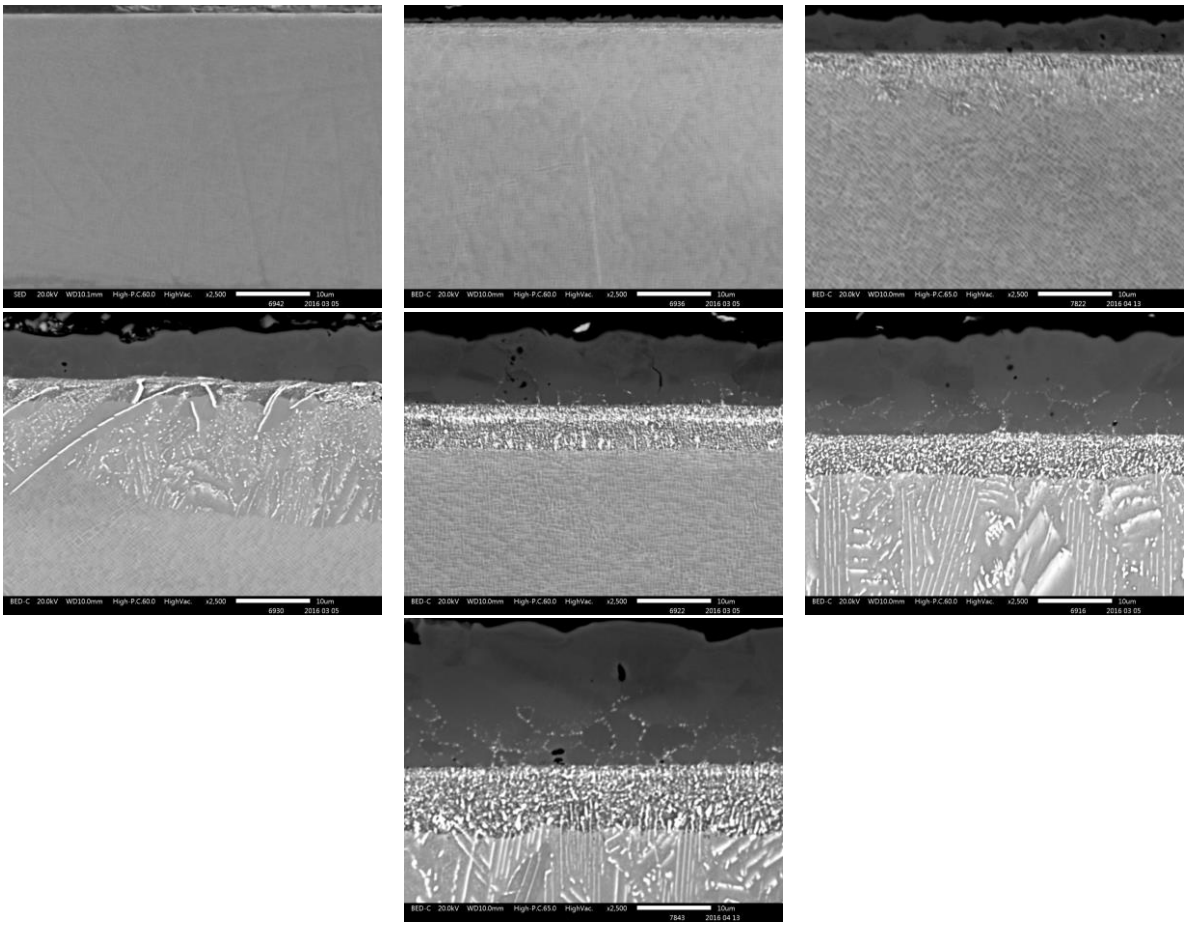

Fig. A5 – vapour phase aluminising results from temperature variation trials upon the alloy CMSX-10N, 800°C (a), 850°C (b), 900°C (c), 950°C (d), 1000°C (e), 1050°C (f), 1100°C (g)

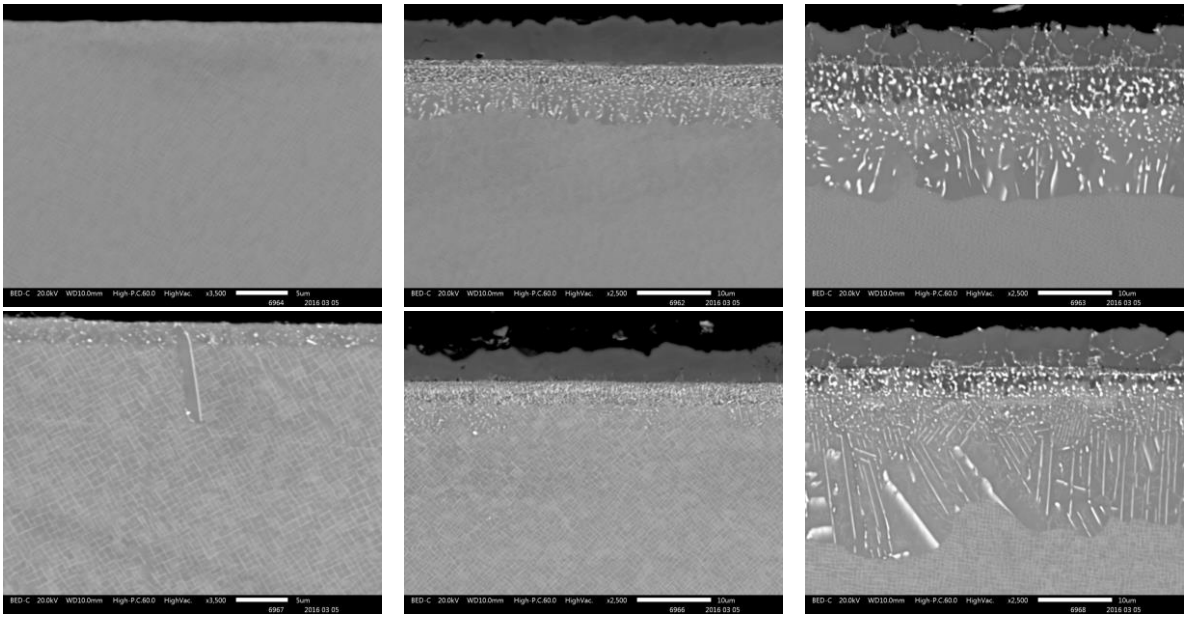

Fig. A6 – carburising and vapour phase aluminising results from rapid 5 minute hold time trials upon the alloys CMSX-4 and CMSX-10N, SX-4 carburised (a), SX-4 aluminised 'green' (b), SX-4 aluminised HT'd (c), SX-10N carburised (d), SX-10N aluminised 'green' (e), SX-10N aluminised HT'd (f)

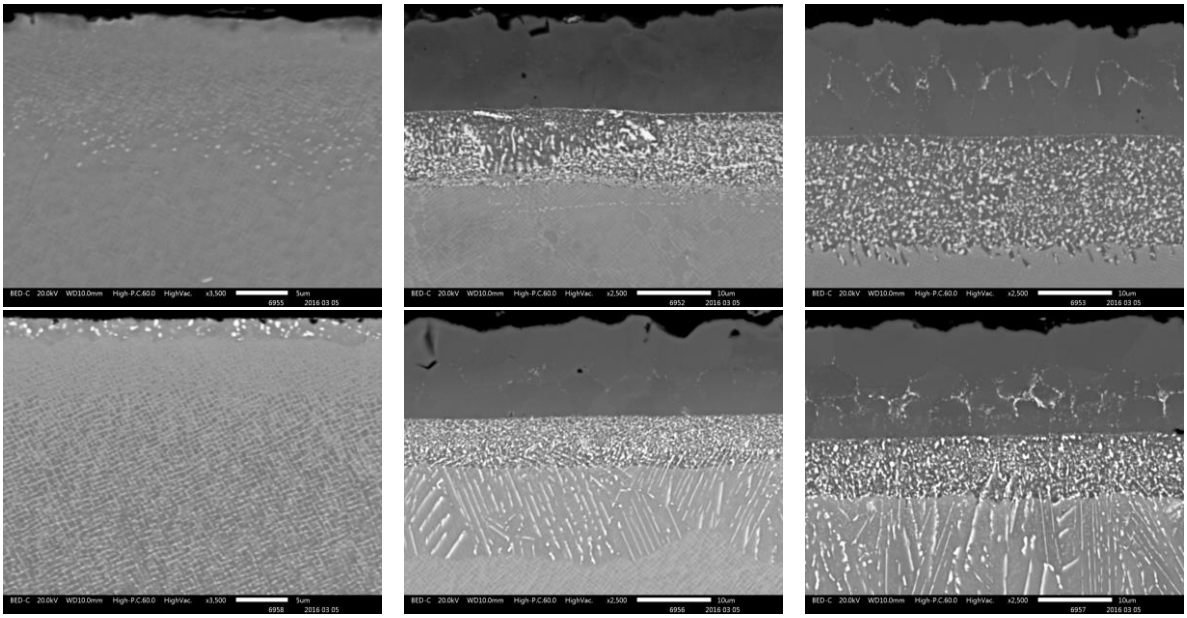

Fig. A7 – carburising and vapour phase aluminising results from interrupted climb 700°C hold for 1 hour trials upon the alloys CMSX-4 and CMSX-10N, SX-4 carburised (a), SX-4 aluminised 'green' (b), SX-4 aluminised HT'd (c), SX-10N carburised (d), SX-10N aluminised 'green' (e), SX-10N aluminised HT'd (f)

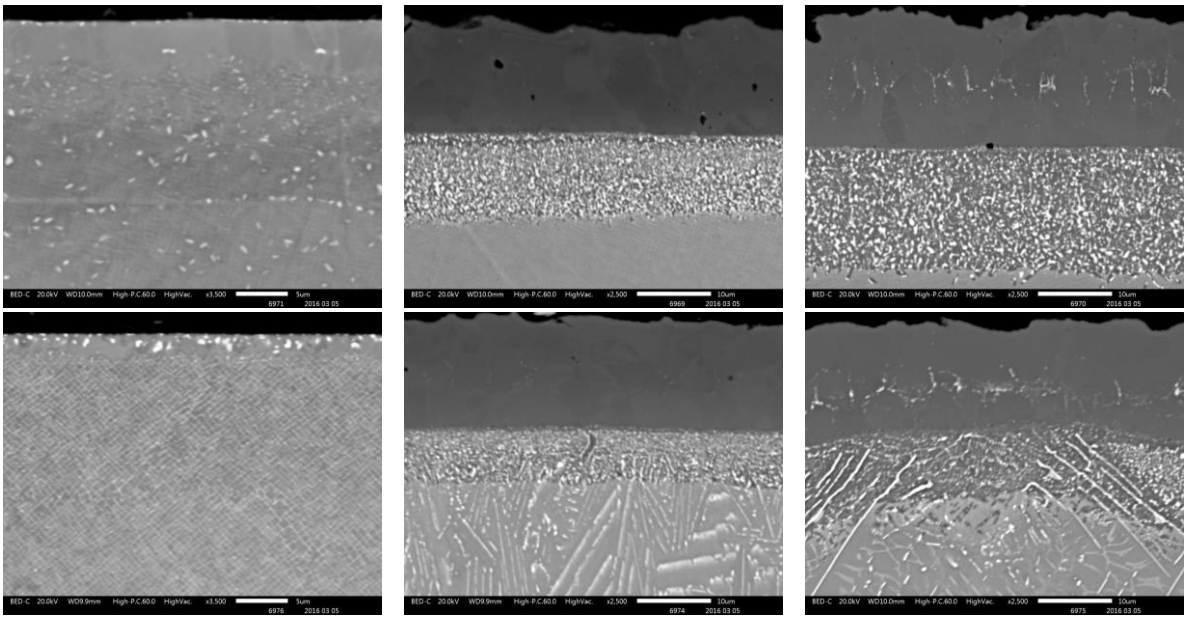

Fig. A8 – carburising and vapour phase aluminising results from slow climb trials upon the alloys CMSX-4 and CMSX-10N, SX-4 carburised (a), SX-4 aluminised 'green' (b), SX-4 aluminised HT'd (c), SX-10N carburised (d), SX-10N aluminised 'green' (e), SX-10N aluminised HT'd (f)

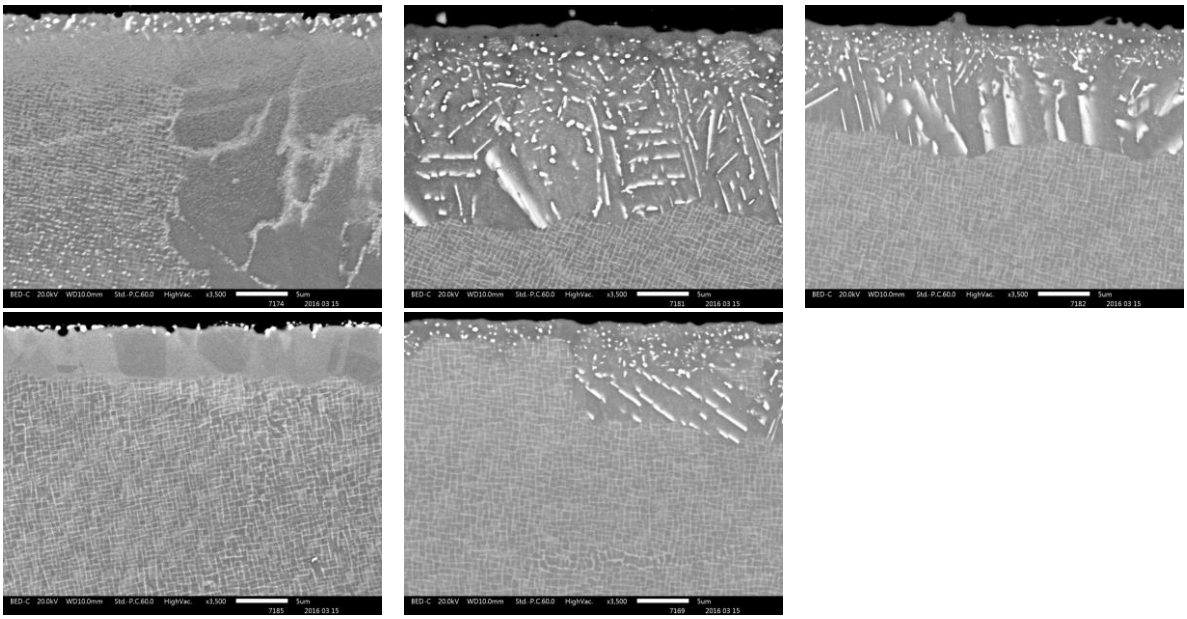

Fig. A9 – carburising results from 5 special trials upon the alloy CMSX-10N, thin M1™ (a), medium M1™ (b), thick M1™ (c), PVA parting layer (d), steel box filled with M1™ metal powder only and topped with M7™ (e)

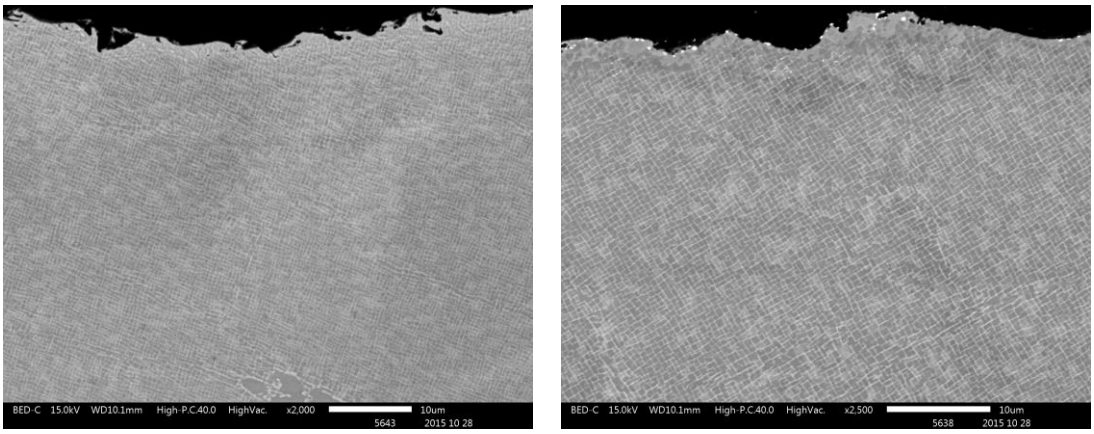

Fig. A10 – SEM micrographs effect of grit blasting CMSX-10N with 220 mesh alumina grit at 45 PSI, post-blast (a), post-heat treatment (b)

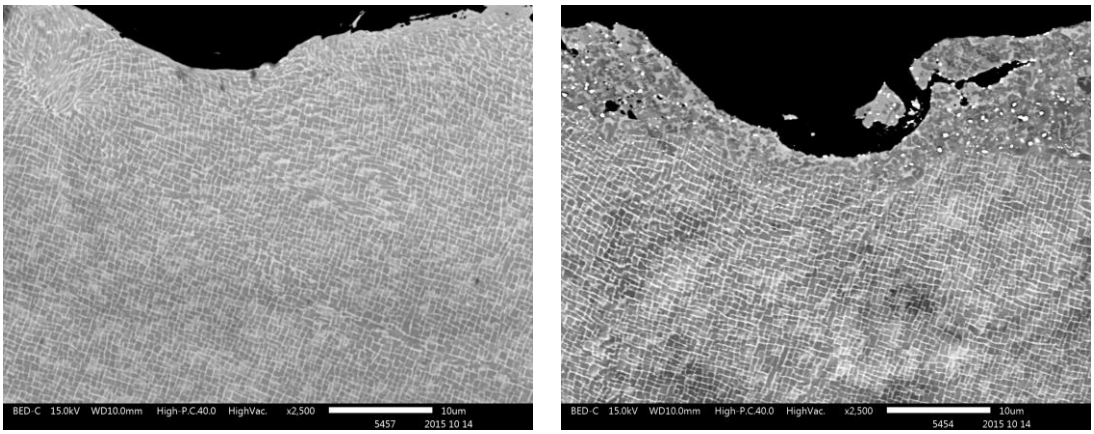

Fig. A11 – SEM micrographs effect of grit blasting CMSX-10N with 60 mesh alumina grit at 45 PSI, post-blast (a), post-heat treatment (b)

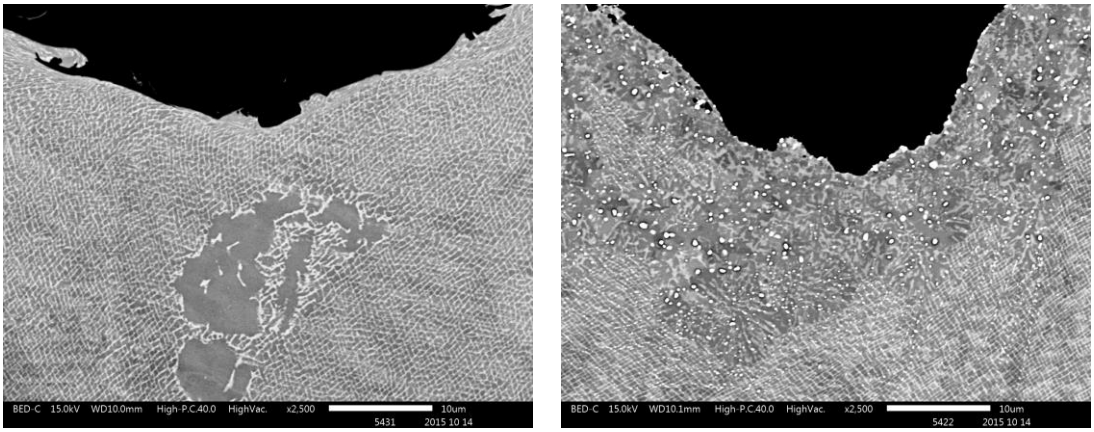

Fig. A12 – SEM micrographs effect of grit blasting CMSX-10N with 20 mesh alumina grit at 45 PSI, post-blast (a), post-heat treatment (b)

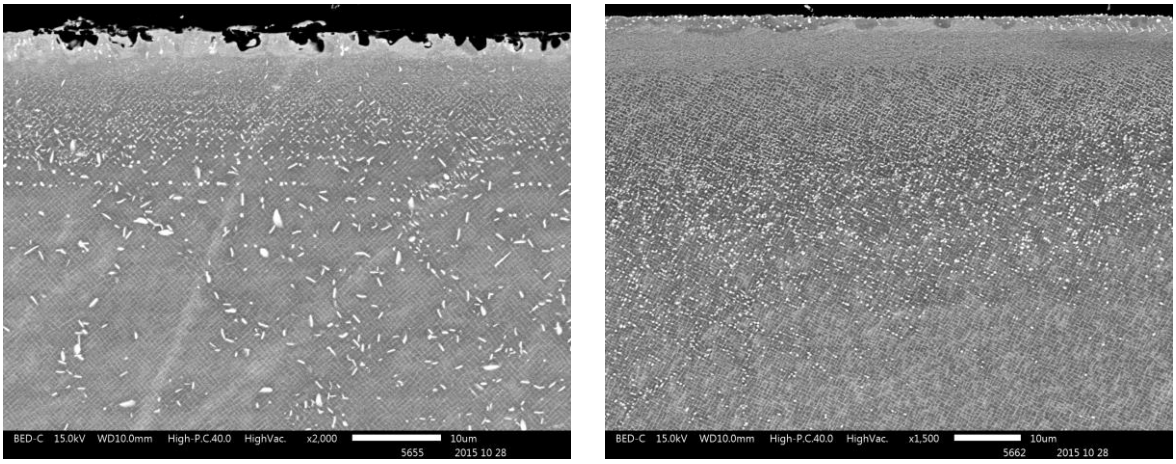

Fig. A13 – SEM micrographs ground smooth surface finish carburised sub-surface region upon alloy CMSX-4 (a) and CMSX-10N (b)